SEISMIC PERFORMANCE OF MULTI-STOREY FRAMES WITH SLIM-FLOOR BEAM-TO-COLUMN JOINTS

A Thesis Submitted for obtaining
the Scientific Title of PhD in Engineering
from
Politehnica University Timișoara
in the Field of Civil Engineering
by

Eng. Rafaela-Florina DON

PhD Committee Chair:	Prof. Dr.
PhD Supervisor:	Prof. Dr. Adrian Ciutina
Scientific Reviewers:	Prof. Dr.
	Prof. Dr.
	Prof. Dr.

Date of the PhD Thesis Defence: dd.mm.2023

The PhD thesis series of UPT are:

1. Automation
2. Chemistry
3. Energetics
4. Chemical Engineering
5. Civil Engineering
6. Electrical Engineering
7. Electronic Engineering and Telecommunications
8. Industrial Engineering
9. Mechanical Engineering
10. Computer science and Information Technology
11. Science and Material Engineering
12. Systems Engineering
13. Energy Engineering
14. Computers and Information Technology
15. Materials Engineering
16. Engineering and Management
17. Architecture
18. Civil Engineering and Installations
19. Electronics, Telecommunications and Information Technologies

Politehnica University Timișoara, Romania, initiated the above series to disseminate the expertise, knowledge and results of the research carried out within the doctoral school of the university. According to the Decision of the Executive Office of the University Senate No. 14/14.07.2006, the series includes the doctoral theses defended in the university since October 1, 2006.

România, 300223 Timişoara, Bd. Vasile Pârvan no. 2B
Tel. / Fax: +40-(0)256 404677
E-mail: editura@upt.ro

Acknowledgement

……
……
……
……
……
……
……
……
……
……

Timişoara, Month 2023 Rafaela-Florina Don

DON, Rafaela-Florina

Seismic performance of multi-storey frames with slim-floor beam-to-column

(Performanța seismică a structurilor multietajate în cadre cu noduri grindă-stâlp de tip slim-floor)

PhD theses of UPT, Series X, No. YY, Editura Politehnica, 2023, … pages, ... figures, … tables.

ISSN:

ISBN:

Key words:

multi-storey steel-concrete composite frames, moment-resisting frames, concentrically-braced frames, dual concentrically-braced frames, beam-to-column joints, bolted end plate connections, slim-floor, seismic performance, nonlinear static and dynamic structural analyses, finite element analysis

Abstract:

……
……
……
……
……
……
……
……
……
……
……
……
……
……
……
……

Table of contents

List of figures

List of tables

List of notations, abbreviations and acronyms

Notations

Chapter 1
.. ..

Chapter 2
.. ..

Chapter 3
.. ..

Chapter 4
.. ..

Chapter 5
.. ..

Chapter 6
.. ..

Abbreviations

.. ..

Acronyms

.. ..
.. ..

REZUMAT

Planșeul subțire de tip *slim-floor* este o soluție alternativă la planșeele clasice. Caracteristica definitorie a acestuia este dată de integrarea profilului asimetric al unei grinzi de oțel, dar și al altor componente, în planșeul de beton armat. Odată cu anii 1990, când acestor sisteme compuse le sunt recunoscute avantajele arhitecturale considerabile la scară largă, planșeele de tip *slim-floor* încep să fie utilizate cu succes în practica de construcții a clădirilor de birouri și a celor rezidențiale. Cu toate acestea, datorită utilizării actuale a grinzilor din planșeele de tip *slim-floor* sub formă de grinzi articulat-simplu rezemate, aplicarea acestora este limitată la sistemele de preluare a forțelor gravitaționale. Utilizarea grinzilor sub această formă este incompatibilă cu proiectarea la seism a cadrelor, ce în conformitate cu norma seismică europeană, EN 1998-1, trebuie realizată prin aplicarea principiilor *Metodei de proiectare la capacitate*. Însă prin *Metoda de proiectare la capacitate* li se impune anumitor elemente structurale ale cadrelor necontravântuite, precum grinzilor, să se deformeze sau să aibă caracter ductil, în timp ce altora, ca îmbinărilor și stâlpilor, să nu se deformeze sau să aibă caracter neductil.

Primul aspect problematic al utilizării curente a nodurilor de planșee de tip *slim-floor* în contextul sistemelor în cadre este constituit de îmbinarea grindă-stâlp care, în loc să fie total rezistentă și rigidă sau chiar semi-rigidă, este articulată. Al doilea aspect problematic este legat de asigurarea caracterului ductil al unor membre, ce în cazul de față, se referă direct la abilitatea grinzii planșeului de tip *slim-floor* de a fi disipativă în ciuda înglobării parțiale în beton, dar și a existenței unei tălpi inferioare mai late a grinzii. Prin urmare, soluția actuală a planșeului de tip *slim-floor* nu este compatibilă cu proiectarea la seismicitate moderată spre ridicată. Un alt aspect ce pune dificultăți este constituit de faptul că proiectarea acestor planșee este în principal realizată prin intermediul unor autorizații tehnice. Până la intrarea în vigoare a noii versiuni a codului european pentru calculul construcțiilor compuse, prEN 1994-1-1, în care anumite reguli vor fi incluse, proiectarea este rezervată din punct de vedere al accesibilității, iar aplicațiile sunt limitate.

Studiul de față este creat cu scopul de a dezvolta o soluție tehnică pentru noduri grindă-stâlp aparținând unui planșeu de tip *slim-floor*, făcând astfel sistemele cu planșee subțiri pretabile structurilor în cadre proiectate la seismicitate ridicată (de exemplu, indice al acțiunii seismice S_δ mai mare decât 6.50 m/s^2). Rezultate ale unor analize cu element finit (în termeni de transfer al tensiunilor și de dezvoltare a deformațiilor specifice plastice, "plastic strain") referitoare la răspunsul la forțe laterale al nodurilor grindă-stâlp *slim-floor* cu diverse configurații au fost obținute în cadrul studiului de masterat al autoarei. Aceste rezultate au condus la dezvoltarea soluției propuse în studiul curent. Cerințele de rezistență și rigiditate au fost estimate prin intermediul unor analize structurale efectuate anterior încercărilor experimentale. Analizele necesare proiectării finale au fost urmate de încercări experimentale în regim monoton și ciclic pe specimene reprezentând ansamble unilaterale de noduri grindă-stâlp. Principala componentă disipativă, grinda planșeului de tip *slim-floor*, a fost realizată din jumătate dintr-un profil IPE 600, pe care o placă metalică lată (cu lățimea x grosimea: 380 x 20 mm) a fost sudată cu rol de talpă inferioară. Strict tălpii inferioare a grinzii *slim-floor* asimetrice i s-a aplicat o secțiune redusă numită *Reduced Flange Section* (*RFS*), considerându-se dimensiunile propuse în studiul curent.

Secțiunea transversală finală a grinzii *slim-floor* include conectori de tip *concrete dowels* și armături, fiind parțial înglobată în beton. Înălțimea totală a planșeului a fost de 370 mm. Ambele încercări experimentale în regim monoton și ciclic au evidențiat un răspuns histeretic cu caracter ductil, stabil și simetric al nodurilor, îndeplinind criteriul AISC 341-16 prin dezvoltarea unei capacități de rotire Starea Limită Ultimă de ± 45.4 miliradiani. Considerând clasificările pe criterii de rezistență și rigiditate prevăzute în codul prEN 1993-1-8, nodurile au fost încadrate în categoria celor cu rezistență totală și semi-rigide în cazul utilizării în cadre necontravântuite, respectiv rigide – atunci când fac parte din cadre contravântuite. Ulterior calibrării modelului numeric de referință, concluziile încercărilor experimentale cu privire la mecanismul de cedare cu caracter ductil - constând în dezvoltarea unei articulații plastice în zona disipativă a grinzii *slim-floor* și în răspunsul elastic al îmbinării cu șuruburi – au fost de asemenea dublate de analizele cu element finit. Mai mult de atât, acuratețea modelului numeric a făcut posibilă studierea detaliată a influenței mai multor parametri asupra rezistenței, rigidității și capacității de rotire a nodului grindă-stâlp de tip *slim-floor*, evidențiind componentele critice, precum secțiunea redusă numită *Reduced Flange Section*.

Bazat pe rezultatele experimentale și numerice, a fost dezvoltată o procedură de proiectare și detaliere adresată grinzilor compuse *slim-floor* a căror secțiune transversală are forma I, iar acestea sunt conectate la stâlpi metalici prin îmbinări cu șuruburi. Baza procedurii de proiectare este reprezentată de principiile *Metodei de proiectare la capacitate* pentru noduri metalice și compuse ale cadrelor necontravântuite din clasa de ductilitate 3, dar și de anumite reguli de proiectare din varianta pre-normativă a EN 1994-1 pentru planșee de tip *slim-floor*. În plus, o metodă pentru asigurarea unui caracter ductil al grinzii *slim-floor*, prin intermediul aplicării unei secțiuni reduse *Reduced Flange Section*, a fost propusă în studiul de curent. În vederea evaluării performanței seismice a sistemelor structurale în cadre cu noduri grindă-stâlp de tip *slim-floor*, un model numeric al nodului a fost creat pe baza rezultatelor obținute pe cale experimentală. În acest scop, partea plastică a curbei înfășurătoare, ce corespunde zonei disipative înglobate în beton a grinzii *slim-floor,* a fost folosită pentru definirea răspunsului în domeniul neliniar al acestei componente. Modele realiste ale îmbinării cu șuruburi, panoului de inimă al stâlpului și contravântuirii au fost create. Evaluarea performanței seismice a fost realizată pe cadre necontravântuite cu patru etaje, pe cadre contravântuite centric cu șaisprezece etaje și pe cadre duale cu același număr de niveluri prin aplicarea unor analize neliniare statice și dinamice. În toate dintre aceste studii de caz, noduri grindă-stâlp de tip *slim-floor* au fost utilizate. Performanța seismică a fost evaluată pe criteriile ultimei versiuni ale codului seismic european în termeni de drifturi de etaj la Starea Limită de Serviciu și Starea Limită Ultimă, rotiri plastice ale grinzilor *slim-floor* și modul de dezvoltare al mecanismului global al structurii. Atât pe baza rezultatelor din analizele *Pushover* cu *N2* cât și pe a celor obținute prin aplicarea *Response-History Analysis* cu șapte accelerograme, s-a concluzionat că nodurile grindă-stâlp *slim-floor* pot fi integrate în sisteme structurale în cadre, iar performanța seismică a acestora este una adecvată. Mai mult de atât, nodurilor grindă-stâlp de tip *slim-floor* li se pot aplica principiile *Metodei de proiectare la capacitate*, date fiind abilitatea de a disipa energie seismică în capetele grinzii și suprarezistența altor componente precum îmbinarea cu șuruburi, sudurile adiacente și panoul de inimă al stâlpului.

SUMMARY

The slim-floor is an alternative flooring solution to classic flooring systems. The defining feature of the slim-floor is the integration of the asymmetric steel beam and other components into the reinforced concrete slab. Since the 1990s, when this composite system was recognised as providing considerable architectural advantages, slim-floors have been successfully applied to office and residential buildings. However, due to the fact that slim-floor beams are currently used as simply-supported beams with pinned end connections, their application is limited to gravity load-resisting systems. This application is incompatible with the seismic design of frame systems, which according to the European seismic code, EN 1998-1, should be performed by applying capacity design principles. Nevertheless, capacity design requires specific structural members of Moment-Resisting Frames such as the beams, to yield or to be dissipative, while other components such as the connections and columns, not to yield or to be non-dissipative.

The first issue of the existing slim-floor joints in the context of framed systems is the beam-to-column connection, which is pinned instead of full-strength and rigid or semi-rigid. The second issue is related to ensuring member ductility, which in this case directly refers to the ability of the slim-floor beam to be dissipative, despite the partial concrete encasement and also the existence of the wider lower flange of the beam. Therefore, the slim-floor solution in its present form is not compatible with design for moderate-to-high seismicity. An additional issue resides in the actual design of the slim-floor, which is mainly governed by technical approvals. Until the new version of the composite European code, prEN 1994-1-1, comes into force, in which some rules will be included, design is only fairly approachable, and applications limited.

The current study is developed with the aim to provide a technical solution for slim-floor beam-to-column joints, which would make the shallow flooring system applicable to framed structures designed for high seismicity (e.g., seismic action index S_δ higher than 6.50 m/s^2). Some Finite Element Analysis results (in terms of stress transfer and plastic strain development) on the response of slim-floor beam-to-column joints with different configurations subjected to lateral loads were investigated as part of the Master Thesis of the author. These led to the development of the technical solution proposed within the current study. The resistance and stiffness demands were estimated by means of pre-test structural analyses. Following advanced pre-test investigations needed for the final design, monotonic and cyclic experimental tests were performed on sub-assembly specimens, which consisted of single-sided slim-floor beam-to-column joints. The main dissipative component, the slim-floor beam, was made from half of an IPE 600 steel profile, on which a wide steel plate (w x t: 380 x 20 mm) was welded as its lower flange. Exclusively to the lower flange of the asymmetric slim-floor beam, a *Reduced Flange Section* (*RFS*) was applied considering dimensions provided in the current study. The final cross section of the slim-floor beam included concrete dowels and rebars, and was partially encased in concrete. The total floor height was 370 mm. Both the monotonic and cyclic tests evidenced a ductile, stable and symmetric hysteretic response of the joints which fulfilled the criterion of AISC 341-16 by developing a rotation capacity at Significant Damage of ± 45.4 mrad. Considering the resistance and stiffness classifications of

prEN 1993-1-8, the joints were full-strength and semi-rigid according to criteria for unbraced frames, respectively rigid corresponding to the classification applied to braced frames. Following the calibration of the reference numerical model, the experimental conclusions related to the ductile failure mechanism, consisting of the development of a plastic hinge in the dissipative zone of the slim-floor beam, and to the elastic response of the bolted connection were reinforced by means of FEA. Moreover, the reliability of the numerical model also provided the opportunity to further investigate the influence of several parameters on the resistance, stiffness and rotation capacity of the slim-floor beam-to-column joint and to emphasize critical components, such as the *RFS*.

Based on experimental and numerical outcomes, a design and detailing procedure addressed to I-composite slim-floor beams connected to steel columns through bolted connections were developed. The basis of the design procedure consisted of the main principles of capacity design for steel and composite joints of Moment-Resisting Frames for *Ductility Class 3* and of some design rules from the pre-normative version of EN 1994-1 for slim-floors. In addition, a method for ensuring ductility of the SF beam was provided through the implementation of a *Reduced Flange Section*. In order to assess the seismic performance of framed systems with slim-floor beam-to-column joints, a numerical model of the joint was developed based on experimental data. For this purpose, the plastic part of the envelope curve corresponding to the concrete-encased dissipative zone of the slim-floor beam was used to define the nonlinear response of the component. Realistic models of the bolted connection, of the web panel and of the braces were defined. The seismic performance assessment was performed on 4-storey Moment-Resisting Frames, 16-storey Concentrically-Braced Frames and on 16-storey Dual Concentrically-Braced Frames by applying nonlinear static and nonlinear dynamic analyses. In all the case studies performed in the framework of the dissertation slim-floor beam-to-column joints were used. The seismic performance was evaluated on criteria of the latest version of the European seismic code in terms of interstorey drifts at Damage Limitation and Significant Damage, plastic rotation of the slim-floor beams and development of global mechanism. Based on the results of the *Pushover* with *N2* analyses, as well as on those of the *Response-History Analyses* with seven accelerograms, slim-floor beam-to-column joints could be integrated in framed systems and do provide adequate seismic performance. Furthermore, slim-floor beam-to-column joints are also applicable to capacity design principles, by providing seismic energy dissipation at the beam ends, and the overstrength of other components such as the bolted connection, the adjacent welds and the column web panel.

KURZFASSUNG

Das Slim-Floor-System ist eine alternative Lösung zu klassischen Deckensystemen. Kennzeichnend für das Slim-Floor-System ist die Integration des asymmetrischen Stahlträgers und anderer Komponenten in die Stahlbetonplatte. Seit den 1990er Jahren, als die erheblichen architektonischen Vorteile des Verbundsystems erkannt wurden, werden Slim-Floor-Systeme erfolgreich bei Büro- und Wohngebäuden eingesetzt. Da Slim-Floor-Träger derzeit jedoch als einfach gestützte Träger mit gelenkigen Endverbindungen verwendet werden, ist die Anwendbarkeit auf Systeme für den vertikalen Lastabtrag beschränkt. Diese Anwendung ist mit der seismischen Bemessung von Rahmensystemen nicht vereinbar, die gemäß der Europäischen Erdbebennorm EN 1998-1 nach dem Grundsatz der Kapazitätsbemessung erfolgen soll. Laut Kapazitätsbemessung müssen jedoch bestimmte Strukturelemente von biegesteifen Rahmen, wie z.B. die Träger, nachgiebig oder dissipativ sein, während andere Komponenten, wie z.B. die Verbindungen und Stützen, nicht nachgiebig oder nicht dissipativ sein dürfen.

Der erste problematische Aspekt des derzeitigen Einsatzes von Slim-Floor-Systemen im Zusammenhang mit Rahmensystemen ist die Verbindung zwischen Träger und Stütze, welche gelenkig und nicht volltragfähig und starr ausgeführt wird. Der zweite problematische Aspekt bezieht sich auf die Gewährleistung der Duktilität einiger Bauteile, die in diesem Fall direkt mit der Fähigkeit des Slim-Floor-Trägers zusammenhängt, welcher trotz der teilweisen Einbettung in Beton und der Existenz eines breiteren unteren Trägerflansches dissipativ sein soll. Daher ist die derzeitige Slim-Floor-Lösung nicht mit der Auslegung für mittlere bis hohe Seismizität geeignet. Ein weiterer problematischer Aspekt ist die Bemessung der Slim-Floor-Systeme, welche hauptsächlich über technische Zulassungen erfolgt. Bis zum Inkrafttreten der neuen Version der europäischen Norm für die Berechnung von Verbundkonstruktionen prEN 1994-1-1 in die einige Regeln für Slim-Floor-Systeme aufgenommen werden, ist die Bemessung im Hinblick auf die Zugänglichkeit und die Anwendungsmöglichkeiten begrenzt.

Die vorliegende Studie zielt darauf ab eine technische Lösung für Slim-Floor-Träger-Stützen-Anschlüsse zu entwickeln, sodass diese für Rahmensysteme mit hoher seismischer Belastung geeignet sind (z. B. seismischer Wirkungsindex S_δ größer als 6.50 m/s^2). In der Masterarbeit der Autorin wurden Ergebnisse durch Finite-Elemente-Analysen (in Bezug auf die Spannungsübertragung und Entwicklung plastischer Dehnungen) zum Tragverhalten verschiedener Slim-Floor-Träger-Stützen-Anschlüsse unter horizontaler Belastung erzielt. Diese Ergebnisse führten zur Entwicklung der in der vorliegenden Studie vorgeschlagenen Lösung. Die Festigkeits- und Steifigkeitsanforderungen wurden mit Hilfe von Strukturanalysen geschätzt, die vor den experimentellen Versuchen durchgeführt wurden. Den für die endgültige Auslegung erforderlichen Analysen folgten experimentelle monotone und zyklische Versuche an Probekörpern, die einseitige Träger-Stützen-Anschlüssen darstellen. Das Hauptdissipationsbauteil, der Slim-Floor-Träger, wurde aus der Hälfte eines IPE 600-Profils hergestellt, auf das eine breite Stahllplatte (b x t: 380 x 20 mm) als Unterflasch geschweißt wurde. Der untere Flansch des asymmetrischen Slim-Floor-Trägers erhielt einen reduzierten Querschnitt unter Berücksichtigung der in dieser Studie vorgeschlagenen Abmessungen und wird als *Reduced Flange Section* (*RFS*)

bezeichnet. Der endgültige Querschnitt des Slim-Floor-Systems enthält Betondübel und Bewehrung und ist teilweise in Beton eingebettet. Die Gesamthöhe der Decke beträgt 370 mm. Sowohl monotone als auch zyklische experimentelle Versuche zeigten eine duktile, stabile und symmetrische hysteretische Antwort der Anschlüsse, die das Kriterium des AISC 341-16 durch die Entwicklung einer Rotationskapazität von ± 45.4 Milliradiant im Grenzzustand der Tragfähigkeit (GdT) erfüllen. Unter Berücksichtigung der Festigkeits- und Steifigkeitskriterien der Norm prEN 1993-1-8 wurden die Anschlüsse als volltragfähig und teilstarr in nicht ausgesteiften Rahmen und als starr in ausgesteiften Rahmen eingestuft. Nach der Kalibrierung des numerischen Referenzmodells wurden die Schlussfolgerungen der experimentellen Versuche zum duktilen Versagensmechanismus - bestehend aus der Entwicklung eines Fließgelenks in der dissipativen Zone des Slim-Floor-Trägers und der elastischen Antwort der Schraubverbindung - auch durch Finite-Elemente-Analysen bestätigt. Darüber hinaus ermöglichte die Zuverlässigkeit des numerischen Modells eine detaillierte Untersuchung des Einflusses verschiedener Parameter auf die Festigkeit, Steifigkeit und Rotationskapazität der Verbindung zwischen dem Slim-Floor-Träger und der Stütze, wobei kritische Komponenten wie der *RFS* hervorgehoben wurden.

Auf der Grundlage der experimentellen und numerischen Ergebnisse wurde ein Bemessungs- und Detaillierungsverfahren für Slim-Floor-Verbundträger entwickelt, deren Querschnitt I-förmig ist und die mit Stahllstützen durch Schraubverbindungen verbunden sind. Die Basis des Bemessungsverfahrens sind die Prinzipien der Kapazitätsbemessung für Stahl- und Verbundanschlüsse von biegesteifen Rahmender Duktilitätsklasse 3, aber auch bestimmte Bemessungsregeln aus der pränormativen Fassung der EN 1994-1 für Slim-Floor-Systeme. Darüber hinaus wurde in der vorliegenden Studie eine Methode vorgeschlagen, mit der die Duktilität von Slim-Floor-Systemen durch die Anwendung des *RFS* sichergestellt wird. Zur Bewertung des seismischen Verhaltens von Rahmensystemen mit Slim-Floor-Träger-Stützen-Anschlüssen wurde ein numerisches Modell des Anschlusses auf der Grundlage experimentell erzielter Ergebnisse erstellt. Zu diesem Zweck wurde der plastische Anteil der Umhüllenden verwendet, welcher dem in Beton eingebetteten dissipativen Bereich des Slim-Floor-Trägers entspricht, um die Antwort im nichtlinearen Bereich dieses Bauteils zu definieren. Es wurden realitätsnahe Modelle der Schraubverbindung, des Stützenstegfelds und der Verbände erstellt. Die Bewertung des Erdbebenverhaltens wurde für vierstöckige biegesteife Rahmen, sechzehnstöckige durch konzentrische Verbände ausgesteifte Rahmen und Dualrahmen mit der gleichen Anzahl von Stockwerken durch Anwendung statischer und dynamischer nichtlinearer Analysen durchgeführt. In all diesen Fallstudien wurden Slim-Floor-Träger-Stützen-Anschlüsse verwendet. Das seismische Verhalten wurde nach den Kriterien der neuesten Version des Europäischen Erdbebencodes in Bezug auf die Geschossverschiebungen im Grenzzustand der Gebrauchstauglichkeit (GdG) und im Grenzzustand der Tragfähigkeit (GdT), die plastischen Rotationen der Träger und die Entwicklung des globalen Versagensmechanismus der Struktur bewertet. Auf der Grundlage der Ergebnisse der *Pushover*-Analyse mit *N2* und der Ergebnisse, die durch die Anwendung der *Response-History-Analysis* mit sieben Beschleunigungskurven erzielt wurden, wurde die Schlussfolgerung getroffen, dass Slim-Floor-Träger-Stützen-Anschlüssen in Rahmensysteme integriert werden können und ihr seismisches Verhalten ausreichend ist. Außerdem können diese Anschlüsse auf die Grundsätze der Kapazitätsbemessung angewandt werden, da sie in der Lage sind, seismische Energie an den Trägerenden abzuleiten und in anderen Bauteilen wie den Schraubenverbindungen, angrenzenden Schweißnähten und im Stützenstegfeld übermäßig widerstandsfähig zu sein.

1. INTRODUCTION

1.1 Slim-floor system

1.1.1 Generalities

Slim-floor stands for a wide range of flooring solutions derived from the registered trademark "*Slimflor®*" introduced for the first time in the early 1990s by British Steel plc. [1]. According to Mullet and Lawson [2], the registered trademark "*Slimflor®*" was inspired by the Nordic flooring construction method known as "top hats". The "top hats" flooring system was made of an assembly of four welded steel plates and was an already established solution on the Swedish construction sector before becoming popular on the European continent.

Slim-floors could be defined as compact building flooring systems whose central structural component is generally a built-in asymmetric steel beam. Apart from the asymmetric steel beam, the technical solution implies the use of reinforced concrete and, generally, of steel-concrete connecting devices, the objective of the latter being to ensure a unitary function of components made of materials with different properties (see Fig. 1-1).

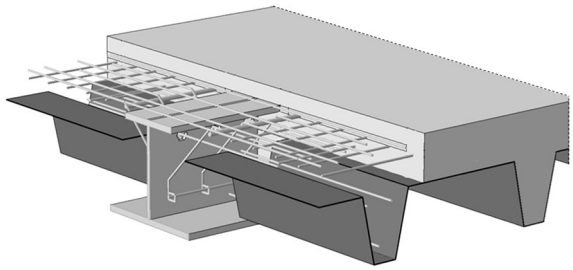

Fig. 1-1. Example of a slim-floor system with asymmetric steel beam, reinforced concrete and concrete dowels – based on Braun et al. [3]

The need for lighter flooring solutions emerged primarily from the need to reduce the impact of flooring systems on the weight of buildings. According to [1], the flooring system was proven to have the highest impact of all structural elements on the overall weight of tall steel buildings. Recent studies have shown that, in addition to achieving higher performance than if the materials functioned separately, composite elements exercise a positive influence on the construction speed and on the reduction of self-weight of buildings [1] [4]. As a consequence of this, but due to other factors as well (i.e., the compromise of vertical space: between architectural freedom and the economic costs it implies or the necessity to accommodate under-floor technical equipment), lighter flooring systems were intensely investigated in the last decades [4] [5] [6].

1.1.2 Description of the solution

Slim-floor solutions share a characteristic feature, also suggested by their name "*slim*", compactness. This compactness is achieved by integrating the steel

profile of the beam in the overall height of the floor. Due to their compact configurations, these flooring systems could be regarded as alternative flooring solutions to the regular composite downstand system with reinforced concrete slab supported on steel beams. In general, the components most commonly found in slim-floor systems would be the following ones:

- built-in asymmetric beam obtained from a steel profile; the lower beam flange is wider than the top one to support prefabricated slabs or trapezoidal steel sheets;
- reinforced concrete;
- one or more types of steel-concrete connecting devices.

In some of the early slim-floor systems, the steel cross section of the beam was obtained by either welding the bottom or the top flange on a half I or H-steel profile (i.e., *IFB Type A*, *IFB Type B;* see Fig. 1-2a-b) or by doubling the lower beam flange with an additional wider steel plate (i.e., *SFB*; see Fig. 1-2c) [7].

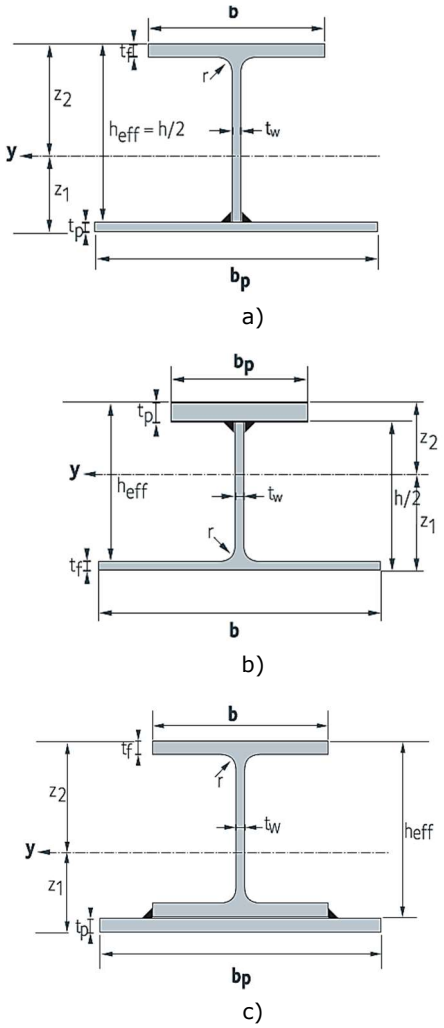

Fig. 1-2. Examples of slim-floor beam cross sections [7]: a) *IFB type A*; b) *IFB Type B*, c) *SFB*

1.1.3 Examples of slim-floors

After the introduction of the slim-floor system to a wider market, a rise of interest in compact flooring solutions emerged. As a result of this interest, a range of slim-floor systems was developed. Some examples are mentioned and shown in the following: (see Fig. 1-3a-e):

- *Asymmetric Slimflor® Beam* (i.e., known as *ASB* [8]),
- *iTECH* floor beam [9],
- *Composite Slim-Floor Beam* (i.e., *CoSFB*, [3]),
- *Deltabeam®* [10],
- *Ultra-Shallow Floor Beam®* (i.e., *USFB*, [11]).

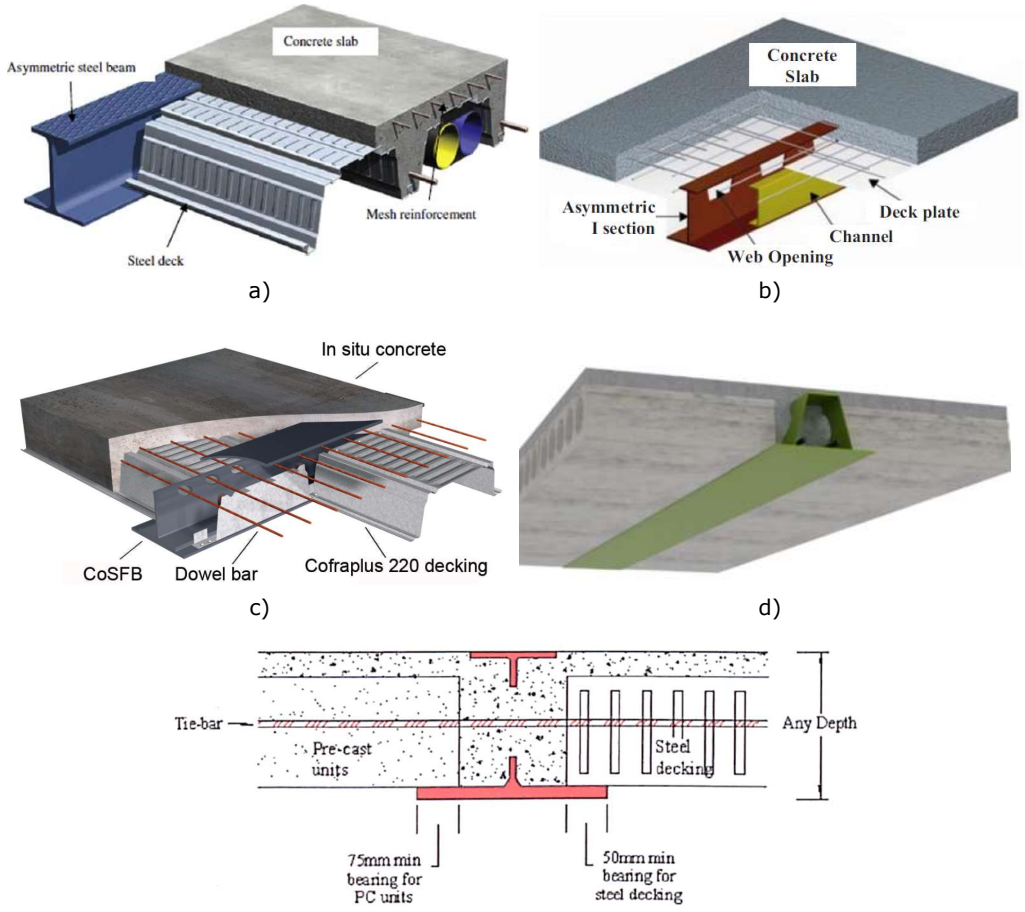

Fig. 1-3. Examples of slim-floors from literature: a) *Asymmetric Slimflor® Beam* [12]; b) *iTECH* [9]; c) *Composite Slim-Floor Beam* [3]; *Deltabeam®* [13]; *Ultra Shallow Floor Beam®* [14]

The slim-floor systems shown in Fig. 1-3a-e are the result of more recent developments, which mainly aimed at improving the resistance and stiffness and extending the range of application. Each slim-floor solution from Fig. 1-3a-e has particularities, some of which residing in the geometry of the steel beam, in the components of the configuration or even in the shear connection. Apart from the

natural bond between steel components and concrete, shear studs welded on the top or lower flange of the steel beam, a patterned or textured top beam flange (*ASB*), large (*iTECH and USFB® beams*) or relatively small openings (*CoSFB*) in the beam web or hollow core beam sections with large openings could be used to assure the shear connection (*Deltabeam®*). However, these slim-floor systems are just some of the currently available flooring solutions. More configurations and details can be found in Schäfer and Braun [15].

1.1.4 Advantages

- **Compactness**. Among the most significant advantages of the slim-floors is the reduced overall height of the system. This is achieved by using steel beams with half of the cross section of regular beams and by their embedment in concrete – as an alternative to composite downstand beams. Due to the compactness of the flooring system, vertical space is gained, which could ultimately result in additional storeys at the same total height of a building [7].
- **Reduction of façade costs**. Moreover, the reduced overall thickness of the flooring system also reflects positively on façade costs. In some studies, it has been estimated that the overall thickness of the floor could be reduced by approximately 300 mm per storey [1]. In one of the catalogues of one slim-floor solutions developer, the total height of the floor is around 400 mm in case *the Composite Slim Floor Beam CoSFB* is used [16]. Depending on the storey height of the building, one or more storeys could be gained. To exemplify the significance of the floor thickness reduction to high-rise buildings, a sketch was provided in one catalogue of a steel producer [16] (see Fig. 1-4).
- **Reduction in floor weight**. Another significant advantage of the slim-floors is the reduced weight of the flooring system, as compared to the downstand composite beam. A reduced weight of the flooring system is achieved through compact steel cross sections and through the integration of the beam in the overall thickness of the floor. This is particularly important to multi-storey building design, as stated in several brochures of different developers of slim-floor solutions (e.g., [16] [10]), where a weight reduction in the flooring system could optimise the material use in the entire structure.
- **Inherent fire resistance**. Due to the encasement of the steel beam in concrete, some slim-floor systems have a fire resistance in the range of 60÷90 minutes without supplementary protective measures [16].

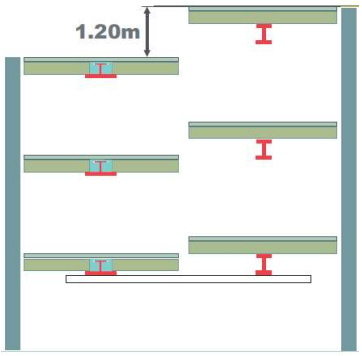

Fig. 1-4. Impact of reduced floor thickness according to [16]

1.1.5 Challenges

- **Limited code coverage**. The design of composite structural elements is carried out according to the requirements of the European code for composite construction EN 1994-1-1 [17], but slim-floor systems are not included in the current version of the code. Although design rules are provided in the British Standard BS5950: Part 1:1990 [18], these are targeted specifically at slim-floor systems with hollow core precast slabs.
- **Design governed by technical approvals**. Although technical approvals were released, they were issued for certain slim-floor solutions. For instance, a National Technical Approval was released by the DIBt (German Institute for Civil Engineering) in Germany, allowing the usage of the *Composite Slim-Floor Beam CoSFB* of one developer of slim-floor solutions [19]. More recently, the German Institute for Civil Engineering DIBt released another National Technical Approval for the use of shallow beams with hollow core sections [20].
- **Limited application**. Generally, the application of slim-floors is currently limited. Apart from the limited code coverage, which hinders design and wider use, slim-floor systems are currently used as simply-supported beams with nominally pinned beam-to-column connections. This limits slim-floors to non-seismic regions and to gravity load-bearing systems of structures.

1.1.6 Applications

Since their introduction to the construction market in the 1990s, slim-floor systems have been efficiently applied to mid- to high-rise steel and composite structures of buildings throughout Western and Nordic European countries and even in China [7]. In most cases, the functions of these buildings are office, residential or medical care and recovery units [6] [21]. According to a slim-floor solutions developer [16], requirements at the Ultimate Limit State (i.e., resistance, stability) and at the Serviceability Limit State (i.e., vibration) could be met. Thus, the application to multi-storey buildings is no longer a novelty in civil engineering.

Examples of the current implementation of slim-floors into structural design are briefly discussed in this section. The use of slim-floor systems in these applications over the "classic" flooring system with composite downstand beams was motivated by factors as: the possibility of gaining an additional floor; increased floor-to-ceiling space; built-in fire protection due to concrete encasement; structural lightness; fulfilment of certain sustainability requirements.

A limitation shared by slim-floor applications, including the case studies that are presented in this section, is the low seismicity of the regions where the buildings with slim-floor systems were erected on.

Montevideo Rotterdam (2005)

Montevideo Rotterdam is a high-rise building erected in Rotterdam, The Netherlands [22] (see Fig. 1-5). The main design concept was flexibility of the space. Considering this as the main objective for the top section of the building, where high-end residential spaces were foreseen, an adaptation of structural design was required. Thus, the structure of the top section of *Montevideo Rotterdam* was built with braced steel frames and a shallow flooring system made of *Integrated Floor Beams* and prefabricated concrete slabs. The overall height of the flooring system was 300 millimetres. The combination of the shallow flooring system with light steel frames allowed for versatile and open spaces, meeting the design objective. At the end of the

construction in 2005, the 152 meters high building offered extensive residential, office and commercial spaces with panoramic views of the bay area in Rotterdam.

Fig. 1-5. *Montevideo Rotterdam* [23] [24]

Area 22 (2009)

Area 22, finished in 2009, houses a modern multipurpose environment with accommodation, office, commercial and car park possibilities in Trento, Italy [25]. The design concept on which the structural system was developed was primarily meant to address the function versatility of the building. Thus, two distinct building volumes were created to serve different activities: accommodation and commercial (30 and 15 meters, respectively). The steel frames, made of high-strength steel columns, were coupled with a shallow flooring system consisting of *Integrated Floor Beams* and pre-stressed concrete hollow core slabs, whose overall height varied from 240 to 500 millimetres.

Brussels Environment (2014)

Brussels Environment houses the environmental agency of the city of Brussels in Belgium. The unusual aesthetic of the building (see Fig. 1-6) was the result of a design strategy targeted primarily at attaining the following: eco-friendliness, openness and transparency towards citizens. By choosing a design like this, the government organisation planned to tackle important environmental and construction-related topics, as well as to set an example of good practice. To support the design strategy, the steel structure was developed to be light, easily demountable and reusable. The steel frame, made of tubular column cross sections and rolled sections for the beams, was combined with a shallow flooring system. In this case, the flooring system consisted of *Slim Floor Beams* made of HEB and HEM cross

sections with 15÷25 millimetres welded steel plates and prefabricated concrete slabs. Finished in 2014, *Brussels Environment* is regarded as the largest passive building in Belgium, covering both office and educational spaces [26].

Fig. 1-6. *Brussels Environment* Building [27]

Delft city hall and train station (2017)

The new Delft city hall and train station is a multipurpose building with office, commercial and public spaces erected in Delft, The Netherlands, in 2017 (see Fig. 1-7). One method to address the different spaces within the building in an environmentally friendly manner was the use of a shallow flooring system. In this case, the flooring solution was based on *Integrated Floor Beams*, to which an increase in the open and usable space was attributed [28].

Fig. 1-7. Delft city hall and train station [29]

Zero Newton® Tower (2018)

The *Zero Newton® Tower* is an on-going urban design project of a multi-storey building in the city of Nantes in France. Designed as an architectural landmark, the building is suspended on a 28 meters high concrete core, while lattice beams support a predominantly light steel frame. Paired with the light steel frame is a shallow flooring system of 280 millimetres height consisting of *Composite Slim-Floor Beams CoSFB*, which in comparison to a regular all-concrete solution, helped gain an additional floor. With construction having had started in 2018, the *Zero Newton® Tower* is expected to house panoramic office spaces, an art gallery and a restaurant.

1.2 Research motivation

Slim-floors were introduced to the construction market as improved technical solutions to "classic" downstand beams [1]. Because they were developed to address existing practical challenges, the architectural and technical potential of slim-floors can be easily utilized, making them, in consequence, a competitive solution [7]. However, their application is currently limited. In the case of simply-supported slim-floor beams, the application is mainly governed by technical approvals (e.g., examples of permits: [19] [20]) due to a lack of coverage by the current design codes. A good example of this is Germany. But for seismic design applications the constraint is the actual form in which the slim-floor beams are currently used. Because the beams are used as simply-supported elements, their application is limited to structures designed for non-seismic regions, where they are integrated in gravity load-bearing systems.

This is the context in which the current study was launched. As the advantages and the extent to which these flooring systems can impact architectural design and erection costs have been proven several times before, what would widen the application rage of slim-floors to seismic design is the development of moment-resisting slim-floor beam-to-column joints. This challenge is doubled by the fact that the current state of the art is limited. The development of a moment-resisting slim-floor beam-to-column joint configuration supported by experimental, analytical and numerical confirmation could stir the interest of research institutes and industry partners and could result in a wider implementation of the slim-floors.

1.3 Definition of the aim and objectives

The dissertation aims at the development and the seismic performance assessment of a moment-resisting slim-floor beam-to-column joint suitable for structures designed for medium-to-high seismicity. To achieve this aim, the following objectives were established:

- pre-test numerical investigations: development of a slim-floor moment-resisting beam-to-column joint that would satisfy the: (i) joint rotation criterion of ±40 mrad imposed by modern seismic codes, e.g., AISC 341-16 [30]; (ii) capacity design rules according to the intended failure mechanism;
- experimental investigations: development of experimental tests (i.e., under monotonic and cyclic loading) to evaluate the mechanical characteristics (i.e., stiffness and bending / shear resistance) and to demonstrate the rotation capacity of the slim-floor beam-to-column joint specimens;
- numerical investigations: calibration of a numerical model, as well as the development of a parametric study to optimise the proposed solution;

- analytical approach: development of a design procedure and detailing for moment-resisting slim-floor beam-to-column joints;
- structural analyses: integration of experimental results in structural models containing slim-floor beam-to-column joints and assessment of seismic performance with nonlinear static and dynamic analyses.

1.4 Structure of the thesis

The current study is structured in six main chapters and a concluding section, resumed as follows:

- **Chapter 1: Introduction**. In this first introductory chapter, an overview on the evolution of slim-floors and the general description of the basic current configuration of slim-floors are included. In accordance with the current applications of slim-floors, the most important advantages of the solution are discussed. Challenges, which result from the application of slim-floors to seismic design, are defined and discussed. In this context, the objectives that support the achieving of the main scope of the current study are defined.
- **Chapter 2: State of the art**. Existing research with relevance to the subject of the current study is analysed within this chapter. As the proposed application represents a new direction of study on composite shallow flooring systems, the current and pre-normative European code requirements on steel and concrete composite structures are approached.
- **Chapter 3: Experimental program**. Detailed information on the configuration of the test specimens and the experimental test setup, instrumentation, boundary conditions, selected loading protocols, test measurements and observations, as well as the interpretation of the test results are presented in this chapter.
- **Chapter 4: Numerical program**. The outcomes of the calibration process, i.e., configuration of the numerical model, the material models, and the results of the reference numerical model are described in Chapter 4. The chapter is completed by a parametric study with twelve additional numerical models. Following the parametric study, solutions of joint response enhancement are provided.
- **Chapter 5: Design procedure**. In Chapter 5, the description of the proposed technical solution, the summary of the design methodology, the detailed design and detailing procedure and recommendations are provided.
- **Chapter 6: Structural analyses**. Based on experimental and numerical data of the tested specimens, a numerical model of the slim-floor beam-to-column joint is developed in Chapter 6. Following nonlinear static and dynamic analyses on lateral-resisting structures such as Moment-Resisting Frame, Concentrically-Braced Frame and Dual Concentrically-Braced Frame, in which the SF joint model was incorporated, plastic rotation demands and interstorey drifts demands are obtained. These are compared to experimental results and the European seismic code limits.
- **Chapter 7: Conclusions**. Final conclusions of the current study are drawn in Chapter 7. Possible improvements, personal contributions, a list of scientific publications, as well as future research activities are furthermore discussed in this chapter.

2. STATE OF THE ART

2.1 Review of previous research studies on slim-floors

2.1.1 Malaska, M. (PhD Dissertation) [31] (2000)

Introduction of semi-continuity in slim-floor construction

The doctoral dissertation of Malaska [31] was focused on the study of slim-floor beam-to-column joint characteristics (i.e., bending moment resistance, stiffness and rotation capacity) under the static loads. According to Malaska, the typical beam-to-column joint configuration used in office and residential buildings throughout Finland comprises of built-in asymmetrical slim-floor beams connected to concrete filled tubes of circular or rectangular hollow sections. As considered in the thesis [31], in conventional design cases, the beam-to-column connections are treated as rigid or nominally pinned. However, slim-floor beam-to-column connections were designed as nominally pinned resulting in a simple form of construction, although semi-continuity was considered by the author to lead to material economy and a better performance under service loading conditions (i.e., reduced cracking, deflections and vibration). Motivated by the advantages of semi-continuity in slim-floor beam-to-column joints, as well as by the previous studies on slim-floors carried out at Helsinki University of Technology [32] [33] [34], this research direction was considered relevant. The thesis follows the accomplishment of two main goals: development of an experimental program on slim-floor beam-to-column joints to prove the advantages of joint semi-continuity and development of a simplified mathematical model for the calculation of joint characteristics.

The experimental program included the monotonic testing of six double-sided beam-to-column joint specimens, two of which were made of bare steel components and four were composite. According to Malaska [31], the joint specimens were the internal joints of a braced frame. The parameters experimentally investigated were: (i) bare steel specimens: the position of the actuators on the slim-floor beams; (ii) composite specimens: the longitudinal reinforcement ratio (ρ [%] = 0.92 ÷ 1.43), the concrete class (C25/30 ÷ C35/45) and the position of the actuators on the slim-floor beams. The slim-floor beams were made of welded steel plates which resulted in an asymmetrical cross section, with the lower flange wider than the top flange. In the composite specimens, the lower flange of the beam was used to support the profiled metal decking (see Fig. 2-8a-b). The concrete was poured *in situ*. Instead of regular headed studs, the steel-to-concrete infill interaction was assured by transverse rebars of 16 mm in diameter that were welded on the top flange of the beam. The reinforcement was realised with ductile longitudinal and transverse rebars, the last being inserted into the web of the beam. The anchorage of the longitudinal reinforcement was continuous around the column. An additional layer of mesh was positioned on top of the longitudinal reinforcement to improve control on concrete cracking. The composite column had a rectangular hollow section -a common solution in the Finnish construction sector. A 25 mm thick shear steel plate was inserted through the column, to which 4 bolts M36, Gr. 8.8 assured the connection to the two

slim-floor beams (see Fig. 2-8c). Material tests revealed the following characteristics of the components:

- steel slim-floor beam (S355): $f_{y,flanges}$ = 387 N/mm^2; $f_{y,web}$ = 376 N/mm^2;
- steel shear plate (S355): f_y = 364 N/mm^2, f_u = 531 N/mm^2;
- column (S355): f_y = 453, f_u = 528 N/mm^2;
- rebars (A500HW): $f_{y,D12}$ / $f_{y,D16}$ / $f_{y,D20}$ = 546 / 575 / 553 N/mm^2;
- concrete: f_c = 34.5 ÷ 46.8 N/mm^2.

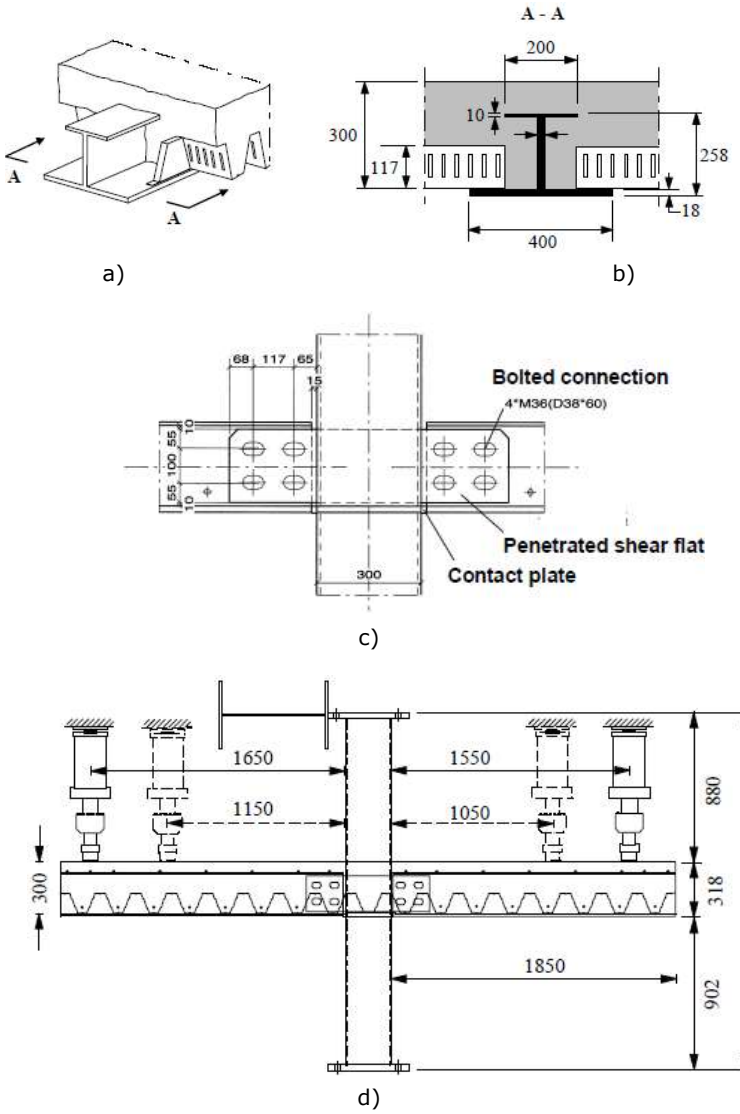

Fig. 2-8. Images from Malaska [31]: a) composite slim-floor system; b) cross section of the composite slim-floor configuration; c) bolted beam-to-column connection; d) test setup

The global dimensions of the joint specimens were the following: slim-floor beam length was 1.85 meters, column height was 2.10 meters, width of the concrete

slab was width was 1.50 meters. According to the test setup (see Fig. 2-8d), two actuators applied loads monotonically at the ends of the slim-floor beams. The hydraulic actuators applied the loads in displacement control until the bare steel tests were stopped; as the tests ended, the two bare steel specimens had not evidenced plastic deformation development. Alternatively, during the elastic range, the tests on the four composite specimens were carried out in force control and eventually in displacement control. The test on composite specimens ended when the deformation of the beams was out of the practical range.

According to the study, the results of the bare steel specimens evidenced a flexible behaviour up to connection rotations of 15 or 23 mrad, depending on the specimen. After reaching 30 mrad, one of the specimens suffered a weld failure of the lower beam flange to the contact plate. Apart from this, the steel shear plate and the bolts remained elastic. Considering these, Malaska concluded that the joint behaved as nominally pinned. Unlike the bare steel specimens, due to the developed bending resistance (i.e., 347 ÷ 489 kNm, depending on the specimen) and initial stiffness, the joints were classified as rigid and partial-strength. Although a pronounced concrete cracking was evidenced (see Fig. 2-9a), a negligible relative slip was recorded. Thus, a full interaction was assumed. According to Malaska [31], the weakest component of the joint was represented by the reinforcement, which begun to yield at approximately 250 kNm. Depending on the specimen, plastic deformations were developed in the flanges of the slim-floor beam (between monotonic rotations of 23 ÷ 47 mrad) and in the steel shear plate (see Fig. 2-9b). The on-site measurements recorded the initiation of the steel shear plate yielding almost simultaneously with the yielding of the longitudinal reinforcement. The influence of a higher concrete class (C35/45 instead of C25/30) was not evidenced. However, according to the experimental results of the study, a higher longitudinal reinforcement ratio led to higher bending resistance.

a) b)

Fig. 2-9. Details regarding the failure mode of the composite specimens from Malaska [31]: a) concrete crack pattern; b) deformation of the steel shear plate

From an analytical point of view, a mathematical model of the joint was developed for the calculation of the joint characteristics, i.e., bending moment resistance, initial stiffness and rotation capacity. The results of this model were calibrated against experimental results. According to [31], more research on the topic would be needed to obtain more accurate results.

2.1.2 Wang, Y., Yang, L., Shi, Y., Zhang, R. [35] (2008)

Research on the load-bearing capacity of slim-floor beams

The scientific paper of Wang et al. [35] was centred on the study of the hogging bending capacity and on the flexural stiffness of composite slim-floor beams through monotonic experimental tests and advanced finite element analysis. The motivation for this study was the limited analytical and experimental data on the negative moment behaviour frame slim-floor beams with deep decking.

Two slim-floor beams with the same configuration, but different longitudinal reinforcement ratios (see Fig. 2-10a) were tested in the experimental program. The 6 meters long slim-floor beams had asymmetric cross sections made up of welded steel plates. The beams were connected to the columns through a rigid welded connection and partially encased in reinforced concrete. The reinforcement of the slab was realised with longitudinal (f_y = 370.3 N/mm^2; f_u = 556.7 N/mm^2; Ø: 12 mm at 150 / 75 mm) and transverse (f_y = 401.3 N/mm^2; f_u = 577.8 N/mm^2; Ø: 6 mm) rebars. In order to anchor the longitudinal rebars, some were welded to the column and others were bent downwards. The width of the slim-floor system was 750 mm. Similarly to the beams, the columns were made up of steel plates. The length of the columns was 2.5 meters. The materials of the components were: steel grade Q235-B (f_y = 313.7 N/mm^2; f_u = 508.2 N/mm^2), concrete class C30 (f_c = 14.3 N/mm^2).

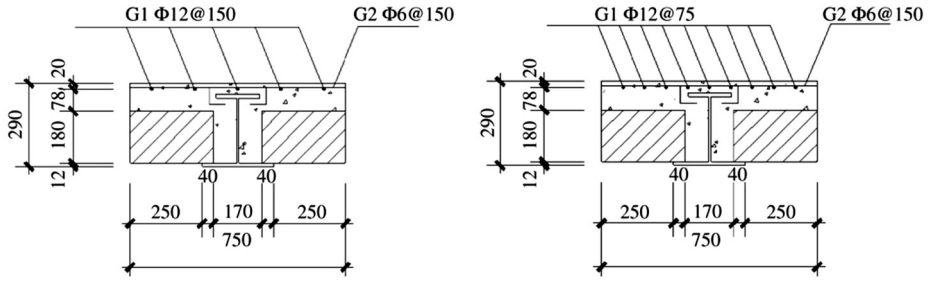

a)

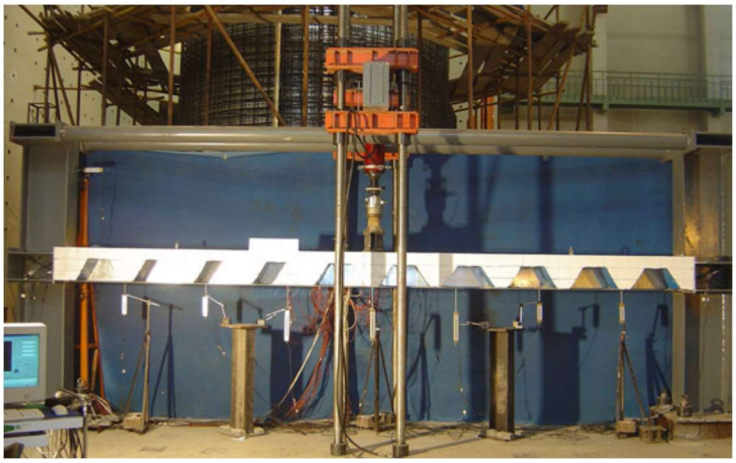

b)

Fig. 2-10. Images from Wang et al. [35]: a) cross sections of slim-floor beams; b) test setup

The monotonic tests were carried out in displacement control on the test setup shown in Fig. 2-10b. The actuator was positioned in mid-span and pushed downwards. During the two experimental tests, similar phenomena was observed: emergence of transverse cracks in the concrete at 10.2 % of the ultimate load value and their gradual development up to 78.5 % of the ultimate load - when the lower flange of the beam started to yield and the concrete to crush in the mid-span. The tests ended when the deflection at mid-span reached the limit of the actuator. At the end of the tests, the ultimate applied load was 445.58 kN for one specimen and 475.97 kN for the second one, while the deflections at mid-span were 130.5 mm in the first case and 130 mm in the second. According to the authors, the test results of the two specimens evidenced similarities in terms of failure mode and developed ductility. Based on the force – displacement curve at mid-span in which the elastic limit (i.e., 380.3 kN for one slim-floor beam, 385.3 kN for the other one) was exceeded, the authors claimed that the specimens demonstrated high ductility. Apart from that, Wang et al. [35] concluded that, since the force – deformation curves were similar in the elastic range, the influence of a higher longitudinal reinforcement percentage on the initial stiffness could not be proven. However, the specimen with a higher longitudinal reinforcement percentage developed a 6.34 % higher ultimate resistance. Local instrumentation recorded the development of plastic strains in both the flanges and the web of the slim-floor beams at the beam ends and at mid-span. According to other measurements, the reinforcement bars had yielded. Since the transverse strains were evenly distributed to slim-floor beam, to the reinforcement bars and the concrete infill, Wang et al. [35] assumed a full interaction of the components.

Within the study of Wang et al. [35], a numerical model of one of the tested slim-floor beam specimens was developed with a finite element modelling software and allowed for an in-depth analysis of the stress and plastic strain distributions. Also, part of this study was a proposal for a calculation method of the ultimate slim-floor beam resistance.

Considering these results, the authors concluded the study by stating that evidence of plastic hinge development at the beam ends and at mid-span was provided. According to the authors of the paper, the tested composite slim-floor beams demonstrated significant ductility. Another conclusion of Wang et al. [35] and Zhang [36] was related to the influence of the reinforced concrete ribs. In both studies (i.e., [35] and [36]), the concrete ribs are considered to have insignificant influence on the stiffness of the slim-floor beam and could, therefore, be neglected from the calculation of the loading resistance and stiffness.

2.1.3 De Nardin, S., El Debs, A. L. H. C. [37] (2011)

Research on slim-floor beam-to-column composite connections

The scope of the study performed by De Nardin et al. [37] was to investigate the influence of the slim-floor system on the bending moment resistance of the beam-to-column connection. To this end, an experimental program which incorporated monotonic tests on, firstly beam specimens, and followingly on beam-to-column joint specimens was developed. In the first experimental phase, three asymmetrical slim-floor beams fabricated from welded steel plates were tested monotonically under flexure. The difference between the specimens resided in the shear connection: (i) no shear connectors, (ii) shear connectors positioned horizontally on either side of beam web and (iii) shear connectors placed vertically on the inner face of the lower beam flange. As stated by the authors, the aim of the initial tests was to establish the most

efficient positioning of the shear connectors. De Nardin et al. [37] concluded that, based on the higher loading capacity (i.e., approximately 18 % higher than the slim-floor with no connectors and 3 % higher than the beam with horizontal connectors) and on the lower interface slip of the slim-floor beams with shear connectors welded on the inner face of the lower beam flange, this beam typology had to be further integrated in tests on joints.

Subsequently, two double-sided beam-to-column joint specimens were monotonically tested. To study the influence of the reinforced concrete on the slim-floor beam-to-column connection, while one specimen contained exclusively steel components, the other one included a reinforced concrete slab of 1.25 meters width. Considering the results obtained from member tests with various positions of shear studs, the joint specimens contained slim-floor beams with shear studs welded on the inner side of the top flange (see Fig. 2-11a). The characteristics of the shear studs were the following: 19 mm in diameter; 75 mm in height. The length of each beam was 1.65 meters, and the material was A-36 (flanges: f_y = 305 N/mm^2; web: f_y = 297 N/mm^2). The connection of the beams to the column was realised through a steel shear plate inserted through the column and three M16 bolts on either side of the column (see Fig. 2-11b). The column had a composite cross section consisting of welded U steel profiles and concrete (compressive strength f_c = 30.1 N/mm^2). Profiled steel sheets (f_y = 280 N/mm^2) of 0.8 mm thickness were positioned on the lower beam flange. Rebars of diameter 12.5 and 16 mm were used in the longitudinal direction, and of 5 mm were used in the transverse direction. The reinforcement was continuous around the column, except for two bars that were discontinued.

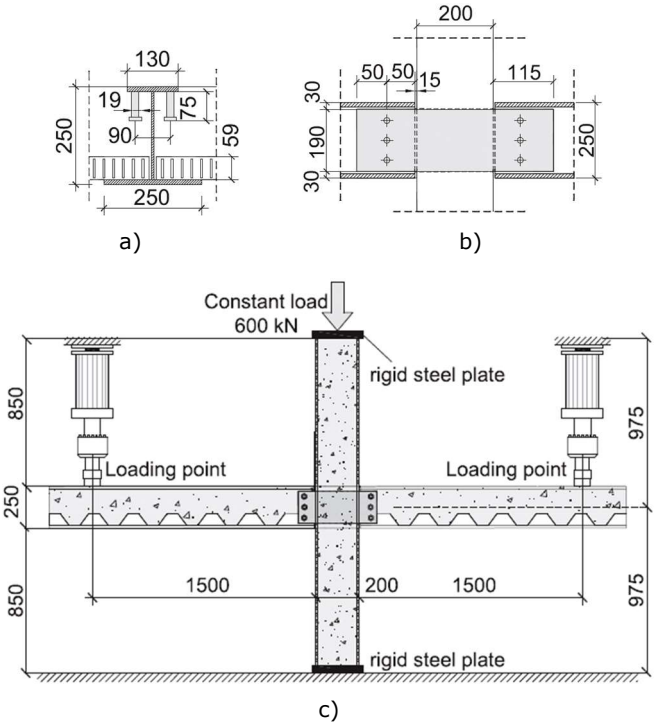

Fig. 2-11. Images from De Nardin et al. [37]: a) cross section of slim-floor beam; b) bolted beam-to-column connection; c) test setup

According to De Nardin et al. [37], the loading protocol for the two joint specimens (i.e., bare steel and slim-floor system) consisted of a compressive axial force equal to $0.2 \cdot N_u$ (where N_u is the axial load resistance of the column defined in the Brazilian Code) being applied on the top of the column. At the same time, two hydraulic actuators pushed downwards the free end of each beam in displacement control (see Fig. 2-11c). Based on the on-site observations and on the measurements taken during the experimental tests, the beam-to-column connections of the bare steel specimen acted as pinned. As the test was stopped, no damage was identified in the components of the specimen. Alternatively, the bending moment resistance of the beam-to-column connection of the specimen with partially encased beams was significantly higher (i.e., 163 kNm vs. 2.68 kNm). Although cracks of the concrete were observed, the relative slip was very small (i.e., 0.1 mm). Because of this, Nardin et al. [37] assumed a full interaction. The degradation of the specimen with partially-encased slim-floor beams started with the emergence of cracks in the concrete situated in the proximity of the beam-to-column connections (at approximately 40 kN of applied load). When the test was stopped, at the maximum vertical load of 108.7 kN, the local instrumentation revealed the yielding of the longitudinal reinforcement bars. The authors observed that, as the cracking of the concrete intensified, the internal forces were redistributed to the rebars, and identified this as the main cause for the rapid increase in longitudinal reinforcement strain rate. On the other hand, the slim-floor beam itself and the shear plate did not suffer any plastic deformations.

In the conclusions of the research paper of Nardin et al. [37], the authors classify the beam-to-column connection of the bare steel specimen as nominally pinned. In comparison to the results of the bare steel specimen, the one with partially encased slim-floor beams developed a rotation capacity of approximately 30 mrad, a hogging bending moment resistance of 163 kNm and an initial stiffness of 53.75 kNm/mrad (as opposed to 2.85 kNm/mrad). Due to these results, the authors classified the connection of the specimen with composite slim-floor beams as semi-rigid and partial-strength. The authors also concluded that the presence of the reinforced concrete contributed in a significant manner to the beam-to-column moment transfer mechanism.

2.1.4 Braun, M. et. al [38] (2014)

Research leading to the release of concrete dowels technical approval

The focus of the scientific paper of Braun et al. [38] was set on the investigation of the load bearing behaviour of concrete dowels and on establishing the most influential parameters on the overall resistance of composite slim-floor beams (i.e., *CoSFB*). Included in this paper were also the steps that led to the general technical approval [19] that currently regulates the use of concrete dowels on the construction market. The motivation of this study [38] was driven by the lack of design rules for this application and by the interest in optimizing the interaction between shallow beams and concrete, as this interaction was believed to be the key to more efficient construction. The technique involving the use of concrete dowels was previously used in bridge construction. As stated in the paper, the "classic" use of shear connectors welded on the top of the beam flange would lead to an increase in the overall height of the flooring system, which was contradictory to the concept of slim-floors. On the other hand, the height decrease in the already shallow slim-floor beam sections would lead to reduced stiffness and load bearing capacity. To address this, the authors used shear restraints in the form of rebars inserted into pre-drilled

openings in the web of the beam. During the pouring process, the web openings would be sealed up with concrete (see Fig. 2-12a).

Four *CoSFB* specimens of two different lengths were experimentally tested. The first two beam specimens were part of a test group called "*Biegeträgerversuche*" whose main goal was to study the sagging bending resistance of the mid-span section. The configuration of these two 8 meters long specimens is shown in Fig. 2-12a. The *"Schubträgerversuche"* was the second test group and constituted of two beam specimens with the same configuration as the "*Biegeträgerversuche*" (see Fig. 2-12a), but half the span length (i.e., 4 meters), primarily to investigate the behaviour of concrete dowels. In the *"Schubträgerversuche"* the number of concrete dowels was half than in the other specimens. All four *CoSFB* specimens were 2.5 meters wide and incorporated the following components:

- HEM-220 hot-rolled steel profile (S355);
- wider steel plate welded onto the lower flange of the HEM-220 (S355);
- concrete dowels: rebars of 12 mm equally spaced at 125 mm;
- reinforcement: mesh Q257, mesh Q188, inclined rebars (Ø: 12 mm), transverse rebars (Ø: 10 mm);
- concrete slab (concrete class: C30/37);
- deep steel decking (*Cofradal* 200).

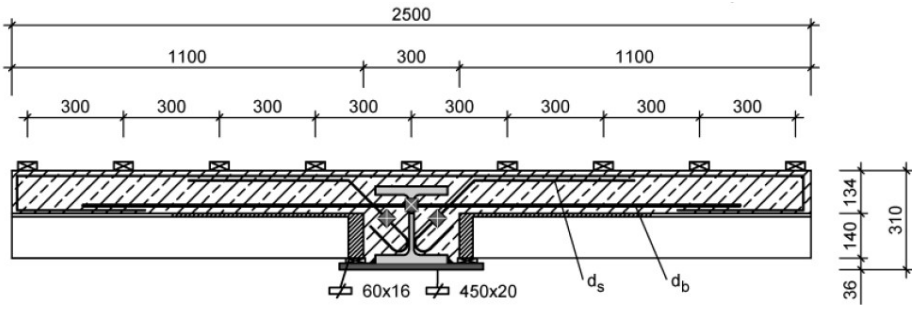

a)

b)

Fig. 2-12. Images from Braun et al. [38]: a) cross section of the composite slim-floor beam *CoSFB*; b) experimental test setup

The beam specimens were mounted in the experimental stand and tested in a four point setup (see Fig. 2-12b). In the case of "*Biegeträgerversuche*", the applied load was approximately 950 kN. An almost double value of the load was utilized in *"Schubträgerversuche"*. While the bending moment in the centre had the same value in all specimens, the shear force at the beam ends of the *"Schubträgerversuche"* was twice as much as in the case of the "*Biegeträgerversuche*". The study showed that, in both the 8 and the 4 meters long specimens, a ductile global behaviour of the *CoSFBs* was evidenced. Apart from that, local instrumentation recorded the participation of the concrete dowels in the transfer of stresses and strains in both tested typologies. Both "*Biegeträgerversuche*" and *"Schubträgerversuche"* failed due to concrete crushing. Another common finding valid for all specimens was an experimentally higher value of the effective width, as opposed to the computed one. Differences were found in the relative slips; the maximum relative slip of the longer specimens was 3 mm. In the case of the shorter specimens, higher slip values were recorded: 11.9 mm in the beam specimen with 100 % of the concrete dowels; 17.2 mm in the specimen with 50 % of the concrete dowels.

The load-bearing capacity of the concrete dowels and the influence of different parameters (i.e., compressive strength of concrete, rebar diameter of concrete dowels, diameter of the beam web perforations, thickness of the beam web) were studied through a series of push-out tests [39] [40]. The most important conclusions that were drawn by the authors following the push-out tests were:

- the influence of the inclined reinforcement and of the diameter of the perforations from the beam web could not be experimentally confirmed;
- all force – relative slip curves evidenced a high initial stiffness and a pronounced plastic behaviour;
- most common failure mode was fracture of the rebars of the concrete dowels;
- increased beam web thickness enhanced the concrete dowels' resistance;
- an increased concrete compressive strength led to a higher stiffness of the concrete dowels;

Braun et al. [38] established the following range of validity:

- use of concrete dowels in steel-concrete composite slabs of multi-storey structures limited to sagging bending moment regions;
- the steel beam cross section of the *CoSFB* with concrete dowels could be made of a simple hot-rolled profile, a hot-rolled profile with an additional steel plate or half of a hot-rolled profile with a welded lower flange;
- the steel grade should be at least S355;
- the steel beam could be either completely or partially integrated in concrete;
- the concrete class should be in the following range: C25/30 ÷ C55/67.

2.1.5 Yang, L., Wang, Y., Shi, Y. [41] (2015)

Pseudo-dynamic experimental tests on frame slim-floor beams

The study carried out by Yang et al. [41] was centred on the investigation of the load-bearing capacity of the slim-floor beam (see Fig. 2-13a) through pseudo-dynamic and pseudo-static experimental tests. As defined in the paper, the target applications are seismic-resistant structures. To this end, an experimental program on a 3D full-scale structure was developed. The plane layout of the full-scale structure consisted of a span by two bays – each of 6 meters. In elevation, the frame incorporated two storeys of 2.5 meters each. The structural system on the tested direction (i.e., transverse direction with one span) was MRF. The slim-floor beams

were connected to the columns through welded beam-to-column connections (see Fig. 2-13b). To ensure the load transfer, the welding of the beam flanges to the column was performed with full-penetration groove welds. The materials of the structural elements were:

- steel grade Q235-BF (f_y = 270 N/mm^2);
- concrete class C30 (f_c = 30.3 ÷ 30.8 N/mm^2);
- transverse rebars (f_y = 362.2 N/mm^2; Ø: 6 mm);
- longitudinal rebars (f_y = 366.5 N/mm^2; Ø: 12 mm);
- corrugated steel sheets MMR-238.

The anchorage of the longitudinal rebars was realised through the welding of the rebars to the columns (see Fig. 2-13c) and by bending the rebars downwards. Apart from the transverse and longitudinal reinforcement, each concrete rib was reinforced with a rebar of 20 mm in diameter. The slim-floor beam was made of welded steel plates with a wider lower flange than the top one. The columns had a rectangular hollow section.

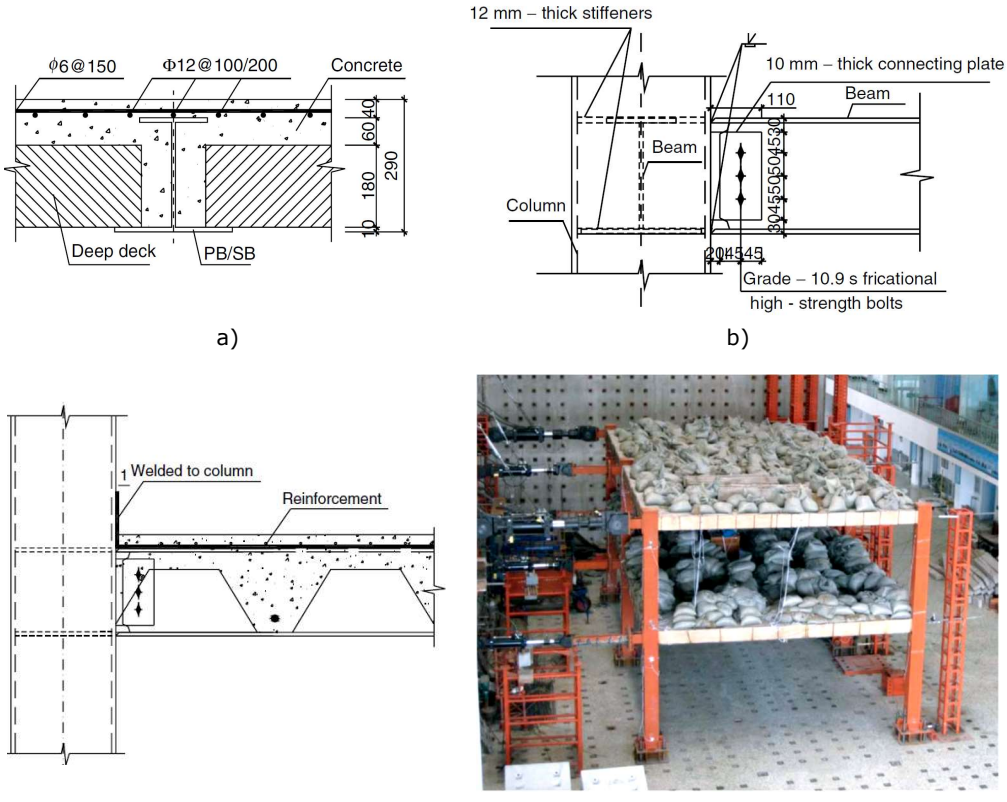

Fig. 2-13. Images from Yang et al. [41]: a) cross section of slim-floor beam; b) welded beam-to-column connection; c) anchorage of longitudinal reinforcement; d) test setup

During the experimental tests, the 3D structure specimen was gravitationally loaded with a uniformly distributed load of 4 kN/m^2 applied on the first storey and 2 kN/m^2 on the top one (see Fig. 2-13d). According to the paper, the pseudo-dynamic

test was performed with the ground motion record of El Centro (N-S) in three subsequently peak accelerations: 0.05 g, 0.10 g and 0.20 g. During the pseudo-dynamic test, the development and limited propagation of cracks in the concrete slab were observed. Based on the on-site observations and on the recorded measurements, Yang et al. [41] concluded that the response of the structure with slim-floor beam-to-column joints was in the elastic range up to and including 0.10 g, while at 0.20 g a pronounced crack opening was observed. The pseudo-static experimental test was performed on the same test setup. Up to 240 kN, force control was used by progressively increasing the lateral load on the specimen. After reaching 240 kN, the test was performed in displacement control up to 4.5 times the yield displacement Δ_y and stopped once the slim-floor system started to suffer dislocations of the concrete slab. During the pseudo-static test, the failure mechanism developed gradually and followed this sequence of events (see Fig. 2-14a-c):

- up to 220 kN: emergence and development of concrete cracks in the negative bending moment area near to the beam-to-column connections; small local deformations of the corrugated steel sheets;
- 230 kN: fracture of longitudinal rebar and sudden widening of the cracks in the concrete slab near the neighbouring columns (top storey);
- $2 \cdot \Delta_y$ displacement: fracture of other longitudinal bars (top storey) and emergence of two first weld cracks (slim-floor beam flange-to-column weld);
- $3 \cdot \Delta_y$ displacement: multiple weld fractures of the longitudinal rebars-to-columns (first storey); cracks in most of the beam flange-to-column welds;
- $4 \div 4.5 \cdot \Delta_y$ displacement: decrease of load as weld failure numbers increased; buckling of the column base; significant dislocations of the concrete slab.

The hysteretic force-displacement curve constructed by the authors evidenced an overall relatively symmetric response of the top storey, despite the positive peak value being 15.3 % lower than the negative one. A backbone curve was constructed by the authors from the measurements recorded at the top storey. According to Yang et al. [41], a good ductility of the tested specimen was demonstrated by values of the ductility factors μ_Δ larger than four.

a) b) c)

Fig. 2-14. Progressive damage to the test specimen of Yang et al. [41]: a) buckling of steel sheets; b) example of reinforcement bar fracture; c) lower beam flange-to-column weld failure

2.1.6 Duarte da Costa, J. (PhD Dissertation) [42] (2018)

Experimental tests on slim-floor beams with concrete dowels positioned in the hogging bending region

In the doctoral thesis of Duarte da Costa [42] the influence of components (e.g., reinforced concrete slab, beam-to-column connection) on the behaviour of

composite slim-floor joints under hogging bending moments was studied. To identify the most influential joint components, this study included an experimental program performed on slim-floor beam-to-column joint specimens and advanced finite element simulations. According to Duarte da Costa [42], the motivation for this study resided in the lack of specific design rules for semi-continuous joints (including slim-floor joints), in which case both the Serviceability and Ultimate Limit State design (i.e., SLS, ULS) would be positively influenced. As observed by Duarte da Costa [42], most composite joints modelled as nominally pinned possess a certain rotational stiffness and bending resistance due to the presence of the continuous longitudinal reinforcement. On the other hand, some continuous joints display flexibility and are sometimes only partial-strength. Therefore, these two different types of joint modelling, simple and continuous, are idealizations which, as stated in this study, do not reflect reality. Considering this, the aim of the study was also to provide an analytical design procedure for the calculation of the stiffness and rotation capacity of composite slim-floor joints under hogging bending moments.

The experimental campaign was performed on three sets of beam-to-column joints categorised according to their configuration:

- "*series B*": four joint specimens without the bolted beam-to-column connection (see Fig. 2-15a);
- "*series C*": one joint specimen without concrete slab (see Fig. 2-15b);
- "*series E*": three joint specimens with composite slim-floor beam (*CoSFB)* including both the bolted beam-to-column connection and the reinforced concrete slab (see Fig. 2-15c).

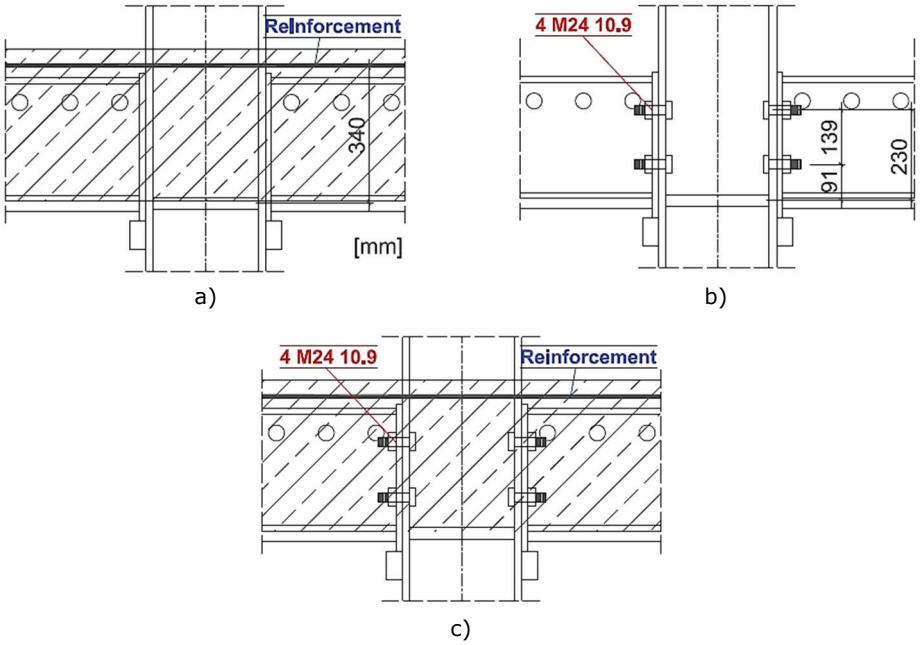

Fig. 2-15. Images from Duarte da Costa et al. [43]: different configurations of joint specimens: a) "*series B*"; b) "*series C*"; c) "*series E*"

The *CoSFB* incorporated an HEA-320 profile with an additional 500 mm wide lower plate made of steel S355, B500B rebars (longitudinal: Ø = 12, 16, 20 mm;

transverse of Ø = 8 mm; concrete dowels of Ø = 12 mm) and concrete C35/45 (see Fig. 2-16d). The column had an HEB-300 profile made of S355. The joint specimens were double-sided internal joints, whose *CoSFBs* were connected to the column through a relatively thin end-plate (15 mm) and four bolts M24, Gr. 10.9. (valid for "*series E*"). In "*series B*" the bolted connection was omitted, whereas the reinforcement was ignored in "*series C*" Duarte da Costa [42] stated that the steel decking was not included in the study, as only the longitudinal behaviour of the joint specimens was of interest. Material tests revealed the following characteristics:

- HEA-240: f_y = 499 N/mm^2, f_u = 554 N/mm^2;
- additional welded lower steel plate: f_y = 412 N/mm^2, f_u = 534 N/mm^2;
- end-plate: f_y = 425 N/mm^2, f_u = 549 N/mm^2;
- HEB-300: f_y = 429 N/mm^2, f_u = 526 N/mm^2;
- concrete: $f_{c,cyl}$ = 45 ÷ 61 N/mm^2;
- rebars: $Ø_{12}$ / $Ø_{16}$ / $Ø_{20}$: f_y = 534 / 547/ 578 N/mm^2.

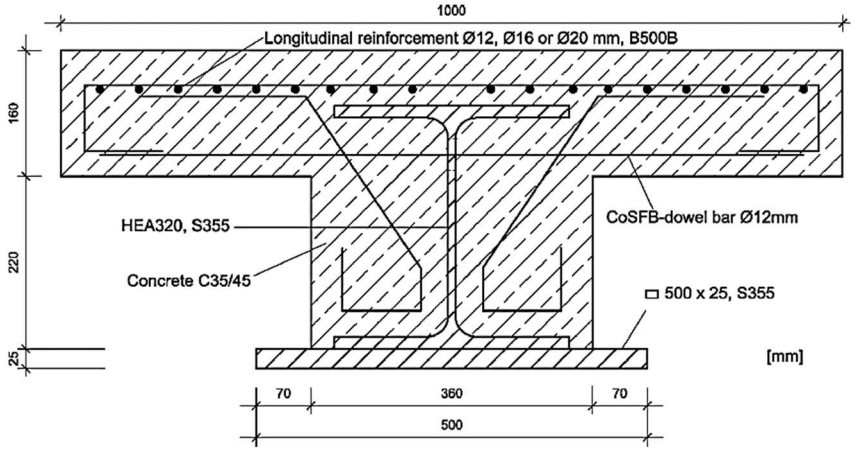

Fig. 2-16. Cross section of the *CoSFB* (from *"series E"*) from Duarte da Costa et al. [43]

According to the test setup (see Fig. 2-17), each beam was approximately 2.63 meters long and had vertically restrained ends. In those specimens where *CoSFBs* were tested, the width of the concrete slab was 1 meter. The hydraulic jack introduced a monotonic load in displacement control by pulling the column upwards and subjecting the beam-to-column joints to hogging bending.

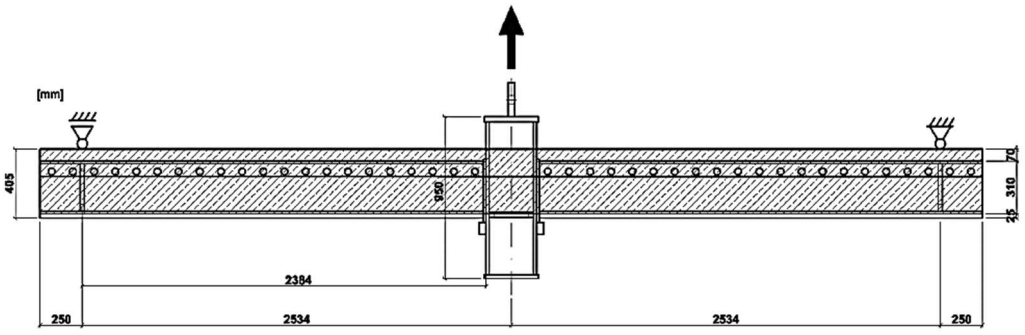

Fig. 2-17. Test setup from Duarte da Costa et al. [43]

For the joint specimens from "*series B*" (without beam-to-column bolted connection) the following failure modes were observed: longitudinal reinforcement failure in two specimens (at 95, 110 mrad of monotonic hogging rotation), shear failure of the slab (at 42 mrad) and increased transversal bending (see Fig. 2-18a-b). The bare steel joint specimen from "*series C*" evidenced a pronounced deformation of the end plate in bending followed by a thread stripping failure mode at 68 mrad (see Fig. 2-18c-e). No clear failure mode could be identified for the joint specimens from "*series E*" which incorporated both a reinforced concrete slab and a bolted beam-to-column connection. However, in this last series of tests, the highest hogging bending resistance was obtained.

Considering the results of the experimental program, the following conclusions were drawn in the study of Duarte da Costa [42]:

- the high ductility of the composite *CoSFB* joints was the result of both large reinforcement ratio and rebar diameter;
- the stiffness of beam-to-column joints could be increased by a larger amount of reinforcement;
- larger reinforcement diameters decreased the value of stiffness;
- through the comparison of the results of "*series C*" to "*series E*" (bare steel vs. *CoSFB* joint), no significant difference in stiffness was found.

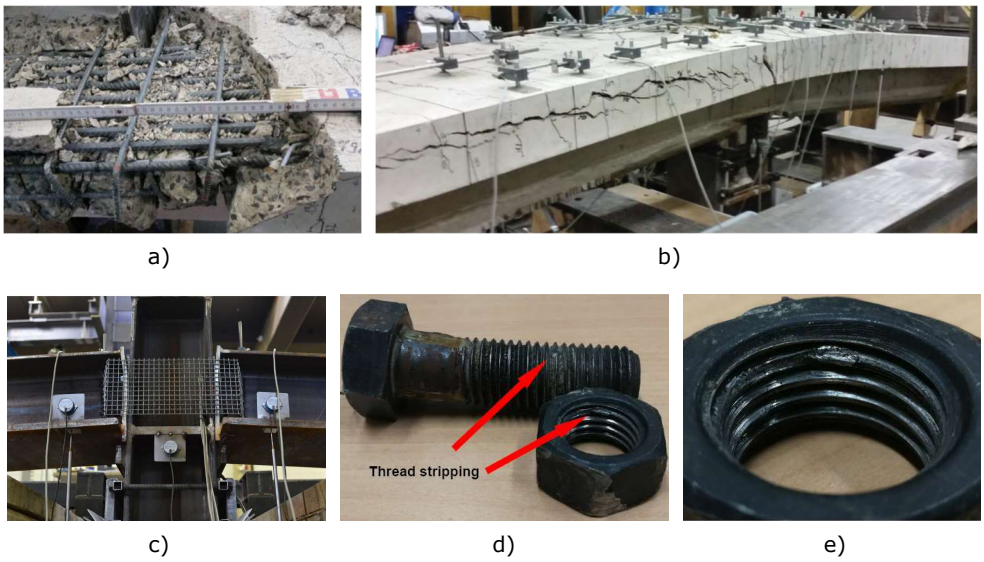

Fig. 2-18. Failure modes. "*Series B*": a) longitudinal reinforcement failure; b) failure of the concrete slab; "*Series C*": c) large deformation of the end-plates; d) & e) thread stripping

This study [42] also incorporates the calibration of finite element numerical models and the development of a parametric study. The modelling was carried out in Abaqus with *C3D8R* (for steel parts, concrete, bolts) and *B31* elements (for reinforcement). The interaction between steel components and concrete was achieved through "*general contact*". Whereas in the normal direction a "*hard contact*" was defined, a "*friction / penalty contact*" option with a friction coefficient of 0.4 was selected. Regarding material-related numerical modelling options, "*concrete damaged plasticity*" was used for concrete. The steel components were modelled accounting for both the elastic and plastic responses. For an improved computational time, double

symmetry boundary conditions were used leading to only of a quarter of the entire numerical model being replicated. The numerical analysis was performed with the *"dynamic, explicit"* option, while the load was applied with *"smooth step"*. According to Duarte da Costa [42], as good correlations between the numerical models and the experimental tests were obtained, a parametric numerical program represented the subsequent step. The parametric study included variations on the number and diameter of rebars, as well as on the reinforcement ratio. Considering the results of the parametric study, it was concluded that the concrete encasement has little influence on the performance (i.e., bending resistance, stiffness, rotation capacity) of the joints. However, a high influence of the reinforcement ratio and rebar diameter was underlined by the results of the parametric study. As stated in the conclusions of the numerical program, the greatest rotation capacity was evidenced by the numerical model with the highest reinforcement ratio and rebar diameter. Another conclusion resulted from the parametric study was the higher value of the effective length of the joint than that provided by the European code.

Also included in this study [42] was a method for the calculation of the effective length, stiffness and rotation capacity of a composite joint. In the calculation of the effective length, Duarte da Costa [42] introduced new terms which accounted for the number of main cracks and the transmission length. It was considered that this approach to the computation of the effective joint length could lead to a more accurate stiffness of composite joints. According to the study, the rotation capacity of the composite joint, which is the slab elongation divided by the lever arm measured from the centre of the reinforcement to the centre of compression, could be more simply calculated due to the method provided by Duarte da Costa [42]. Through this method, the ultimate ε_{smu} and the yield ε_{smy} elongation of the reinforced concrete corresponding to an ultimate strain capacity ε_{su} of 5 % could be graphically determined. The accuracy of this method was verified through comparison of the analytic to the experimental and numerical results and considered validated. However, the method is limited to composite joints under non-cyclic loading.

2.1.7 Kyriakopoulos, P., et al. [44] (2022)

Behaviour of slim-floors under extreme deformations

Kyriakopoulos et al. [44] performed experimental and analytical studies on *Deltabeams*® subjected to extreme deformations. Researchers in this study considered that the investigation of the behaviour of shallow flooring systems in extreme deformation situations could enrich the knowledge about slim-floors and expand the applicability of *Deltabeams*® to structures designed for ductility and robustness. The authors also acknowledged the limited research on slim-floors in this context and the lack of code guidelines. In response, a study was launched in cooperation with an industrial partner. In brief, the *Deltabeam*® [10] is an innovative shallow flooring system due to its fast construction and architectural versatility. This solution is realised with perforated steel plates welded in a trapezoidal shape and with reinforced concrete infill. In addition, the implementation of this solution is facilitated by the range of integrated structural solutions provided by the same developer. When used as multi-span beams, the continuity of *Deltabeams*® is ensured by so-called *Gerber joints*. Because of that, the continuous *Deltabeam*® could present advantages to more rare and extreme design scenarios such as seismic action or column loss.

In the study of Kyriakopoulos et al. [44], the experimental program included six *Deltabeam*® specimens with different configurations (see Fig. 2-19a-c). According

to the scientific paper, the beam specimens were divided into two test groups (i.e., *type 1*, *type 2*) depending on the investigated parameters. The tests performed on *type 1* specimens investigated of the influence of the different steel beam profile and the number of shear connectors (see Fig. 2-19a-b). *Type 2* specimens had a different shape of the cross section from those in the other test group, a different position of the stirrups and shorter transverse rebars (see Fig. 2-19c). What differentiated the specimens from the second group from one another was the profile of the beam.

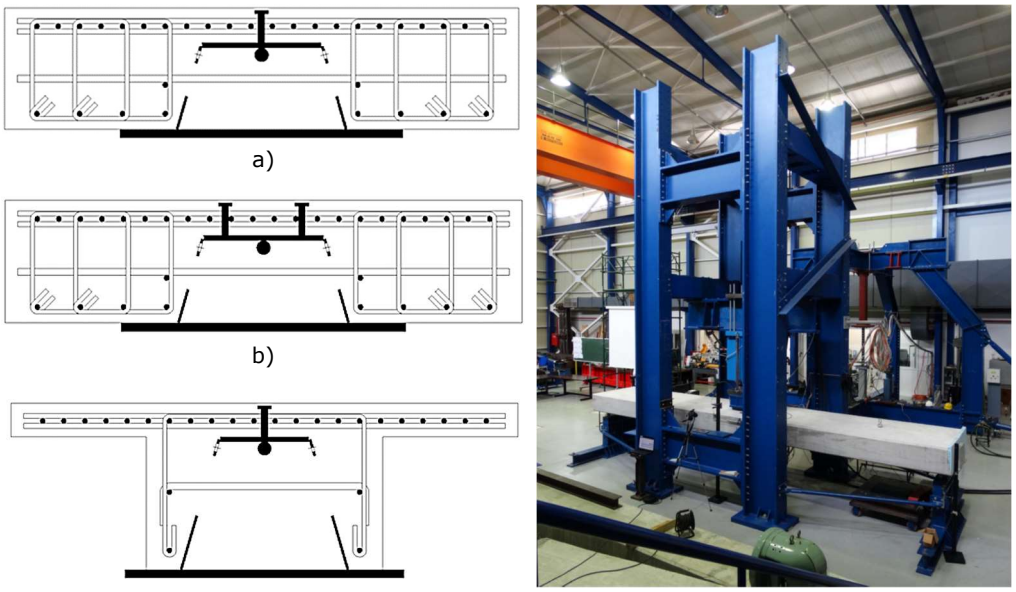

Fig. 2-19. Images from Kyriakopoulos et al. [44]: *Deltabeam*® configurations: a) & b) specimens type 1; c) specimens type 2; d) test setup

Detailed information regarding the components were presented in [44]. The reinforcement of the concrete infill was realised with meshes of longitudinal and transverse rebars and stirrups of B500B steel grade (f_y = 514 N/mm^2). Apart from the transverse rebars inserted in the web openings of the beam profile, shear studs were welded on the top plate of the beam (Ø: 16 mm, h: 75 mm). The concrete class was C30/37 with an average compressive strength of 38.81 MPa. The steel profile of the beam was made from S355.

The experimental tests were monotonically performed in displacement control on a three point loading setup (see Fig. 2-19d). All beam specimens were 7.7 meters long and 1.2 meters wide. The actuator was positioned at mid-span and pushed downwards. The loading protocol was divided in different phases: (i) loading cycles up to serviceability deflection of L/260; (ii) displacement up to a deflection of 150 mm; (iii) displacement up to 450 mm.

According to the authors, the results of the experimental tests revealed an overall ductile behaviour of the *type 1* specimens. As the stroke capacity of the of the actuator was reached, the tests were stopped. The most important conclusions drawn by the authors from this series of tests were:

- although the emergence of fine concrete cracks was recorded immediately after reaching the serviceability deflection, dislocations were limited to the

top of the concrete infill; the authors attributed this behaviour to the confinement ensured by the presence of the stirrups (see Fig. 2-20a);
- two shear stud rows reduced the relative slip.

The main conclusions of Kyriakopoulos et al. [44] on the results of *type 2* specimens were:
- compared to the other specimen from the same test series, one specimen suffered relatively earlier cracking which led to a reduction of load; a slight hardening was evidenced;
- while limited concrete dislocations in the mid-width were recorded, pronounced spalling was evidenced in the areas without stirrups (see Fig. 2-20b); the limited dislocation was attributed by the researchers to the confinement of the concrete infill;
- due to a higher value of the strains recorded in the bottom plate of the beam profile than the yield limit, to the integrity of the concrete infill and to the lack of web buckling, it was considered that the *Deltabeams*® could be used in a wider variety of applications such as design for ductility and robustness.

Kyriakopoulos et al. [44] also developed a finite element numerical model which evidenced a good correlation to the results of the experimental tests.

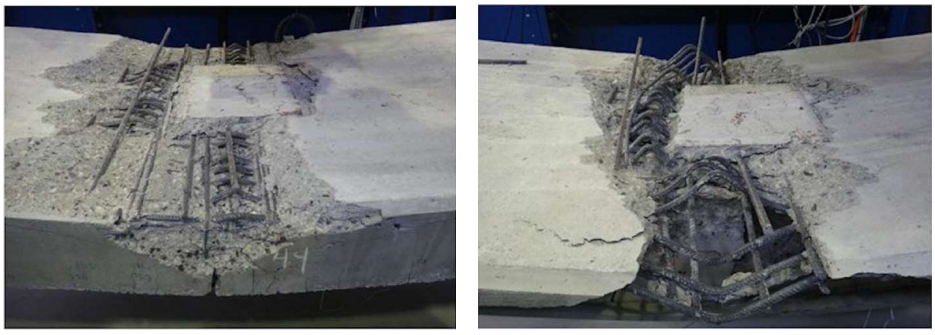

a) b)

Fig. 2-20. Images from Kyriakopoulos et al. [44]: degradation state of specimens at the end of the tests: a) *type 1*; b) *type 2*

2.2 Design for earthquake resistance

2.2.1 Seismic action definition

The European seismicity for a return period of action of 475 years is illustrated through zonation maps in prEN 1998-1-1 [45]. As shown in Fig. 2-21a,b, most European countries experience some level of seismicity, but an increased seismic hazard is prevalent in southern and eastern Europe. A crucial factor in the definition of site-specific elastic response spectrum is the site category, as seismic waves propagate differently in distinct soil types. To address this, a simplified description of the site conditions is provided in prEN 1998-1-1 [45], Annex B.

In general, seismic action is specified through return periods in years $T_{LS,CC}$ or through its probability of exceedance $P_{t,LS,CC}$ [50]. The return periods of seismic action are provided in prEN 1998-1-2 [51]. For a common building structure categorised in Consequence Class 2 (CC2), the return periods are shown in Fig. 2-22, in accordance with the code [51].

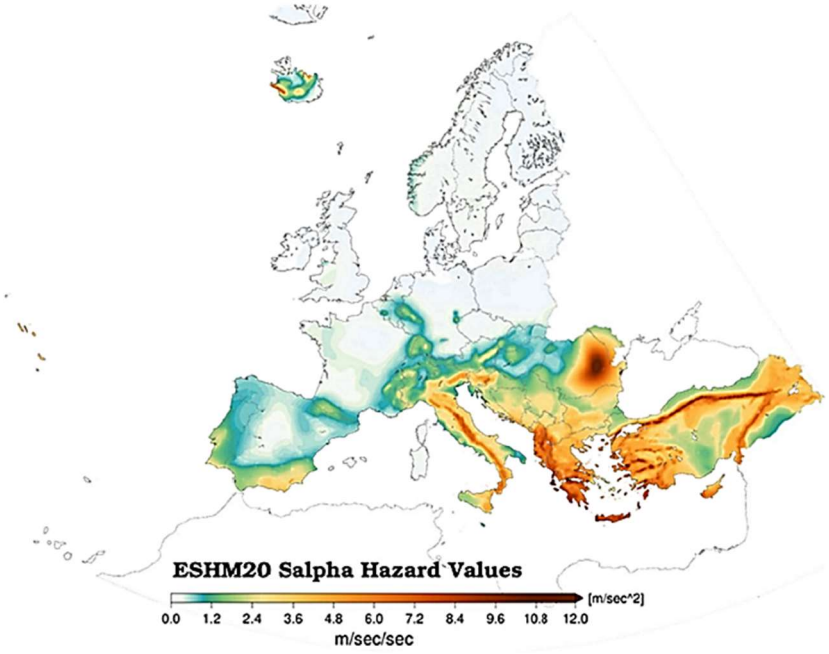

a)

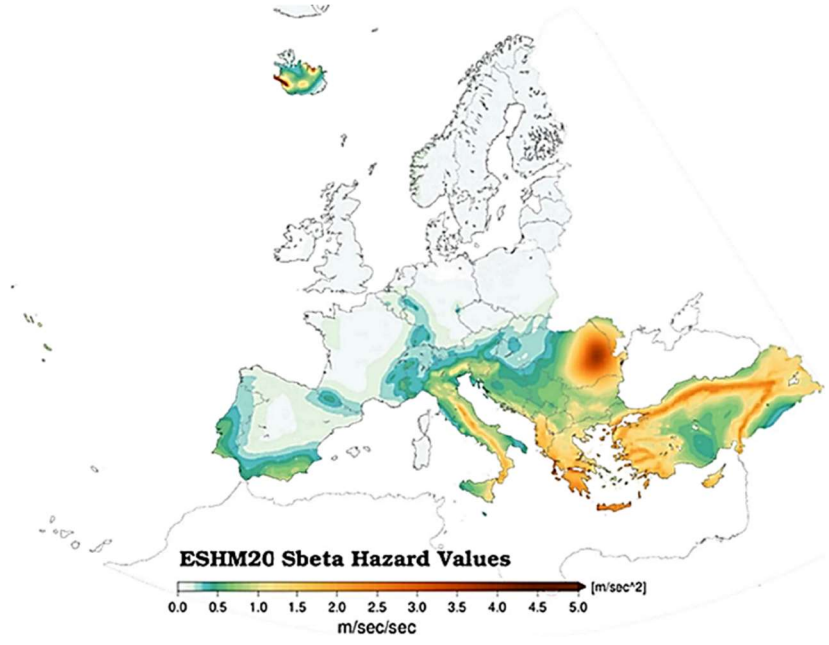

b)

Fig. 2-21. European seismicity maps according to [45] illustrated for: a) maximum response spectral acceleration (constant acceleration range) of the horizontal elastic response spectrum; b) spectral acceleration at the vibration period T_β of the horizontal elastic response spectrum

Consequence Class	Limit State		
	DL	SD	NC
CC2 - normal	60 years	475 years	1600 years

Fig. 2-22. Return periods of seismic action $T_{LS,CC2}$ in years for CC2 according to [51]

Depending on the range of seismic action index S_δ, the following seismic action classes are defined in prEN 1998-1-1 [45]:

- very low (S_δ < 1.30 m/s^2);
- low (1.30 m/s^2 < S_δ < 3.25 m/s^2);
- moderate (3.25 m/s^2 < S_δ < 6.50 m/s^2);
- high (S_δ > 6.50 m/s^2).

In relation to the importance of a building, consequence classes were introduced in prEN 1990 [52] (see Fig. 2-23a) and are necessary to be used in the application of the seismic normative [45] [51]. Common structures (e.g., office and residential buildings, see Fig. 2-23b) should belong to Consequence Class 2 (CC2) and are associated to medium individual, societal, economic and environmental consequences. The purpose of a consequence class is to categorise the consequences of structural failure in terms of human lives, economic, social or environmental loss.

Consequence Class	Indicative qualification of consequences	
	Personal injury or human life loss	Economic, social or environmental consequences
CC0 - lowest	very low	insignificant
CC1 - lower	low	small
CC2 - normal	medium	considerable
CC3 - higher	high	very great
CC4 - highest	extreme	huge

a)

Consequence Class	Description of consequence	Examples
CC1	lower	storage, agricultural buildings
CC2	normal	residential and office buildings
CC3	higher	concert halls, grandstands

b)

Fig. 2-23. Consequence classes as defined in prEN 1990 [52]: a) socio-economic and environmental impact of consequence classes to; b) examples of buildings categorised according to the Consequence Classes

In order to evaluate the seismic performance of the structure at the given *Limit States* (LS), performance or amplification factors are used. These performance factors are provided in prEN 1998-1-2 [51] and their value is dependent on both the Consequence Class and the *Limit State*. For regular structures categorised in CC2, the values of the performance factors at Damage Limitation (DL), Significant Damage (SD) and Near Collapse (NC) are shown in Fig. 2-24.

Consequence Class	Limit State		
	DL	SD	NC
CC2 - normal	0.5	1.0	1.5

Fig. 2-24. Performance factors $\gamma_{LS,CC2}$ for CC2 according to [51]

2.2.2 Code provisions for high ductility structures

Configuration of structures

"*A well designed seismic resistant structure should be characterized by a good balance between strength, stiffness and ductility between its members, connections and supports"* (Bertero [53]).

Although not compulsory to apply, good practice rules regarding the configuration of seismic-resistant structures are provided in prEN 1998-1-2 [51]. According to these recommendations, building structures for seismic-resistance could be designed accounting for the following characteristics:

- structural simplicity;
- structural regularity;
- uniformity, symmetry and redundancy;
- bidirectional resistance and stiffness;
- torsional resistance and stiffness;
- diaphragmatic behaviour at storey level;
- equate foundation.

A simple, regular, uniform and symmetrical disposition of the structural elements ensures similar resistance and stiffness characteristics in both directions, while the assigning a peripheral position to the main structural elements that withstand inertial forces caused by seismic action, helps limit torsional motions. Apart from that, as floor systems ensure the transfer of seismic action to the vertical structural elements and assure in-plate stiffness, their role is particularly important. For that matter, large openings, especially near the columns, should be offered careful consideration.

The aim of these recommendations regarding structural configuration is to provide clear und uniform paths for the transmission of the seismic actions and lead to a more predictable behaviour of the structure.

Ductility Classes and behaviour factors

According to prEN 1998-1-1 [45], building structures are divided into three *Ductility Classes* depending on their dissipation capacity: *Ductility Class 3* (DC3), *Ductility Class 2* (DC2) and *Ductility Class 1* (DC1). Different global and local design requirements are applied in accordance with the *Ductility Class*. While design rules for DC3 and DC2 structures are provided in prEN 1998-1-2 [51], prEN 1993-1-1 [54] should be used to evaluate DC1 structures.

Structures designed on the concept of high and medium ductility (DC3, DC2) can be relied on to sustain plastic deformations caused by seismic action. Thus, the behaviour of these structures can be characterised as dissipative and larger values of the behaviour factor q could be employed, than for DC1 structures. As a consequence of higher behaviour factors q, DC2 and DC3 structures are designed with reduced seismic forces. As explained in Landolfo et al. [50], the design with reduced seismic forces has economic advantages, yet the structural resistance and stiffness are lower

than those of the structures designed in DC1. Low dissipative structures (DC1) do not fulfil the conditions to apply a plastic design for static loads, therefore they can be calculated using global elastic analyses, with disregard to inelastic behaviour.

As defined in prEN 1998-1-2 [51], q is the behaviour factor computed as the product between q_S, q_D and q_R which are behaviour factor components accounting for overstrength, deformation and energy dissipation capacity, respectively. The values corresponding to each of the behaviour factors and of the behaviour factor are provided in the seismic code in accordance with the *Ductility Class* of the structure.

STRUCTURAL TYPE	Ductility Class 3 (DC3)			
	q_S	q_D	q_R	q
Moment-Resisting Frames (MRFs)				
▪ portal frames, single storey MRFs with class 3 and 4 cross sections	1.5	-	-	-
▪ portal frames, single storey MRFs with class 1 and 2 cross sections		3.3	1.1	5.5
▪ multistorey MRFs		3.3	1.3	6.5
Concentrically-Braced Frames (CBFs)				
▪ with diagonal bracings	1.5	2.4	1.1	4
▪ with V-bracings				
▪ with X-bracings over single or two storeys				
Dual Frames				
▪ MRFs with CBFs	1.5	2.9	1.1	4.8
▪ MRFs with EBFs		3.3	1.3	6.5
▪ MRFs with buckling restrained braces		3.3	1.3	6.5

Fig. 2-25. Upper limit values of the behaviour factors for MRFs, CBFs and Dual Frames according to prEN 1998-1-2 [51]

Material ductility requirements

According to prEN 1993-1-1 [54], it should be verified that a minimum level of ductility could be assured by material properties. For steel, the following rules are given in accordance with the type of analysis:

- for plastic global analysis Eq. (2.1) should be verified; additionally, the elongation at failure should be at least 15 %:

$$\frac{f_u}{f_y} \geq 1.10 \qquad (2.1)$$

- for elastic global analysis, Eq. (2.2) should be verified; additionally, the elongation at failure should be at least 12 %.

$$\frac{f_u}{f_y} \geq 1.05 \qquad (2.2)$$

In order to meet the requirements of ductility, reinforcing steel used in composite structures, where plastic resistance is applied, should be ductility class B or C according to prEN 1994-1-1 [55] and to EN 1992-1-1 [56].

Performance requirements

According to prEN 1998-1-1 [45], the structural design of buildings is required to ensure the protection of human lives, the limitation of damage and the operational state of crucial facilities for civil protection in the event of an earthquake. To meet

these performance requirements, structures are to be designed in a way that the *Limit States* (LS) are not exceeded under a specific seismic intensity. To measure the performance of a structure, the damage state must be evaluated at a certain phase associated with a seismic intensity, a *Limit State*, and compared to be limitation imposed by the code [51]. In accordance with prEN 1998-1-1 [45], the following four *Limit States* ought to be considered in the seismic design of structures:

- Fully Operational (OP):
  - damage to main structure: slight damage, yet economically repairable;
  - state of main structure: operational.
- Damage Limitation (DL):
  - damage to main structure: slight damage, negligible permanent drifts, but economically repairable; structural members retain complete resistance despite a limited decrease in stiffness;
  - damage to ancillary components: minor damage, yet repairable;
  - state of main structure: operational.
- Significant Damage (SD):
  - damage to main structure: significant damage, moderate permanent drifts; although possible, the repair might not be economic;
  - damage to ancillary components: significant;
  - state of main structure: retains vertical-load bearing capacity.
- Near Collapse (NC):
  - damage to main structure: extensive damage, large permanent drifts;
  - damage to ancillary components: collapsed;
  - state of main structure: retains vertical-load bearing capacity.

According to [57], apart from conventional methods founded on specification criteria, design based on performance criteria is continuously gaining momentum.

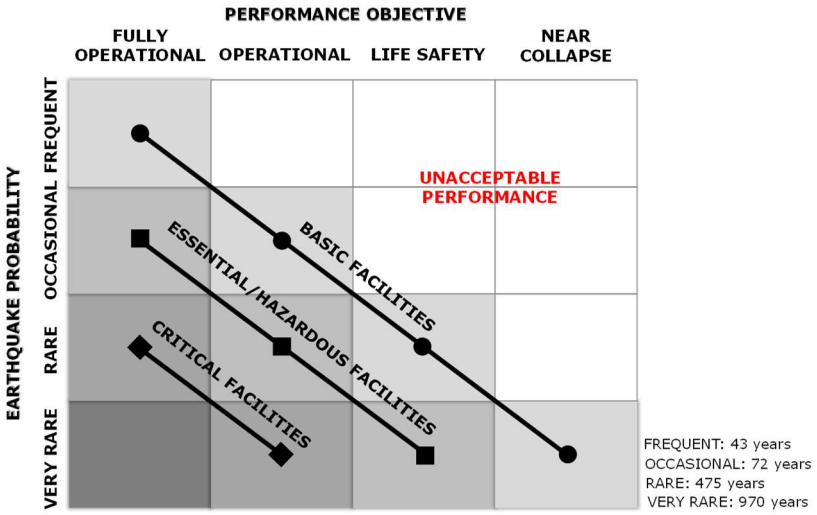

Fig. 2-26. Seismic performance objectives based on *OSEAC Vision 2000* [58]

The application of *Performance-Based Design* procedure ensures a predictable behaviour of the structure at a specific *Limit State*, made possible by implementing certain performance objectives from the starting point of the design. Each performance objective is correlated to a maximum level of acceptable damage to a

structure subjected to a certain seismic intensity. To exemplify, the structure of a common building should be:

- fully operational under frequent seismic events;
- operational under occasional seismic events;
- sufficiently stable to prevent human injury despite significant structural damage under rare seismic events;
- in a critical state due to extensive damage, yet not collapsed under very rare seismic events (see Fig. 2-26 based on *SEAOC Vision 2000* [58]).

Currently, in several literature examples, e.g., [57] [59] [60], the merits of *Performance-Based Design* are underlined and regarded as strong basis for a wider future implementation of the procedure. As concluded by Fujitani et al. [57], the increasing effort to evaluate structures on seismic performance will lead to improved assessment methods and, eventually, to a healthier construction market.

Verifications at Serviceability Limit States

According to prEN 1990 [52], Fully Operational (OP) and Damage Limitation (DL) are *Serviceability Limit States* (SLS), whose main concerns are the functionality of the structure under normal use, the confort of the users and the appearance of the building. Design verifications that ensure the limitation of structural damage at a *Limit State* and, at the same time, help satisfy the performance requirements, are given in prEN 1998-1-1 [45] and prEN 1998-1-2 [51].

In Fully Operational (OP) *LS*, the drifts resulting from the seismic design situation should be smaller than the deformations that are acceptable to the functioning of the facility's services. In addition, the resistances should be based on those of the ancillary elements.

Damage Limitation (DL) *LS* may be considered satisfied when the interstorey drifts due to seismic action (associated to DL) remain within the imposed limit (see Eq. (2.3)), although this check is not mandatory. To account for the sensitivity of the ancillary components (e.g., infill walls, cladding, parapets, curtain walls, ceilings, etc.), the drift limitation at DL *LS* should be associated to their ductility (through different values of the coefficient λ_{ns} multiplied by the storey height h_s).

$$d_{r,DL} \leq \lambda_{ns} \cdot h_s \qquad (2.3)$$

λ_{ns} is 0.0025 for Group 4 unreinforced masonry units.

λ_{ns} is 0.0045 for brittle materials attached to the structure (e.g., Group 1, 2 and 3 masonry units).

λ_{ns} is 0.0075 for ductile ancillary components.

λ_{ns} is 0.010 for ancillary components fixed in a way which does not interfere with structural deformations.

Verifications at Ultimate Limit States

According to prEN 1990 [52], Significant Damage (SD) and Near Collapse (NC) are classified as *Ultimate Limit States* (ULS), whose focus is on the prevention of human injury or loss, unacceptable economic or environmental loss. Relevant design checks are given in prEN 1998-1-1 [45] and prEN 1998-1-2 [51].

Significant Damage (SD) criterion scope is primarily to ensure the stability of the whole structure in the seismic design situation, including cases as overturning and sliding. The fulfilment of this scope could be realised through the limitation of drifts, of second order effects and through capacity design. The drift criterion at SD is

considered satisfied when the interstorey drifts caused by seismic action (associated to SD) remain within the imposed limit expressed by Eq. (2.4). In this case, the value of the coefficient λ_s is dependent on structural types found in prEN 1998-1-2 [51].

$$d_{r,SD} \leq \lambda_s \cdot h_s \tag{2.4}$$

λ_s is 0.020 for moment-resisting frames and dual frames.
λ_s is 0.015 for braced frames and inverted pendulum structures.
λ_s is 0.010 for light-weight structures.

The control of the second order effects (P-Δ) is performed in accordance with code [51] (see Eq. (2.5)). In structures designed in *Ductility Class 3* (DC3), if $q_s < \gamma_{rm} \cdot \Omega_d$, the interstorey drift sensitivity coefficient θ is required to be checked at each storey. Another specific requirement for DC3 structures is related to the design overdesign ratio Ω_d; Ω_d is dependent on the structural system, but should not be considered smaller than 1. Values of the interstorey drift sensitivity coefficient θ smaller than 0.10 allow for the disregard of the *P-Δ* effects, while values bigger than 0.30 are unacceptable. When the value of the interstorey drift sensitivity coefficient θ is between 0.10 and 0.30, *P-Δ* effects could be considered. To this end, several methods are provided by prEN 1998-1-2 [51].

$$\theta = \frac{P_{tot} \cdot d_{r,SD}}{\gamma_{rm} \cdot \Omega_d \cdot q_R \cdot V_{tot} \cdot h_s} \tag{2.5}$$

Apart from the drift limitation at *Limit States* and from second order effects limitation, the global plastic mechanism at Significant Damage (SD) *LS* is controlled through the capacity design. This method ensures the seismic energy dissipation through plastic hinges (specific zones from ductile structural members designed to sustain inelastic deformations). Applying capacity design requires a distinction be made between the structural elements according to their role; while controlled seismic energy dissipation is allowed in dissipative zones of ductile components, it is restricted in non-dissipative ones. According to the code [51], a sufficient ductility of the dissipative zones is achieved by ensuring the required cross sectional class and by restricting the accordingly width-to-thickness ratio *b*/*t*. For instance, all elements of structures designed in DC3, and for which the behaviour factor *q* is bigger than 3.5, are required to have cross sectional class 1. Additional rules for ensuring ductility depend on the structural type and are given in prEN 1998-1-2 [51].

The aim of the Near Collapse (NC) *LS* is primarily to prevent structural collapse. According to the seismic code [51], in case NC is considered, the deformation limits or other relevant limits given in prEN 1998-3 [61] should not be exceeded.

2.2.3 Code provisions for moment-resisting beam-to-column joints

As slim-floors joints are not specifically treated in the codes, the typical rules for moment-resisting beam-column joints could be used for guidance. In this study, the slim-floor beam is designed as a ductile member with dissipative zones.

Resistance of the joint

According to prEN 1998-1-2 [51], horizontal forces in MRFs are resisted by structural components through flexure. The primary dissipative components of MRFs designed for DC3 are the beams. In the current study, this means that the main structural fuse is the slim-floor beam, and the dissipation of seismic energy occurs at

its ends. To "force" the development of plastic hinges in the beams, the weak beam-strong column concept is adopted. While methods of ensuring ductility in the steel beams are applied (i.e., limitation of width-to-thickness ratio and of cross sectional class, *Reduced Beam Section*), the adjacent non-dissipative structural components (e.g., columns) and connections are designed considering material overstrength γ_{rm} and strain hardening γ_{sh}. The factor for random material variability can be found in EN 1998-1-2 [51] and should be selected in accordance with the steel grade of the ductile structural elements. The strain hardening factor for dissipative zones from MRFs needs to be calculated in DC3, as shown in Eq. (2.6) from [51]. According to the seismic code, the section class of the beams should be 1. In the code for composite steel and concrete structures, prEN 1994-1-1 [55], both 1 and 2 section classes are accepted for beams. The steel grade of the beams should be in the range of S235 to S460 [55].

$$\gamma_{sh} = \frac{f_y + f_u}{2 \cdot f_y} \leq 1.2 \tag{2.6}$$

According to the seismic code [51], the bolted beam-to-column connection of the joints designed in DC3 could be full-strength or "non-yielding" to meet the resistance and stiffness requirements. The full-strength criterion is considered a prerequisite for joints of Moment-Resisting Frames in Landolfo et al. [50]. To achieve this, the seismic code requires the beam-to-column connection to be designed accounting for the effects of material overstrength γ_{rm} and strain hardening γ_{sh}, as shown in Eq. (2.7), where $M_{b,pl,k}$ is the plastic bending resistance of the beam, and the design shear force $V_{Ed,G}$ (due to non-seismic actions) and $V_{Ed,M}$ (due to the application of the plastic moments with opposite signs at the ends of the beam) are projected from the centre of the plastic hinge to the column face with the distance s_{hc}.

$$M_{con,Rd} \geq \gamma_{rm} \cdot \gamma_{sh} \cdot \left(M_{b,pl,k} + s_{hc} \cdot V_{Ed,M}\right) + s_{hc} \cdot V_{Ed,G} \tag{2.7}$$

According to [51], when full-strength beam-to-column connections are used in MRFs or Dual Frames, the concept of strong column web should be applied. The design of the columns should include the minimum overstrength $\Omega_{d,}$ which is calculated with Eq. (2.8) from [51], where $M_{b,pl,Rd}$ is the plastic bending resistance of the beam from which the bending moment due to non-seismic actions $M_{Ed,G}$ is subtracted, and then divided by the bending moment due to seismic actions $M_{Ed,E}$. Section class 1 is recommended for columns, while the steel grade should be in the range of S235÷S690.

$$\Omega_d = min\left(M_{b,pl,Rd} - M_{Ed,G}\right)/M_{Ed,E} \tag{2.8}$$

Stiffness of the joint

To classify the beam-to-column joint, its stiffness must be calculated. The stiffness of the joint is computed in accordance with the provisions of EN 1993-1-8 [62] and EN 1994-1-1 [17]. As the joint solution is designed for seismic action, it is necessary to take into consideration both the hogging and the sagging stiffness.

According to Landolfo et al. [50], beam-to-column joints of Moment-Resisting Frames should be designed as rigid or semi-rigid.

Rotation capacity of the joint

Both the European and the American design codes require the achieving of a certain rotation of the moment beam-to-column joints designed for high ductility. According to the European code [51], joints designed in DC3 should develop a plastic rotation capacity of θ_p = ±30 mrad. The American National Standard AISC 341-16 [30] requires ±40 mrad which include both elastic and plastic rotations of the joint.

2.2.4 Additional aspects regarding composite joints

Asymmetric cyclic degradation of composite joints

According to several studies, e.g., [63] [64] [65], composite moment-resisting beam-to-column joints subjected to alternate bending moments generally experience an asymmetric cyclic degradation in strength and stiffness due to the presence of the concrete slab. This has implications on the computer-aided modelling of such joints and, ultimately, on the overall seismic performance of the structure. As seismic design relies on capacity design and because, in comparison to bare steel joints, composite action has been proven to increase both flexural strength and stiffness, the disregard of the composite action could shift the development of plastic hinges from the beams to the web panel. For instance, El Jisr et al. [63] established that the hogging bending resistance of composite beams was 10 % higher than that of the expected bare steel beam due to the contribution of longitudinal rebars and steel decking, and deemed more obvious in shallow beam depths (h ≤ 330 mm) with high reinforcement ratios (8 ÷ 13 mm^2/cm). The sagging resistance of relatively shallow composite beams (h ≤ 500 mm) was found to be 60 ÷ 80 % higher than the plastic bending resistance of the bare steel beam. Therefore, it is recommended in this study to consider the composite action in the modelling of the joints and to add it to the sagging bending resistance in the strong column–weak beam check in order to control the global mechanism. In terms of stiffness, this study concluded that the effective stiffness of shallow composite beams in sagging bending was approximately 1.6 times that of the bare steel beam. Due to the previously mentioned reasons, composite joint models should account for the effects of the composite action.

Connections with Reduced Beam Section

The *Reduced Beam Section* (*RBS*) is the technique based on the deliberate, controlled and specific "weakening" of a structural element's cross section in order to allow for seismic energy dissipation. The main principle on which the *RBS* is based was developed in the 1980s by André Plumier [66] and has, since then, been growing in popularity. Not only does the *RBS* allow for seismic energy dissipation, but also reduce the demand on the adjacent structural elements, while still complying with the deflection limitations.

The geometry of the *RBS* can vary. Examples of *RBS* shapes are shown in Fig. 2-27, which were extracted from Plumier [66]. Additional to these shapes (i.e., with constant cut; with tapered cut), the so-called radius cut is shown in Fig. 2-28a,b. According to Jones et al. [67], the radius cut is the most used geometry of *RBS*. The reason for this was given in the study performed by Engelhardt [68]. In this study, it was concluded that, whereas 60 % of constant and tapered cut specimens fracture in the *RBS*, the same phenomenon occurs to only about 5 % of radius cut specimens after local buckling. Thus, it was concluded in [68] that the radius cut *RBS* connections are more ductile than the constant and the tapered cut ones. As shown in [67], this

was attributed to the shape of the *RBS*: radius cut *RBS* connections are less prone to stress concentration.

RBS connections have been extensively researched since their introduction. The optimisation of the *RBS* shape could increase local member ductility and decrease the likelihood of stress and strain concentration ([67] [69] [70] [71]). Currently, both the American and the European codes include *RBS* connections. In Europe, the dimensions, e.g., *a*, *b*, *c*, *r*, and the position $s_{h,c}$ of the *RBS* are provided in prEN 1998-1-2 [51] (see Fig. 2-28a,b, Eq. (2.9)-Eq. (2.13)).

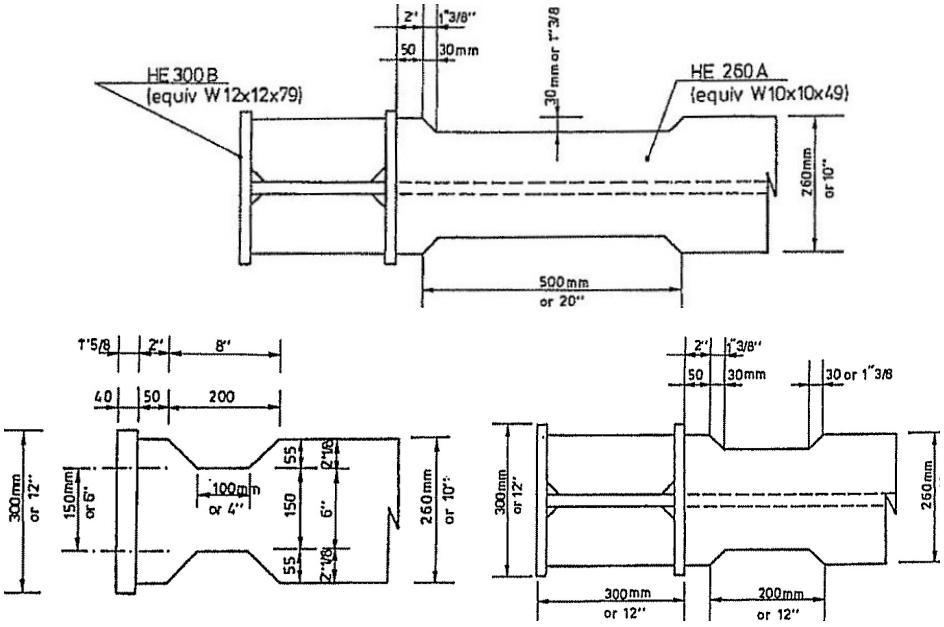

Fig. 2-27. Different *RBS* geometries developed in the research project *ARBED-EU* from [66]

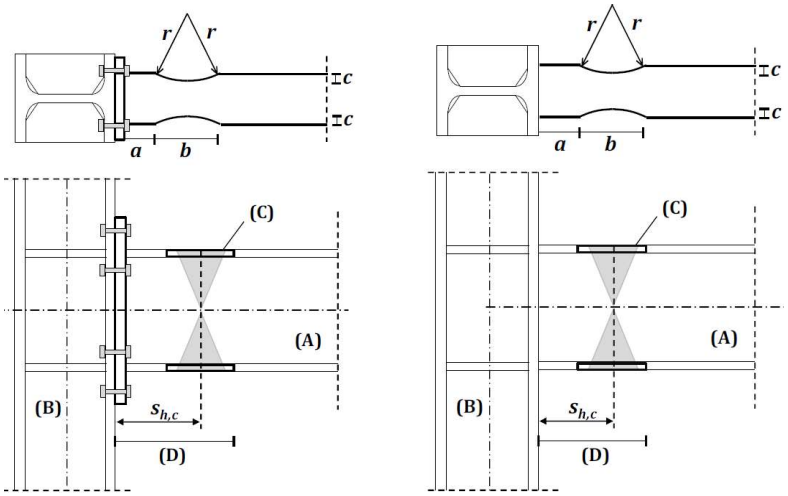

Fig. 2-28. Bolted and welded joint configurations with *RBS* from prEN 1998-1-2 [51]

Distance from column face to *RBS*: $a = 0.6 \cdot b_f$ (2.9)

Length of the *RBS*: $b = 0.75 \cdot d_b$ (2.10)

Flange cut of the *RBS*: $c = 0.20 \cdot b_f$ (2.11)

Radius of the flange cut: $r = \frac{4 \cdot c^2 + b^2}{8 \cdot c}$ (2.12)

Distance from column face to *RBS* centre: $s_{h,c} = \left(a + 0.5 \cdot b + t_p\right)$ (2.13)

2.3 Concluding remarks

In the review of the state-of-the-art an **increasing trend of interest** in slim-floors was evidenced. According to the herein review of the research studies on slim-floors, the following main directions of study were identified:

- flexural behaviour of slim-floor beams under gravity loads [5] [72] [9] [35];
- simple [37] or semi-continuous [31] slim-floor beam-to-column joints;
- rotation capacity of slim-floors [42] [43];
- shear connectors in slim-floors, including concrete dowels [38] [3];
- fire resistance of slim-floors [73];
- deformation [74] and vibration control in slim-floors [75].

Recurring characteristics of slim-floors. In a significant number of reviewed studies, slim-floor systems with asymmetric steel beams were characterised as ductile and considered to ensure a full shear interaction, to which low relative slips are attributed to.

Slim-floor beam-to-column connection. The recurrence of the slim-floor beam-to-column connection as a main subject of interest was another conclusion drawn from the review of the state-of-the-art. In the reviewed studies, bolted (e.g., [37] [31] [42] [38]) and welded (e.g., [35] [41]) beam-to-column connections were investigated. Due to more advantages in terms of material use and to a better performance in Serviceability, e.g., diminished cracking and vibration, lower deflections, in several studies such as [31] [37] [42] the influence of semi-continuity on the overall slim-floor beam-to-column joint performance was investigated. In the previously mentioned studies, the stiffness classification of the joint was upgraded from nominally pinned to semi-rigid due to the continuity of the longitudinal rebars. However, as slim-floor beam-to-column joints were regularly designed as simple forms of construction with nominally pinned connections, the potential provided by semi-rigidity would not be exploited due to the current lack of design rules for semi-continuous joints.

Reinforcement of concrete slab in slim-floors and frequent failure mechanisms. Another frequent topic in the reviewed state-of-the-art was the reinforcement of the concrete slab in slim-floor systems [31] [37] [42]. Apart from the influence on the stiffness of the joint, an increase in the hogging bending resistance was attributed to the presence of longitudinal rebars. Specifically, the

performance of slim-floor beam-to-column joints with bolted connections, e.g., flush end-plate, with shear flat, was enhanced by the longitudinal rebars of the concrete slab. However, in these cases, the first bolt row was positioned under the top flange of the beam. Because of this, the tension under hogging bending moments was predominantly transferred by the longitudinal rebars. Thus, the most common failure mechanism for slim-floors with flush end-plate connections and with shear flats was the **fracture of the longitudinal rebars in tension**. Since tension was mainly transmitted by longitudinal rebars, the failure mechanism was expected. In studies with welded connections [35] [41], the **influence of longitudinal rebars was less evident**. However, in the study of Yang et al. [41], the influence of longitudinal rebars could not be ignored, as the fracture of several rebars initiated a multitude of weld failures.

Another failure mechanism to consider is the **shear failure of the concrete slab** in the area behind the column. In the study of Demonceau [76] on single-sided composite beam-to-column joints tested under monotonic and cyclic loads, the area of the concrete slab located behind the column "failed" in shear. To prevent this failure mode, it was recommended in the study to ensure a minimum area of transverse rebars.

Limited studies on slim-floors for seismic applications and European code design rules. Research studies on slim-floor beam-to-column joints for seismic applications are limited. One example is the study of Yang et al. [41], in which the seismic performance of a full-scale 3D structure with slim-floor beam-to-column joints was investigated. Apart from the different study direction, the loading, e.g., pseudo-dynamic and pseudo-static, that was considered in the experimental campaign of Yang et al. set this study apart. Therefore, the study of Yang et al. [41] has most in common with the current research on slim-floor beam-to-column joints for seismic applications.

Although a solid framework for beam-to-column joint design is provided by in European codes (e.g., composite [17] [55] and seismic [1] [45] [51]), neither include slim-floor systems. More particularly, comprehensive rules for designing steel and composite seismic-resistant structures, provisions for ensuring sufficient global and local ductility, as well as structural and member verifications are currently available in the European codes but make no reference to the particular case of slim-floors.

3. EXPERIMENTAL PROGRAM

The experimental program performed in the current study was aimed at the investigation of the seismic performance of slim-floor beam-to-column joints. In line with this aim, the following objectives were established:

- design and development of a technical solution for slim-floor beam-to-column joints applicable to framed structural systems in Ductility Class 3;
- design and development of the beam-to-column joint specimens, experimental test setup, measuring system;
- performing monotonic and cyclic experimental tests;
- interpretation of results and assessment of seismic performance.

3.1 Pre-test analyses

The configuration of the slim-floor beam-to-column joint specimens was established based on both advanced pre-test Finite Element Analyses and pre-test structural analyses (see Fig. 3-29).

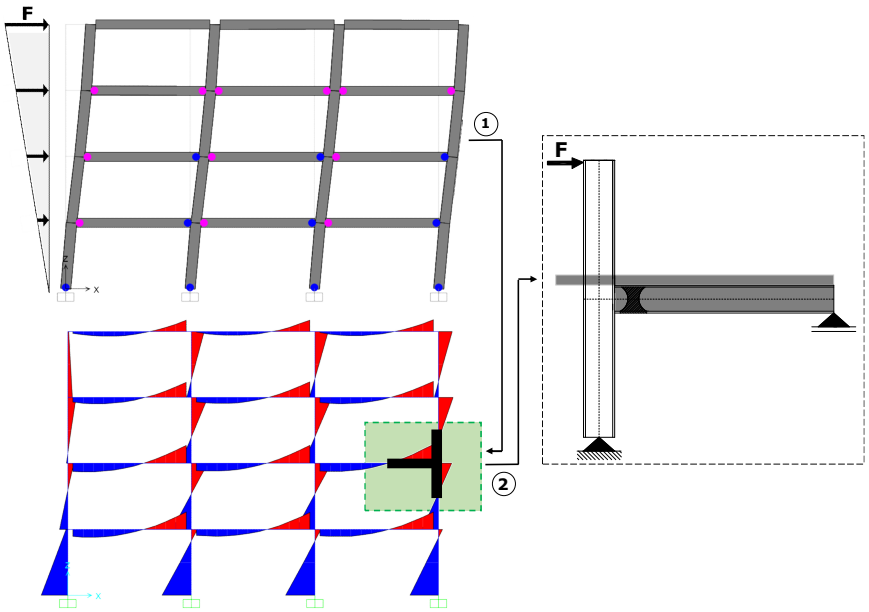

Fig. 3-29. Methodology used to establish the configuration of the specimens and test setup

The technical solution for slim-floor beam-to-column joints that is proposed in the current study was developed on the FE numerical investigations performed in the framework of the master thesis entitled *"The numerical investigation of beam-to-column connections for slim-floor systems"* [77]. In the master thesis, several bolted slim-floor beam-to-column joint configurations were analysed under sagging and hogging bending and led to the conclusion that the failure mode under sagging

bending would be that of the tensioned bolts. Moreover, the previously mentioned failure mode would occur even if larger bolt diameters were used. This aspect was mainly attributed to the wider bottom flange of the slim-floor beam, which possessed higher resistance than the bolted connection. In consequence, the FE pre-test numerical investigations that were conducted within the doctoral dissertation were aimed the development of a technical solution for slim-floor beam-to-column joints that would be characterized by the following: (i) an elastic response of the connection and the column web panel and (ii) formation of the plastic hinge in the "dissipative zone" of the slim-floor beam.

As qualitatively illustrated in Fig. 3-29, preliminary structural analyses were performed on a Moment-Resisting Frame in order to estimate the cross sections for the slim-floor beams and the columns. Based on the results of the preliminary structural analyses, the cross section of the slim-floor beam and column were established. However, the testing capabilities of the CEMSIG laboratory were also taken into consideration. The overall dimensions and details of the slim-floor beam-to-column joint assemblies are presented in Section 3.2.

3.2 Configuration of the specimens

Two slim-floor beam-to-column joints were configured as identical planar specimens and incorporated the following components (see Table 3-1):

- steel beam with a welded steel plate as the lower flange;
- steel column;
- bolted beam-to-column connection;
- reinforced concrete slab with longitudinal, transverse and inclined rebars;
- concrete dowels.

Table 3-1 – Details regarding the joint specimens

Components	Material	Details: cross sections, lengths, diameters
Steel beam - *RFS* - lower flange	S355	½ IPE-600 + Pl. 380 x 20, L_{beam} = 2680 mm L_{RFS} = 290 mm, l_{RFS} = 100 mm $L_{beam,lf}$ = 2680 mm, $l_{beam,lf}$ = 380 mm, $t_{beam,lf}$ = 20 mm
Steel column - stiffeners - doubler plates	S355	HEB-340, L_{column} = 2930 mm t_{ccp} = 20 mm, 4 pieces t_{cwp} = 12 mm, 2 pieces
Bolted connection - bolts - end-plate	-	 8*M36, grade 10.9 HV h_{ep} = 500 mm, w_{ep} = 300 mm, t_{ep} = 30 mm
Concrete slab	C30/37	L_{slab} = 3160 mm, l_{slab} = 1500 mm, class C30/37
Reinforcement - transverse - longitudinal - inclined	B500B	 Ø: 10 mm; spacing: 125 mm Ø: 10 ÷ 20 mm; spacing: 100 mm Ø: 10 mm; spacing: 125 mm
Concrete dowels rebars	B500B	Ø: 10 mm; web openings: 40 mm; spacing: 125 mm

The **slim-floor beam (SF beam)** was the key component of the joint due to its role as the primary structural fuse to dissipate seismic energy. Thus, the main goal for the SF beam in terms of seismic design strategy was to obtain a ductile structural member. Another design goal was to achieve a shallow SF beam, which is the primary characteristic of slim-floors systems in the current practice. The overall reduced height of the entire flooring system puts the slim-floor solution at an advantage over the "classic" composite downstand beam [1]. To exemplify this, a comparison of the

downstand configuration to the slim-floor system is shown in Fig. 3-30. The reason the composite IPE-450 beam is compared to ½ IPE-600 slim-floor beam is the similarity of their mechanical characteristics (see Table 6-9). For example, the total floor height of the IPE-450 with a concrete slab of 120 mm is 570 mm. Alternatively, the overall height of a slim-floor system made of ½ IPE-600 integrated in the floor height through encasement is 200 mm shallower than the "classic" configuration. Whereas the mechanical characteristics are similar, the advantage of the slim-floor resides in the reduced thickness of the floor.

To address the need for cross sectional compactness, certain measures were taken. Thereby, the procedure that was implemented in order to obtain the steel SF beam is illustrated in Fig. 3-31 and was partly based on the available instructions [7]. First, the SF beam was obtained from a regular steel profile (IPE-600) cut in half. Followingly, a wide steel plate was welded on the half I-profile as the lower flange. The dimensions of the wide steel plate were: 380 mm in width and 20 mm in thickness. The width of the welded steel plate or bottom flange of the beam was designed to ensure a minimum support to the profiled steel sheets and the reinforced concrete slab, as recommended by manufacturers [7]. By analysing the resulted built-up cross section, the asymmetry of the SF steel beam is easily recognisable.

In order to obtain a ductile SF beam, which could sustain high inelastic deformations in the plastic range, a *Reduced Flange Section* (*RFS*) was applied to the lower flange of the steel beam. As exercised in the current practice, the application of a *Reduced Beam Section* (*RBS*) is an efficient method of enhancing ductility [66] [67]. Usually, in symmetric steel profiles a *Reduced Beam Section* is applied to both beam flanges. However, as recommended in FEMA 547 [78], the independent trimming of the lower beam flange could be used in the rehabilitation of moment frames. In the current study, due to an increased width of the lower beam flange and also to the strategy of attaining a balanced flexural response (sagging response similar to hogging bending response), only the bottom flange was trimmed. As the reduction of the section was applied to one beam flange, the technique was named *Reduced Flange Section* (*RFS*). Following the application of a *RFS* (see *RFS* dimensions in Fig. 3-31), a relatively symmetric cross section was obtained in the dissipative zone of the SF beam. The final cross section had a height of 370 mm and was obtained from half of an IPE-600 profile with *RFS* in the welded steel plate / lower flange.

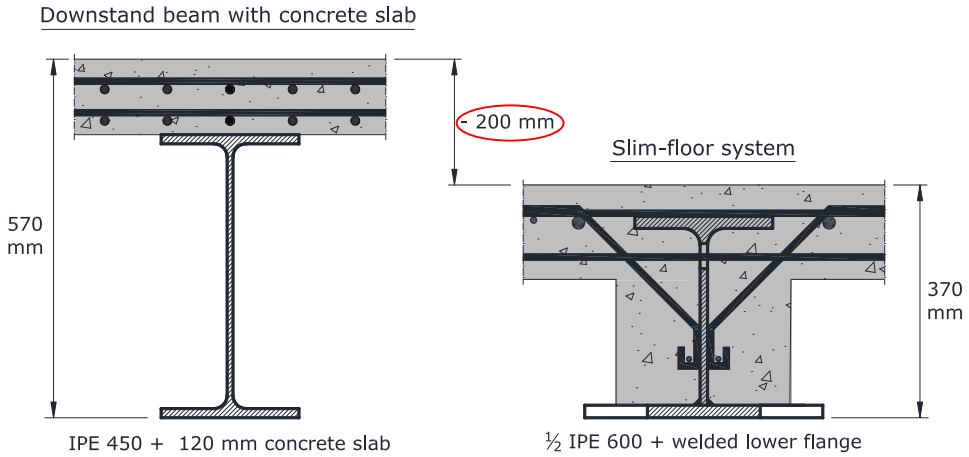

Fig. 3-30. Comparison of the "classic" floor configuration (downstand beam) to the SF system

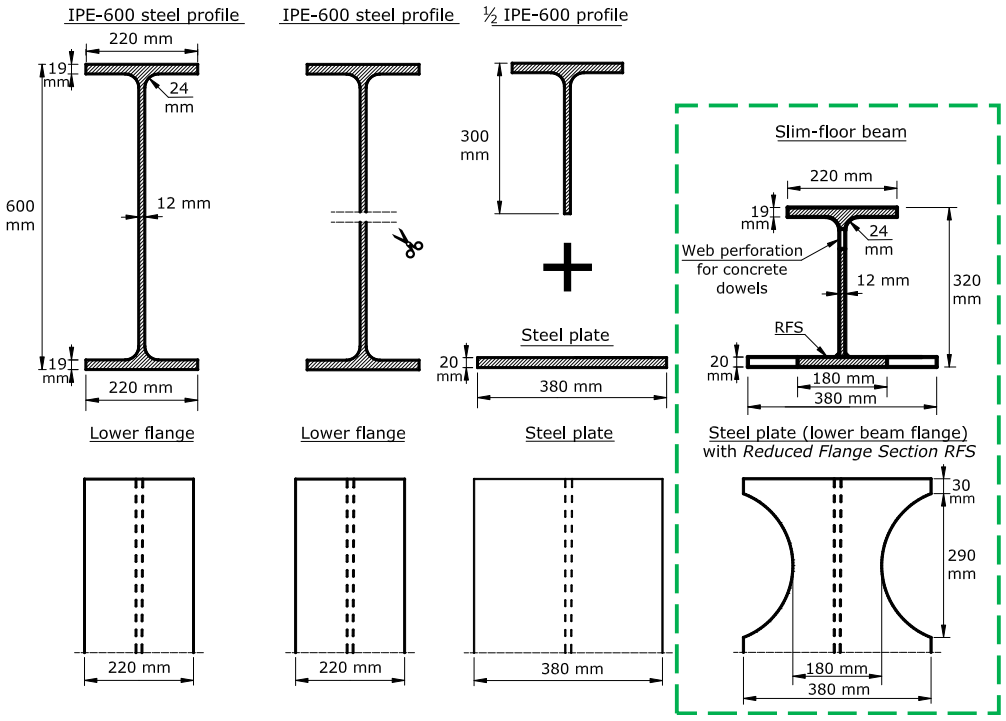

Fig. 3-31. Illustration of the phases involved in obtaining the slim-floor beam [7]

The **beam-to-column connection** consisted of an extended bolted connection (see Fig. 3-32d). As recommended in the European seismic norm [51] for composite connections, the beam-to-column connection was realised with bolts grade 10.9. These were disposed on four rows. In accordance with capacity design [51], the bolted connection and the beam flange weldments were designed to remain in the elastic range. Based on pre-test finite element investigations and analytical calculations, the diameter of the bolts was 36 mm. On the other hand, to ensure the overstrength of the weldments, full penetration butt welds were used to weld the flanges of the SF beam. Other steel components were welded with single or double fillet welds with a throat thickness of $0.7 \cdot t_{min}$., where t_{min} is the smallest thickness of the welded components according to prEN 1998-1-2 [51] and prEN 1993-1-8 [79].

The **column** was made of an HEB-340 profile equipped with doubler plates of 12 mm and continuity plates of 15 mm in thickness.

The **concrete slab** had 1500 mm in width and, together with the partially-encased steel SF beam, represented the composite slim-floor solution. The plastic effective width in the potential dissipative zone of the SF beam was calculated according to EN 1998-1 [46] and resulted in the following values: 1200 mm in hogging and 900 mm in sagging bending. These values were obtained for a span of 6 m. The concrete slab was additionally extended with 630 mm beyond the axis of the column in order to assure the anchoring of longitudinal rebars (see Fig. 3-32a-c). The reinforcement of the concrete slab (see Fig. 3-32a-c) consisted of embedded transverse, longitudinal and inclined rebars of 10 mm in diameter and fulfilled the ductility requirements of prEN 1993-1-1 [54] and of prEN 1994-1-1 [55] (i.e., 15 % elongation; f_u / f_y ≥ 1.10; ductility class B or C). The two longitudinal rebars that were

closest to the beam had a diameter of 20 mm. Apart from regular slab reinforcement, concrete dowels were also implemented (see Fig. 3-32c). The advantage of concrete dowels is that the technique could ensure full shear interaction without increasing the overall height of the floor, as shown in [38]. Moreover, a National Technical Approval for the use of concrete dowels has been issued in Germany [19]. The addition of concrete dowels to the slim-floor beam-to-column joints satisfied the requirements of the National Technical Approval [19]: B500B reinforcing steel, S355 or higher steel grade for the SF beam, concrete class in the range of C25/30 ÷ C55/67. In accordance with these, the steel grade of the SF beam was S355, the concrete class was C30/37 and the rebars of the concrete dowels were made of steel B500B. In the web of the SF beam, openings of 40 mm in diameter spaced at 125 mm were made. Subsequently, rebars of 10 mm in diameter were inserted in the web openings. Overall, the reinforcing of the concrete was meant to assure full shear interaction between the steel components of the joints and the concrete. Deep trapezoidal steel decking was not installed, similarly to [42]. However, as the use of decking is common practice, the influence of the component was investigated numerically.

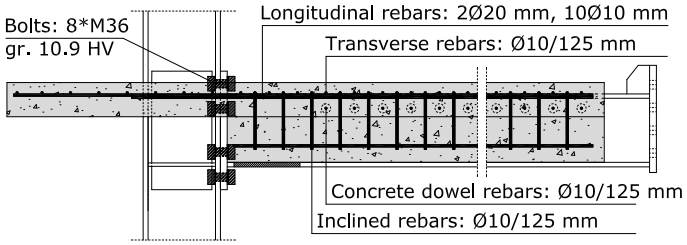

a)

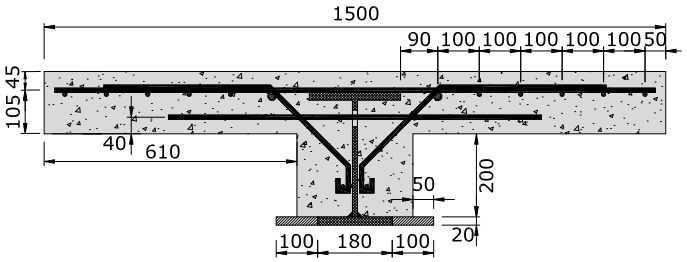

b)

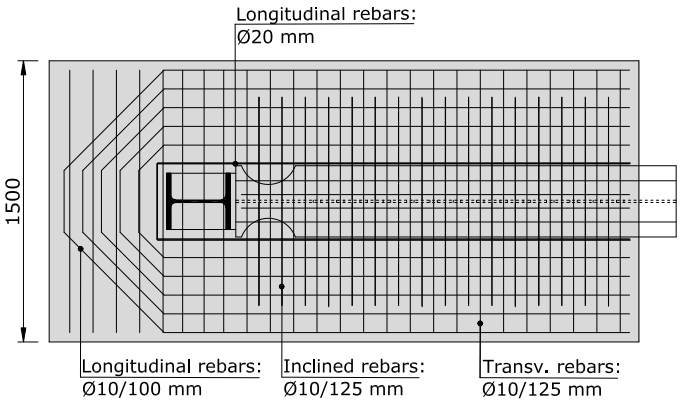

c)

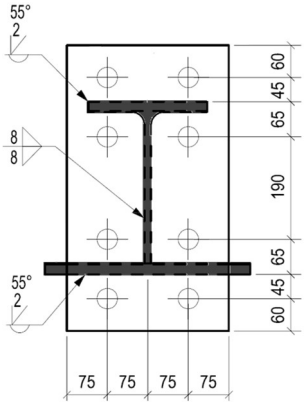

d)

Fig. 3-32. Views of the joints: a) side; b) front; c) top; d) bolted beam-to-column connection

Details of the slim-floor beam-to-column joint specimens during fabrication and installation on the test rig are shown in Fig. 3-33a-f.

a) b)

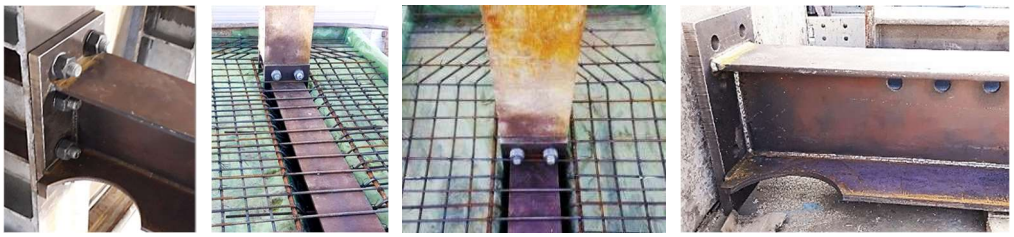

c) d) e) f)

Fig. 3-33. SF beam-to-column joint specimens: a) & b) joint on the experimental stand; c) bolted beam-to-column connection; d) & e) reinforcement layout; f) steel beam with *Reduced Flange Section* and web openings for concrete dowels

3.3 Experimental investigation

3.3.1 Test setup, instrumentation, loading protocols

The main objectives of the experimental tests performed on the two joint specimens aimed at the following: (i) assessment of the monotonic and of the cyclic response; (ii) evaluation of the load transfer mechanism, failure mode, rotation capacity, initial joint stiffness and bending moment resistance.

Pre-test activities included the installation of the specimens in the test rig, setting up of the measuring system and whitewashing of the joint specimens. The hydraulic actuator load was positioned at the top of the column. As boundary conditions, a pinned support was set at the base of the column and a double-pinned pendulum was positioned at the free-end of the beam. Furthermore, a lateral frame system was used to prevent the out-of-plane deformations during the tests. The measuring system consisted of global and local instrumentation (see Fig. 3-34a-c). A sketch containing the arrangement of the displacement transducers set for global measurements is shown in Fig. 3-34a.

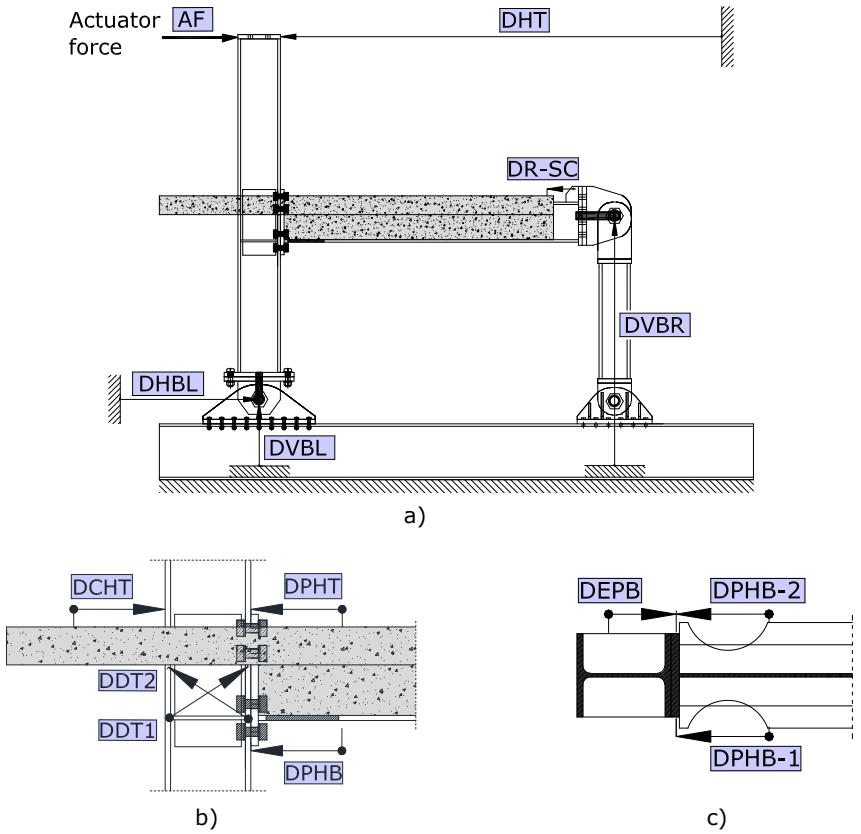

Fig. 3-34. Global and local instrumentation setup: a) global; b) & c) local

Global instrumentation monitored:

- force in the actuator (actuator force, AF),
- displacement at the tip of the column (DHT),
- displacement at the supports (DHBL; DVBL; DVBR).

Local instrumentation recorded the deformation of the following components:

- column web panel (DDT1; DDT2),
- dissipative zone of the SF beam, recorded in *RFS* (DPHT; DPHB-1; DPHB-2),
- concrete slab - the portion located behind the column (DCHT),
- end-plate and column flange component (DEPB),
- relative slip between the SF beam and the reinforced concrete slab (DR-SC).

The deformation of the end-plate and column flange component (DEPB) was recorded by a displacement transducer positioned on the end-plate in line with the centre of the bottom flange of the beam, as shown in Fig. 3-34c. Thus, the deformation of the bottom part of the end-plate and column flange component was monitored experimentally. A second displacement transducer, which could specifically record the deformation of the top part of the end-plate and column flange could not be installed due to the presence of the concrete slab. However, the rotation of the end-plate and column flange was calculated in a hybrid manner, using experimental measurements and FEM results. Details are further discussed in Section 3.4.3.

The experimental program included monotonic and cyclic tests. The tests were performed in displacement control by introducing the load through a hydraulic actuator at the top of the column. One specimen was subjected to monotonic loading considering an incremental increase of the load in hogging bending followed by a reversed load in sagging bending. The other joint specimen was tested under cyclic loading using the AISC 341-16 [30] protocol. The corresponding bending moment and rotation were calculated considering Eqs. (3.14), (3.15), (3.16) and the sketch from Fig. 3-35. The horizontal top displacement Δ was obtained after the translations caused by tolerances and / or deformations at supports were subtracted.

$$M = F_{beam} \times (L_{beam} - 0.5 \times h_{column}) \tag{3.14}$$

$$\theta = \frac{\Delta}{L_{column}} \tag{3.15}$$

$$F_{beam} = \frac{F_{actuator} \times L_{column}}{L_{beam}} \tag{3.16}$$

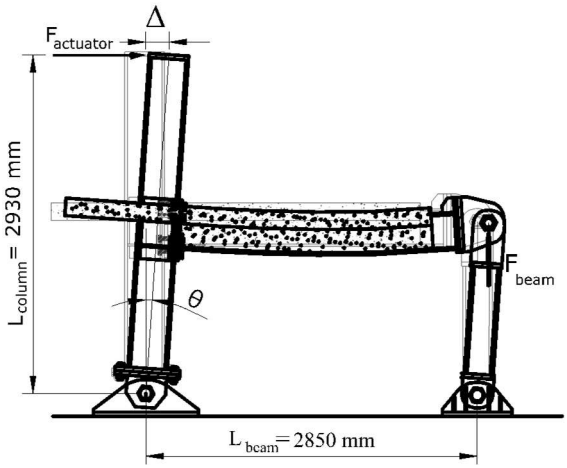

Fig. 3-35. Sketch for the calculation of the bending moment and rotation at the column line

3.3.2 Material characteristics

Material samples from the components of the joint specimens were tested (see Fig. 3-36a-d). The material tests performed on steel coupons revealed the average values of stress and elongation centralised in Table 3-2, while the tests on concrete cubic samples (dimensions: 150 x 150 mm) at 28 days resulted in the mean values shown in Table 3-3. Considering the obtained material characteristics, the steel grades (i.e., S355, B500B) and the concrete class (i.e., C30/37) were confirmed.

Table 3-2 – Average results of material tests on steel samples

Material sample	Standard material class	f_y [N/mm^2]	f_u [N/mm^2]	f_u / f_y	A [%]	A_g [%]
½ IPE-600	S355	390	492	1.26	31.20	16.30
Lower beam flange	S355	406	519	1.28	27.14	14.20
End-plate	S355	415	-	-	-	-
Reinforcing bars	B500B	515	625	1.21	27.50	14.24

Table 3-3 – Average results of material tests on concrete cubic samples

Material sample	Standard material class	A_c [mm^2]	F_{max} [N/mm^2]	f_c [N/mm^2]
Concrete cubes	C30/37	22.500	876	38.92

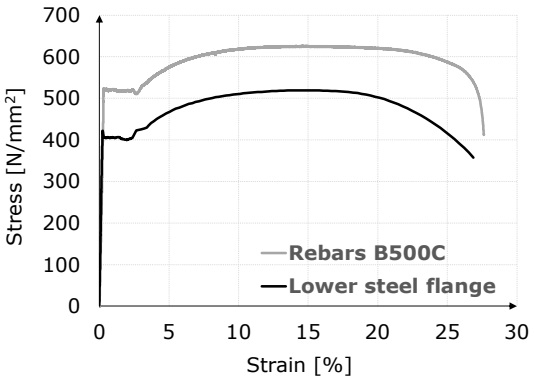

a)

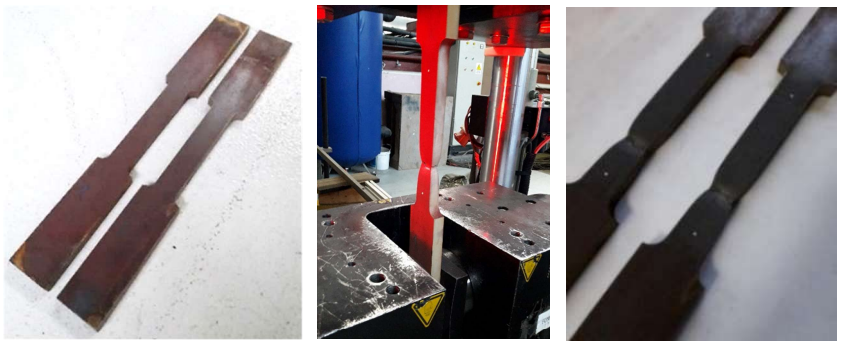

b) c) d)

Fig. 3-36. Material tests: a) σ-ε curves (rebars, lower beam flange); b) c) d) coupon tests

3.3.3 Monotonic response

Joint specimen ***SF J-M*** was subjected to a monotonic test. The corresponding moment-rotation curve, with rotation and bending moment calculated at column centreline, is shown in Fig. 3-37a. The overall monotonic response was captured by photo recordings (see Fig. 3-37c,d,e) and visual assessment.

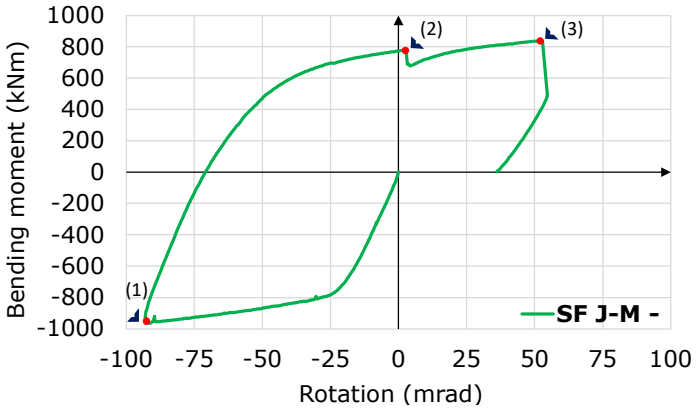

a)

b)

c) d) e)

Fig. 3-37. Monotonic response: a) *M-Φ* curve (bending moment, rotation at column centreline); b) specimen in maximum hogging *"1"*; c) significant cracks in the concrete slab *"1"*; d) stiffener weld failure *"2"*; e) lower beam flange-to-end-plate weld failure *"3"*

The following phenomena were observed during monotonic testing under hogging bending:

- compression deformation in the *RFS*;
- transversal cracks in the concrete slab; the cracks occurred predominantly in the vicinity of the dissipative zone of the SF beam (see Fig. 3-37c);
- small steel-concrete relative slip; the maximum relative slip of 0.83 mm occurred between the top flange of the SF beam and the concrete slab at the maximum bending moment value.

The specimen *SF J-M* reaching maximum hogging bending (see Fig. 3-37b) corresponds to marking "1" on the *M-θ* curve in Fig. 3-37a. In reverse load, under sagging bending, the weld of one of the stiffeners to the column flange fractured at a bending moment of 730 kNm and approximately zero rotation (see Fig. 3-37d). This weld failure is marked "2" on the monotonic moment-rotation curve. Following the first weld failure, a second weld fracture occurred, this time between lower SF beam flange and the end plate (see Fig. 3-37e). As a result of the second weld failure, a significant drop in the bending resistance occurred. The decrease can be seen on the moment-rotation curve in Fig. 3-37a after marking "3". The monotonic test was stopped after the second weld failure.

As evidenced by the post-test inspection of the welds, the first failure could have been caused by fabrication faults. The importance of high quality welding procedures in *RBS* connections was underlined by other studies, e.g., Jones et. al [67]. As pointed out in Jones et. al [67], adequate welds allow for specimens to perform beyond the elastic range without fractures. In the current study on SF joints, the lower stiffeners were strengthened prior to the cyclic test to prevent another weld failure.

3.3.4 Cyclic response

Joint specimen ***SF J-C*** evidenced a symmetric and stable hysteretic response in terms of bending resistance, rotation and initial stiffness, as shown in the corresponding cyclic moment-rotation curve in Fig. 3-38a. The cyclic moment-rotation curve was obtained by calculating both the bending moment and the rotation at the column centreline.

Prior to an analysis of rotations sustained by components and to the calibration of a numerical model, the symmetric flexural response of the joint assembly was attributed to the geometry of the SF beam in the dissipative zone.

On-site observations during the cyclic test revealed the following phenomena:

- initiation of transverse cracks in the reinforced concrete slab starting with cycles of ± 10 mrad (see Fig. 3-38c);
- visible deformation of the *RFS* (see Fig. 3-38d); elongation and opening of cracks in the reinforced concrete slab;
- weld failure of the continuity plate (i.e., column stiffener) to the column flange during the first cycle of ± 60 mrad (see Fig. 3-38b); the rotation of the joint specimen at the failure of the previously mentioned weld was - 46 mrad (see Fig. 3-38e);
- substantial cracking of the concrete slab; cracking mainly occurred in the proximity of the dissipative zone of the SF beam; however, dislocations of the concrete were not evidenced (see Fig. 3-38f).

The weld failure of the stiffeners was followed by other weld failures, e.g., SF beam bottom flange-to-end plate weld. After the drop in bending resistance, the cyclic test was stopped.

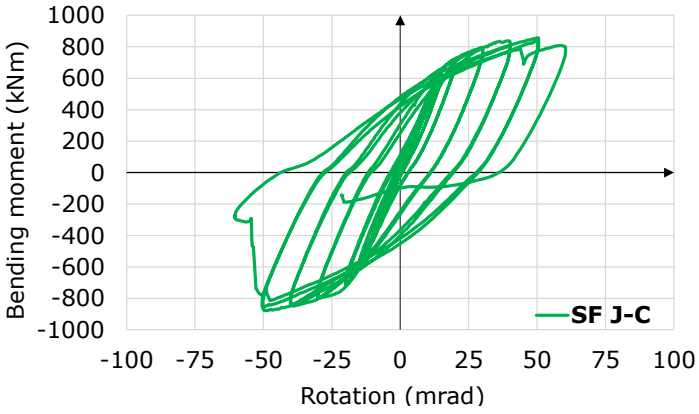

a)

b) c)

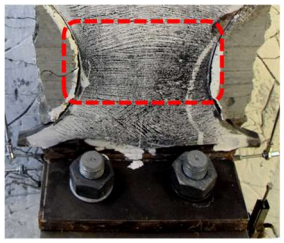

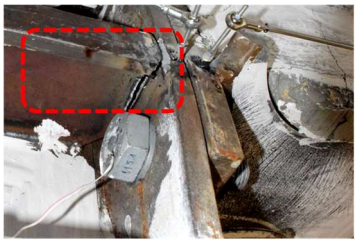

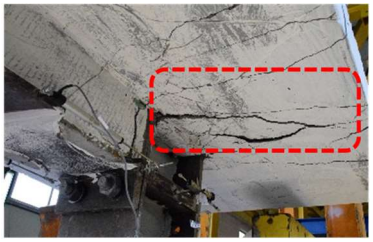

d) e) f)

Fig. 3-38. Cyclic response: a) *M-Φ* curve (bending moment, rotation at column centreline); b) specimen at -60 mrad; c) initiation & opening of cracks in the concrete slab near the dissipative zone; d) yielded *RFS*; e) weld failure; f) significant cracks in the concrete slab

By comparison the tested joint specimens, *SF J-M* and *SF J-C*, some similarities between the monotonic and cyclic responses can be observed. This subject is discussed in the following section.

3.4 Analysis of experimental results

3.4.1 Bending resistance of the beam-to-column connection and of the dissipative zone of the SF beam

The probable maximum bending moment and the shear force used for the design of the bolted beam-to-column connection were calculated in accordance with prEN 1998-1-2 [51]. Details regarding the procedure can be found in Annex 1 of the study. The resistance of the bolted beam-to-column connection under both sagging and hogging bending was calculated considering real material characteristics, and centralised in Table 3-4. In the calculation of the hogging bending resistance of the connection, the two upper bolt rows, consisting of four M36, 10.9 HV bolts and rebars of diameter 10 and 20 mm, were accounted for. Referring to the rebars, their number was established based on the plastic effective width under hogging bending. The resistance of the connection in sagging bending was calculated by considering the two lower bolt rows, consisting of four M36, 10.9 HV bolts.

As it can be seen in Table 3-4, the sagging and hogging bending moment resistance of the beam-to-column connection ($M_{Rd,conn}$) were higher than the maximum bending moment developed in the connection during the experimental tests. Ratios between the bending resistance $M_{Rd,conn}$ and the bending moment developed during the tests $M_{Ed,conn}$ were calculated, and can be seen in Table 3-4.

Table 3-4 – Bending moment demand and bending moment resistance of the beam-to-column connection

Bending moment	$M_{Ed,conn}$	$M_{Rd,conn}$	$M_{Ed,conn}$ / $M_{Rd,conn}$
Hogging bending [M^-]	873 kNm	1040 kNm	0.84
Sagging bending [M^+]	838 kNm	896 kNm	0.94

Hogging and sagging bending moment resistances of the dissipative zone of the SF beam are shown in Table 3-5. Details regarding this calculation are shown in Annex 1. The ratios between the bending resistance of the connection and the dissipative zone of the SF beam are: 1.29 in hogging bending, 1.16 under sagging bending. Considering the higher resistance of the connection in comparison to that of the dissipative zone of the SF beam, an adequate overstrength of the first was demonstrated.

Table 3-5 – Plastic bending resistance of the dissipative zone

	$M_{Rd,PH}$	$M_{Rd,PH}$ (projected at column face)
Hogging bending [M^-]	733 kNm	804 kNm
Sagging bending [M^+]	704 kNm	772 kNm

3.4.2 Influence of the loading procedure

On the one hand, the monotonic test was performed in order to assess the joint response (i.e., in terms of initial stiffness, bending moment resistance, rotation capacity, failure mechanism), to calibrate a numerical model, as well as to develop and validate the analytical design procedure. On the other hand, the results of the cyclic test were used to assess the seismic performance of the proposed SF beam-to-column joint typology.

The response of the joint specimens was characterised based on criteria, as follows: joint rotation capacity, flexural resistance and initial stiffness. These

characteristics were derived from the experimental monotonic and cyclic moment-rotation curves.

The monotonic moment-rotation curve of *SF J-M*, calculated with the bending moment at the column face and the rotation at the column centreline, is shown in Fig. 3-39a together with its mirrored form. In the first part of the monotonic test, the joint specimen was subjected to hogging bending. The correlation the first part of the monotonic test to the monotonic hogging bending response evidenced a high bending resistance and rotation capacity of the *SF J-M* joint specimen (i.e., -907 kNm; -93 mrad). However, the response of the joint specimen *SF J-M* was not fully developed due to the weld failure of one stiffener and could not be, therefore, entirely analysed: 52.9 mrad, 787.2 kNm.

The cyclic moment-rotation curve of joint specimen *SF J-C* is illustrated in Fig. 3-39b. As shown in this figure, the hysteretic loops are stable and symmetric, while the cyclic degradation is reduced. Thus, the hogging and sagging bending response from the cyclic experimental test are similar and comparable:

- "positive" cyclic response (hogging bending): 53.3 mrad; 795.4 kNm;
- "negative" cyclic response (sagging bending): -50.1 mrad; -816.1 kNm.

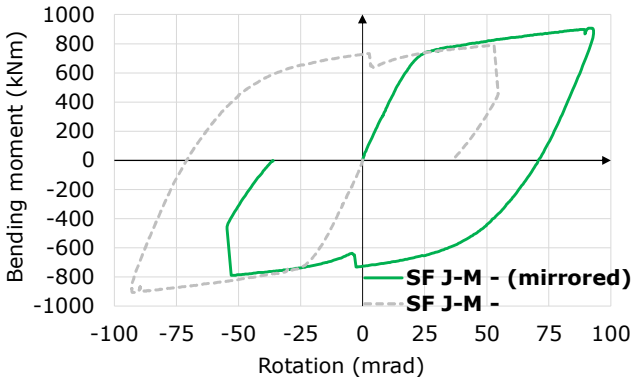

a)

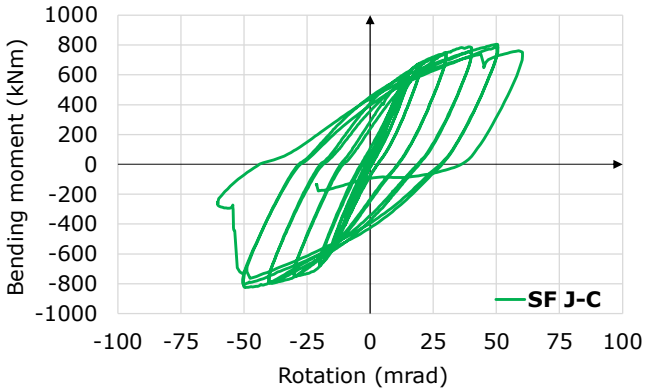

b)

Fig. 3-39. *M-θ* curves (*M* – at column face; *θ* – at column centreline): a) monotonic & mirrored monotonic; b) cyclic

A comparison of the monotonic to the cyclic moment-rotation curve can be seen in Fig. 3-40. The cyclic curve is represented in green, the monotonic curve – in

dark blue. Whereas the overlapping in hogging bending is different in terms of bending resistance and rotation capacity, similarities can be identified on the comparison of the monotonic to the cyclic curve: the maximum rotation and bending resistance under "positive" cyclic loading is similar to the rotation and bending resistance under "positive" monotonic loading. Noticeable on the "negative" part of the moment-rotation curves is the similarity of the monotonic to the cyclic initial stiffness. Overall, the monotonic and cyclic moment-rotation curves share common characteristics and are comparable. However, some differences between the two curves were expected, as cyclic loading is generally more demanding on specimens.

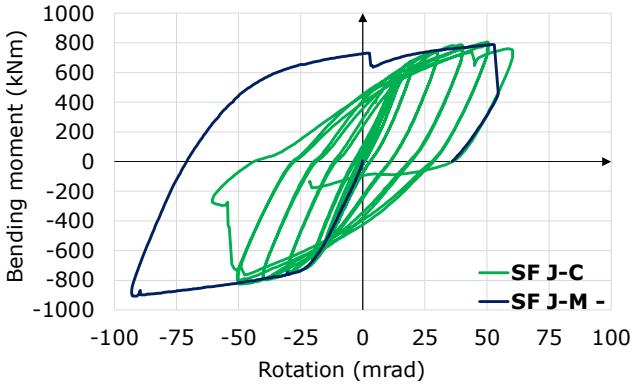

Fig. 3-40. Comparison of monotonic to cyclic *M-θ* curve (*M* – at column face; *θ* – at column centreline)

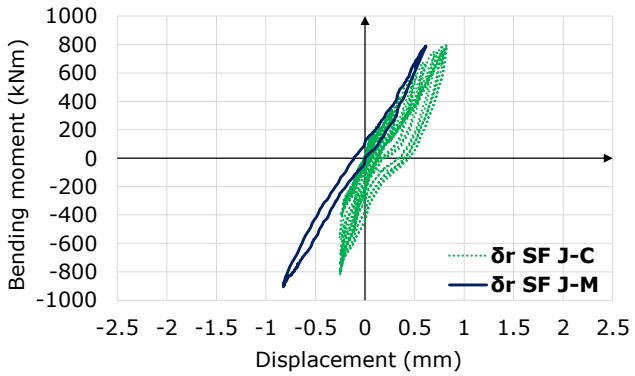

Fig. 3-41. Comparison of the relative slip produced under monotonic and under cyclic loading

Another comparison of the monotonic and cyclic responses was performed in terms of relative slip between the steel beam and the concrete slab. The relative slip values are important to characterise the shear interaction in composite beams. As examples from the literature have evidenced, a low relative slip could be considered an indication of a full shear interaction. The relative slips δ_r in monotonic and cyclic loading are shown in Fig. 3-41, with the following maximum values: 0.83 mm under monotonic loads (occurred in maximum hogging bending); 0.80 mm under cyclic loads (obtained in sagging bending). Considering the low values, full shear interaction could be assumed in both monotonic and cyclic tests, meaning that the concrete dowels, together with natural bond, assured a composite behaviour of the beams.

3.4.3 Contribution of components to joint rotation

The overall rotation of the SF beam-to-column joints was considered as a sum of rotations corresponding to the following components:

- elastic rotation of the SF beam and column,
- dissipative zone with *RFS* of the SF beam,
- end plate and the column flange in bending,
- column web panel in shear.

Elastic rotation of the SF beam and column

Elastic rotations corresponding to the SF beam and column were included in the moment-rotation curve of the joint assemblies (see Fig. 3-40). The parts of the previously mentioned SF beam and column were located outside of the joint area. The initial stiffness of the joint assemblies is, thus, the result of elastic deformations corresponding to the dissipative zone, beam-to-column connection, web panel, and also SF beam and column parts located outside of the joint area.

The elastic rotation of the SF beam and column was θ_{el} = 0.008 rad and corresponded to an initial stiffness of $S_{j,el}$ = 94815 kNm/rad.

Rotation of the dissipative zone

Deformations at the top and at the bottom of the dissipative zone were recorded by linear variable displacement transducers LVDT during the monotonic and cyclic tests (DPHT, DPHB-1, DPHB-2). To calculate the overall rotation of the dissipative zone, Eq. (3.17) was used. In Eq. (3.17), DPHB-1 and DPHB-2 are LVDTs which monitored deformations at the bottom of the dissipative zone, and DPHT – at the top of the dissipative zone. The term z_{PH} is the lever arm between the upper and lower LVDTs.

The resulted rotations of the dissipative zone during the monotonic and cyclic tests are presented in Fig. 3-42 and Fig. 3-43.

$$\theta_{b,PH} = \frac{0.5\,x\,(DPHB_1 + DPHB_2) + DPHT}{z_{PH}} \qquad (3.17)$$

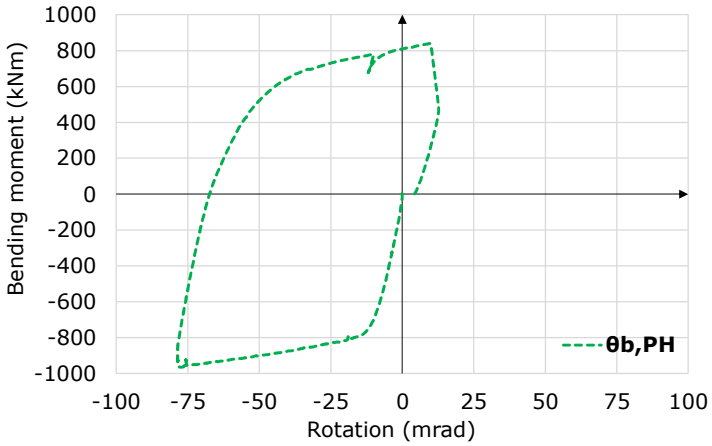

Fig. 3-42. Rotation of the dissipative zone under monotonic loads

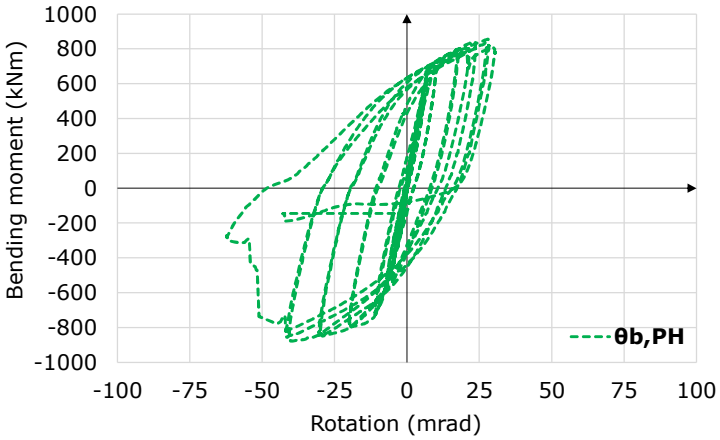

Fig. 3-43. Rotation of the dissipative zone under cyclic loads

Rotation of the end plate and column flange

A hybrid method was used to obtain the overall rotation of the end plate and column flange in monotonic loading, as deformations at the top part of the connection could not be experimentally recorded due to the presence of the concrete slab. Thus, the following were considered: the calibrated numerical model of the joint (see Chapter 4, Section 4.2) to calculate the deformation at the top part of the component ($DEPT_{FEM}$); measurements recorded by a LVDT to calculate the deformation at the bottom part of the component ($DEPB_{exp}$). To obtain the deformations of the end plate and column flange at the top part of the connection, two points were created in the numerical model to simulate a virtual displacement transducer ($DEPT_{FEM}$). The points were placed on the top stiffener and on the end-plate, as shown in Fig. 3-44. The deformation at the top of the component was calculated as the relative displacement between the two points (virtual LVDT). The deformation at the bottom part of the component was recorded experimentally by a LVDT (see DEPB in Fig. 3-44).

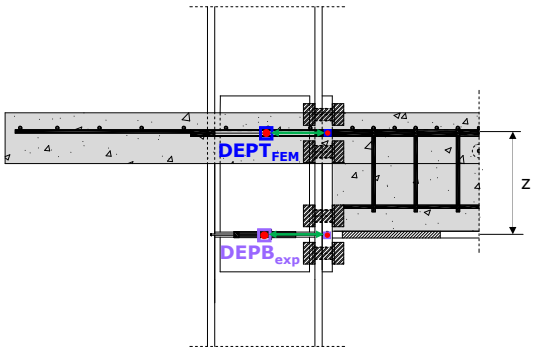

Fig. 3-44. Position of LVDTs used to calculate the rotation of the end plate & column flange under monotonic loading

In monotonic loading, the overall rotation of the component end plate and column flange was calculated with Eq. (3.18). The sum consisting of the deformation at the top and at the bottom of the end plate and column flange ($DEPT_{FEM}$; $DEPB_{exp}$) is divided by the lever arm z_{EP}. In this case, the lever arm is the distance between the

two measuring points. The rotation of the end-plate and column flange component in monotonic loading is shown in Fig. 3-45.

$$\theta_{EP} = \frac{DEPT_{FEM} + DEPB_{exp}}{z_{EP}} \quad (3.18)$$

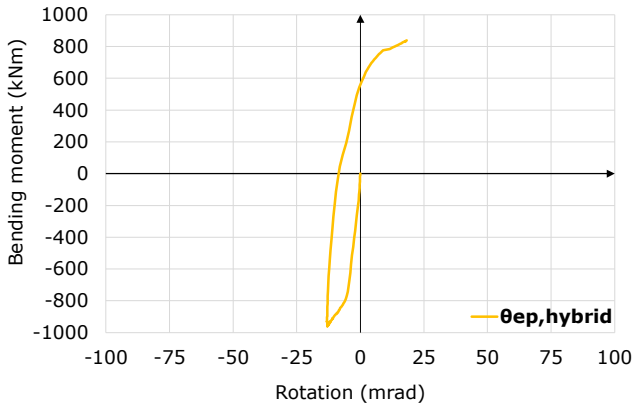

Fig. 3-45. Rotation of end-plate & column flange under monotonic loads (hybrid method)

The rotation of the end-plate and column flange component could not be accurately calculated under cyclic loading due to several factors. Apart from the technical difficulty of placing a LVDT at the upper part of the beam-to-column connection, the calibrated numerical model could not be used in this particular case. Referring to the latter, the calibrated numerical model was subjected to one complete cycle of loading, whereas the specimen *SF J-C* - up to cycles of ±60 mrad.

Rotation of the web panel

The rotation of the web panel was calculated with Eq. (3.19) from [80], in which the measurements of the LVDTs, e.g.,DDT1, DDT2, placed diagonally on the column, the initial length of each LDVT (L_{DDT2}, L_{DDT1}) and the vertical and horizontal distances between the fixed points of the LVDTs, were considered. Sketches corresponding to the deformation of the component are shown in Fig. 3-46, and the results, under monotonic and cyclic loading, are presented in Fig. 3-47a-b.

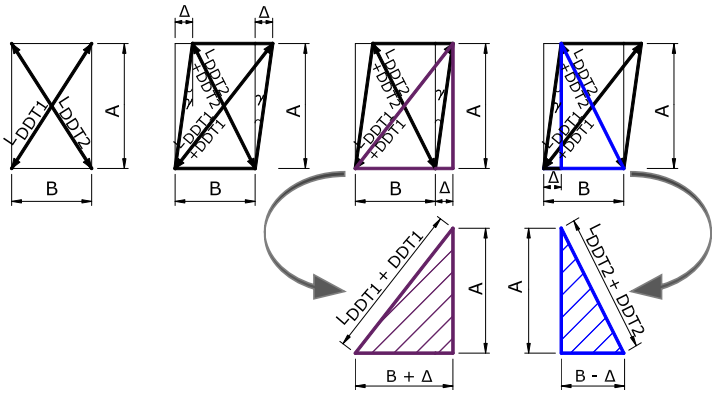

Fig. 3-46. Schematic deformation of the web panel under shear forces

$$\theta_{cw} = \frac{(DDT2 + L_{DDT2})^2 - (DDT1 + L_{DDT1})^2}{4 \cdot A \cdot B} \qquad (3.19)$$

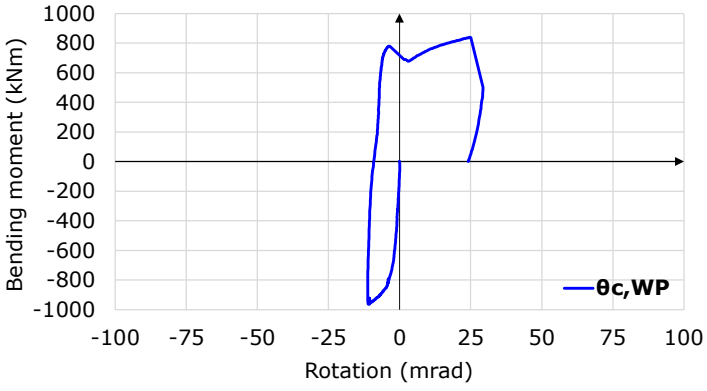

a)

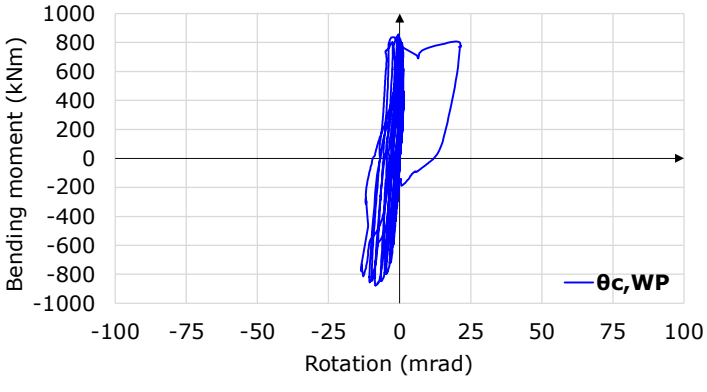

b)

Fig. 3-47. Rotation of the web panel under: a) monotonic loading; b) cyclic loading

Comparison of rotations of joint components

Comparisons of deformations sustained by components such as the dissipative zone of the SF beam $\theta_{b,PH}$, the end-plate and column flange $\theta_{ep,hybrid}$, and the web panel $\theta_{c,WP}$ under monotonic and cyclic loading are shown in Fig. 3-48a,b.

Referring to Fig. 3-48a, it should be noted that the monotonic results under sagging bending could not entirely characterize the rotation of the components, due to the weld failure of one of the stiffeners. Therefore, the discussion will focus on the results obtained under hogging bending. As shown in Fig. 3-48a, the dissipative zone of the SF beam sustained the highest plastic deformations. Smaller plastic deformations were sustained by the end-plate and column flange in bending and by the web panel component. The following rotation values were calculated for the maximum value of the hogging bending moment (under monotonic loading):

- 76.3 % of the total rotation was sustained by the dissipative zone $\theta_{b,PH}$;
- 12.7 % sustained by the end plate and column flange in bending $\theta_{ep,hybrid}$;
- 11.0 % was sustained by the web panel $\theta_{c,WP}$.

The rotations of the dissipative zone $\theta_{b,PH}$ and of the web panel $\theta_{c,WP}$ under cyclic loading are shown in Fig. 3-48b. As previously mentioned, the rotation of the end-plate and column flange component under cyclic loading could not be calculated. During the cycles sustained under hogging bending, the dissipative zone sustained the highest plastic deformations at the maximum value of the bending moment. As shown in Fig. 3-48b, the deformation of the web panel component was significantly smaller than that of the dissipative zone. A similar distribution to the previous one was observed under the cycles in sagging bending, with the rotation of the dissipative zone sustaining the highest rotations.

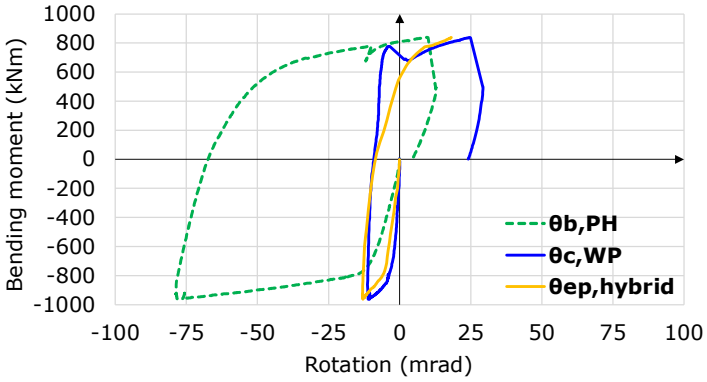

a)

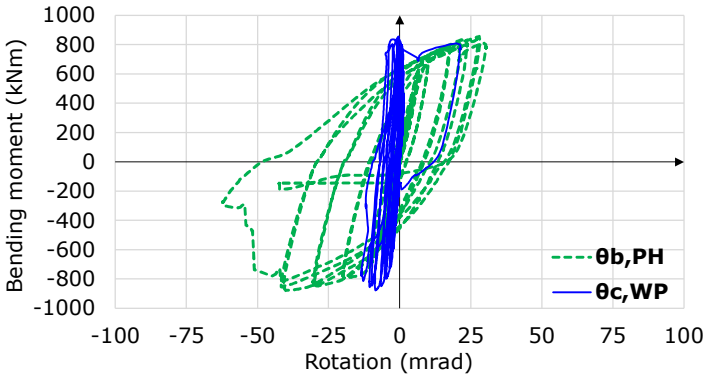

b)

Fig. 3-48. Rotation of joint components recorded during the: a) monotonic test; b) cyclic test

3.4.4 Assessment of seismic performance

To evaluate the seismic performance of slim-floor beam-to-column joints, an envelope curve was constructed under both hogging and sagging bending. Followingly, an overall joint rotation was calculated at each Limit State on the most unfavourable of the two envelope curves. For this assessment, the overall joint rotation was calculated at the column centreline and contained the rotations of dissipative zone of the SF beam, of the bolted connection and that of the web panel. The bending moment in Fig. 3-49a was calculated at column face.

Considering the provisions of FEMA P-795 [47], envelope curves were constructed in hogging and sagging bending, respectively, by selecting the peak

rotations (minimum and maximum) and the corresponding bending moments from the first cycle of each amplitude. The resulted envelope curves are shown in Fig. 3-49a,b and a comparison of their characteristics is shown in Table 3-6. Once again, these results underline the response similarity of *SF J-C* in cyclic hogging and sagging bending. The only identifiable difference between the envelope curves emerged in the last cycles of ± 60 mrad (see Fig. 3-49b), where a limited rotation resulted on the envelope curve under hogging bending. Regarded as the most unfavourable of the two, the envelope curve obtained under hogging was selected for the next steps.

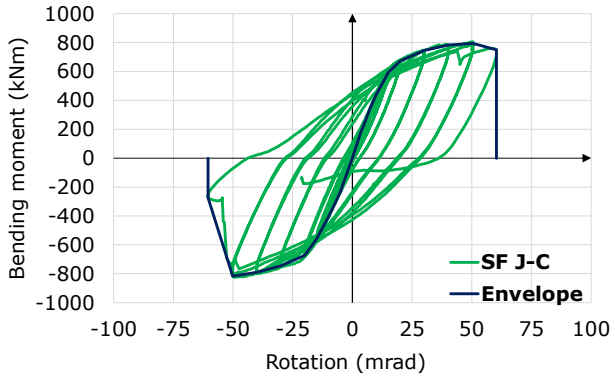

a)

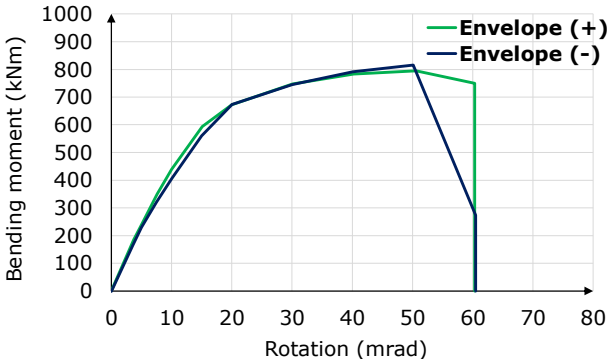

b)

Fig. 3-49. Envelope curves: a) construction; b) comparison of hogging to sagging curve

Table 3-6 – Comparison of envelope curves: hogging vs. sagging (see Fig. 3-49b)

SF J-C	Bending moment		Rotation	Stiffness
	$M_{Rd,max}$	M_j	θ_j	$S_{j,ini}$
Hogging bending [M^-]	816.1 kNm	560 kNm	15.0 mrad	37347 kNm/rad
Sagging bending [M^+]	795.4 kNm	594 kNm	15.1 mrad	39407 kNm/rad
		Difference [%]:		5.2 %

As a second step in the evaluation of the seismic performance, the procedure described in Vulcu et al [48] was followed. According to [48], the rotation at each performance level (i.e., Damage Limitation DL; Significant Damage SD; Near Collapse NC) is identified on the selected envelope curve (here, the envelope curve under hogging bending). The rotation at the DL corresponds to the yield rotation, which is

computed using the ECCS [49] procedure. This rotation is found at the intersection of the initial stiffness to a tangent to the envelope curve having a slope of 10 % of the initial stiffness. The rotation at NC corresponds to a 20 % value of the maximum or ultimate recorded bending moment / rotation on the descending branch. Finally, the rotation at SD was calculated as 75 % of the rotation at NC.

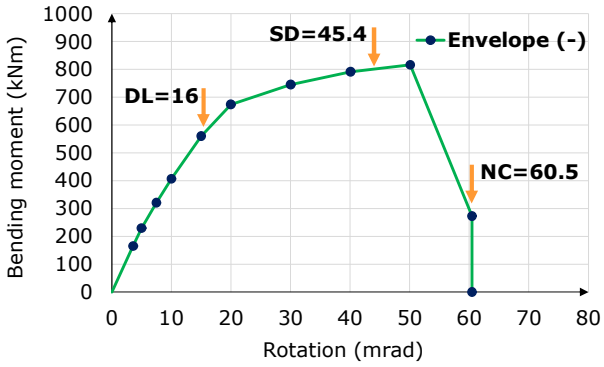

a)

DL:

16 mrad

b)

SD:

45.4 mrad

c)

NC:

60.5 mrad

d)

Fig. 3-50. Evaluation of the seismic performance: a) identification of performance levels on the envelope curve; joint rotation during the cyclic test at: b) DL; c) SD; d) NC

As shown on the envelope curve in Fig. 3-50a, the following joint rotations resulted: ± 16 mrad at DL; **± 45.35 mrad at SD**; ± 60.5 mrad at NC. The damage

state of the joint specimen corresponding to these joint rotations is shown in Fig. 3-50b-d. As the rotation of ± 45.4 mrad at SD exceeded the AISC 341-16 [30] criterion of ± 40 mrad, an adequate ductility and rotation capacity of the SF beam-to-column joint was met.

3.5 Concluding remarks

The experimental program on slim-floor beam-to-column joint assemblies consisting of monotonic and cyclic tests was presented in Section 3. The main components of the joint specimens are, as follows: ▪ slim-floor beam consisting of an asymmetric steel cross section with a *RFS* (S355), ▪ end-plate bolted connection with 8*M36 bolts, grade 10.9, ▪ H-profile steel column (S355) and ▪ reinforced concrete slab (class C30/37; B500B reinforcing bars and ▪ rebars for concrete dowels. The main objective of the experimental tests was to attain a joint rotation capacity of ± 40 mrad at Significant Damage, as required by AISC 341-16 [30].

The novelty of the tests resided in the following:

- the use of a bolted moment-resisting connection (extended two ways beam-to-column connection with high strength bolts and full-penetration groove welds) for SF beams;
- the application of a *RFS* to the lower flange of the SF beam as one measure to ensure member ductility and to prevent the brittle failure of the bolted connection;
- SF beam-to-column joints subjected to cyclic experimental tests.

Monotonic experimental test. Joint specimen *SF J-M* was tested under a monotonic load applied by an incremental increase of the load under hogging bending, followed by a reversed load under sagging bending. After reaching a considerable bending moment of - 907 kNm and a rotation of - 93 mrad in hogging bending, a weld fracture occurred at load reversal (i.e., sagging bending). The fractured weld was between one of the stiffeners and the column flange. The fracture of this weld rapidly led to multiple weld failures under reverse load (see Fig. 3-37a). While the value of the bending moment at the time of the first failure was high (i.e., 730 kNm), the failure mechanism was not expected. A post-test inspection of the welds revealed some fabrication faults, which led to the strengthening of the stiffeners-to-column flange welds prior to the cyclic test.

Cyclic experimental test. The cyclic test was performed on joint specimen *SF J-C*. The cyclic test was performed by applying the loading protocol of AISC 341-16 [30]. During the cyclic test, high plastic deformations were sustained by the dissipative zone of the SF beam – observed on-site by the cracking and flaking of the whitewash, but also supported by the measurements recorded by the instrumentation. The test was stopped after the first cycle of ± 60 mrad, when the weld between the lower flange of the SF beam and the end-plate fractured. This specimen evidenced a **symmetric** and relatively **stable hysteretic behaviour** with a low degradation of stiffness. This behaviour can be considered adequate for beam-to-column joints of Ductility Class 3 structures.

SF beam-to-column joint rotation. The evaluation of the seismic performance was carried out by using the provisions of FEMA P-795 [47] for the construction of the envelope curves. Furthermore, the ECCS procedure [49] was used to calculate joint rotations corresponding to Damage Limitation, Significant Damage and Near Collapse. The following joint rotations were obtained:

- ± 16 mrad at DL,

- **± 45.4 mrad at SD** and
- ±60.5 mrad at NC.

As the achieved rotation at SD is ±45.4 mrad, meaning with 13 % more than required rotation of ±40 mrad, the **AISC 341-16 criterion** [30] **is fulfilled**.

Most of the **joint rotation was provided by the dissipative zone of the SF beam** regardless of the bending direction or loading protocol – confirmed by measurements recorded by local instrumentation. The results correspond to observations made during the experimental tests and confirm the **development of a plastic hinge in the dissipative zone with *RFS***.

Classification of SF joint according to the EN 1993-1-8 resistance and stiffness criteria. The implementation of capacity design to the SF beam-to-column joint, according to which the overstrength of the end-plate connection and of the adjoining welds should be ensured in dissipative joints, led to the use of an extended end-plate connection with high strength bolts and the application of a *RFS* to the lower flange of the steel beam. Thus, the bolted connection developed higher bending moment resistances than those of the connected member, i.e., the reduced section of the SF beam. Consequently, according to the resistance classification of EN 1993-1-8, the joint is **full-strength**. Considering the stiffness criterion of EN 1993-1-8, the joint is **semi-rigid** when used in unbraced frame and rigid if used in braced structural systems.

Future research activities could include the extension of the experimental campaign in order to incorporate more tests and the study of more parameters. Of particular interest would be the experimental testing of double-sided SF beam-to-column joints (sub-assembly tests) and of a full-scale frames with two spans (system level tests).

4. NUMERICAL PROGRAM

4.1 Development of the Reference Numerical Model

4.1.1 Considerations on finite element modelling

The numerical investigations performed within the current study were carried out with SIMULIA Abaqus FEA [81]. Finite element analyses (FEA) were used in the following activities: pre-test numerical investigations [77], calibration of the reference model (*RM*) and parametric study.

Regarding the modelling possibilities, several finite element shapes and types are currently available. For instance, in Ahmed and Nethercot [82] and in Calado et al. [83], the feasibility of finite element numerical models developed with shell elements was demonstrated. Alternatively, a combination of the element types could also be used. For example, in Chou et al. [84], the numerical model was created with both shell elements for steel components and with solid elements for concrete components. In other studies that were centred on the assessment of different connections, the use of solid elements was proven efficient in the modelling of both welded (e.g., Shin et al. [85]; Kim et al. [86]; Kiamanesh et al. [87]; Schäfer et al. [88]), as well as bolted connections (e.g., Vegte and Makino [89]).

With regard to the selection of different parameters of the material model, several options are available in the Abaqus software [81]: concrete damaged plasticity model for concrete, plasticity or plastic model for steel components. The software also allows the use of an isotropic, kinematic or isotropic-kinematic hardening. According to Shin et al. [85], an isotropic model could be implemented for steel components subjected to monotonic loading, in which case the true stress and true strain, generated from the engineering stress-strain curve, can be used as input. In studies as Calado et al. [83], Shin et al. [85], Kim et al. [86] and Vegte and Makino [89], a kinematic hardening model was used in the context of cyclic loading. In other studies, a combined isotropic-kinematic hardening model was employed (e.g., Chou et al. [84], Kiamanesh et al. [87] and Schäfer et al. [88]).

4.1.2 Description of the Reference Numerical Model

The reference numerical model (see Fig. 4-51a) was created with both solid and beam elements. With the sole exception of the rebars, which were modelled with beam elements, all other components of the reference numerical model (*RM*) were created with solids. An image of the disassembled *RM* in which all components are visible, is shown in Fig. 4-51b.

Regarding the interaction law that defines the way in which components interfere with each other (see Fig. 4-51a), the following criteria were applied:

- "*tie constraint*" (modelling of: welds);
- "*embedded constraint*" (modelling of: rebars-to-concrete slab interaction);
- "*contact interaction*" (modelling of: interaction of the different model components such as between concrete slab, steel SF beam and column, respectively between bolts, end-plate and column flange).

As for the "*contact interaction*" - a contact law was defined considering both normal and tangential properties. The normal contact was defined as a "*normal hard*

contact" that allowed separation; the tangential contact was defined as a "*friction / penalty contact*" with a friction coefficient of $\mu = 0.6$. The value $\mu = 0.6$ of the friction coefficient resulted from the calibration process of the finite element (FE) joint model, as the use of other values of μ generated different results from the experimental ones (i.e., different moment-rotation curve).

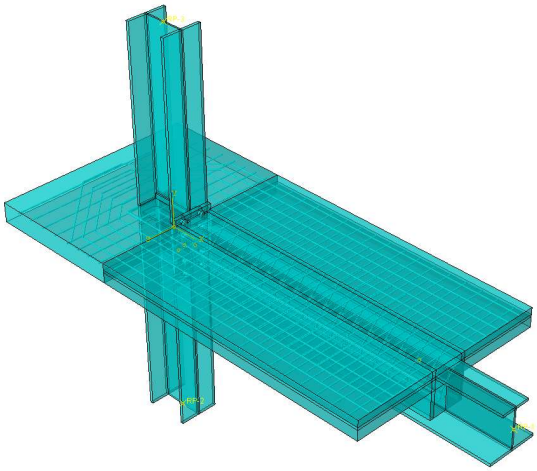

a)

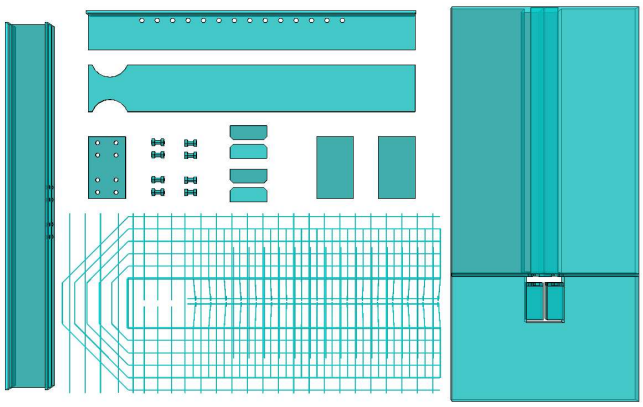

b)

Fig. 4-51. Reference numerical model (*RM*): a) 3D view; b) components of *RM*

The type of analysis that was used in the numerical program was "*dynamic, explicit*", also accounting for geometrical nonlinearity. The preference for this type of analysis was motivated by the large amount of contact surfaces assigned to the numerical model. A "*static, general*" type of analysis would have had computational difficulties. The material stress-strain relationships considered for the main components of the FE model of the *RM* were calibrated against the data obtained from material test samples. For the concrete slab a "*concrete damaged plasticity*" material model was implemented with the following elastic and plastic characteristics:

- elastic properties: Young's modulus E = 30000 N/mm^2; Poisson's ratio v = 0.2;
- nonlinear response in compression (see Fig. 4-52a):

- the stress-strain relationship up to the maximum resistance was obtained using the average strength from compression tests on cubes at 28 days (f_c = 38.9 N/mm^2) and Eq. 5.1 from EN 1992-1-1 [56];
- the stress-strain relationship (post maximum resistance) was computed to account for a relatively low amount of confinement - based on a model proposed by Li et al. [90];

▪ nonlinear response in tension (see Fig. 4-52b) was based on the bilinear softening model of Grassl et al. [91].

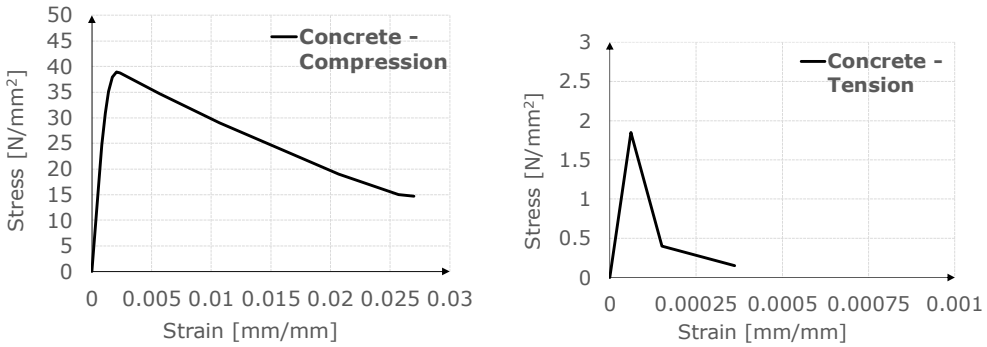

a) b)

Fig. 4-52. Material model of concrete in: a) compression; b) tension

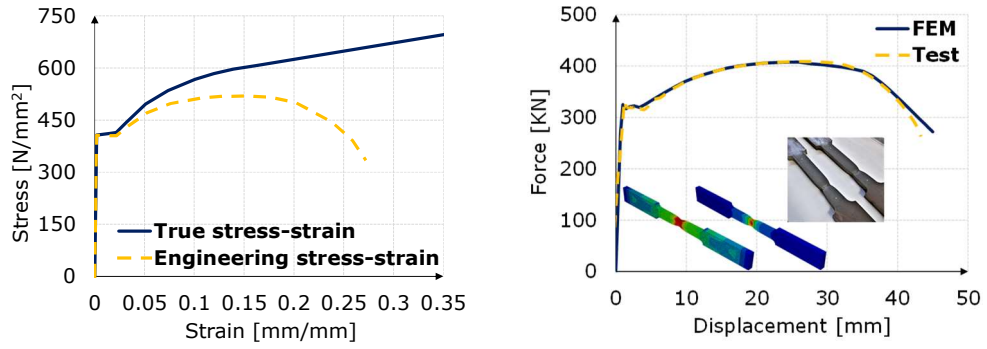

a) b)

Fig. 4-53. Material model calibration (lower steel plate): a) engineering stress-strain vs. true stress - true strain curve; b) comparison: test vs. FE simulation

As the *RM* was calibrated against the results of the monotonic test with one "negative" loading ramp followed by a "positive" one, the material model of the steel components was defined through a combined isotropic-kinematic hardening considering the *"half cycle"* option to define the hardening parameters. Elastic properties were defined considering Young's modulus (E = 210000 N/mm^2) and Poisson's ratio (ν = 0.3). The stress-strain relationships were calibrated against the results of tensile tests. The material of the bolts was based on a calibrated model of a T-stub test with failure mode three, as documented in [92]. Regarding the lower SF beam flange, the engineering stress-strain curve and the true stress–true strain curve (computed using Eqs. D.1 and D.2 from EN 1993-1-5 [93]) are shown in Fig. 4-53a. It is important to mention that the equations for the true stress-true strain can be used up to the ultimate strength values (see the engineering curve). Thus, the true

stress-true strain curves were extended with additional trial points. This allowed for a precise reproduction of the tensile test in terms of force-displacement (see Fig. 4-53b). Therefore, the resulting true stress-true strain curve of the main steel components is shown in Fig. 4-54.

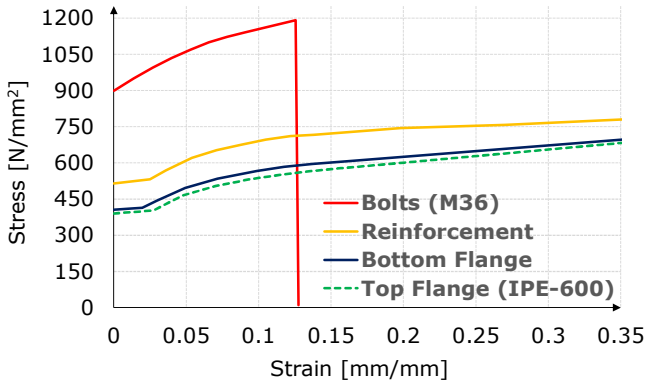

Fig. 4-54. True stress-true strain curves of the top & bottom flange, reinforcing bars & bolts

Regarding the imposed boundary conditions – one extremity of the column simulated a pinned support, while the other a simple support. Also, possible out-of-plane deformations were prevented. The load was applied in displacement control on the free end of the SF beam.

Global meshing was adapted to the components as a function of their size and geometry. Considering this, the mesh size of FE model components was the following:

- 15 mm for the ½ IPE-600 (steel part of the SF beam);
- 12 mm for the welded lower SF beam flange;
- 10 mm for the end-plate;
- 8 mm for the bolts;
- 14 mm for the steel column;
- 14 mm for the concrete slab;
- 20 mm for the reinforcing bars.

An image of the whole numerical model following the meshing procedure is shown in Fig. 4-55.

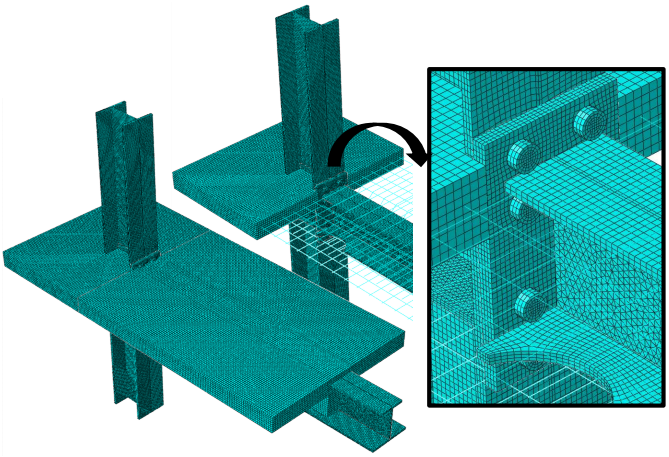

Fig. 4-55. Discretization of *RM* with a detailed view of the SF beam & of the bolted connection

The element types implemented in the FE model were the following:

- linear line elements, type B31 (rebars);
- linear hexahedral elements, type C3D8R (the rest of the solid components).

4.2 Results of calibrated Reference Numerical Model

The numerical model was developed as described in Section 4.1.2 and calibrated against the monotonic moment-rotation experimental curve. A comparison of the experimental monotonic test curve to the curve of the reference numerical model (*RM*) in terms of moment-rotation is shown in Fig. 4-56, which evidences good correlation. The *RM* had accurately reproduced the experimental curve in both hogging and sagging bending. By analytical means, the accuracy of the *RM* was verified and validated, as only minor differences to the experimental curve were found (i.e., error values between 0.1 ÷ 3.2 %). Markings *"A"* and *"B"* from Fig. 4-56 indicate the points of maximum hogging and sagging bending. The stress and the equivalent plastic strain distribution corresponding to these points on the moment-rotation curve (points *"A"* and *"B"*) are displayed in Fig. 4-57a-f, Fig. 4-58a-f and Fig. 4-59a-d.

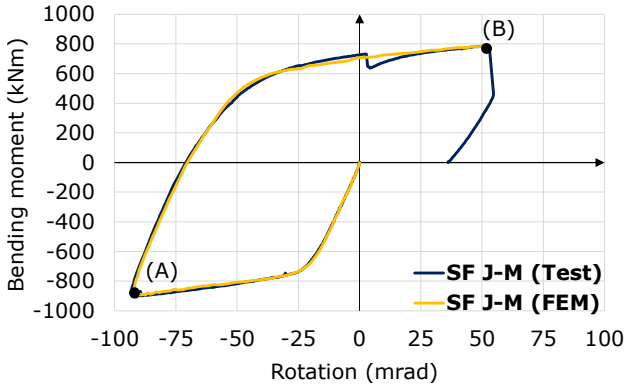

Fig. 4-56. Comparison of response curves: experimental test versus reference model (i.e., *RM*)

The performance of the *RM* in hogging bending was considered adequate - with high values of bending resistance and rotation as proof. At the peak of hogging bending (see Fig. 4-56, point *"A"*), a high concentration of stresses and plastic strains was evidenced in the dissipative zone of the SF beam (see Fig. 4-57d, Fig. 4-58e). Although other small plastic deformations were observed in both the upper and lower continuity plates, in the end-plate, in the upper two bolt rows and in the column flange, the plastic strain values were much lower than those developed in the dissipative zone. A more detailed assessment of the plastic strain in the components of the *RM* revealed that the maximum values were merely localised phenomena (see Fig. 4-58a, Fig. 4-58c, Fig. 4-59a, Fig. 4-59c). Considering this, it could be claimed that the results of the *RM* supported experimental observations: development of plastic strains in the dissipative zone of the SF beam, a mainly elastic response of the end-plate connection (see Fig. 4-57c) and the intense cracking of the concrete slab.

The role of the tensioned longitudinal rebars was assessed. FEA proved the engagement of longitudinal rebars on the entire width of the concrete slab (1500 mm) despite a more conservative value of the plastic effective width computed analytically (1200 mm). Although the yielding of these rebars was not reached, the stress in the reinforcement was significant, e.g., 85 ÷ 90 % of yielding stress (see Fig. 4-60).

Maximum hogging bending – point *"A"* in Fig. 4-56

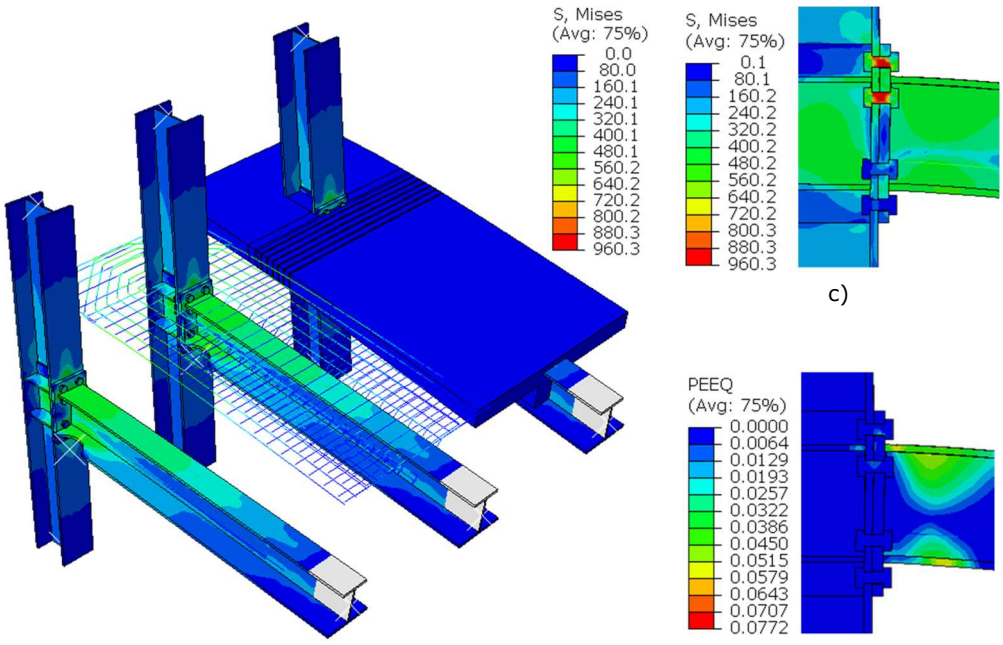

Maximum sagging bending – point *"B"* in Fig. 4-56

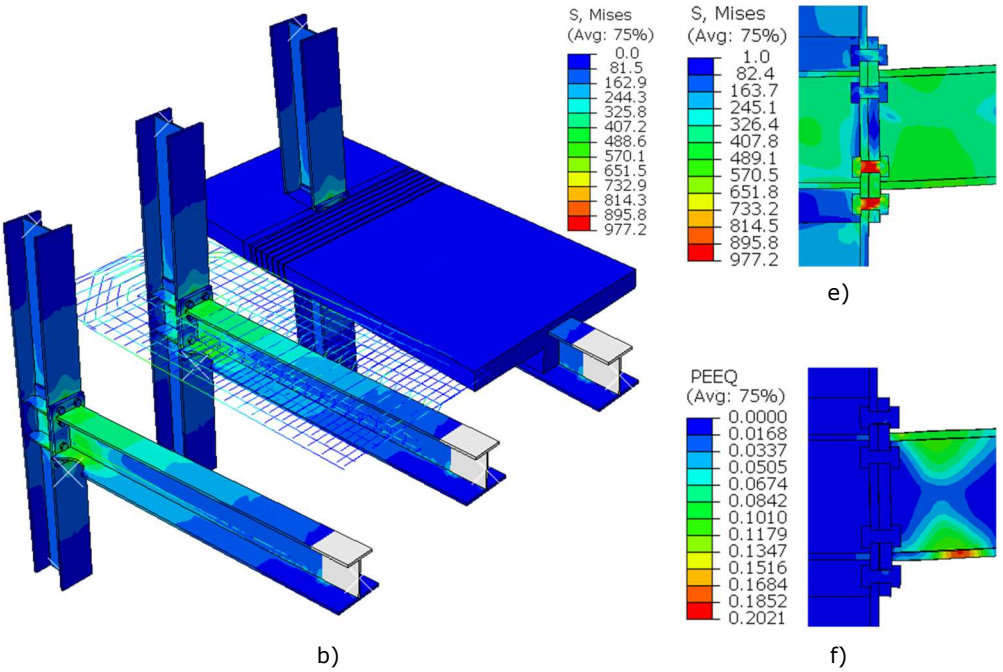

Fig. 4-57. *RM* results in maximum hogging & sagging bending: a) & b) FE model stress distribution; c), d), e), f) bolted connection von Mises stress & equivalent plastic strains

Similar to the peak point in hogging, in maximum sagging bending (see Fig. 4-56, point *"B"*), most plastic deformations were developed in the dissipative zone of the SF beam (see Fig. 4-57f, Fig. 4-58f). Although localised plastic deformations occurred in some components, they were not representative of the response of the respective elements (see Fig. 4-58b, Fig. 4-58d, Fig. 4-59b, Fig. 4-59d).

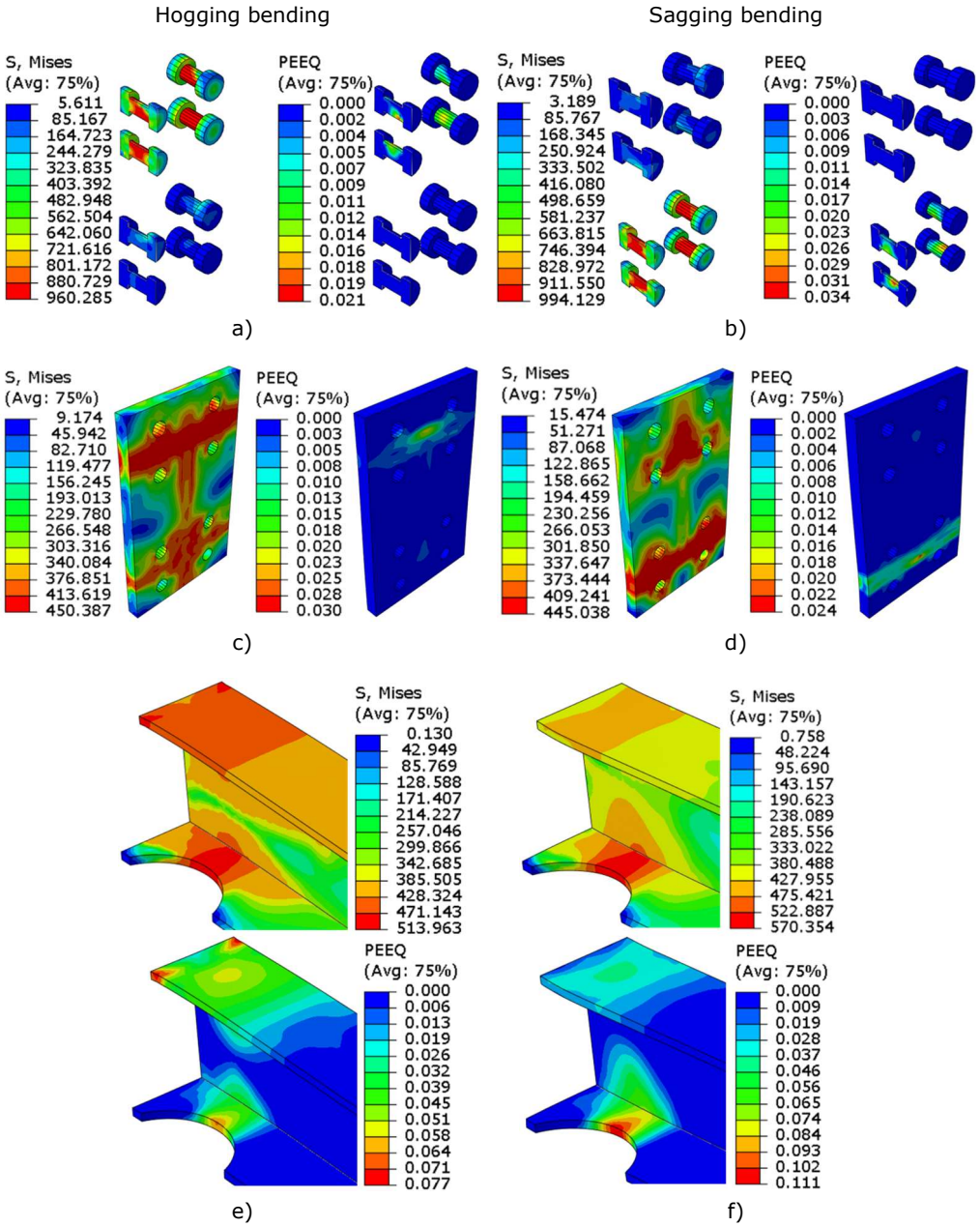

Fig. 4-58. *RM* results in maximum hogging & sagging bending. Von Mises stress & plastic strain distribution in: a), b) bolts; c), d) end-plate; e), f) dissipative zone of the SF beam

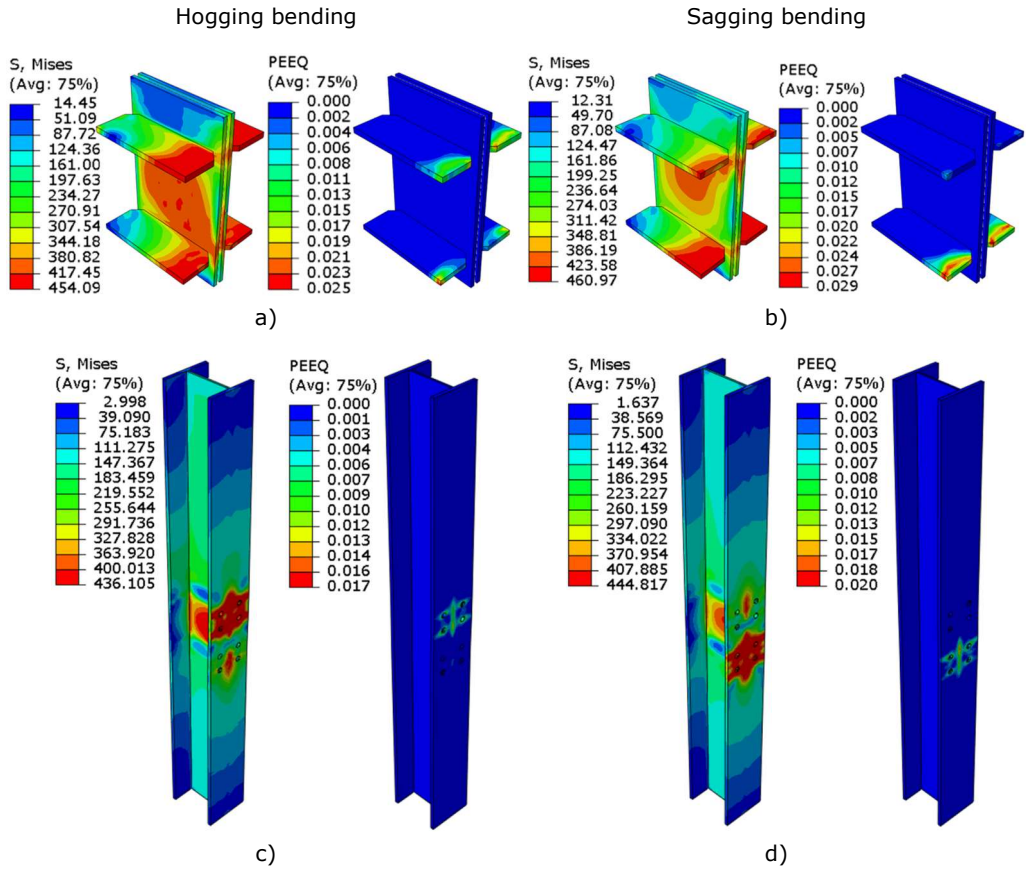

Fig. 4-59. *RM* results in maximum hogging & sagging bending. Von Mises stress & plastic strain distribution in a), b) stiffeners & doubler plates; c), d) column

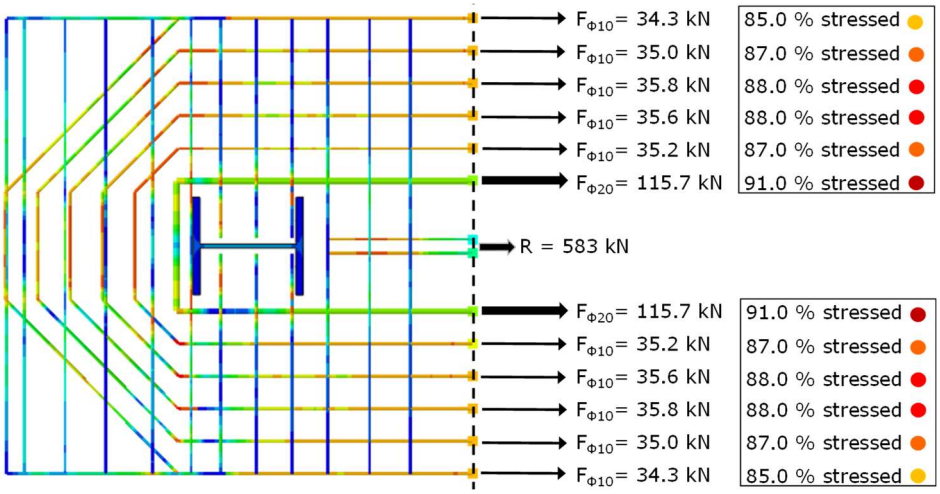

Fig. 4-60. *RM* results in maximum hogging bending (related to Fig. 4-56, point *"A"*): tension force in the longitudinal rebars

The results of the *RM* under sagging bending proved similarities between the experimental and numerical outcomes, e.g.: similar *M-θ* responses (i.e., experimental versus numerical curve of *RM*; see Fig. 4-56) and the same failure mechanism driven by the development of plastic deformations in the dissipative zone of the SF beam.

Similarities were also identified between the hogging and sagging bending response of the *RM*, such as the development of predominantly plastic strains of high values in the dissipative zone of the SF beam, and the elastic response of the end-plate connection. These developments could be regarded as evidence of a ductile behaviour of the dissipative zone of the SF beam - which was in accordance with the design strategy. One of the measures taken to achieve a ductile response of the SF beam-to-column joints was the application of *RFS* in the lower flange of the SF beam. More results are available in Annex B of the current study.

4.3 Parametric study

A parametric study was developed (see overview of the developed FE models in Table 4-7). In addition to analysing the influence of the current joint components, the parametric study included the new parameters, such as backing plates, trapezoidal steel sheets, etc. The applied displacement corresponded to an interstorey drift of ±93 mrad, which was the value of the maximum joint rotation attained during the monotonic test. However, some FEA were stopped before this value was reached (models M_3, M_4, M_9 and M_{10}). The results of FE models from the parametric study are discussed in parallel to those of the *RM* (i.e., *Reference Model*).

Table 4-7 – Parametric study. Overview of the analysed parameters

Model	Analysed parameter	Applied loading
RM	Numerical reference model	Sagging / Hogging
M_1	No reduced flange section	Sagging / Hogging
M_2	No concrete slab	Sagging / Hogging
M_3	No concrete dowels	Sagging / Hogging
M_4	No concrete dowels, frictionless contact	Sagging / Hogging
M_5	Higher ratio of longitudinal rebars	Hogging
M_6	With backing plates	Sagging
M_7	Higher concrete class (C35/45)	Sagging
M_8	Higher concrete class (C40/50)	Sagging
M_9	With ribs (reinforced concrete slab)	Sagging / Hogging
M_{10}	With trapezoidal steel sheets	Sagging / Hogging
M_{11}	With rib stiffener on top beam flange	Sagging / Hogging
M_{12}	Decoupled dissipative zone	Sagging / Hogging

4.3.1 Influence of *RFS*

To study the influence of the *RFS*, FE model M_1 was created. In contrast to the *RM*, model M_1 did not contain the *RFS* (see Fig. 4-61a). In comparison to the results of the *RM*, higher stresses were developed in the connection area of the model M_1 under maximum hogging and sagging bending values, as shown in the von Mises stress distributions in Fig. 4-61b-d. Increased stress values in the bolts of model M_1 led to the **failure of the two lower bolt rows** under sagging bending (Fig. 4-61c), this finding being the most important consequence that followed the removal of the *RFS*. The occurrence of this **fragile failure mode** was a significant change of the failure mechanism, which in the *RM* with *RFS*, was ductile. This outcome was

consistent with the results of an experimental study carried out by Plumier [66]. In the study of Plumier, beam-to-column joints, whose only variable parameter was the Reduced Beam Section *RBS*, sustained different failure modes. Whereas a failure of the bolts occurred in joints without *RBS*, those with *RBS* sustained high deformations within this component.

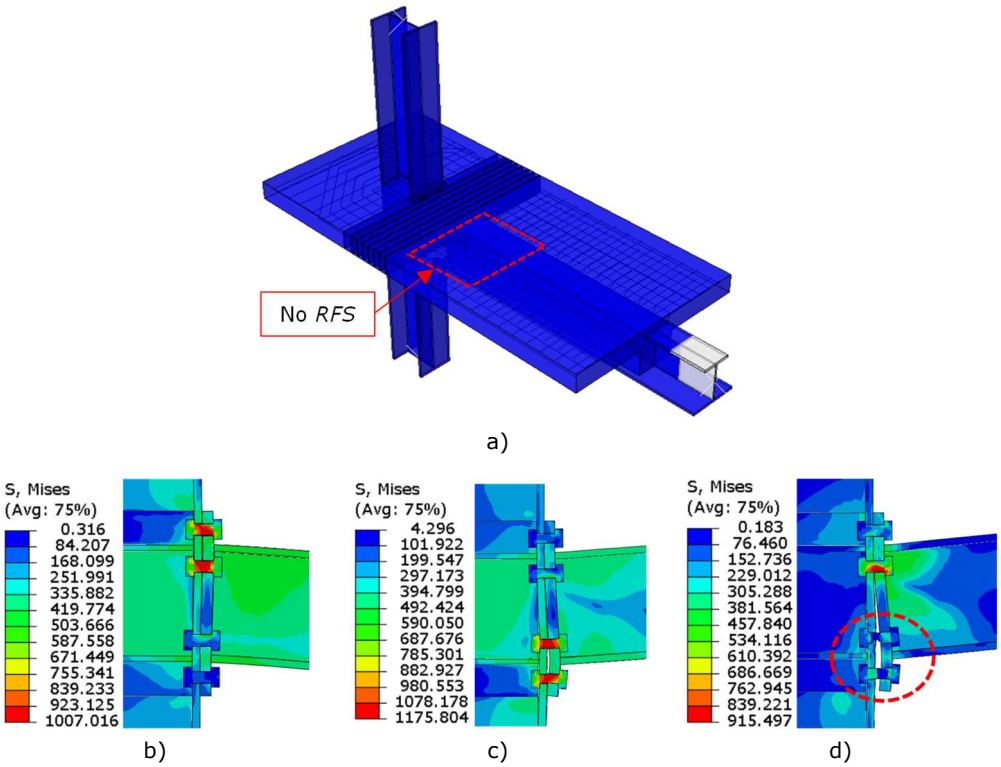

Fig. 4-61. Model M_1 (without *RFS*): a) model M_1; stress distribution in the joint under: b) maximum hogging; c) maximum sagging before bolt failure; d) sagging after bolt failure

Without the *RFS*, **stresses are mainly transferred to the bolts** under both hogging and sagging bending. This is supported by the results shown in Fig. 4-61b,c. In Fig. 4-62a-d, where distributions of strains and stresses in the bolts and in the SF beam are shown prior to the brittle failure under sagging bending, more evidence of this can be found. By comparing the stresses and plastic strains in the bolts to those developed in the SF beam, significantly higher values can be observed in the first. The failure mechanism developed in FE model M_1 under sagging bending is brittle and thus, not in line with the design strategy. The failure of the bolts under sagging bending can also be seen on the moment-rotation curve (see Fig. 4-63a). The moment-rotation curve corresponding to model M_1 (see Fig. 4-63a) evidenced an **asymmetric response** of the joint. Although the hogging response was similar to that of the *RM*, a decrease of 18 % in joint rotation at maximum bending and a sudden drop occurred in sagging bending. The drop in resistance under sagging bending corresponded to the failure of the two lower bolt rows. Compared to the *RM*, the curve of M_1 exhibited an increase of 17 % in sagging bending resistance and an increase of 4 % in initial stiffness. However, despite gaining some resistance and stiffness, **considerable ductility is lost** if the *RFS* is not applied.

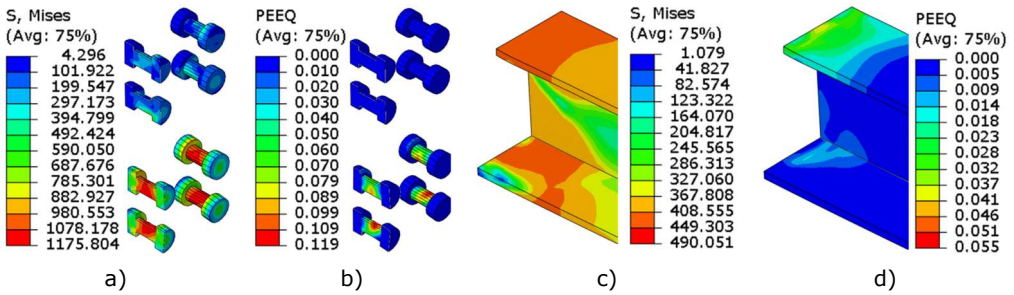

Fig. 4-62. Model M_1 - influence of *RFS* under sagging bending: stresses & plastic strain distributions within the: a) & b) bolts; c) & d) SF beam

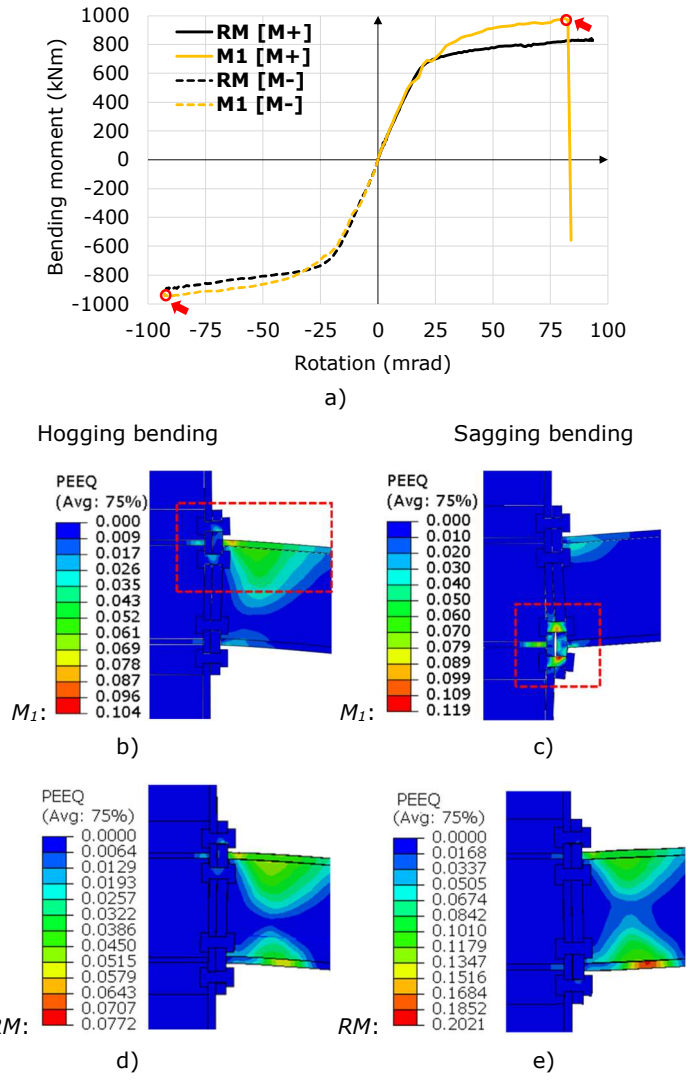

Fig. 4-63. Model M_1 - influence of *RFS*: a) comparison of *M-θ* curves (M_1 to the *RM*); stresses & plastic strains under hogging & sagging bending in: b) & c) model M_1; d) & e) *RM*

A comparison of the M_1 to the *RM* in terms of plastic strain distribution under maximum hogging and sagging bending evidenced the following (Fig. 4-63a-d):

- hogging bending: uneven plastic strain distribution, with a 35 % increase in strains in the upper half of the SF beam (see Fig. 4-63b); oppositely, balanced strain distribution was evidenced on the height of dissipative zone in the *RM*, and the bolted connection remained elastic (see Fig. 4-63d).
- sagging bending: fragile failure of lower bolt rows in model M_1 (see Fig. 4-63c); oppositely in the *RM*, large plastic deformations of the dissipative zone indicated the development of a ductile plastic mechanism (see Fig. 4-63e).

4.3.2 Influence of reinforced concrete slab

The objective of the model M_2 was to emphasize the influence of the reinforced concrete slab (RCS) on the performance of the joint. To this end, the RCS was removed (see Fig. 4-64b) and FEA were performed in hogging and sagging bending.

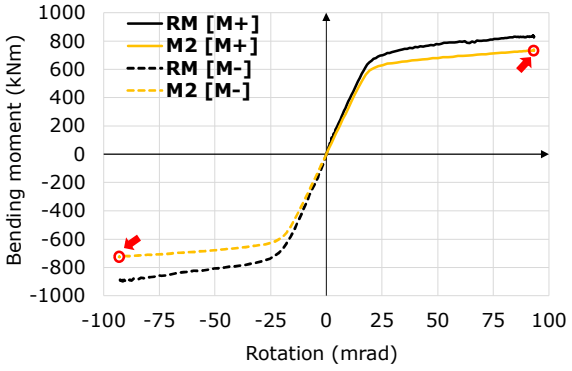

a)

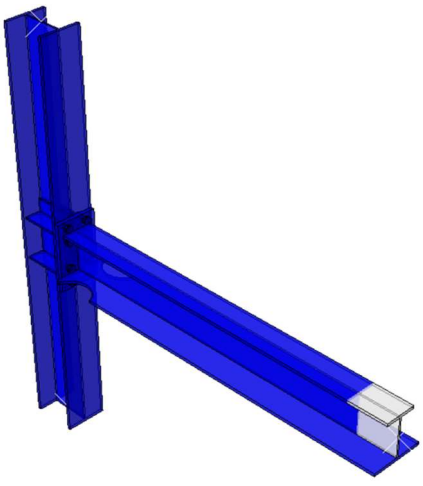

b)

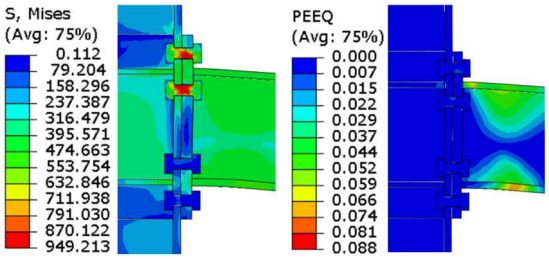

c) hogging bending

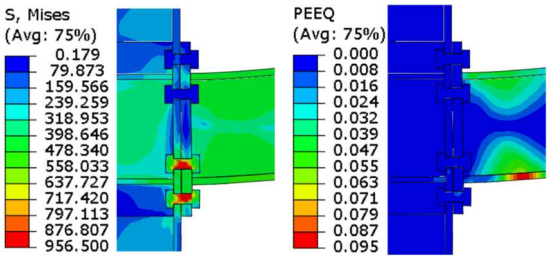

d) sagging bending

Fig. 4-64. Model M_2 - influence of RCS: a) comparison of *M-θ* curves (M_2 to *RM*); b) model M_2; c) & d) stress & plastic strain distributions under maximum hogging & sagging bending

The comparison of the curves (M_2 to *RM*) is shown in Fig. 4-64a. Model M_2, which did not have a RCS, had a decrease of 12 % in sagging bending resistance and of 19.7 % in hogging bending. The *RM* developed higher bending resistances due to the contribution of the compressed RCS under sagging bending and to the tensioned longitudinal rebars under hogging bending. The stiffness of model M_2 decreased: 14 % in hogging, -12 % in sagging bending. In conclusion, the **performance of the model M_2 was inferior** to that of the *RM*, in terms of bending resistance and stiffness.

4.3.3 Influence of concrete dowels

Concrete dowels were removed from FE model M_3 and analyses were performed under hogging and sagging bending. The comparison of the curves (M_3 to *RM*) is shown in Fig. 4-65. As observed on Fig. 4-65, the removal of concrete dowels was somewhat influential on the bending resistance and initial stiffness of model M_3. However, as this could be the outcome of stresses still being transmitted through friction and the inclined rebars, the removal of concrete dowels was combined with the selection of a *"frictionless contact"* between the components in FE model M_4.

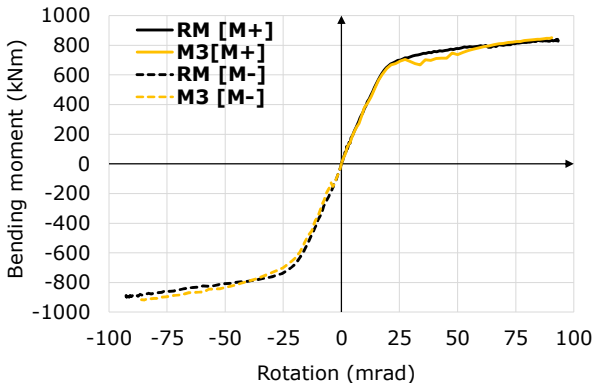

Fig. 4-65. Model M_3 - influence of concrete dowels: comparison of *M-θ* curves: M_3 to *RM*

Influence of concrete dowels and "frictionless contact"

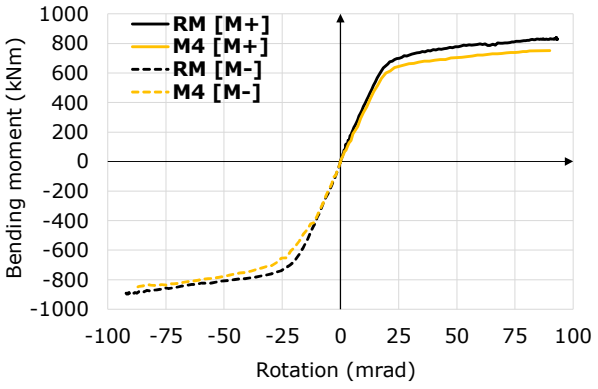

Fig. 4-66. Model M_4- influence of concrete dowels & frictionless contact between components: comparison of *M-θ* curves: M_4 to *RM*

The removal of the concrete dowels together with the selection of a frictionless contact between the components led to the following results (see Fig. 4-66):

- **increased relative slip** between the steel SF beam and the RCS (17.6 mm);
- a reduction of 9 % in bending resistance and of 12.5 % in initial stiffness under sagging bending.

The maximum relative slip occurred in hogging bending and, in comparison to that of the *RM* (0.85 mm), the recorded value in model M_4 was high: 17.6 mm. Therefore, the importance of the **concrete dowels should not be underestimated**, even if the joint solution contains inclined rebars. This conclusion is especially valid in seismic regions, where multiple loading cycles could diminish friction.

4.3.4 Influence of higher longitudinal reinforcement ratio

The influence of higher longitudinal reinforcement ratio was analysed on model M_5 under hogging bending. The reinforcement of the concrete slab of the *RM* included 10 longitudinal rebars of diameter 10 mm and 2 rebars of diameter 20 mm. Continuity of the longitudinal rebars around the column was ensured (see in Fig. 3-32c). Alternatively, the diameter of all longitudinal rebars of model M_5 was increased to 20 mm with the aim to investigate whether the parameter would enhance the hogging bending resistance.

As evidenced in Fig. 4-68, the hogging bending resistance and the initial stiffness of model M_5 increased, as compared to the *RM*. The increase in bending resistance was 4 %, while that in initial stiffness was roughly 6 % higher than that of the *RM*. At values of the bending moment of 450 kNm, portions of the concrete slab under compression began to develop plastic deformations. Furthermore, at values of the hogging bending moment equal to 800 kNm, severe cracking of compressed concrete slab portions (e.g., behind the column, in the dissipative zone) was evidenced. At 940 kNm, a transverse rebar located behind the column fractured causing the drop in resistance on the *M-θ* curve.

A higher longitudinal reinforcement ratio combined with the same concrete class as the one used in the *RM* (e.g., C30/37), so with the same compressive and tensile concrete resistance, led to the failure of the concrete. Consequently, a higher longitudinal reinforcement ratio led to an **undesired and earlier failure of the concrete slab under compression.** More results are available in Annex B.

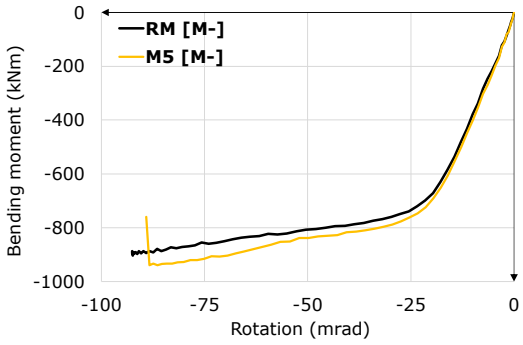

Fig. 4-67. Model M_5 - influence of higher ratio of longitudinal rebars under hogging bending: comparison of *M-θ* curves (M_5 to *RM*)

4.3.5 Influence of backing plates

The addition of backing plates was studied on model M_6. The motivation for the investigation of this parameter was to verify whether the use of backing plates would lower the stresses and the plastic strains in the bolts under sagging bending.

Consequently, backing plates of 18 mm in thickness were added to the two lower bolt rows, and the numerical model was analysed under sagging bending.

As shown on the comparison of the moment-rotation curves corresponding to model M_6 and to the *RM* (see Fig. 4-68a), the responses were similar. Although the stresses in the bolts of model M_6 were slightly lower, e.g., 2.0 %, the reduction in plastic strain was considerable (17.6 % less plastic strain than in the *RM*). Images representing distributions of von Mises stresses and equivalent plastic strains within the bolts of model M_6 are shown in Fig. 4-68b,c. In parallel, stresses and strains distributions are shown for the bolts of the *RM* at the same value of the sagging bending moment (see Fig. 4-68c). The comparison evidenced that the use of backing plates **can reduce the development of plastic strains within the bolts**.

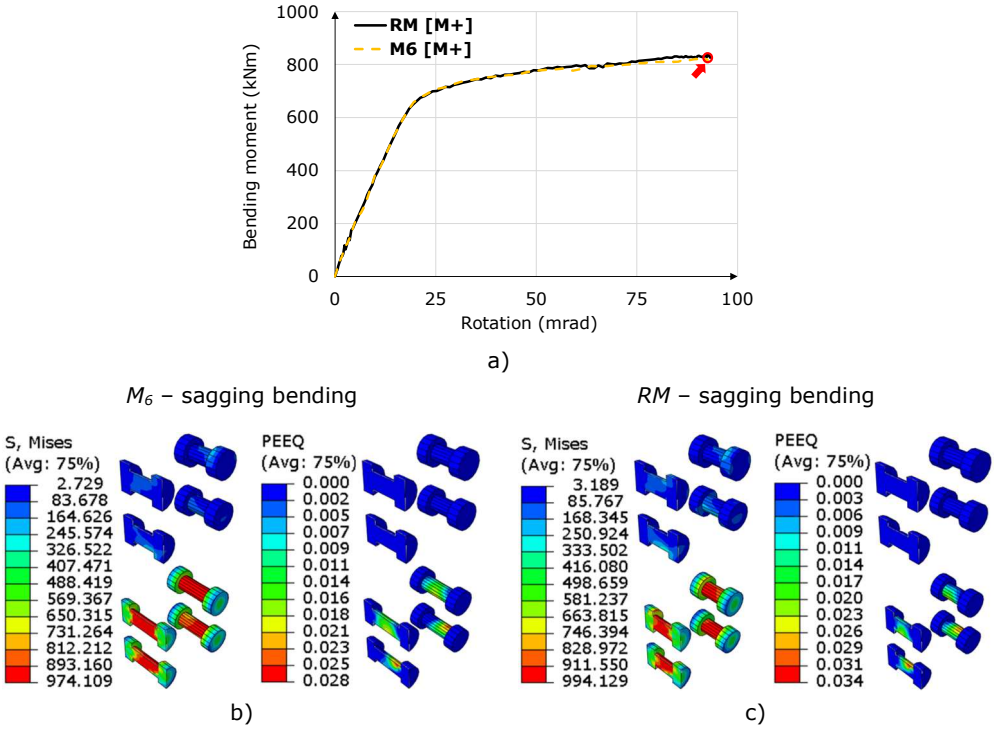

Fig. 4-68. Model M_6 - influence of backing plates under sagging bending: a) comparison of *M-θ* curves (M_6 to *RM*); b) & c) comparison of stresses & plastic strains in the bolts of M_6 & *RM*

4.3.6 Influence of higher concrete classes

The influence of higher concrete classes was investigated on the FE models M_7 and M_8 under sagging bending. Concrete class was increased from C30/37 to C35/45 in model M_7, and to C40/50 in model M_8. Based on the results of the FEA, it was observed that the highest stress and plastic strain values within the concrete itself of both analysed FE models were developed under compression in the concrete slab. The comparisons of moment-rotation curves shown in Fig. 4-69a,b did not evidence significant changes in the bending resistance of FE models M_7 and M_8 due to higher concrete classes. Initial stiffness increased trivially with 0.5 % in model M_7 and remained the same in model M_8. The obtained results could be explained by the fact that the concrete slab was not the weakest component of the joint. More results are available in Annex B of the current document.

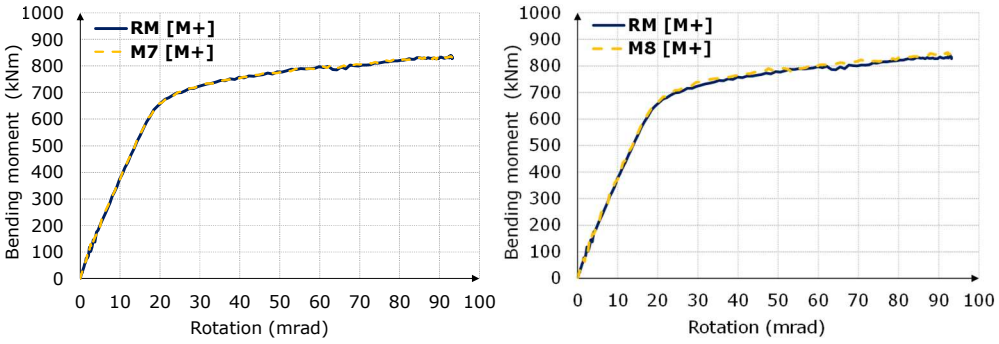

Fig. 4-69. Models M_7 & M_8 – influence of higher concrete classes under sagging bending: comparison of M-θ curves: a) M_7 to *RM*; b) M_8 to *RM*

4.3.7 Influence of concrete ribs

Given the adjoining positioning of the ribs to the dissipative zone (see Fig. 4-70), the addition of concrete ribs to the slab was analysed under sagging and hogging bending on FE model M_9. The importance of adding this parameter was doubled by the practicality of the solution, because in practice, shallow flooring systems usually include concrete ribs following the use of trapezoidal steel sheets with open ribs. In terms of FE modelling, the dimensions of the concrete ribs were adapted to a floor decking system based on *Cofraplus 220* [94]. The material properties that were assigned to the concrete part corresponded to a concrete class C30/37. Furthermore, rebars of 10 mm in diameter and of steel grade B500B were used to reinforce the ribs. The concrete part of the ribs was modelled with solid elements types C3D8R, while the rebars were modelled with wire elements, type B31.

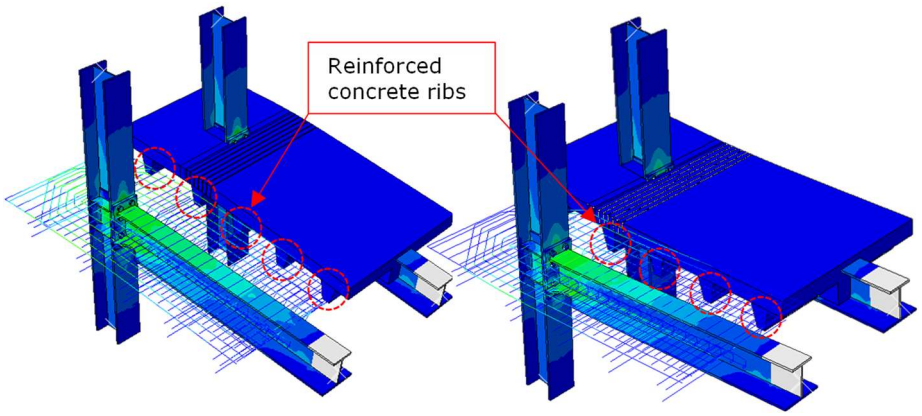

Fig. 4-70. Model M_9 with reinforced concrete ribs

In terms of bending resistance and stiffness, the addition of reinforced concrete ribs did not significantly change the hogging and sagging responses, as compared to those of the *RM* (see Fig. 4-71a). When the analyses were stopped, high rotation values were attained under both hogging and sagging bending for model M_9 (e.g., 88.3 mrad, 89.6 mrad). Moreover, the development of plastic deformations in the dissipative zone was not restrained by the presence of the ribs, while plastic strain

distributions within the bolts and the dissipative zone are similar to those in the *RM* (see Fig. 4-71b-e, Fig. 4-58a-f). More results are included in Annex B.

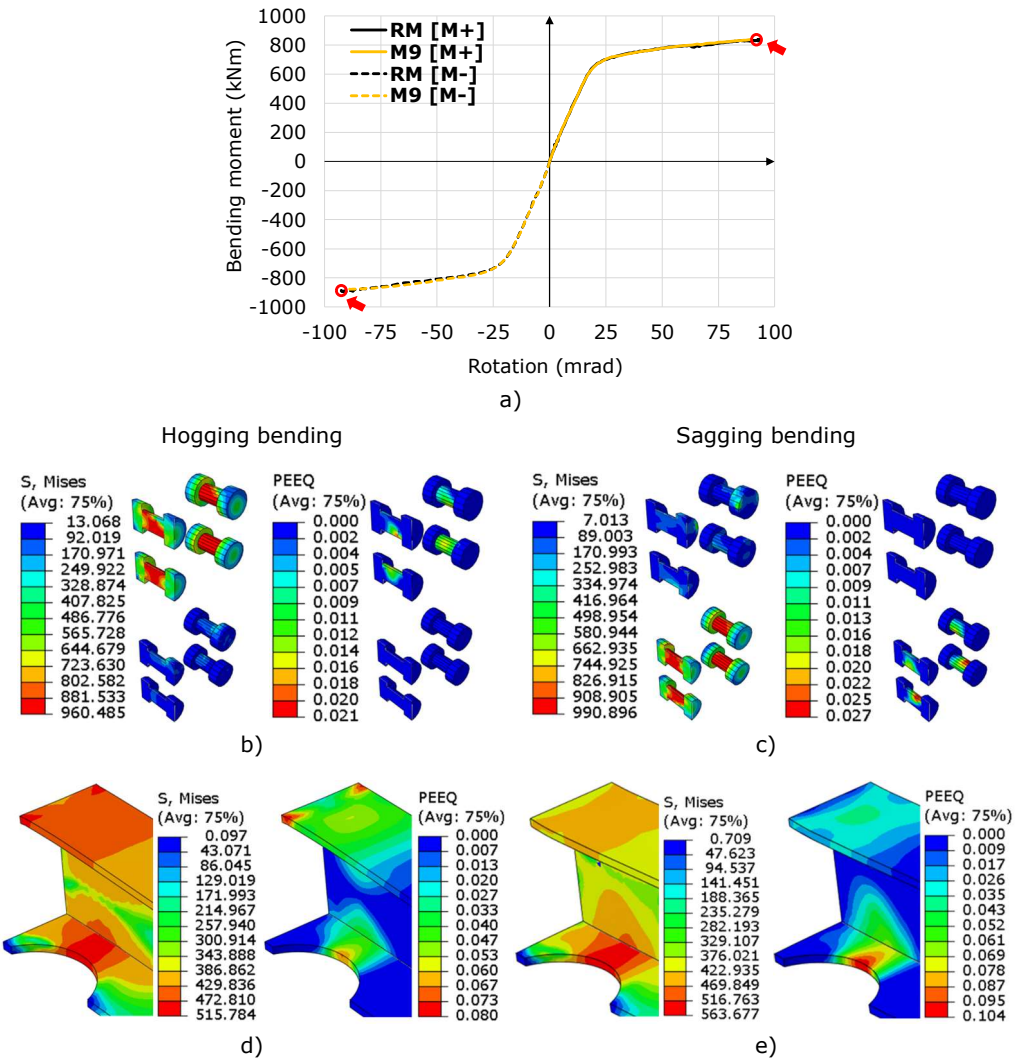

Fig. 4-71. Model M_9 - influence of reinforced concrete ribs; a) comparison of *M-θ* curves (M_9 to *RM*); stress & plastic strain distributions under hogging / sagging bending within b), c) bolts; d), e) dissipative zone of the SF beam

4.3.8 Influence of concrete ribs and trapezoidal steel sheets

Apart from the addition of reinforced concrete ribs, trapezoidal steel sheets based on *Cofraplus 220* [94] were included in the FE model M_{10}. As trapezoidal steel sheets were not added to the tested specimens, this parameter was included in the parametric study. The thickness of the steel sheets was 1.25 mm and the FE modelling was performed with shell elements. Compared to the moment-rotation curve of the *RM*, the results of model M_{10} proved a small influence of the trapezoidal sheets on the response of this model (see Fig. 4-72a). Similar to model M_9, the FEA was stopped before the complete value of the applied displacement was attained. Despite this, the

joint rotation at maximum bending moments was high under both hogging and sagging bending (e.g., 91.8 mrad; 88.3 mrad). The stress and plastic strain distributions in model M_{10} (see Fig. 4-72b-e) were similar to those corresponding to the *RM*. Considering the similarities of models M_9 and M_{10} to the *RM*, it could be concluded that the addition of reinforced concrete ribs and steel sheets does not have an important impact on the behaviour of these models. Wang et al. [35] drew the same conclusion based on experimental tests; in [35], the concrete ribs had a small influence on the evaluation of a joint's performance, which is why they were neglected from resistance and stiffness calculations, and analyses. In the study on SF joints, **neither the concrete ribs, nor the steel sheets prevented the development of plastic deformations in the dissipative zone**.

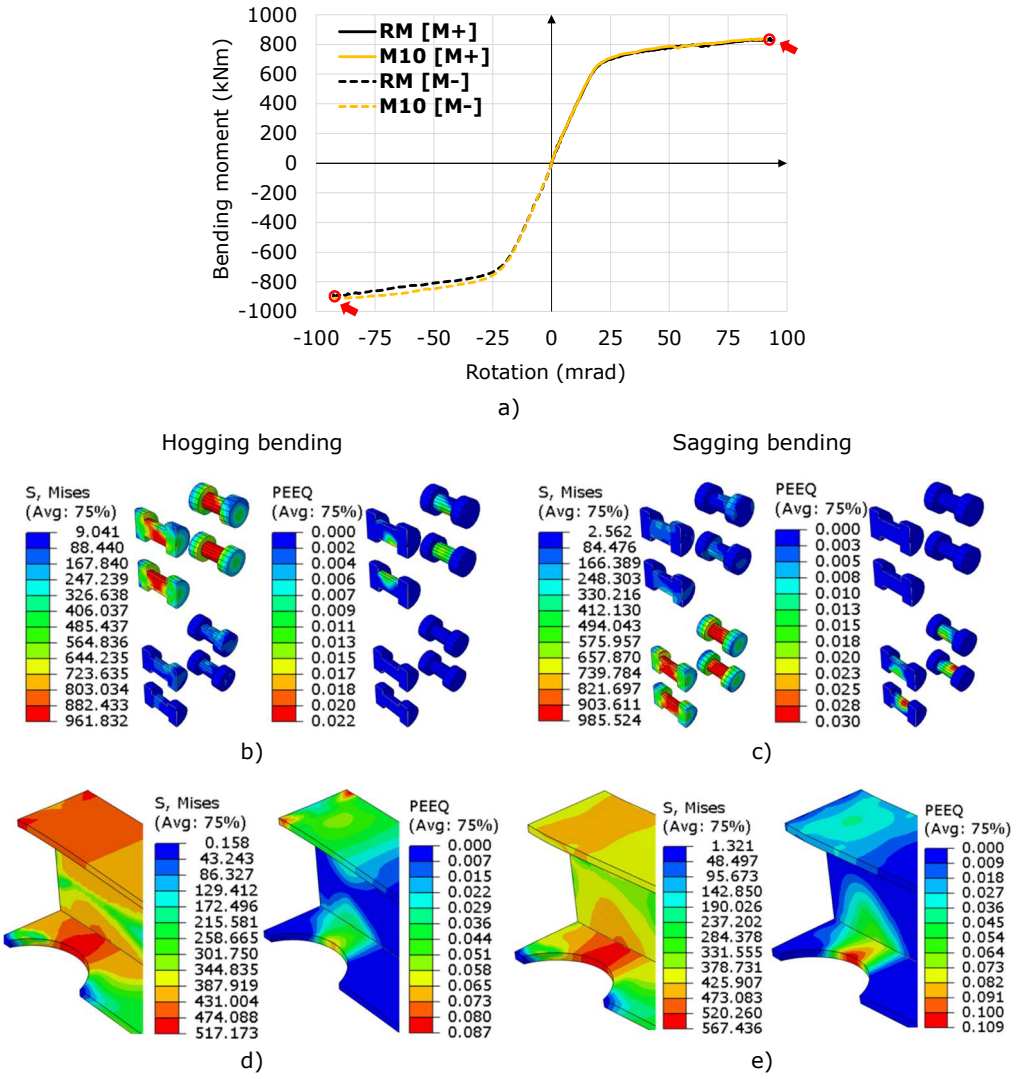

Fig. 4-72. Model M_{10} - influence of steel sheets: a) comparison of *M-θ* curves (M_{10} to *RM)*; stress & plastic strain distributions under hogging / sagging bending within b), c) bolts; d), e) dissipative zone of the SF beam

4.3.9 Influence of a rib stiffener

The addition of a rib stiffener on the top flange of the SF beam was analysed on FE model M_{11} under both hogging and sagging bending. Model M_{11} was developed with the aim to verify whether the addition of a rib stiffener on the top flange of the SF beam would lower stress and plastic strain values in the proximity of the flange-to-end-plate weld (heat-affected zone, HAZ). The importance of reducing stress values in areas adjoining critical welds was previously evidenced in literature (e.g., [95]). This aspect was underlined as being particularly important in cases when design strategy required stable hysteretic behaviour of beams with *RBS*.

In the study on SF joints, a rib stiffener was welded on the middle of the top flange of the SF beam and on the end-plate, as shown in Fig. 4-73. The dimensions of the rib stiffener were the following: 90 x 90 x 25 mm (height x width x thickness). The material model that was used for the rib stiffener was the same as the one used for the top flange of the SF beam. "*Tie constraint*" was used for the modelling of the welds between the rib stiffener, the top flange and the end-plate.

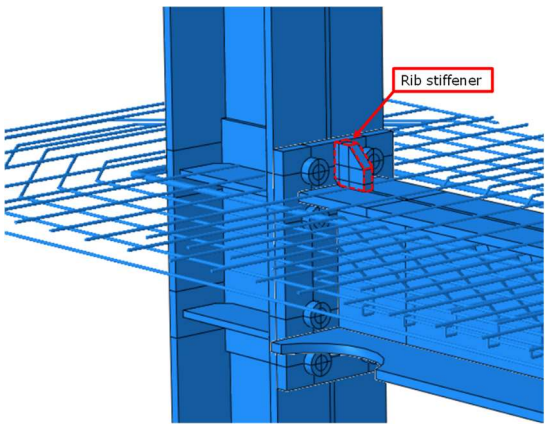

Fig. 4-73. Model M_{11} with welded rib stiffener on the top flange of the SF beam

The results of the FEA are shown in Fig. 4-74a-g and Fig. 4-75a,b. Compared to the moment-rotation curve of the *RM*, the curve corresponding to FE model M_{11} was similar (see Fig. 4-74a). In terms of bending resistance, the response of model M_{11} under hogging was slightly different from that of the *RM*. For a more detailed assessment of the components of model M_{11}, the stress and plastic strain distributions within the bolts, the dissipative zone and the rib stiffener are shown in Fig. 4-74b-g. These illustrations corresponded to the end of the FEA. In comparison to the distributions of stresses and plastic strains within the bolts of the *RM*, the following were evidenced for the bolts of model M_{11}:

- two upper bolt rows under hogging bending (see Fig. 4-74b):
  - 0.92 % reduction in von Mises stresses;
  - 23.8 % reduction in equivalent plastic strain;
- two upper bolt rows under sagging bending (see Fig. 4-74c):
  - 2.8 % reduction in von Mises stresses;
  - 32.3 % reduction in equivalent plastic strain.

Regarding the effect of the rib stiffener on the bolts - although the reduction in stresses was small under both hogging and sagging bending, significant decrease in plastic strain resulted in model M_{11} with rib stiffener.

In the dissipative zone of the SF beam corresponding to model M_{11}, plastic deformation values were higher than those in the *RM* at the end of the FEA, but according to the distributions from Fig. 4-74d,f, these were local phenomena. Furthermore, the distribution of plastic strain in the HAZ was positively affected by the addition of a rib stiffener. As shown in Fig. 4-75a,b, the addition of a rib stiffener on the top flange of the SF beam resulted in a diversion of plastic deformations from the HAZ. Some plastic deformations were also evidenced in the rib stiffener under both hogging and sagging bending, as shown in Fig. 4-74e,g.

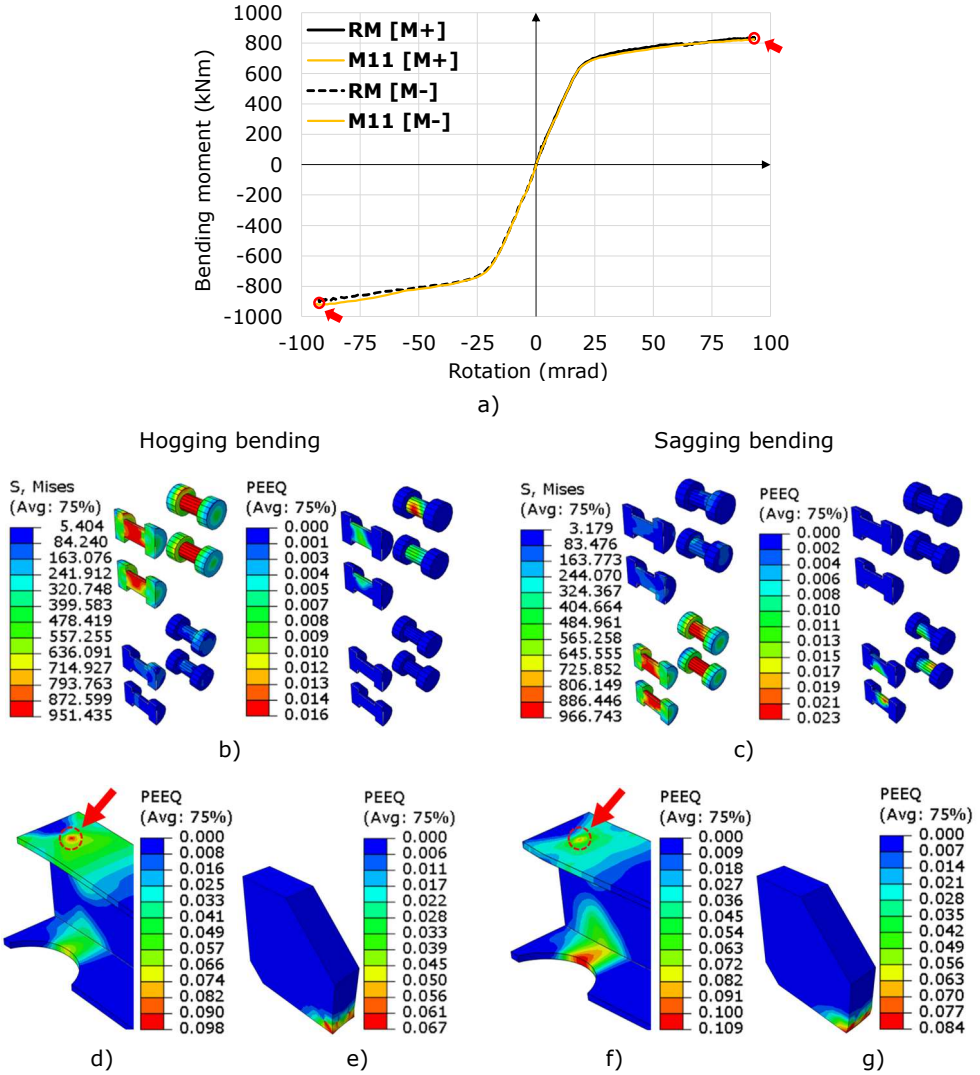

Fig. 4-74. Model M_{11}- influence of rib stiffener: a) comparison of *M-θ* curves (M_{11} to *RM)*; b), c) stress & plastic strain distribution under hogging / sagging bending in bolts; plastic strain distribution in: d), f) dissipative zone; e), g) rib stiffener

Consequently, FEA results proved that, although significant changes on the *M-θ* curve were not evidenced, the addition of a rib stiffener on the top flange of the SF beam leads to an intended behaviour of model M_{11}, and is beneficial in terms of:

- **lowering plastic strains in the bolts under both hogging and sagging bending** (e.g., reduction in the range of 24 ÷ 32 %);
- **diverting the development of plastic strain near the HAZ**.

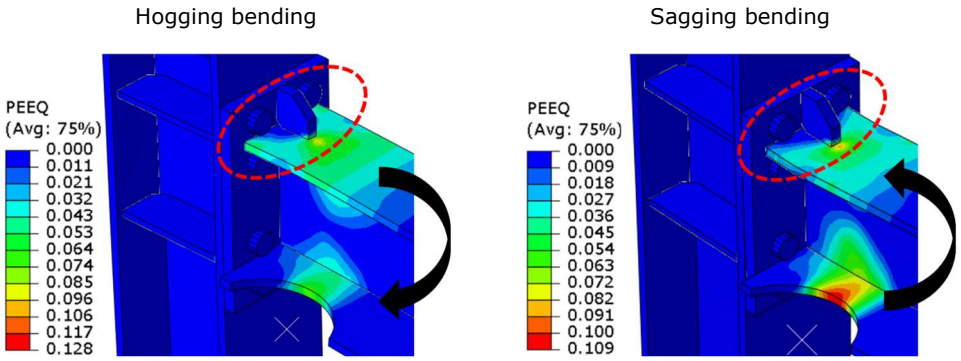

Fig. 4-75. Model M_{11} - influence of rib stiffener: plastic strain distribution in a) maximum hogging; b) maximum sagging bending

4.3.10 Influence of decoupled dissipative zone from concrete

The decoupling of the dissipative zone of the SF beam from the reinforced concrete was studied on FE model M_{12} under hogging and sagging bending. In the design of buckling-restrained braces, the decoupling of steel core from concrete by means of debonding material (e.g., butyl rubber tape, closed-cell extruded polystyrene foam) is an established method of ensuring stable hysteretic behaviour of members. Various examples on the subject are available in literature, e.g., [96] [97], while recent developments are increasing the range of application of decoupled steel components from concrete for enhanced seismic performance (e.g., [98]). The decoupling of the dissipative zone of the SF beam from the reinforced concrete aimed at the reduction of stresses and plastic strains in the beam-to-column connection. To this end, a gap of 3 mm was provided on the contour of the dissipative zone corresponding to the asymmetric steel profile, as shown in Fig. 4-76. The value of the gap was based on existing research studies, such as [98] and [99].

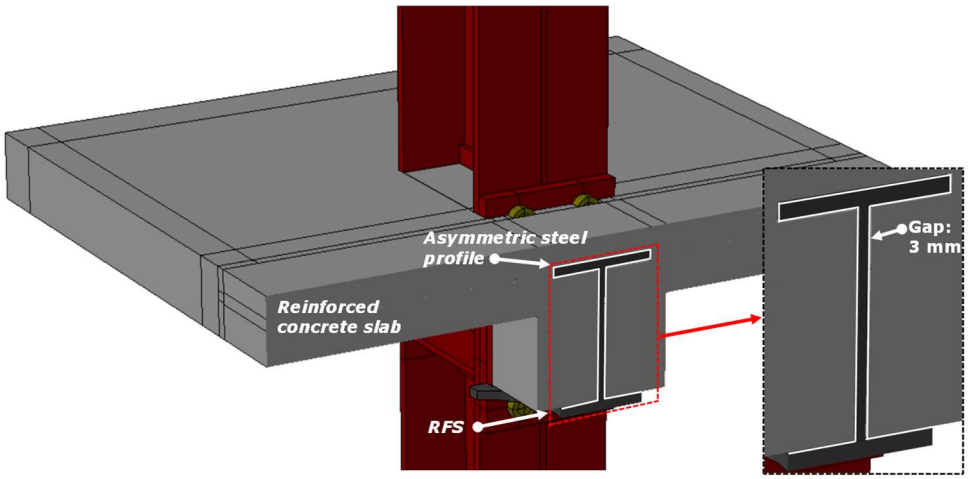

Fig. 4-76. Model M_{12} with dissipative zone of SF beam decoupled from concrete

The moment-rotation curve corresponding to FE model M_{12} is shown in parallel with that of the *RM* in Fig. 4-77a. Apart from a minor reduction in hogging and sagging bending resistance, the moment-rotation curve of model M_{12} is similar to that of the *RM*. Stress and plastic strain distributions within the bolts, corresponding to the point of maximum hogging and sagging bending, are shown in Fig. 4-77b-e. Compared to the *RM*, although the stress reduction in model M_{12} was low (i.e., -1.9 %), a significant decrease in plastic deformation was obtained in the bolts: -14.3 % under hogging bending and –24 % under sagging bending. Smaller values of plastic strain were also observed in the end-plate: -6.7 % under hogging bending and -16.7 % under sagging bending. Based on the obtained results, the decoupling of the dissipative zone of the SF beam from the reinforced concrete was an efficient method of **reducing the development of plastic strain within the bolted beam-to-column connection**.

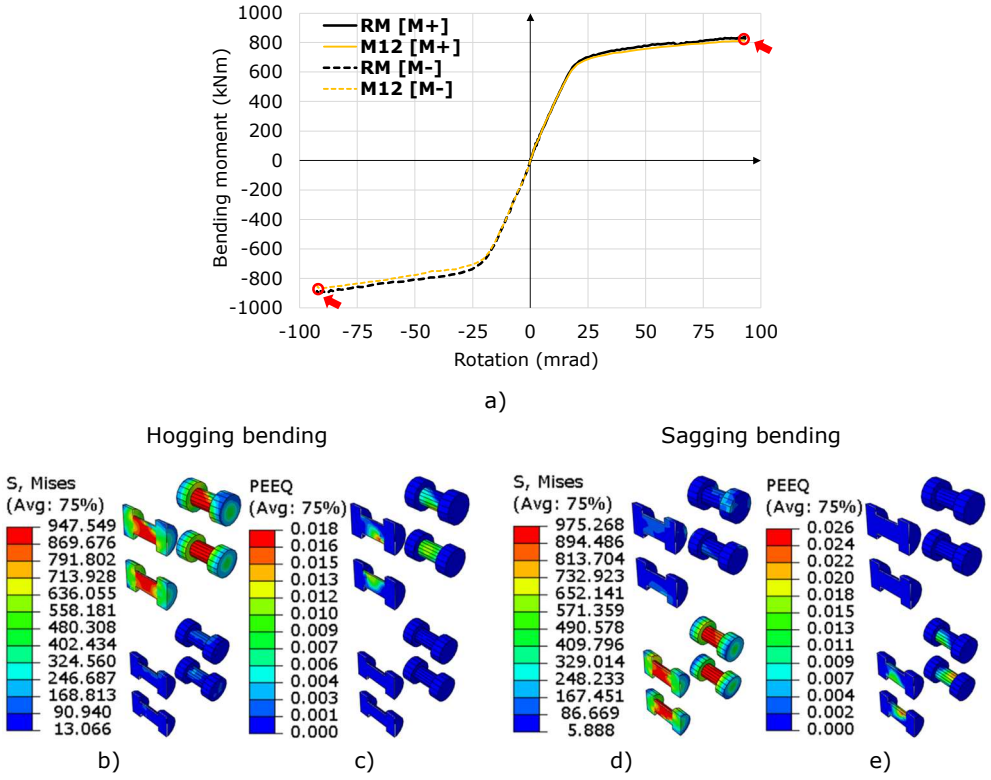

Fig. 4-77. Model M_{12}- influence of decoupled dissipative zone: a) comparison of *M-θ* curves (M_{12} to *RM)*; b), d) stress distribution within bolts; c), e) plastic strain distribution within bolts

4.4 Concluding remarks

The results of the reference FE model (*RM*), as well as of the FE models from the parametric study, were obtained by performing advanced finite element analyses (FEA) and have led to important conclusions. The first of these conclusions is related to the results of the calibration of the reference numerical model *RM*, which evidenced a high accuracy in reproducing the experimental test curve. To support the high correlation of the numerical curve to the experimental one, deviations or aberrations were calculated, and found to be in the range of 0.1 ÷ 3.2 %.

A further conclusion is related to the accuracy of the *RM* in reproducing the development of the failure mechanism. Under maximum hogging bending (see Fig. 4-56, point *"A"*), most plastic deformation was sustained by the dissipative zone of the SF beam. In this case, deformations of the dissipative zone of the SF beam occurred under compression. Other components of the *RM* sustained localised inelastic deformations. Thus, the results of the *RM* under hogging bending supported the observations made during the experimental tests: ductile behaviour of the SF beam and a mainly elastic response of the bolted end plate connection. Under sagging bending (see Fig. 4-56, point *"B"*), the dissipative zone of the SF beam exhibited a ductile behaviour, sustaining high plastic deformations. Overall, in the maximum bending points indicated on the moment-rotation curve corresponding to the *RM*, the highest values of plastic deformations were developed in the dissipative zone of the SF beam. Compared to the dissipative zone of the beam, the equivalent plastic strain within the bolts were low and the distribution limited (localised phenomena), which supports the conclusion that the **failure mechanism was ductile**. This observation is consistent with the conclusions of the experimental study.

The second part of the numerical program was dedicated to the development of a parametric study. The parametric study was focused on isolating parameters that were part of the joint solution (e.g., *RFS*, reinforced concrete slab, etc.) in order to assess their influence, but also included new parameters (e.g., backing plates, reinforced concrete ribs, trapezoidal steel sheets, etc.). The influence of the following parameters was analysed within the parametric study (see overview in Table 4-7):

- reduced flange section *RFS* in model M_1;
- reinforced concrete slab in model M_2;
- concrete dowels in model M_3;
- concrete dowels plus "*frictionless contact*" between components in model M_4;
- longitudinal reinforcement ratio in model M_5;
- backing plates in model M_6;
- concrete class in models M_7 and M_8;
- reinforced concrete ribs in model M_9;
- reinforced concrete ribs and trapezoidal steel sheets in model M_{10};
- rib stiffener welded on the top flange of the SF beam in model M_{11};
- decoupled dissipative zone of SF beam from concrete in model M_{12}.

Considering the numerical results from this section, the ductile behaviour of the SF beam, characterised by the development of a plastic hinge in the dissipative zone of the SF beam and by a mainly elastic response of the end-plate connection (which helped attain a sufficient rotation), could be attributed to the following parameters: the presence of the *RFS* and of the reinforced concrete slab.

Influence of the *RFS*. The application of a *RFS* ensures member ductility which is manifested through to a **balanced or symmetric response the SF beam-to-column joint**. Thus, another important conclusion drawn from the numerical program is that the shape of the SF beam in the dissipative zone has a significant influence on the failure mechanism of the SF beam-to-column joint. Through the application of the *RFS*, the stresses and strains are more evenly distributed on the height of the dissipative zone, which eventually leads to a ductile failure mode in the dissipative zone. On the contrary, if the *RFS* is removed, the lower bolt rows fail under sagging bending (see FEA results of model M_1). Prior to sudden drop in resistance on the moment-rotation curve, the components which sustained the highest plastic strain values were the bolts (e.g., 0.119 mm/mm). Simultaneously, the maximum value of plastic strain within the dissipative zone was half of that in the bolts (e.g., 0.055 mm/mm). A similar conclusion was reached in the study of Plumier [66], in which the failure mechanism of connections with *RBS* and without *RBS* was investigated

experimentally. In the previously mentioned study, it was concluded that that the investigated specimens, which did not include a *RBS*, sustained bolt failure.

Influence of the concrete slab. The presence of the reinforced concrete slab influenced the bending resistance, stiffness and rotation. For example, when the concrete slab was removed from model M_2, the bending resistance, initial stiffness and rotation at maximum bending moments were lower than in the *RM*.

Influence of concrete dowels. The shear interaction was assured by rebars and concrete dowels. Although the concrete dowels were removed from numerical model M_3, the stresses were transferred through inclined rebars and friction, so the moment-rotation curve remained similar to that of the *RM*. Followingly, apart from the removal of the concrete dowels the friction between the components of model M_4 was eliminated. The effect of the latter produced a series of changes, the most important of which being a high value of relative slip, e.g., 17.6 mm. Considering this, it was concluded that the SF beam-to-column joint solution should include concrete dowels. The conclusion is even more important in seismic regions, where multiple loading cycles could diminish friction and lead to undesired consequences.

Influence of increased reinforcement ratio. A higher longitudinal reinforcement ratio of the concrete slab led to a different failure mechanism. The development of plastic strain in the portions of the concrete slab under compression began at values of the bending moment equal to 450 kNm. At 940 kNm, portions of the concrete slab under compression experienced severe cracking and one of the transverse rebars (located behind the column) fractured leading to the end of the analysis. The parameter could be further investigated, but the increase in longitudinal reinforcement ratio should be accompanied by an increase in concrete class.

Influence of backing plates, rib stiffener and decoupled dissipative zone. Considering the investigated parameters, it was concluded that measures could be employed to reduce the development of plastic strain within the beam-to-column connection. In this sense, the addition of backing plates in model M_6, the addition of a rib stiffener in model M_{11} and the decoupling of the dissipative zone from the reinforced concrete in model M_{12} proved efficiency:

- model M_6: 17.6 % less plastic strain within bolts under sagging bending;
- model M_{11}: 32 % less plastic strain within bolts under sagging bending, and 24% less under hogging bending;
- model M_{12}: 24 % less plastic strain within bolts under sagging bending, and 6.7 % less under hogging bending.

Influence of increased concrete class. The increase in the concrete class as a stand-alone parameter in models M_7 and M_8 was found not to be not influential on the initial stiffness. In both of the analysed FE models, the value of initial stiffness remained almost identical with those of the *RM*. A delayed initiation of cracking or even less cracking of the concrete slab could not be demonstrated.

Influence of reinforced concrete ribs and trapezoidal steel sheets. Neither the addition of reinforced concrete ribs nor that of trapezoidal steel sheets to the models M_9, M_{10} prevented the development of a plastic hinge in the dissipative zone of the SF beam. The presence of steel sheets was included in the experimental program of Wang et al. [35], who concluded that the addition of this parameter did not modify the previously obtained failure mechanism.

Results of FEA underlined the central roles of the *RFS* in the dissipative zone of the SF beam as the "weaker" component and of the end-plate connection as the resistant component in obtaining an adequate seismic performance of the SF joint. However, the numerical program should be extended with additional analyses to help establish a range of application for SF beam-to-column joints. For instance, each of the investigated parameters could be further parametric analysed.

5. DESIGN PROCEDURE

Dissipative structural members designed according to the capacity design philosophy exhibit a ductile behaviour under seismic loads [51]. This is the case of the beams of Moment-Resisting Frames and Dual Frames from Ductility Class 3 (DC3). For regular I-profile steel and steel-concrete composite beams, which are covered by modern European codes, ductility can be ensured by the following measures:

- selection of materials and application of rules to ensure material ductility;
- verification of the cross section class;
- limitation of width-to-thickness ratio;
- design by overstrength of the adjacent connections and structural members.

These measures depend on the design concept (DC3, DC2) and on the intensity of the seismic load. The current design procedure is addressed to SF beam-to-column joints designed in DC3 and subjected to a seismicity level defined by a high reference maximum spectral acceleration ($S_{a,475} > 5.0$ m/s^2) [45]. However, as discussed in other sections of the study, SF beam-to-column joints are not covered by current or pre-normative versions of the composite [17] [55] and seismic European codes [46] [51]. Therefore, through the current design procedure, some new rules will be proposed. In addition to these, existing design measures for steel and composite structural members will be extended to slim-floor beam-to-column joints. The purpose of this section is to create a path for the design of SF beam-to-column joints.

5.1 Introduction

5.1.1 Selection of materials

Material selection is to be performed in accordance with the relevant parts of the Eurocodes and the applicable technical approvals. Generally, for joint components of DC3 structures, the material requirements are given in the European codes [54] [55] [56] [51]. A few design rules explicitly for SF beams are given in an official technical approval [19]. All aforementioned rules were centralised in Fig. 5-78.

Material	**Eurocode/technical approval**	**Requirement**
Structural steel	prEN 1993-1-1	$f_u / f_y \geq 1.10$
		Elongation at failure ≥ 15%
	prEN 1994-1-1	Steel grade ≤ 460 N/mm^2
Reinforcing steel	EN 1992-1-1	Class B or C
	prEN 1994-1-1	Steel grade ≤ B500
Concrete dowels	prEN 1994-1-1	Class D1
	Z-26.4-59	B500B
Concrete	*Z-26.4-59*	C25/30 ÷ C55/67
Bolts	prEN 1998-1-2 (composite conn.)	Grade 10.9

Fig. 5-78. Material requirements according to the European codes [54] [55] [56] [51] and the National Technical Approval issued for the *CoSFB* [19]

5.1.2 Joint solution

The components of the SF beam-to-column joint solution are the following: slim-floor beam (steel part); steel column; bolted beam-to-column connection; concrete slab; reinforcement: transverse, longitudinal, inclined; concrete dowels.

The approach to obtaining the steel part of the SF beam is shown in Fig. 5-79a-d. The first three steps are based on another procedure [7]. The slim-floor beam is obtained from half of a steel I-profile. In place of the removed half, a wide steel plate is welded on the remaining half of the steel profile, forming the asymmetric steel SF beam. To the welded steel plate, from now on referred to as "the lower flange" of the SF beam, a *Reduced Flange Section* (*RFS*) is applied (see Fig. 5-79d). As discussed in Section 3.2, the application of the *RFS* was employed to attain member ductility. A summary of the few existing rules is shown in Fig. 5-80. Of these rules, the ones from The National Technical Approval (*Z-26.4-59*) issued for the use of *CoSFB* [19] are directly applicable to SF beams with concrete dowels. Apart from these, in *Annex I* of the draft version of prEN 1994-1-1 [55], additional rules regarding the section class and the transverse shear connectors (see Fig. 5-81) were very recently introduced.

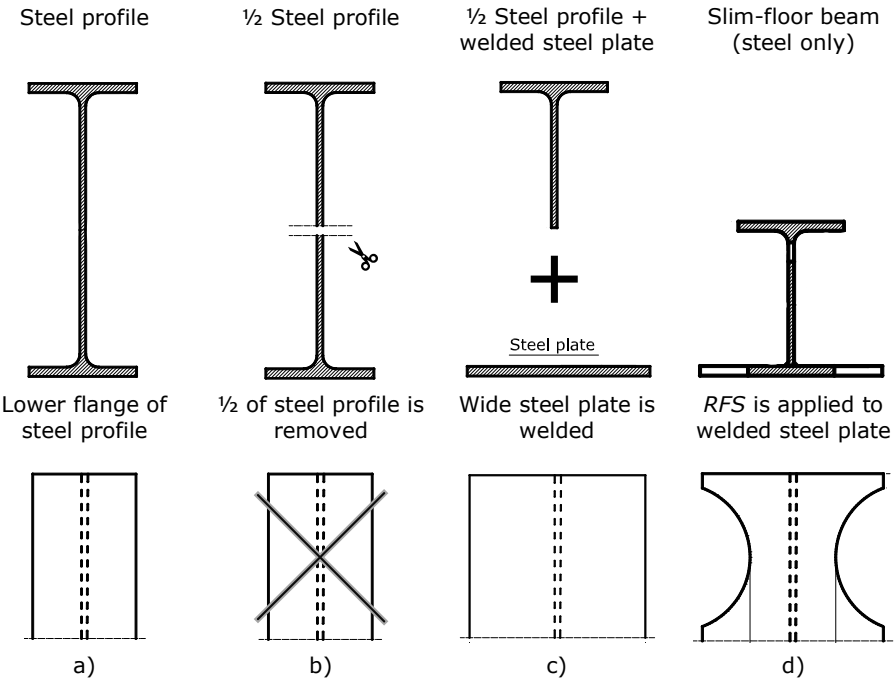

Fig. 5-79. Development of slim-floor beam: a) initial steel profile [7]; b) removal of ½ steel profile [7]; c) welding of wide steel plate [7]; d) application of *RFS* to lower steel plate

	Eurocode/technical approval	**Requirement**
SF beams with concrete dowels	*Z-26.4-59*	S355 or S420
		$t_w \geq 7.5$ mm
	prEN 1994-1-1	Section class 1 or 2
	prEN 1998-1-2	Section class 1

Fig. 5-80. Summary of rules regarding the SF beam according to The National Technical Approval of *CoSFB* [19] and the Eurocodes [55] [51]

	Eurocode/technical approval	Requirement
Concrete dowels / transverse shear connectos	prEN 1994-1-1	Diameter 12 ÷ 20 mm
		Spacing ≥ 125 mm
		Web opening: 2 x $D_{trans,\ rebar}$
	Z-26.4-59	Web opening: 25 ÷ 40 mm; $D_{opening} \geq 13 + D_{trans,rebar}$
		Spacing ≥ 125 mm
		Diameter ≥ 12 mm

Fig. 5-81. Summary of rules regarding the concrete dowels / transverse shear connectors according to prEN 1994-1-1 [55] and The National Technical Approval of *CoSFB* [19]

Whereas high plastic deformations are expected to develop in the SF beam, the end-plate connection and the adjoining welds are to be kept within the elastic range. Therefore, the bolted beam-to-column connection and the adjoining welds should be designed to develop higher resistance than the dissipative zone of the slim-floor beam under both hogging and sagging bending (close to a symmetric response). To achieve this, the end plate should be extended, relative to the beam, both at the top and at the bottom, and the bolts should be grade 10.9 HV. Critical welds such as those of the SF beam flanges to the end-plate and of the stiffeners to the column flanges should be performed with high quality full penetration groove welds, as imposed by [51] and also specified in [100] and [101].

The steel SF beam will be partially encased in reinforced concrete. However, in this SF joint configuration, the transverse and inclined rebars do not contribute directly to the bending resistance in hogging. Instead, the transverse and inclined rebars are influential on shear interaction. Thus, they will not be further detailed in the current design procedure. However, their design should be carried out in accordance with the provisions of EN 1992-1-1 [56].

The column is generally fabricated in a steel or steel-concrete composite solution. The cross section should be made of an H-profile. Additionally, stiffeners and doubler plates could be used for strengthening to fulfil the strong web panel design.

5.1.3 Main steps of the design procedure

The design procedure of the proposed SF beam-to-column joint for seismic resistance encompasses the following main steps:

- Pre-design. Considering the limited existing rules for SF beams with concrete dowels and for steel and composite members, a selection of trial section dimensions and materials for the structural elements should be performed;
- Elastic design. An elastic calculation should be performed in the dissipative zone with *RFS* and in the "full" section of the SF beam under both hogging and sagging bending to obtain mechanical characteristics;
- Plastic design. A plastic calculation should be performed in the dissipative zone with *RFS* under hogging and sagging bending to obtain the plastic bending resistance and the shear force, assuming a fully yielded and strain hardened plastic hinge;
- Design of bolted end-plate connection. An evaluation of design actions is performed at the interface of the end-plate connection (design maximum bending moment and shear force). Followingly, the resistance of the end-plate connection in bending and in shear should be computed;
- Design of web panel (demand and resistance to shear should be calculated);

- Design of welds;
- Evaluation of joint resistance and stiffness.

5.2 Design and detailing of the joint

5.2.1 Pre-design

Pre-design should be based on the evaluation of the necessary resistance and stiffness of the structural members. This evaluation should be performed with specific loads and combinations for the design situation and should account for the dimensions of the structure (e.g., spans, bays, storey height, number of storeys). The information in Section 5.1.1 and in Section 5.1.2 in terms of material and geometrical requirements (see Fig. 5-78, Fig. 5-79a-d, Fig. 5-80, Fig. 5-81) could be regarded as a design starting point. In the pre-design step, the material for the welded lower SF beam flange could be the same as for the "beam", i.e., ½ of the profile. The thickness of the lower SF beam flange could be the same as the one of the top flange. At the interface of the end-plate, the width of the lower SF beam flange should be limited to the width of the end-plate (see Fig. 5-82a for $b_{fi,red}$). However, to assure a minimum support to the concrete slab, the total width of the lower flange b_{fi} should account for two flange outstands of 50 mm [7] (see Eq. (5.20) and Fig. 5-82b).

$$b_{fi} = b_{fs} + 2 \cdot 50 \; mm \tag{5.20}$$

where:
b_{fi} = total width of the welded lower / inferior SF beam flange.
b_{fs} = width of the top / superior beam flange.

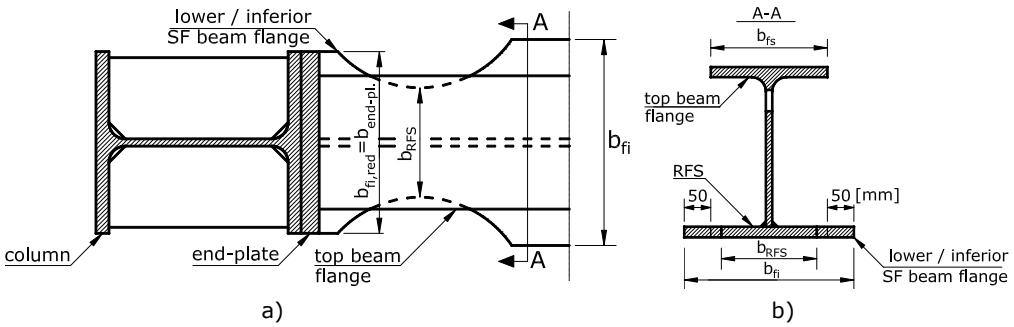

Fig. 5-82. Different widths of the lower SF beam flange: a) width at the interface of the end-plate $b_{fi,red}$; b) flange outstands according to [7]

5.2.2 Dimensioning of the *RFS*

The implementation and the dimensions of the *Reduced Flange Section* (*RFS)* in the lower flange of the SF beam have been proven to be highly influential on the overall behaviour of this SF beam-to-column joint. This has been proven through pre-test FE numerical investigations, through experimental findings and through the results of the numerical parametric study. The "dissipative zone" of the SF beam includes the *RFS*. While the application of the *RFS* is itself a technique targeted at ensuring member ductility, additional measures of enhancing ductility should also be applied (see Fig. 5-78, Fig. 5-80). Thus, it should be checked that the fabrication material provides the required level of ductility, and that the cross section class is 1, in accordance with prEN 1998-1-2 [51]. Details regarding total width and width of the

lower SF beam flange at the interface of the end plate were already provided in Section 5.2.1.

The proposed design provisions of the *RFS* are based on the rules of AISC 358-16 [102] for *Reduced Beam Section* (*RBS*) connections. However, it should be noted that the *RBS* rules of AISC 358-16 [102] were not specifically developed for application to slim-floor beams and that the technique is applied to both beam flanges. Therefore, the proposed rules for the *RFS* imply the following:

- the trimming should be applied only to the lower flange of the SF beam;
- the type of the cut should be radius cut;
- the relevant dimensions of the *RFS* are: (i) the centre of *RFS* ($l_{RFS,cf}$); (ii) the length of *RFS* (l_{RFS}); (iii) the width of *RFS* (b_{RFS}).

The implementation of the proposed provisions has proven high efficiency in developing plastic deformations in the dissipative zone with *RFS* of SF joints. This is attributed to the more "drastic" trimming of the lower SF beam flange. While milder trimmings are efficient *RBS* techniques for flanges of I or H profiles, the lower flange of the SF beam is significantly wider than these. Moreover, downstand configurations imply the concrete slab to be placed on top of the beam. Slim-floors are fully or partially encased in concrete (here, partially encased), thus the downstand and slim-floor configurations are not similar.

Considering the previously mentioned aspects, Eq. (5.21), Eq. (5.22) and Eq. (5.23) are proposed as dimensioning tools for the *RFS*. The centre of the *RFS* ($l_{RFS,cf}$) is established by Eq. (5.21) and measured from the face of the column. The length (l_{RFS}) and the width (b_{RFS}) of the *RFS* are expressed through Eq. (5.22) and Eq. (5.23). All of these dimensions are represented in Fig. 5-83.

$$l_{RFS,cf} = (2/3) \cdot d \tag{5.21}$$

$$l_{RFS} = 0.9 \cdot d \tag{5.22}$$

$$b_{RFS} \leq b_{fs} \tag{5.23}$$

where:
$l_{RFS,cf}$ = centre of the *RFS*.
l_{RFS} = length of the *RFS*.
b_{RFS} = width of the *RFS*.
d = height of the SF beam steel profile, including the bottom flange.
b_{fs} = width of the top / superior beam flange.

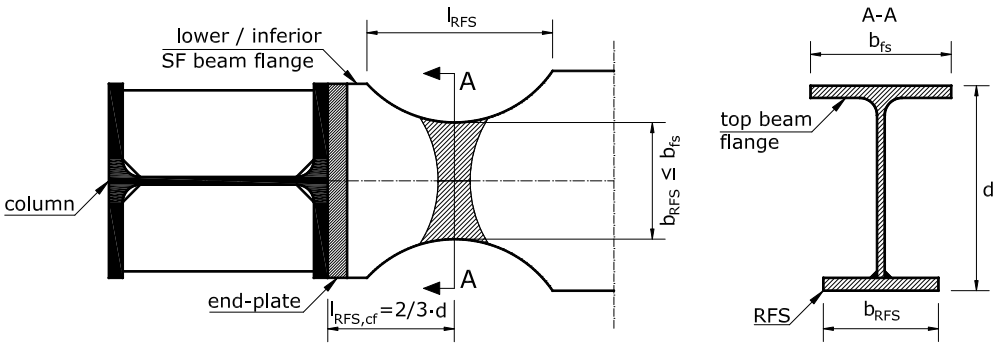

Fig. 5-83. Proposed dimensions of the *RFS* based on AISC 358-16 [102]

It is important to mention that the design of the *RFS* should be the subject of an iterative process. This is motivated by the need of control over the plastic deformations from other components of the SF joint (i.e., end-plate connection, web panel, column flange). The plastic deformations in other components of the SF joint should be reduced as much as possible.

5.2.3 Elastic design

The position of elastic neutral axis (*ENA*) could be determined through an iterative process based on the strip model from Vayas [103]. To calculate the mechanical characteristics of the SF beam, an elastic distribution of stresses should be considered on the height of the cross section. Due to the variable geometry of the SF beam, this should be performed in both the dissipative zone with *RFS* and in the "full" section of the beam. The following components could be disregarded in the elastic design: the area of concrete under tension (hogging and sagging bending); the reinforcement under compression (sagging bending). The calculation shall be performed in distinct situations: dissipative zone with *RFS* under (1) sagging bending / (2) hogging bending; "full" section under (3) sagging bending / (4) hogging bending.

Elastic effective width

The elastic effective width has a decisive role on the portion of compressed concrete and on the number of tensioned longitudinal rebars. According to Table 7.5 I from EN1998-1 [46], the elastic effective width for an interior frame under sagging and hogging bending, is computed as shown in Eq. (5.24) and Eq. (5.25). The values used in these equations are limited to beams where the continuity of the longitudinal reinforcement is ensured [46].

$$b_{eff,elastic,M+} = 2 \cdot b_e = 2 \cdot (0.0375 \cdot L) \tag{5.24}$$

$$b_{eff,elastic,M-} = 2 \cdot b_e = 2 \cdot (0.05 \cdot L) \tag{5.25}$$

where:
$b_{eff,elastic,M+ / M-}$ = elastic effective width in sagging / hogging bending.
b_e = partial effective width for elastic analysis (effective breadth).
L = length of the beam.

Moment of inertia in sagging bending I_1 – in the dissipative zone and in the "full" section

The steel profile's centroid G_a represents the centre of the steel profile, whose position is determined analytically. The centroid of the concrete G_c corresponds to the centre of the compressed concrete section located above the *ENA*, whose position is also determined by analytical means. The centroid of the composite cross section G_m is assumed to be located between G_a and G_c. The coordinates of the centroids G_a and G_c relative to the *ENA* are d_a and d_c. Coordinate z is the distance measured from the *ENA* to an arbitrarily chosen point (in this example, to the lower edge of the top SF beam flange). The area of the steel SF beam A_a can be computed, whereas the concrete area under compression could be expressed through an equation with one unknown factor. Considering these, that unknown geometrical value is the coordinate z. Coordinates d_a and d_c could also be expressed through equations with the same unknown geometrical value z. Sketches of the two cross sections of the SF beam where the elastic design is performed (dissipative zone with *RFS*; "full" section) are

shown in Fig. 5-84a,b. In these figures, the above mentioned terms are illustrated. Given the exemplified positions of the *ENA* (see Fig. 5-84a, Fig. 5-84b), the equation of static moments is expressed by Eq. (5.26). The modular ratio *n* should be computed according to Eq. 5.6, EN 1994-1-1 [17]. As the solution to the equation of static moments is represented by the value of coordinate *z*, all equations containing it are solvable. The moment of inertia in sagging bending of the dissipative zone with *RFS* and of the "full" section of the SF beam can be calculated with Eq. (5.27).

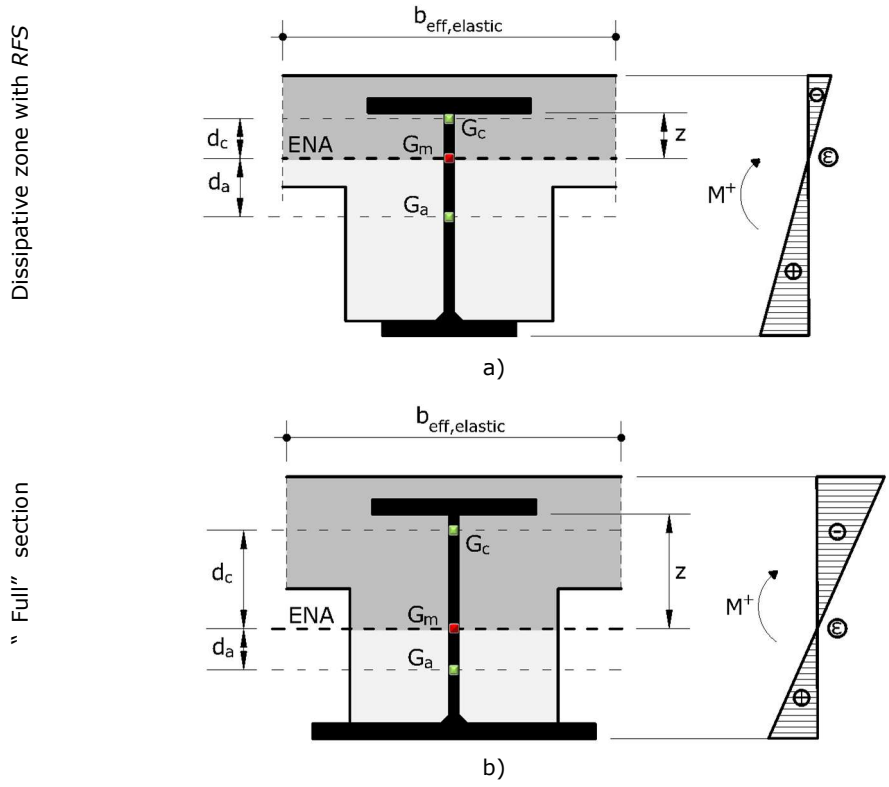

Fig. 5-84. Calculation of I_1 under sagging bending in: a) *RFS*; b) "full" section of the SF beam

$$A_a \cdot d_a = \left(\frac{A_c}{n}\right) \cdot d_c \tag{5.26}$$

$$I_1 = I_a + A_a \cdot d_a^2 + \left(\frac{I_c}{n}\right) + \left(\frac{A_c}{n}\right) \cdot d_c^2 \tag{5.27}$$

where:
A_a = area of a portion of the asymmetric steel profile of the SF beam under tension;
A_c = area of a portion of concrete under compression;
d_a = coordinate of the centroid G_a relative to the position of the *ENA;*
d_c = coordinate of the centroid G_c relative to the position of the *ENA;*
n = modular ratio, calculated according to Eq. 5.6, EN 1994-1-1 [17];
I_a = moment of inertia about the strong axis corresponding to the portion of the asymmetric steel profile of the SF beam under tension;

I_c = moment of inertia about the strong axis corresponding to the concrete portion under compression;
I_1 = moment of inertia about the strong axis under sagging bending.

Moment of inertia in hogging bending I_2 – in the dissipative zone and in the "full" section

The position of the centroid G_a, which corresponds to centre of the steel profile of the SF beam, should be analytically determined. The centroid of the reinforcement G_s is located in the centre of the group of active (tensioned) longitudinal rebars. The position of the concrete's centroid G_c corresponds to the centre of the compressed concrete area located under the *ENA*. The centroid of the composite cross section G_m is assumed to between G_a and G_c. The coordinates of the centroids G_a, G_s and G_c relative to the *ENA* are d_a, d_s, and d_c. Coordinate z represents the distance from the *ENA* to a point chosen arbitrarily - here, the lower edge of the top SF beam flange. The areas of the steel profile A_a and of the rebars A_s can be calculated, while the area of concrete under compression could be written as an equation with one unknown factor (coordinate z). Coordinates d_a, d_s, and d_c could also be expressed through equations with z. Given the sketches from Fig. 5-85a,b with exemplified positions of the *ENA* in the dissipative zone with *RFS* and in the "full" section, the equation of static moments could be expressed through Eq. (5.28), whose solution will result in the value of z. Once z is found, all other geometrical dimensions can be calculated. The moment of inertia in hogging bending (I_2) of the dissipative zone with *RFS* and of the "full" section of the SF beam can be calculated with Eq. (5.29).

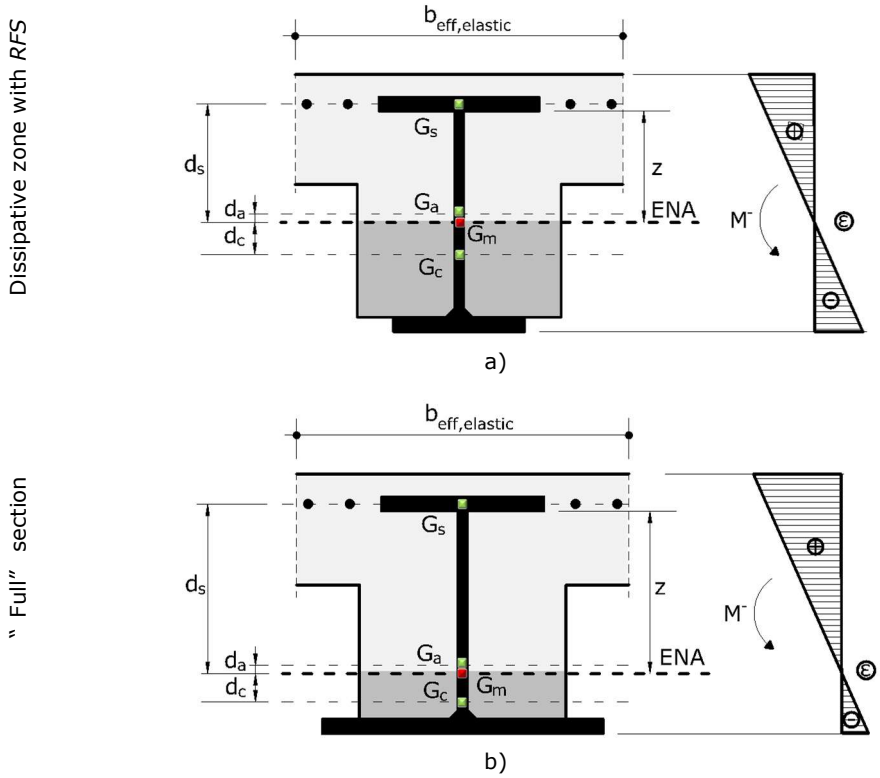

Fig. 5-85. Calculation of I_2 under hogging bending in: a) *RFS*; b) "full" section of the SF beam

$$A_a \cdot d_a + A_s \cdot d_s = \left(\frac{A_c}{n}\right) \cdot d_c \tag{5.28}$$

$$I_2 = I_a + A_a \cdot d_a^2 + \left(\frac{I_c}{n}\right) + \left(\frac{A_c}{n}\right) \cdot d_c^2 + A_s \cdot d_s^2 \tag{5.29}$$

where:
A_s = area of longitudinal rebars under tension;
d_s = coordinate of the centroid G_s relative to the position of the *ENA*;
I_c = moment of inertia about the strong axis corresponding to the longitudinal rebars under tension;
I_2 = moment of inertia about the strong axis under hogging bending.

Equivalent moment of inertia I_{eq} – in the dissipative zone with RFS and in the "full" section

According to the current [46] and pre-normative version [51] of the European seismic design code, the equivalent moment of inertia of a composite beam I_{eq} could be approximated to the value obtained with Eq. (5.30).

$$I_{eq} = 0.6 \cdot I_1 + 0.4 \cdot I_2 \tag{5.30}$$

where:
I_1, I_2= moment of inertia about the strong axis under sagging / hogging bending.

5.2.4 Plastic design

The position of plastic neutral axis (*PNA*) could be determined through an iterative process based on the strip model from Vayas [103]. A plastic distribution of stresses is assumed on the height of the dissipative zone with *RFS*. Plastic design is performed by disregarding the following from the calculation: the tensioned area of concrete under hogging bending and sagging bending, and the compressed longitudinal rebars under sagging bending.

Location of the plastic hinge

The potential location of the plastic hinge is the dissipative zone of the SF beam. More specifically, the development of the plastic hinge is expected to occur in the centre of the *RFS*, which should be measured from the column face and can be established through Eq. (5.21).

Plastic effective width

The value of the plastic effective width of the concrete slab influences the compressed area of concrete under sagging bending and, under hogging bending - the number of tensioned rebars. The plastic effective width of an inner frame in sagging and hogging bending should be calculated in accordance with Table 7.5 II from EN 1998-1 [46], as shown in Eq. (5.24) and Eq. (5.25):

$$b_{eff,plastic,M+} = 2 \cdot b_e = 2 \cdot (0.075 \cdot L) \tag{5.31}$$

$$b_{eff,plastic,,M-} = 2 \cdot b_e = 2 \cdot (0.1 \cdot L) \tag{5.32}$$

where:
$b_{eff,plastic,M+}$= plastic effective width under sagging bending.
$b_{eff,plastic,M-}$= plastic effective width under hogging bending.
b_e = partial effective width for plastic analysis.
L = length of the beam.

Resistance to sagging bending of the dissipative zone with RFS

An example of the position of the *PNA* is shown in Fig. 5-86. According to this sketch, *PNA* is in the top flange of the SF beam. Coordinate *z* represents the distance measured from the *PNA* to an arbitrarily chosen point (here, the upper edge of the top steel SF beam flange). Assuming this position of the *PNA*, the areas of the components located above the *PNA* (e.g., a part of the concrete slab and a part of the top beam flange) are under compression. Oppositely, the area of all components located under the *PNA* (e.g., the remaining part of the top SF beam flange, the web of the steel beam and lower SF beam flange) are under tension. Considering the previously mentioned convention, an equality of sums of tensile and compressive stress resultants should be written (see Eq. (5.33)). The sum of tensile stress resultants (F_t) should be computed with Eq. (5.34). The sum of the compressive stress resultants (F_c) should be calculated with Eq. (5.35). The area of compressed concrete is determined by the value of the plastic effective width. The compressive stress resultant of this compressed area (F_{cc}), along with the resultants F_{at}^{fs} and F_{ac}^{fs}, could be expressed through equations containing the unknown *z*, and incorporated in the egality of sums. The tensile stress resultant from the lower flange of the SF beam and the tensile stress resultant from the web of the SF beam could be calculated with the following expressions: Eq. (5.36) and Eq. (5.37). Once the egality is solved and *z* is calculated, all other geometrical characteristics of the cross section could be found.

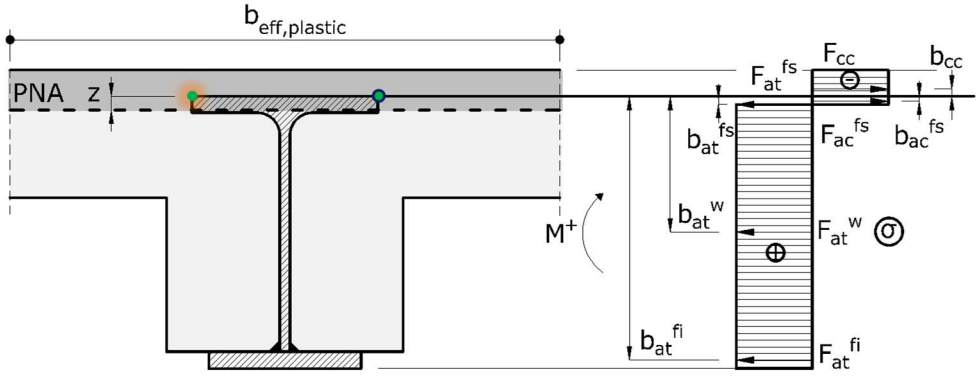

Fig. 5-86. Sketch for plastic sagging resistance calculus of the dissipative zone with *RFS*

$$F_t = F_c \tag{5.33}$$

$$F_t = F_{at}^{fi} + F_{at}^{w} + F_{at}^{fs} \tag{5.34}$$

$$F_c = F_{cc} + F_{ac}^{fs} \tag{5.35}$$

$$F_{at}^{fi} = A_a^{fi} \cdot \left(\frac{f_y}{\gamma_a}\right) \tag{5.36}$$

$$F_{at}^{w} = A_a^{w} \cdot \left(\frac{f_y}{\gamma_a}\right) \tag{5.37}$$

where:
F_{at}^{fi} = tensile stress resultant from the lower SF beam flange.
F_{at}^{w} = tensile stress resultant from the SF beam web.
F_{at}^{fs} = tensile stress resultant from the top SF beam flange under the *PNA*.
F_{cc} = compressive stress resultant from the concrete located above the *PNA*.
F_{ac}^{fs} = compressive stress resultant from the top SF beam flange above the *PNA*.
γ_s = partial safety factor for the reinforcement (γ_s = 1.15).
γ_a = partial safety factor for structural steel equivalent to γ_{M0} (γ_a = 1.0).
γ_c = partial safety factor for the concrete's resistance (γ_c = 1.50).
f_{sk} = yield strength of the reinforcement bars.
f_y = yield strength of the steel SF beam.
f_{ck} = characteristic compressive cylinder strength of concrete at 28 days.
A_a^{fi} = area of the lower / inferior SF beam flange.
A_a^{w} = area of the SF beam web.
A_s = area of the reinforcement bars.
A_a^{fs} = area of the top / superior SF beam flange.

Eq. (5.38) should be used to calculate the plastic resistance of the dissipative zone with *RFS* under sagging bending. The lever arms are relative to the upper edge of the top SF beam flange (see Fig. 5-86), where the bending resistance was calculated, as an example.

$$M_{pl,Rd,RFS} = F_{at}^{fi} \cdot b_{at}^{fi} + F_{at}^{w} \cdot b_{at}^{w} + F_{at}^{fs} \cdot b_{at}^{fs} - F_{cc} \cdot b_{cc} - F_{ac}^{fs} \cdot b_{ac}^{fs} \tag{5.38}$$

where:
b_{at}^{fi} = lever arm measured from the centroid of lower SF beam flange to the compression centre of the cross section.
b_{at}^{w} = lever arm measured from the centroid of SF beam's web to the compression centre of the cross section.
b_{at}^{fs} = lever arm measured from the tensioned area of the top SF beam flange centroid to the compression centre of the cross section.
b_{cc} = lever arm measured from the centroid of the compressed concrete area to the compression centre of the cross section.
b_{ac}^{fs} = lever arm measured from the compressed top SF beam flange centroid to the compression centre of the cross section.

Resistance to hogging bending of the dissipative zone with RFS

An example of the position of the *PNA* is shown in Fig. 5-87, where the *PNA* is on the height of the steel SF beam web. Coordinate *z* represents the distance measured from the *PNA* to an arbitrarily chosen point (here, the lower edge of the top SF beam flange). Given the position of the *PNA*, a general convention is applied:

- areas of components located above the *PNA* are under tension, e.g., rebars, top flange of the SF beam, a part of the steel SF beam's web;

- areas of components located under the *PNA* are under compression, e.g., a part of the concrete surrounding the steel SF beam's web, the remaining part of the SF beam's web, the lower flange of the SF beam.

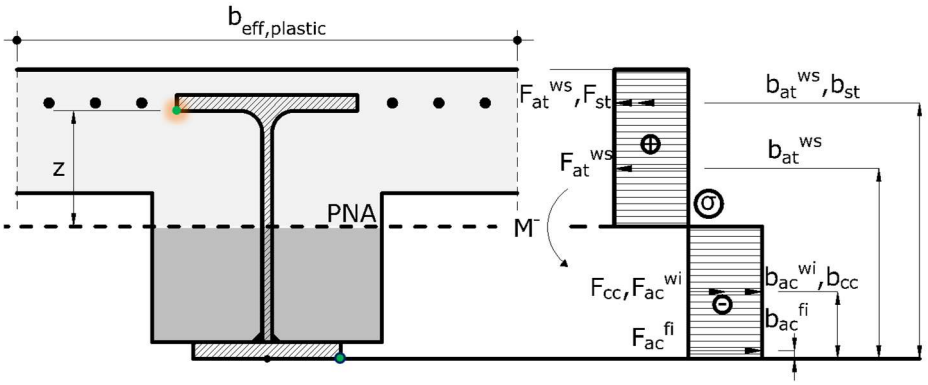

Fig. 5-87. Sketch for plastic hogging resistance calculus of the dissipative zone with *RFS*

Followingly, an equality of sums of tensile and compressive stress resultants should be written (see Eq. (5.33)). The sum of tensile stress resultants (F_t) and the sum of compressive stress resultants (F_c) should be calculated with Eq. (5.39) and Eq. (5.40), respectively. The tensile stress resultants from the rebars and from the top flange of the SF beam could be calculated with Eq. (5.41) and Eq. (5.42), while the compressive stress resultant from the lower flange of the SF beam – with Eq. (5.43). The rest of the resultants, which depend on the position of the *PNA* (i.e., F_{at}^{ws}, F_{ac}^{wi}, F_{cc}), could be expressed through equations containing the unknown z, and included in the equality. Once z is computed, the equations with it become solvable.

$$F_t = F_{st} + F_{at}^{fs} + F_{at}^{ws} \tag{5.39}$$

$$F_c = F_{cc} + F_{ac}^{fi} + F_{ac}^{wi} \tag{5.40}$$

$$F_{st} = A_s \cdot \left(\frac{f_{sk}}{\gamma_s}\right) \tag{5.41}$$

$$F_{at}^{fs} = A_a^{fs} \cdot \left(\frac{f_y}{\gamma_a}\right) \tag{5.42}$$

$$F_{ac}^{fi} = A_a^{fi} \cdot \left(\frac{f_y}{\gamma_a}\right) \tag{5.43}$$

where:
F_{st} = tensile stress resultant from rebars.
F_{at}^{fs} = tensile stress resultant from the top SF beam flange.
F_{ac}^{fi} = compressive stress resultant from the lower SF beam flange.
F_{at}^{ws} = tensile stress resultant from the SF beam flange above the *PNA*.
F_{ac}^{wi} = tensile stress resultant from the SF beam flange under the *PNA*.
F_{cc} = compressive stress resultant from the concrete located under the *PNA*.

γ_s = partial safety factor for the reinforcement bars (γ_s = 1.15).
γ_a = partial safety factor for structural steel equivalent to γ_{M0} (γ_a = 1.0).
γ_c = partial safety factor for the concrete's resistance (γ_c = 1.50).
f_{sk} = yield strength of the rebars.
f_y = yield strength of the steel SF beam.
f_{ck} = characteristic compressive cylinder strength of concrete at 28 days.
A_a^{fi} = area of the lower / inferior SF beam flange.
A_a^{w} = area of the SF beam web.
A_s = area of the reinforcement bars.
A_a^{fs} = area of the top / superior SF beam flange.

The plastic resistance of the dissipative zone with *RFS* under hogging bending should be computed with Eq. (5.44). For exemplification, the lever arms from Fig. 5-87 are relative to the lower edge of the lower SF beam flange.

$$M_{pl,Rd,RFS} = F_{st} \cdot b_{st} + F_{at}^{fs} \cdot b_{at}^{fs} + F_{at}^{ws} \cdot b_{at}^{ws} - F_{cc} \cdot b_{cc} - F_{ac}^{fi} \cdot b_{ac}^{fi} - F_{ac}^{wi} \cdot b_{ac}^{wi} \quad (5.44)$$

where:
b_{st} = lever arm measured from the reinforcement centroid to the compression centre of the cross section.
b_{at}^{fs} = lever arm measured from the top SF beam flange centroid to the compression centre of the cross section.
b_{at}^{ws} = lever arm measured from the tensioned SF beam web centroid to the compression centre of the cross section.
b_{cc} = lever arm measured from the centroid of the compressed concrete area to the compression centre of the cross section.
b_{ac}^{fi} = lever arm measured from the lower SF beam flange centroid to the compression centre of the cross section.
b_{ac}^{wi} = lever arm measured from the compressed SF beam web centroid to the compression centre of the cross section.

Shear demand in the dissipative zone with RFS

The shear demand in the centre of the dissipative zone with *RFS* of the SF beam should be calculated according to the prEN 1998-1-2 [51], as shown in Eq. (5.45), Eq. (5.46) and Eq. (5.47).

$$V_{Ed,RFS} = V_{B,Ed,M} + V_{B,Ed,G} \quad (5.45)$$

$$V_{B,Ed,M} = \left(\frac{2 \cdot M_{Pl,Rd,RFS}}{L_h}\right) \quad (5.46)$$

$$V_{B,Ed,G} = \frac{\left[\left(G_k + \psi_{2,i} \cdot Q_k\right) \cdot L_0\right]}{L_h} \quad (5.47)$$

where:
$V_{Ed,RFS}$ = shear demand in the dissipative zone with *RFS*.
$V_{B,Ed,M}$ = design shear force due to the application of the plastic moments with opposite signs at the end sections of the SF beam.
$V_{B,Ed,G}$ = design shear force to be determined on the basis of the equilibrium of the beam under non-seismic actions.

$M_{pl,Rd,RFS}$ = plastic bending resistance of the dissipative zone with *RFS*.
L_h = distance between the dissipative zones on the length of the span.
G_k = permanent load from a non-seismic design situation.
Q_k = live load from a non-seismic design situation.
$\psi_{2,i}$ = combination factor applied to a variable action, according to [52].
L_0 = length of the beam (axis-to-axis distance between the columns).

5.2.5 Beam-to-column bolted connection

Design bending moment and shear force sustained by the connection

The maximum bending moment and the shear force used for the design of the bolted beam-to-column connection should be computed in accordance with prEN 1998-1-2 [51] as shown in Eq. (5.48) and Eq. (5.49). Additionally, in line with the seismic code [51], the bolted connection, designed as non-dissipative one, should account for overstrength.

$$M_{Ed,conn} = \gamma_{rm} \cdot \gamma_{sh} \cdot \left(M_{Pl,Rd,RBS} + V_{Ed,RFS} \cdot e\right) \tag{5.48}$$

$$V_{Ed,conn} = \gamma_{rm} \cdot \gamma_{sh} \cdot V_{Ed,RFS} \tag{5.49}$$

where:
$M_{Ed,conn}$ = maximum design bending moment for the bolted connection.
γ_{rm} = material overstrength factor [51].
γ_{sh} = strain hardening factor [51].
e = distance from the centre of the dissipative zone to the column face.
$V_{Ed,conn}$ = design shear force for the bolted connection.

Resistance of the bolted connection under bending and shear

According to EN 1993-1-8 [62], the resistance of the beam-to-column connection under sagging bending consists of a sum of resistances given by the bolts under tension. In EN 1993-1-8 [62], the compression centre of bolted end plate connections should be assumed to be in line with the centre of the compression flange of the connected member. In the current study, based on the results of the calibrated numerical model (*RM*), the centre of compression under sagging bending was located 5 mm above the top flange of the SF beam steel profile. Considering the small difference to the value provided by the centre of the compression flange of the connected member (EN 1993-1-8 [62]), it is recommended that the rules of European code be followed. The sagging bending resistance of the beam-to-column connection could be expressed through Eq. (5.50). The resistance under hogging bending is equal to the sum of resistances given by the bolts, as well as by the longitudinal rebars under tension (see Eq. (5.51)). As previously discussed, the position of the centre of compression is established according to [62].

$$M_{Rd,conn,sag} = \Sigma F_{r,b,i} \cdot t_{b,i} \tag{5.50}$$

$$M_{Rd,conn,hog} = \Sigma F_{r,b,i} \cdot t_{b,i} + F_{t,r,i} \cdot t_{r,i} \tag{5.51}$$

where:
$M_{Rd,conn,sag}$ = moment resistance of the connection under sagging bending.
$M_{Rd,conn,hog}$ = moment resistance of the connection under hogging bending.

$F_{t,b,i}$ = resistance of bolt under tension.
$t_{b,i}$ = distance measured from the compression centre of the cross section to the centre of the considered bolt (lever arm).
$F_{t,r,i}$ = resistance of longitudinal rebars under tension.
$t_{r,i}$ = distance measured from the compression centre of the cross section to the centre of the considered reinforcement bar (lever arm).

The design resistance of a bolt row under tension is calculated in accordance with the code [62] and should be taken as the minimum value of the following tension resistances: bolt row in tension ($F_{t,b}$) end plate in bending ($F_{t,ep,Rd}$), column flange in bending ($F_{t,fc,Rd}$), column web in transverse tension($F_{t,wc,Rd}$) and beam web in tension ($F_{t,wb,Rd}$). As the current solution includes a SF beam, the last of the previously mentioned resistances should be replaced with the web of the SF beam.

The shear resistance of the bolted connection per shear plane should be calculated in accordance with EN 1993-1-8 [62], as shown in Eq. (5.52).

$$F_{V,Rd} = \frac{\alpha_v \cdot f_{ub} \cdot A_s}{\gamma_{M2}} \tag{5.52}$$

where:
a_v = factor for property classes 10.9 (a_v =0.5).
f_{ub} = ultimate strength of the bolt.
A_s = area of the bolt corresponding to the shear plane.
γ_{M2} = partial safety factor for the resistance of bolts, rivets, pins, welds and plates in bearing.

5.2.6 Column web panel

The current design procedure is based on and proposed for SF beams connected to bare steel columns. Consequently, the case of composite columns (e.g., partially or fully-encased steel profiles), are not covered by the current study.

Design shear force sustained by web panel

According to Landolfo et al. [50], it would be advisable to avoid plastic deformation in the web panel. The demand (i.e., the resulting shear force) should be calculated with Eq. 5.3 from Section 5.3 of EN 1993-1-8 [62]. For single-sided beam-to-column configurations, the previously mentioned equation transforms into Eq. (5.53), as shown below. To establish the design bending moment for the end-plate connection at the column face, Eq. (5.54) should be used. The design bending moment at the column axis should be computed with Eq. (5.55).

$$V_{wp,Ed} = \left(\frac{M_{Ed,conn,red}}{z}\right) - \left(\frac{M_{Ed,cl,red}}{H_{storey}}\right) \tag{5.53}$$

$$M_{Ed,conn,red} = M_{Pl,Rd,RFS} + V_{Ed,RFS} \cdot e \tag{5.54}$$

$$M_{Ed,cl,red} = M_{Pl,Rd,RFS} + V_{Ed,RFS} \cdot \left[e + \left(\frac{h_c}{2}\right)\right] \tag{5.55}$$

where:

$M_{Ed,conn,red}$ = design bending moment of the bolted connection calculated at column face without considering overstrength (i.e., γ_{rm}, γ_{sh}).
z = lever arm of the internal forces.
$M_{Ed,cl,red}$ = design bending moment calculated in the axis of the column.
H_{storey} = storey height.
h_c = height of cross section of the column.

Resistance of the web panel to shear

The design shear resistance of the unstiffened column web panel should be determined with Eq. (5.56), Eq. (5.57) and Eq. (5.58) according to the code [79]. In accordance with the rules of prEN 1998-1-2, Annex E [51] and prEN 1993-1-8 [79] for the detailing of the web panel, the design shear resistance could be increased by the addition of stiffeners and / or supplementary web plates. When transverse web stiffeners in both the tensioned and compressed zones are used, the design shear resistance $V_{wp,Rd}$ could be increased, as shown in Eq. (5.59) for $V_{wp,add,RD}$. However, as recommended in Landolfo et al. [50], it would be advisable to avoid plastic deformation in the web panel. According to [50], this can be achieved by considering only the contribution of the design plastic shear resistance of the unstiffened column web panel $V_{wc,Rd}$ when verifying the web panel shear strength. In case supplementary web plates are used, then the shear area A_{vc} may be increased (see Eq. (5.60) for A_{vp}).

The dimensioning of the supplementary web plates and of the stiffeners should follow the provisions of prEN 1998-1-2 [51] and of prEN 1993-1-8 [79] in terms of depth, width, thickness, position and material.

$$V_{wp,Rd} = \left(\frac{0.9 \cdot f_{y,wc} \cdot A_{vc}}{\sqrt{3} \cdot \gamma_{M0}}\right) \tag{5.56}$$

$$A_{vc} = A - 2 \cdot b \cdot t_f + (t_w + 2 \cdot r) \cdot t_f \tag{5.57}$$

$$A_{vc} \geq \eta \cdot h_w \cdot t_w \tag{5.58}$$

$$V_{wp,add,Rd} = \left(\frac{b_{fc} \cdot t_{fc}^2 \cdot f_{y,fc}}{d_s \cdot \gamma_{M0}}\right) \tag{5.59}$$

$$A_{vp} = b_s \cdot t_s \tag{5.60}$$

where:
$f_{y,wc}$ = yield strength of the web panel.
A_{vc} = shear area of the column.
γ_{M0} = partial safety factor for structural steel applied to resistance of cross sections.
A = cross section area of the column.
b = overall width.
t_f = thickness of the column flange.
t_w = thickness of the column web.
r = root radius.
η = factor for shear area (η = 1.0, according to [104]).
h_w = depth of the column web, measured between the flanges.
b_{fc} = column flange width.

t_{fc} = column flange thickness.
$f_{y,fc}$ = yield strength of the column flange.
d_s = distance measured between the centrelines of the stiffeners.
A_{vp} = gross area of the additional web plates.
b_s = width of the supplementary web plate.
t_s = thickness of the supplementary web plate.

5.2.7 Welds

Considering the fact that the SF beam-to-column joint is designed for seismic resistance, the welds should follow the rules of prEN 1998-1-2, Annex E [51]:

- the lower flange of the SF beam should be connected to the web of the remaining profile through double fillet welds of $0.8 \cdot t_{min}$ thickness;
- the welding of the SF beam flanges to the end-plate (critical weld) should be performed with full penetration groove welds and with reinforcing fillet welds;
- the welding of the SF beam web to the end-plate should be performed with double fillet welds of $0.8 \cdot t_{min}$ thickness; however, these fillet welds should be thinner than 8 mm or the thickness of the SF beam web;
- the welding of the doubler plates to the column web should be performed with groove or longitudinal fillet welds;
- the welding of the stiffeners (critical weld) to the flanges of the column should be performed with full penetration groove welds;
- the welding of the stiffeners to the doubler plates should be performed with fillet welds of $0.8 \cdot t_{min}$ thickness.

All of the previously mentioned welds should fulfil the checks. A detailing example of SF beam-to-column joints concerning the welds, which satisfies the provisions of European codes, is shown in Fig. 5-88.

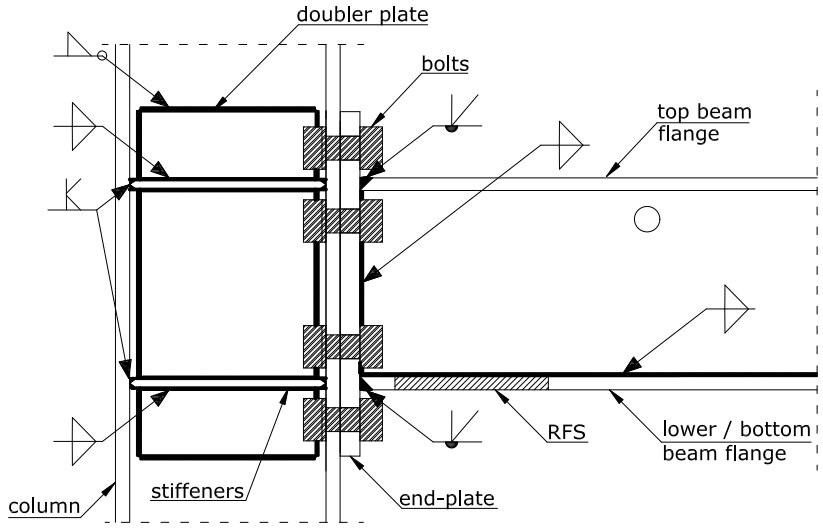

Fig. 5-88. Detailing of the welds for the SF beam-to-column joint

5.2.8 Stiffness of the joint

The calculation of the joint's stiffness should be performed in accordance with the requirements of EN 1993-1-8 [62] and EN 1994-1-1 [17]. Rules of good practice in seismic design of joints are also provided in Landolfo et al. [50]. As the SF beam-

to-column joint is designed for seismic resistance, it is necessary for the calculation to be performed in both hogging and sagging bending.

In accordance with the code [62], the stiffness of the SF joint could be calculated with Eq. (5.61). The stiffness coefficients that are considered in the calculation are k_1, k_2 and k_{eq} and can be found in Table 6.10 of EN 1993-1-8 [62]. These coefficients are appropriate for a unilateral joint configuration with more than one tensioned bolt rows. Followingly, Eq. (5.61) was adapted to the particularities of the SF joint and rewritten as Eq. (5.62). Considering that more than one bolt row is in tension, the components corresponding to the tensioned bolt rows are represented through an equivalent lever arm z_{eq} and an equivalent stiffness coefficient $k_{eq.}$ These are calculated with Eq. (5.63) and Eq. (5.64), respectively, in accordance with [62]. In the assessment of the equivalent lever arm and of the equivalent stiffness, an effective stiffness coefficient should be computed for each bolt row in tension ($k_{eff,r}$). The effective stiffness coefficient for a tensioned bolt row includes the specific components of the joint that should be accounted for (see Eq. (5.65)); the components are found in Table 6.11 from the code [62].

The web panel component in shear is represented by the stiffness coefficient k_1 (see Eq. (5.66)), and should be calculated when the web panel is unstiffened. The stiffness coefficient k_2 represents the column web in compression and is necessary to be evaluated when this component is unstiffened (see Eq. (5.67)). According to EN 1994 part 1-1 [17], when the reinforcement is under tension, the stiffness coefficient $k_{s,r}$ should also be considered as shown in Eq. (5.68).

$$S_j = \frac{E \cdot z^2}{\mu \cdot \Sigma \frac{1}{k_i}} \tag{5.61}$$

$$S_{j,ini} = \frac{E \cdot z_{eq}^2}{\frac{1}{k_1} + \frac{1}{k_2} + \frac{1}{k_{eq}}} \tag{5.62}$$

$$z_{eq} = \frac{\Sigma k_{eff,r} \cdot h_r^2 + k_{s,r} \cdot h_{s,r}^2}{\Sigma k_{eff,r} \cdot h_r \ + k_{s,r} \cdot h_{s,r}} \tag{5.63}$$

$$k_{eq} = \frac{\Sigma k_{eff,r} \cdot h_r \ + k_{s,r} \cdot h_{s,r}}{z_{eq}} \tag{5.64}$$

$$k_{eff,r} = \frac{1}{\Sigma \frac{1}{k_{i,r}}} \tag{5.65}$$

$$k_1 = \frac{0{,}38 \cdot A_{vc}}{\beta \cdot z} \tag{5.66}$$

$$k_2 = \frac{0{,}7 \cdot b_{eff,c,wc} \cdot t_{wc}}{d_c} \tag{5.67}$$

$$k_{s,r} = \frac{A_{s,r}}{3{,}6 \cdot h} \tag{5.68}$$

where:
S_j = secant rotational stiffness of a joint.
E = modulus of elasticity.
z = lever arm (see Fig. 6.15 in EN 1993 part 1-8 [62]).
μ = stiffness ratio.
k_i = stiffness coefficient of component i of the joint.
$S_{j,ini}$ = initial rotational stiffness of a joint calculated with $\mu = 1$
z_{eq} = equivalent lever arm.
k_1 = stiffness coefficient of the column web panel in shear.
k_2 = stiffness coefficient of the column web in compression.
k_{eq} = equivalent stiffness coefficient that represents the main components of the tensioned bolt rows.
$k_{eff,r}$ = effective stiffness coefficient for bolt row r that takes into consideration the stiffness coefficients k_i of the main components.
h_r = distance measured from bolt row r to the centre of the compressed zone.
$k_{s,r}$ = stiffness coefficient of the tensioned longitudinal rebars according to [17].
$h_{s,r}$ = distance measured from the centre of the longitudinal rebars to the centre of the compressed zone.
$k_{i,r}$ = stiffness coefficient for component i relative to bolt row r.
A_{vc} = shear area of the column according to [104].
β = transformation factor.
$b_{eff,c,wc}$ = effective width of the column web in compression according to [62].
t_{wc} = thickness of the column web.
d_c = length of the column web.
$A_{s,r}$ = cross sectional area of the longitudinal rebars in row r within the effective width of the concrete flange.
h = depth of column steel section.

The obtained stiffness value should be compared to the limits that are provided in EN 1993-1-8 [62]. According to the classification in the European code [62], a joint is rigid when equation Eq. (5.69) is satisfied. If the value of the stiffness corresponding to the SF beam-to-column joint is found between the rigid and nominally pinned limits, then the joint should be classified as semi-rigid. According to Landolfo et al. [50], beam-to-column joints of Moment-Resisting Frames should be designed as rigid or semi-rigid.

$$S_{j,ini} \geq \frac{k_b \cdot E \cdot I_b}{L_b} \tag{5.69}$$

where:
k_b = 8 for braced frames and 25 for unbraced frames.
I_b = moment of inertia about the strong axis of the beam.
L_b = length of the beam measured from one column axis to the next.

5.2.9 Resistance of the joint

The calculation of resistance and the classification of joints based on their resistance are provided in Eurocode EN 1993-1-8 [62]. Regardless of the position of the joint in the frame, e.g. joint within column height or joint at the top of the column,

the resistance of full-strength joints should be higher than that of the connected member. Although the use of partial-strength joints in the seismic design of Moment-Resisting Frames is allowed by EN 1998-1 [46], provided that they ensure a ductile hysteretic response under cyclic loads, only full-strength joints are considered in the current study. The use of full-strength joints in Moment-Resisting Frames is also recommended by Landolfo et al. [50].

5.3 Concluding remarks

Applications of slim-floor beam-to-column joints (SF joints) are not covered by the codes, although due to the increasing interest and push in the direction of efficiency and sustainability, this might soon change. Therefore, provisions for slim-floor systems are needed. The current design procedure is based on new rules and on existing design provisions for steel and steel-concrete composite structural members, that were proposed to be extended to SF beam-to-column joints. The design procedure that is proposed within this study is addressed to SF beam-to-column joints of seismic-resistant structures developed to meet Ductility Class 3 (DC3) criteria. Considering the resistance and stiffness classifications of EN 1993-1-8 [62], the beam-to-column joints of Moment-Resisting Frames should be classified as **full-strength** and **rigid or semi-rigid**, according to Landolfo et al. [50]. To obtain an adequate response of the SF joint, several strategies were employed:

- ensuring the ductility of the main fuse (dissipative zone of steel SF beam);
- ensuring the overstrength of the end-plate connection of the web panel;
- ensuring the overstrength of the welds;
- ensuring the overstrength of the adjacent member (column).

The slim-floor beam should be obtained from half of a steel I-profile [7]. A wide steel plate should be welded on the remaining half of the steel profile, forming an asymmetric steel SF beam. **Ductility at member level is obtained through the application of the *RFS*.** As the SF beam is the main component to dissipate seismic energy, the following rules and techniques were proposed for application in the design procedure to ensure the ductility of the SF beam:

- material requirements of the current and of the pre-normative versions of the Eurocodes (i.e., [104] [54] [51]) for dissipative steel-concrete composite and steel structural elements (see Fig. 5-78);
- material requirements of the National Technical Approval (*Z-26.4-59*) for *CoSFB* according to [19];
- rules for the section class for composite shallow flooring systems of the pre-normative version of Eurocode 4 [55] (see Fig. 5-80);
- application of *RFS* to the lower flange of the SF beam.

Consequently, the steel grade of the SF beam profile should be in the range of S355÷S420 [19], and the material should ensure minimum ductility, i.e., $f_u / f_y \geq 1.10$, elongation higher than 15%, in accordance with [104] [54]. According to the pre-normative version of Eurocode 4 [55], the cross section class of the SF beam should be 1. The ***RFS* should be applied to the lower flange of the SF** beam and the type of the trimming should be radius cut. The proposed dimensioning tools of the *RFS* were based on AISC 358-16 [102] for *Reduced Beam Section* (*RBS*) connections. However, due to the larger width of the lower beam flange and to the partial concrete encasement of the steel SF beam– both of which set apart the slim-floor systems from downstand configurations – the dimensions of the *RFS* were adapted to particularities of shallow flooring systems.

The **bolted end-plate connection should be kept within the elastic range**. Thus, the bolted beam-to-column connection should be designed to develop higher resistance than the dissipative zone with *RFS* of the SF beam under both hogging and sagging bending. To achieve this, it was proposed that the type of the end-plate connection should be extended above and below the flanges of the SF beam. Moreover, high strength bolts are recommended. The verification of the bolted connection should be performed in accordance with prEN 1998-1-2 [51] and EN 1993-1-8 [62] including the effects of the material overstrength and of the strain hardening factor. The bending moment and the shear demand for the bolted connection should be calculated considering internal forces from the dissipative zone with *RFS* projected to the column face and multiplied by the strain hardening and the material overstrength factors. The **welds adjoining the bolted beam-to-column connection** should be designed to develop **higher resistance than the dissipative zone** of the SF beam. In accordance with the code [51], the following should be respected:

- critical welds should be performed with full penetration groove welds and reinforcing fillet welds; the following welds should be considered critical:
  - welds between the SF beam flanges and the end-plate;
  - welds between the stiffeners and the column flange;
- fillet welds should have a minimum thickness of $0.8 \cdot t_{min}$, where t_{min} is the minimum thickness of the welded components.

The column should be fabricated either in a steel or in a steel-concrete composite solution from an H-profile. Stiffeners and supplementary web plates could be used for the strengthening of the web panel in accordance with prEN 1998-1-2 [51] and prEN 1993-1-8 [79]. The shear resistance $V_{wp,Rd}$ of the web panel should be taken as the elastic shear resistance of the web panel without a surplus of resistance provided by continuity plates, in accordance with [46] [50].

The methodology used to obtain the steel profile of the SF beam is described in the relevant brochure of ArcelorMittal for slim-floors [7]. Apart from the National Technical Approval for *CoSFB* [19], in which a material range and a web thickness are provided, only the pre-normative version of the Eurocode 4 [55] contains additional information on the steel profile of the SF beam (i.e., cross section class). The current design procedure promotes the application of certain existing code rules for steel and steel-concrete composite elements designed as dissipative structural elements, as well as the rules from the National Technical Approval for *CoSFB* [19]. In addition to these, the use of a *Reduced Flange Section* (*RFS*) was introduced in the current design procedure together with the corresponding dimensions. Essentially, the objective of the proposed design procedure is to obtain an adequate seismic performance of the SF beam-to-column joint (i.e., full-strength and rigid or semi-rigid joints, joint rotation at SD of ± 40 mrad, ductile failure mechanism). As proved by experimental and numerical means, adequate seismic performance can be achieved as long as the plastic hinge development occurs in the SF beam. However, plastic hinge development in the SF beam is only possible if the beam is a ductile structural element, whereas the end-plate connection, the welds and the web panel have sufficient overstrength compared to the dissipative zone with *RFS*.

6. STRUCTURAL ANALYSES

In Chapter 6, mid- and high-rise structures consisting of different lateral load-resisting systems, e.g., Moment-Resisting Frame, Concentrically-Braced Frame, Dual Concentrically-Braced Frame, in which SF beam-to-column joints were integrated, were subjected to structural analyses in individual case studies. The aim of structural analyses was (i) to verify the rotation demand resulted from the seismic action for the SF beam-to-column joint, (ii) to compare it to the experimental rotation capacity and (iii) to assess the seismic performance of structures with SF beam-to-column joints. In accordance with the aim, the following objectives were set:

- to develop a structural model for the tested SF beam-to-column joint;
- to apply nonlinear static and dynamic analyses, e.g., *Pushover*, *Response-History Analysis* to MRF, CBF and D-CBF with SF beam-to-column joints;
- to monitor the sustained damage at the three Limit States, especially at Damage Limitation and Significant Damage, in terms of interstorey drifts and plastic rotations within the dissipative zone of SF beams.

6.1 Moment-Resisting Frame

6.1.1 Design considerations

The current seismic design methodology of steel and steel-concrete composite frame systems relies on the lateral stiffness of frames and on the ductility of specific structural members (or connections) to develop failure mechanisms through which seismic energy is dissipated. According to the current and pre-normative versions of the European seismic code [46] [51], seismic energy dissipation in Moment-Resisting Frames (MRFs) designed for DC3 is realised through the development of ductile mechanisms within beam ends. Other potential plastic hinge zones are located at the base of the columns from the first storey. To apply the strong column – weak beam concept, the ends of SF beams should possess adequate ductility. To this end, the SF beams should be designed as dissipative structural elements. In this view, the beam-to-column connections and the columns should be designed with overstrength and treated as non-dissipative connections and structural elements.

Case studies, analysed frames, initial data

Two planar MRFs were designed and analysed with SAP2000 v21 [105]:

- ***MRF-SF*** (Moment-Resisting Frame with SF beam-to-column joints):
  - SF beams were connected to steel columns;
  - ends of SF beams contained composite dissipative zones;
  - beam-to-column connections were composite;
- ***MRF-RF*** (Moment-Resisting Frame with regular beam-to-column joints):
  - composite beams with partial shear interaction were connected to steel columns;
  - end of beams contained bare steel dissipative zones;
  - beam-to-column connections were bare steel.

A summary of the main input data is presented in Table 6-8, which underlines that the only difference between the two analysed frames was the flooring system.

Table 6-8 – Input data for the analysed MRFs

Characteristics:	*MRF-SF*	*MRF-RF*
No. of spans & span length:	3 x 6.0 m	3 x 6.0 m
No. of storeys & storey height:	4 x 3.2 m	4 x 3.2 m
Flooring system:	Slim-floor system	Downstand beam
Steel grade:	S355	S355
Ductility Class:	DC3	DC3
Behaviour factor:	q = 6.5	q = 6.5
Consequence Class:	CC2 (normal)	CC2 (normal)
Ground conditions:		
Site category:	Type C	Type C
Peak Ground Acceleration:	a_g = 0.30·g	a_g = 0.30·g

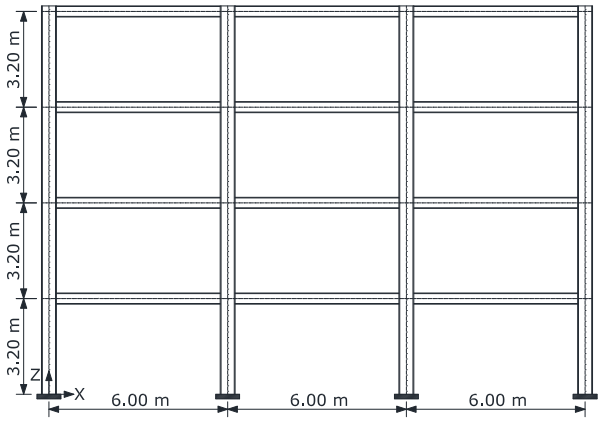

a)

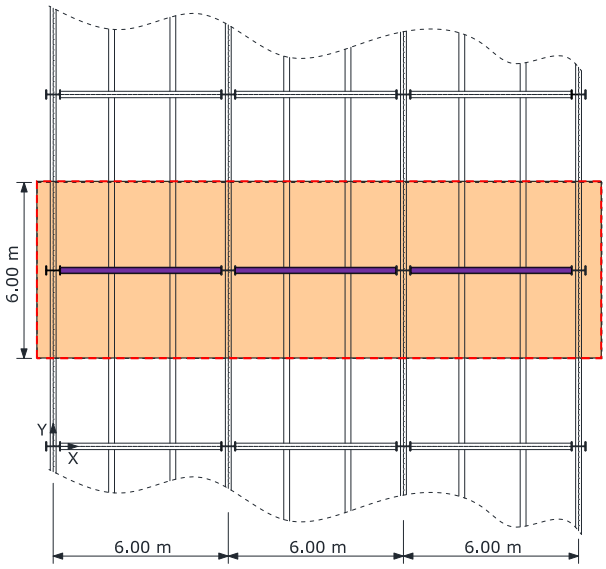

b)

Fig. 6-89. Configuration of the *MRF-SF* and of the *MRF-RF*: a) frame; b) floor layout

MRF-RF was designed as reference for comparison. For a direct comparison of the results, common configuration and dimensions were considered for the frame of *MRF-SF* and of *MRF-RF*. Consequently, a 2D frame with 3 spans of 6 meters and 4 storeys of 3.2 meters was adopted for *MRF-SF* and *MRF-RF* (see Fig. 6-89a). According to the floor plan shown in Fig. 6-89b, the MRFs were placed in the transverse direction (X axis). The longitudinal direction (Y axis) was considered only for the distribution of loads and seismic masses. The category of building was office quarters.

Modelling of the MRF-SF

The structural modelling of the *MRF-SF* was performed as realistic as possible, considering the dimensions, geometry, material and behaviour of structural members as the those of the tested joint specimens.

SF beams with the **same cross section and material** as those of the specimens were modelled. The **geometry respected the dimensions of the SF beams** of the tested joint assemblies. The cross section of the SF beam was variable on the length of the element and contained the dissipative zone with *Reduced Flange Section* (*RFS*), as well as the "full" section (see Fig. 5-82a,b). Regarding the steel component, the asymmetric steel profile of the SF beams was ½ IPE-600 with a welded lower flange (b x t: 380 x 20 mm). As for the reinforced concrete component, this was introduced into the model of the SF beam through an **equivalent moment of inertia I_{eq}** which was calculated considering the variable geometry of the beam.

The SF beam's stiffness and resistance were determined through elastic and plastic calculations of the cross section in the dissipative zone with *RFS* and in the "full" section of the SF beam. Results of these calculations are centralised in Table 6-9. In the elastic range, the mechanical characteristics of the SF beam were defined through the introduction of an equivalent moment of inertia I_{eq}. This equivalent moment of inertia I_{eq} was calculated in the dissipative zone with *RFS* and in the "full" section under sagging and hogging bending, and introduced into the structural analysis software. **Definition of nonlinear response** of the dissipative zone of the SF beam was based on processed experimental data, which is discussed later.

Table 6-9 – Mechanical characteristics of the SF beam and regular beam

Beam	Cross section	Elastic effective width [M⁺ / M⁻] $b_{eff,elastic}$ [mm]	Moment of inertia [M⁺] I_1 [mm⁴]	Moment of inertia [M⁻] I_2 [mm⁴]	Equivalent moment of inertia I_{eq} [mm⁴]
SF beam	"Full" section	450 / 600	4.388×10^8	3.139×10^8	3.888×10^8
	RFS	450 / 600	2.991×10^8	2.514×10^8	2.800×10^8
IPE-450	Dissipative zone (steel)	-	3.374×10^8	3.374×10^8	-

The beam-to-column connection was also modelled realistic. Thus, the modelling was performed by creating a **linear elastic link**, to which the following were assigned: the elastic stiffness of the connection (characterising: bolts, end-plate, column flange) and force-deformation definitions through a *M-θ* curve. Therefore, the elastic stiffness of the beam-to-column connection was included in the analyses.

The columns were bare steel. The panel zone was modelled with a **rotational spring** taking into consideration the stiffness of the web panel and of two supplementary web plates. The strengthening of the web panel was in accordance with the tests, as supplementary plates were part of the joints. End-length offsets were defined with the according lengths and rigidity zone factors. The modelling of the SF beam-to-column joint is illustrated in Fig. 6-90.

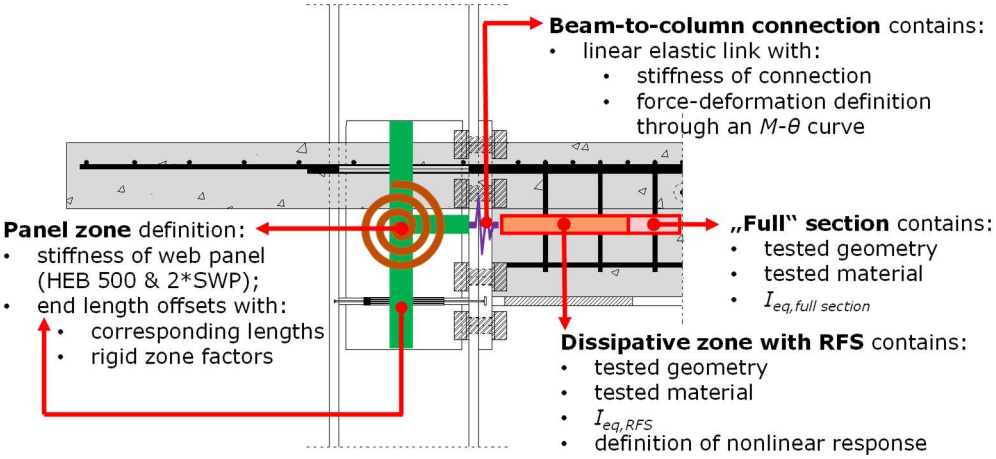

Fig. 6-90. Illustration of the SF beam-to-column joint modelling of the *MRF-SF*

Modelling of the MRF-RF

In the case of *MRF-RF*, regular composite beams with partial shear interaction were rigidly connected to steel columns through steel beam-to-column connections. For the modelling of the beams of *MRF-RF*, the necessary definitions of the regular I-steel cross sections were available in the library database of the software [105] (see Table 6-9). Definition of nonlinear response of the beam ends was also performed.

The concrete slab was regarded as disconnected around the columns from the steel beams on a circular zone in accordance with prEN 1998-1-2 [51]. This was performed in order to be able to disregard the composite action of the beams in *MRF-RF*. However, the presence of the concrete slab in the *MRF-RF* had a lateral-torsional restraining effect and a rigid diaphragm effect on the frame models. These effects were accounted for. The verification of the frames was performed with the design rules and recommendations of the European seismic code prEN 1998-1-2 [51].

Boundary conditions and loads

Regarding the supports - the base of the columns was fixed, and a rigid diaphragm constraint was assigned to each storey level to account for the presence of the concrete slab in *MRF-RF* and of the concrete component, as part of the slim-floor solution, in *MRF-SF*.

The following loads were applied to the two subject frames:

- permanent load uniformly distributed on floors: 5 kN/m^2;
- live load uniformly distributed on floors: 3.8 kN/m^2;
- seismic load: response spectrum characterised by a_g = 0.30·g, soil type soil C, T_B = 0.1 s, T_C = 0.667 s, T_D = 3.94 s in accordance with [45].

The seismic masses for both *MRF-SF* and *MRF-RF* corresponded to one bay of 6.0 m, as shown in Fig. 6-89b. According to the prEN 1998-1-2 [51], the upper limit value of the behaviour factor for MRFs designed in DC3 is 6.5. This value q is restricted by regularity criteria in elevation, which were fulfilled by both of the analysed frames.

Equivalent elastic design

By applying capacity design [51], a distinction between dissipative structural elements (e.g., SF beams, regular beams) and non-dissipative ones (e.g., columns)

should be made. For this, different design load combinations were considered for gravity and seismic situations. The verification of the non-dissipative structural elements was performed with a load combination which included the seismic action magnification factor Ω. The purpose of the seismic magnification factor Ω was to ensure the necessary overstrength of the non-dissipative structural elements in comparison to the dissipative ones. Ω was obtained by multiplying Ω_d (calculated with Eq. (6.70)) by the strain hardening factor (γ_{sh} = 1.2) and the material factor (γ_{rm} = 1.25), as provided in the code [51] and given in Eq. (6.71). The value of Ω was 4.6 in the case of the *MRF-SF*, and 2.4 in that of the *MRF-RF*.

$$\Omega_d = min\left(M_{b,pl,Rd} - M_{Ed,G}\right)/M_{Ed,E} \tag{6.70}$$

$$\Omega = \Omega_d \cdot \gamma_{sh} \cdot \gamma_{rm} \tag{6.71}$$

In accordance with [51], the interstorey drift sensitivity coefficient should be evaluated at each storey. As the value of the coefficient was under 0.1, the analysed frames were not susceptible to 2nd order effects. A side-to-side comparison of the results obtained by applying equivalent elastic analyses on the *MRF-SF* and *MRF-RF* is presented Table 6-10. As underlined by the initial results, the *MRF-SF* and *MRF-RF* have similar fundamental periods and displacements at Damage Limitation and Significant Damage. In addition, the design criterion for both the *MRF-SF* and the *MRF-RF* was the limitation of the lateral deformations. Thus, the cross sections that are presented in Table 6-10 are the result of design governed by deformation control.

Table 6-10 – Results of equivalent elastic analysis

MRF-SF		*MRF-RF*
Structural elements (storey 1 ÷ 4), S355:		
Beams:	SF beams (dissipative zone: section class 1)	IPE-450 (section class 1)
Columns:	HEB-500 (section class 1)	HEB-500 (section class 1)
Displacement checks in the seismic design situation and fundamental periods:		
▪ DL displacement check: $d_{r,max,DL}$ = 0.0073 < 0.0075 => OK		▪ DL displacement check: $d_{r,max,DL}$ = 0.0071 < 0.0075 => OK
▪ SD displacement check: $d_{r,max,SD}$ = 0.014 < 0.020 => OK		▪ SD displacement check: $d_{r,max,SD}$ = 0.015 < 0.020 => OK
▪ Fundamental period: $T_{1,MRF\text{-}SF}$ = 0.672 s		▪ Fundamental period: $T_{1,MRF\text{-}RF}$ = 0.656 s

6.1.2 Evaluation of seismic performance

Definition of nonlinear behaviour

The behaviour of the SF beam in the nonlinear range was defined by a backbone curve, which was obtained as the envelope of the experimental cyclic curve (see Fig. 3-39b). Most important considerations and definitions used to characterise the behaviour of the SF beams in the nonlinear range were as follows:

- the cyclic moment-rotation curve was calculated at the centre of the idealised plastic region of the beam (i.e., dissipative zone with *RFS*):
  - the bending moment was calculated at the centre of the dissipative zone of the SF beam, and included the reinforced concrete slab;
  - the rotation was calculated at column centreline and included rotations corresponding to the following components: elastic rotation of the beam and column parts located outside the joint area, the dissipative zone of

the SF beam, the beam-to-column connection and the column web panel;

- envelope curves were constructed in hogging and sagging bending by selecting the first cycle of each amplitude (e.g., ± 0, ± 3.75, ± 5, ± 7.5, ± 10, ± 15, ± 20, ± 30, ± 40, ± 50 and ± 60 mrad) with the corresponding rotation at column centreline and the bending moment at the dissipative zone; rules of FEMA P-795 [47] were followed;
- the envelope curve was selected conservatively, i.e., being the most unfavourable of the hogging and sagging curves (here, the envelope curve was obtained in hogging bending); the envelope curve was divided into elastic and plastic parts; the latter was used to determine the nonlinear parameters of the plastic hinge;
- the strain hardening factor was calculated according to [50] (γ_{sh} = 1.2);
- the plastic bending resistance of SF beam M_{pl} = 612 kNm was obtained by dividing the maximum bending moment of the envelope curve by the strain hardening factor;
- the yield rotation of the SF beam θ_{pl} was calculated according to Landolfo et al. [50]:

$$\theta_{pl} = \frac{M_{pl} \cdot L_b}{6 \cdot E \cdot I_b} \tag{6.72}$$

where:
M_{pl} = plastic bending resistance of the beam.
L_b = length of the beam.
$I_b = I_{eq}$ (here) = equivalent moment of inertia of the SF beam.

- the response parameters and the acceptance criteria for the SF beam were calculated and adapted based on response parameters and acceptance criteria for I-profile beams from Landolfo et al. [50]. The data from [50] is centralised in Table 6-11.

Table 6-11 – Response parameters, acceptance criteria for beams and columns [50]

	Response parameters			Acceptance criteria		
	a	b	c	DL	SD	NC
Regular beam	$9 \cdot \theta_y$	$11 \cdot \theta_y$	$0.6 \cdot M_{pl}$	$1 \cdot \theta_y$	$6 \cdot \theta_y$	$8 \cdot \theta_y$

Based on the envelope curve, response parameters and acceptance criteria calculated for the SF beam (see Table 6-12 and Fig. 6-91) were introduced into the plastic hinge model for structural members subjected to flexure, i.e., the SF beams.

Table 6-12 – Response parameters and acceptance criteria for SF beams

Plastic hinge properties		
Point	M / M_{pl}	θ / θ_{pl}
A	0	0
B	1	0
C	1.2	4.75
D	0.6	4.75
E	0.6	5.8

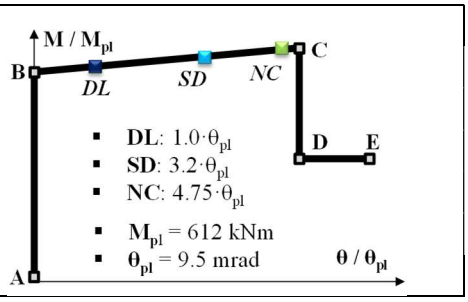

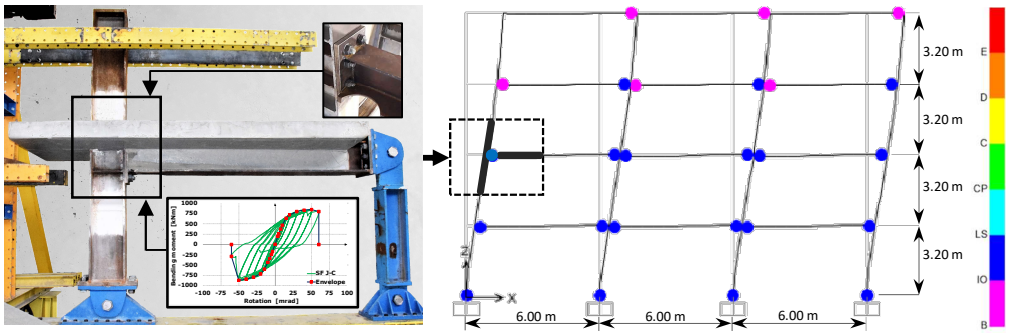

Fig. 6-91. Illustration of the nonlinear behaviour definition of the SF beam

The nonlinear behaviour of the columns in *MRF-SF* was defined by a plastic hinge for members subjected to combined axial loading and flexure. In accordance with EN 1998-3 [106], the following acceptance criteria were imposed: at Damage Limitation DL: $1 \cdot \theta_y$; at Significant Damage SD: $6 \cdot \theta_y$; at Near Collapse NC: $8 \cdot \theta_y$. Following this, the reliability of the SF joint model was verified by performing *Pushover* on a separate SF beam-to-column joint assembly. An illustration containing the SF beam-to-column joint modelling and the static scheme are shown in Fig. 6-92.

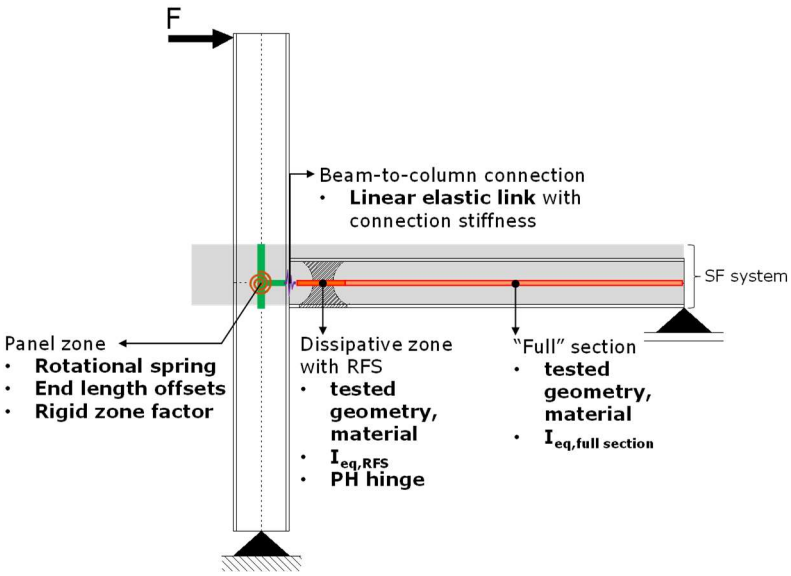

Fig. 6-92. Modelling of SF beam-to-column joint and static scheme

Following the *Pushover* analysis, a capacity curve was obtained. This curve was transformed into a moment-rotation curve calculated at column centreline and then compared to the experimental cyclic curve. As the comparison in Fig. 6-93 proves, the curve corresponding to the SF joint model was similar to the cyclic curve. Thus, a good correspondence between the two curves in terms of initial stiffness, maximum bending resistance and ultimate rotation was confirmed. Following this result, the nonlinear definitions used for the SF joint model were considered truthful, and the model reliable.

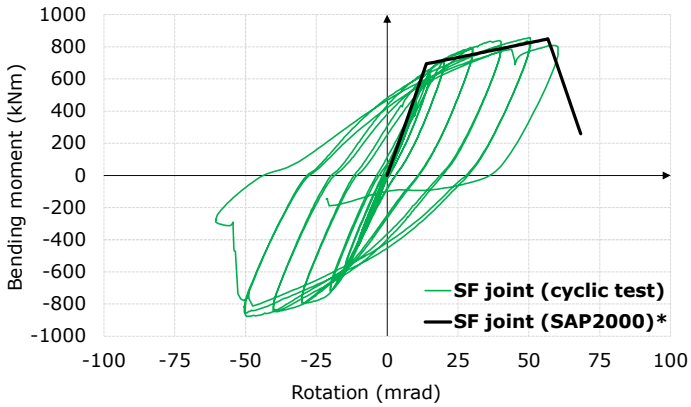

Fig. 6-93. Comparison of experimental cyclic *M-θ* curve (*M*, *θ* at column centreline) to *M-θ* curve of SF joint model (calculated based on the capacity curve)

In a similar manner, potential plastic regions were defined in the structural elements of the *MRF-RF*:

- beam ends: plastic hinge model suited to members subjected to flexure;
- columns: plastic hinge model for members subjected to combined axial loading and flexure. The following acceptance criteria were implemented: $1 \cdot \theta_y$ at DL, $6 \cdot \theta_y$ at SD, $8 \cdot \theta_y$ at NC, according to [106].

For the static nonlinear analyses (i.e., *Pushover*), a triangular lateral pattern of forces was applied since lateral deformations were proportional to forces over the height of the frames. The distribution is shown in Fig. 6-94.

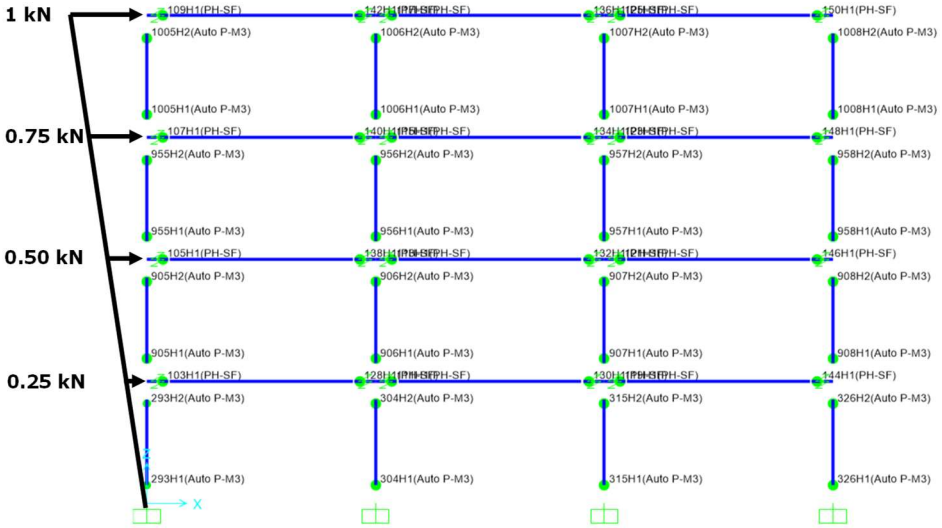

Fig. 6-94. Triangular distribution of lateral forces applied to the *MRF-SF* and *MRF-RF*

Results of nonlinear static analyses (Pushover)

Capacity curves were obtained from *Pushover* analyses on the *MRF-SF* and *MRF-RF*. The response curves are expressed in terms of base shear force relative to the top displacement of the frames, and shown in Fig. 6-95a,b. The comparison of

the two capacity curves is shown in Fig. 6-95c. Despite the evident similarity between the two curves, some differences, although small, can be observed. For example, the elastic stiffness of the curve corresponding to the *MRF-SF* was slightly smaller than that of the *MRF-RF*. However, the fundamental period of the *MRF-SF* was 2 % higher than that of the reference frame. Additionally, the base shear force of the *MRF-SF* at a top displacement of 0.4 m was 2.3 % smaller than that corresponding to the *MRF-RF*.

Furthermore, target displacements corresponding to the three seismic intensity levels were calculated using the *N2 method* [107]. The resulted target displacements are centralised in Table 6-13 and marked on the base shear force-top displacement curves (see Fig. 6-95a,b,c). At DL, the ratio between the PGA and the reference PGA was a_g / a_{gr} = 0.5. At SD, the ratio was a_g / a_{gr} = 1.0, and at NC, the ratio was a_g / a_{gr} = 1.5. The return periods of action, $T_{LS,CC}$, were consistent with Consequence Class 2 (CC2). Structural damage corresponding to each target displacement is illustrated in parallel for both of the analysed frames in Fig. 6-96a,b, and evidenced the following:

- at DL: both frames responded elastic; plastic hinges were not developed;
- at SD: plastic hinges were developed in almost all beam ends of the *MRF-SF* and *MRF-RF*, except for the beams located at the 4th storey; the deformations that were sustained in these plastic hinges corresponded to pre-DL; plastic hinges corresponding to pre-DL deformations were also developed at the base of the columns located at the 1st storey in both *MRF-SF* and *MRF-RF;*
- at NC: half of the plastic hinges that were developed at beam ends reached deformations consistent with DL; in the two analysed frames, neither of 4th storey beams developed plastic hinges; plastic hinges that were developed at the base of the 1st storey columns reached deformations corresponding to DL in both the *MRF-SF* and *MRF-RF*.

In the legend shown in Fig. 6-96a,b, the structural damage was rated implicitly by SAP2000 based on the acceptance criteria of FEMA 356 [108]. A correlation of the FEMA 356 to the European seismic code [45] [51] in terms of structural damage could be considered as follows:

- Immediate Occupancy (IO) corresponds to Damage Limitation (DL);
- Life Safety (LS) corresponds to Significant Damage (SD);
- Collapse Prevention (CP) corresponds to Near Collapse (NC).

The rotations within the plastic hinges of the SF beams were verified as well. At SD, the value of the maximum rotation within the plastic hinges developed in the SF beams was 7.7 mrad. Other details and moment-rotation curves from each SF beam plastic hinge are shown in Annex D of the current study.

The maximum interstorey drifts corresponding to the *MRF-SF* and the *MRF-RF* are presented in Table 6-14. The maximum interstorey drifts, as obtained from the *MRF-SF*, considering all storey to be included, were the following ones: 7.8 mrad at DL, 16.8 mrad at SD and 24.3 mrad at NC.

Although the drift limit of 7.5 mrad from the European seismic code [51] was slightly exceeded at DL by both of the frames, the results which were obtained from applying *Pushover* with *N2 method* could be regarded as proof of good seismic performance. The interstorey drift limit of 20 mrad imposed on MRF structural systems at SD was not exceeded by either of the analysed frames. Moreover, the outcomes of *Pushover* analyses underlined the similarity of the two frames (see Fig. 6-95a,b,c, Fig. 6-96a,b and also Table 6-14). Overall, both the *MRF-SF* and the *MRF-RF* evidenced an adequate seismic performance.

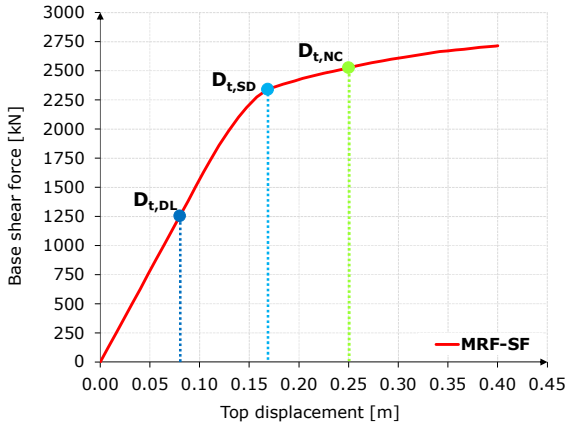

a)

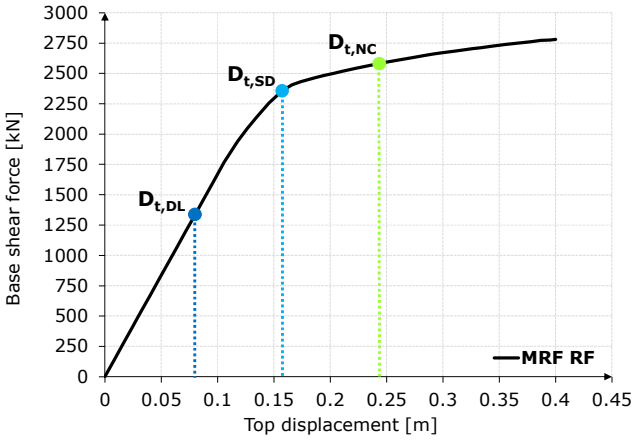

b)

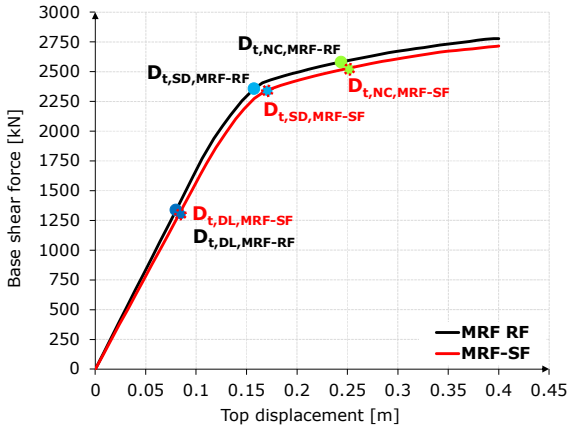

c)

Fig. 6-95. Capacity curves corresponding to: a) *MRF-SF*; b) *MRF-RF*; c) *MRF-SF* vs. *MRF-RF*

Table 6-13 – Seismic action parameters for CC2 and target displacements of *MRF-SF*, *MRF-RF*

Limit States (LS)	Return period of action $T_{LS,CC2}$	Performance factors $\gamma_{LS,CC2}$	Target displacements	
			MRF-SF	*MRF-RF*
Damage Limitation (DL)	60 years	0.5	0.08 m	0.08 m
Significant Damage (SD)	475 years	1.0	0.17 m	0.16 m
Near Collapse (NC)	1600 years	1.5	0.25 m	0.24 m

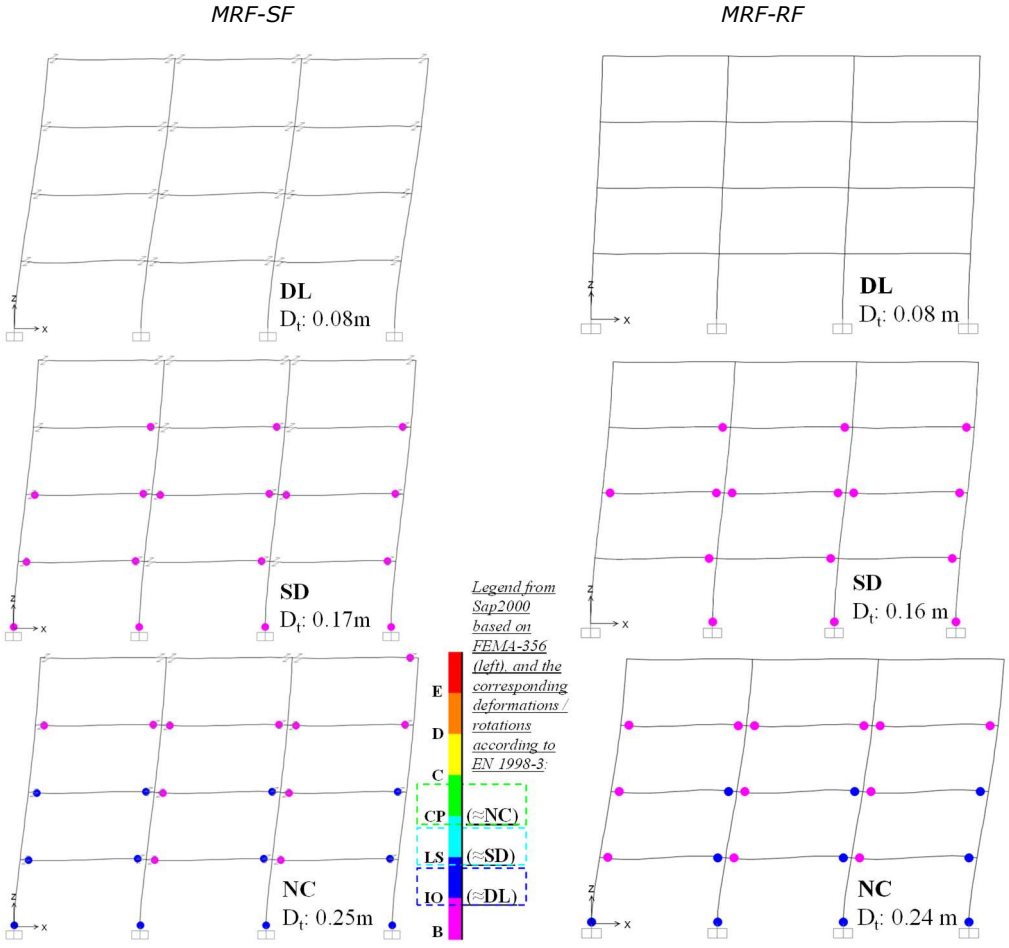

Fig. 6-96. Structural damage at DL, SD & NC from *Pushover* analyses performed on: a) *MRF-SF* (left) and b) *MRF-RF* (right)

Table 6-14 – Maximum interstorey drifts corresponding to the *MRFs* from *Pushover*

Limit States (LS)	*MRF-SF*	*MRF-RF*	prEN 1998-1-2 limits
Damage Limitation (DL)	7.8 mrad	8.0 mrad	7.5 mrad
Significant Damage (SD)	**16.8 mrad**	16.2 mrad	20 mrad
Near Collapse (NC)	24.3 mrad	24.0 mrad	-

Results of nonlinear dynamic analyses (Response-History Analyses)

The seismic performance evaluation was also carried out with *Response History Analyses* (*RHA*). For this purpose, a set of seven semi-artificial accelerograms matching the target spectrum and meeting the criteria of the seismic code [45] was received as input. The set was selected and generated from a database for seismic ground-motion in Europe [109] (see Table 6-15). Each individual accelerogram was also represented in terms of acceleration in time (see Annex D of the current document). The target, mean and scaled target spectra (i.e., 50 %, 75 % and 130 %), along with the individual spectra of the accelerograms, are shown in Fig. 6-97. The outcomes of *RHA* are discussed in terms of average values (from all accelerograms) and maximum values (from the most unfavourable accelerogram). In the case of the *MRF-SF* and *MRF-RF*, the most unfavourable accelerogram was *#A1*, as it caused the highest structural damage.

Table 6-15 – Details regarding the applied accelerograms

Nb.	Record name	Earthquake	Country	Station name	Year	Mw
#A1	00385_H1	Alkion	Greece	Xylokastro-O.T.E.	1981	6.6
#A2	14336_H1	Montenegro	Montenegro	Bar-Skupstina Opstine	1979	6.2
#A3	15613_H2	Izmit	Turkey	Yarimca (Eri)	1999	5.8
#A4	15683_H2	Izmit	Turkey	Usgs Golden Station Kor	1999	5.8
#A5	16035_H2	Faial	Portugal	Horta	1998	6.1
#A6	16889_H1	L'Aquila	Italy	L'Aquila - V. Aterno	2009	6.3
#A7	17167_H1	Aigion	Greece	Aigio-OTE	1995	6.5

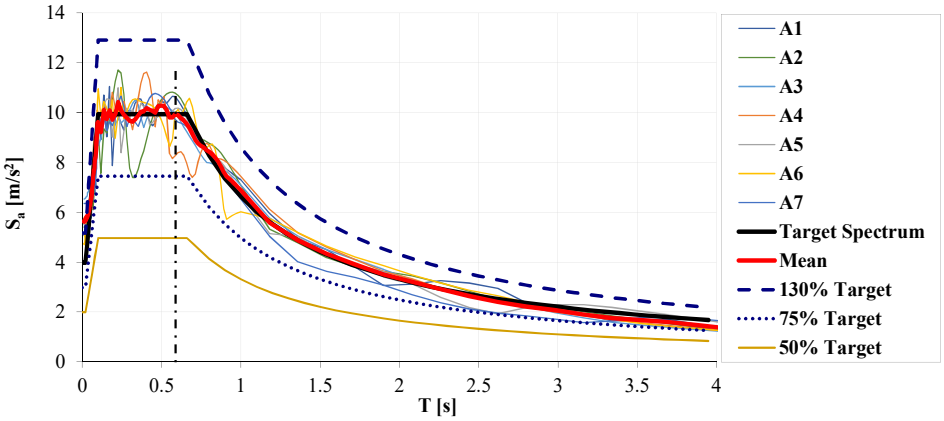

Fig. 6-97. Comparison of elastic response spectra (*#A1* ÷ *#A7*) to the target spectrum

The structural damage sustained at the three Limit States by the *MRF-SF* and the *MRF-RF* is shown in Fig. 6-98a,b. By comparison, it resulted that the structural damage caused by accelerogram *#A1* was the highest. Thus, the maximum values that are presented in this section correspond to *#A1*. Referring to the state of the frames at DL, SD and NC, as shown in Fig. 6-98a,b, the following were observed:

- at DL: both of the frames remained within the elastic range; plastic hinges were not developed in either of the analysed frames;
- at SD: plastic hinges corresponding to pre-DL were developed in half of the beam ends of the *MRF-SF* and the *MRF-RF*; plastic hinges were not developed in the beams located at the 4th storey;

- at NC: more plastic hinges were appeared in the beams ends of the *MRF-SF* and the *MRF-RF*; some of the plastic hinges in the beam ends of the two frames reached deformations consistent with DL; at the bases of columns located at the 1st storey, plastic hinges corresponding to DL were developed.

Compared to the structural damage of the two frames as a result of *Pushover* analyses, plastic hinges were developed at column bases at NC and not at SD.

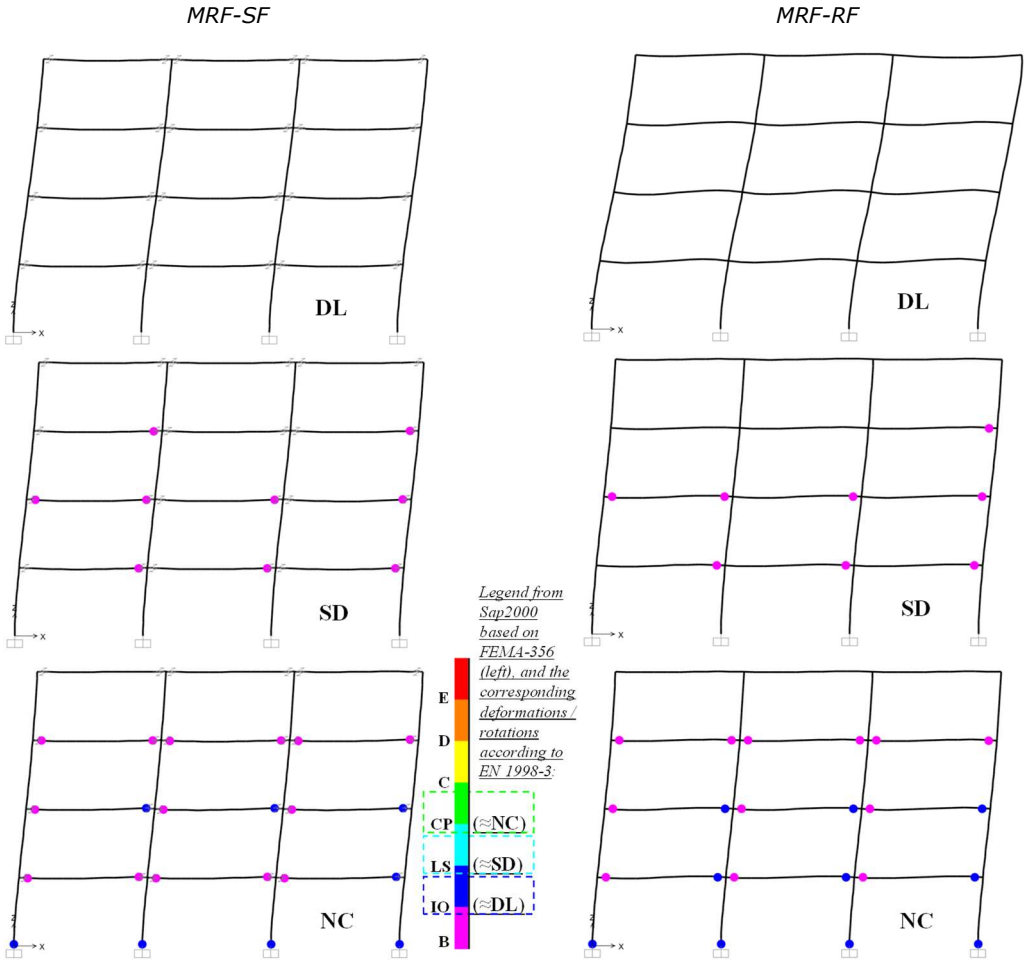

Fig. 6-98. Structural damage at DL, SD & NC from *RHA* with accelerogram *#A1* performed on the: a) *MRF-SF* (left); b) *MRF-RF* (right)

The variation of the top displacement in time, following the application of accelerogram *#A1* to the *MRF-SF* and *MRF-RF*, was recorded at DL, SD and NC and presented side-by-side in Fig. 6-99a,b,c. Comparing the top displacement variations at DL, SD, and NC in both frames, the similarity of these responses is evident.

The maximum top displacement values at the Limit States were centralised in Table 6-16. Given the relatively small difference between the values corresponding to *MRF-SF* and *MRF-RF*, the similarity of the two frame responses is proven.

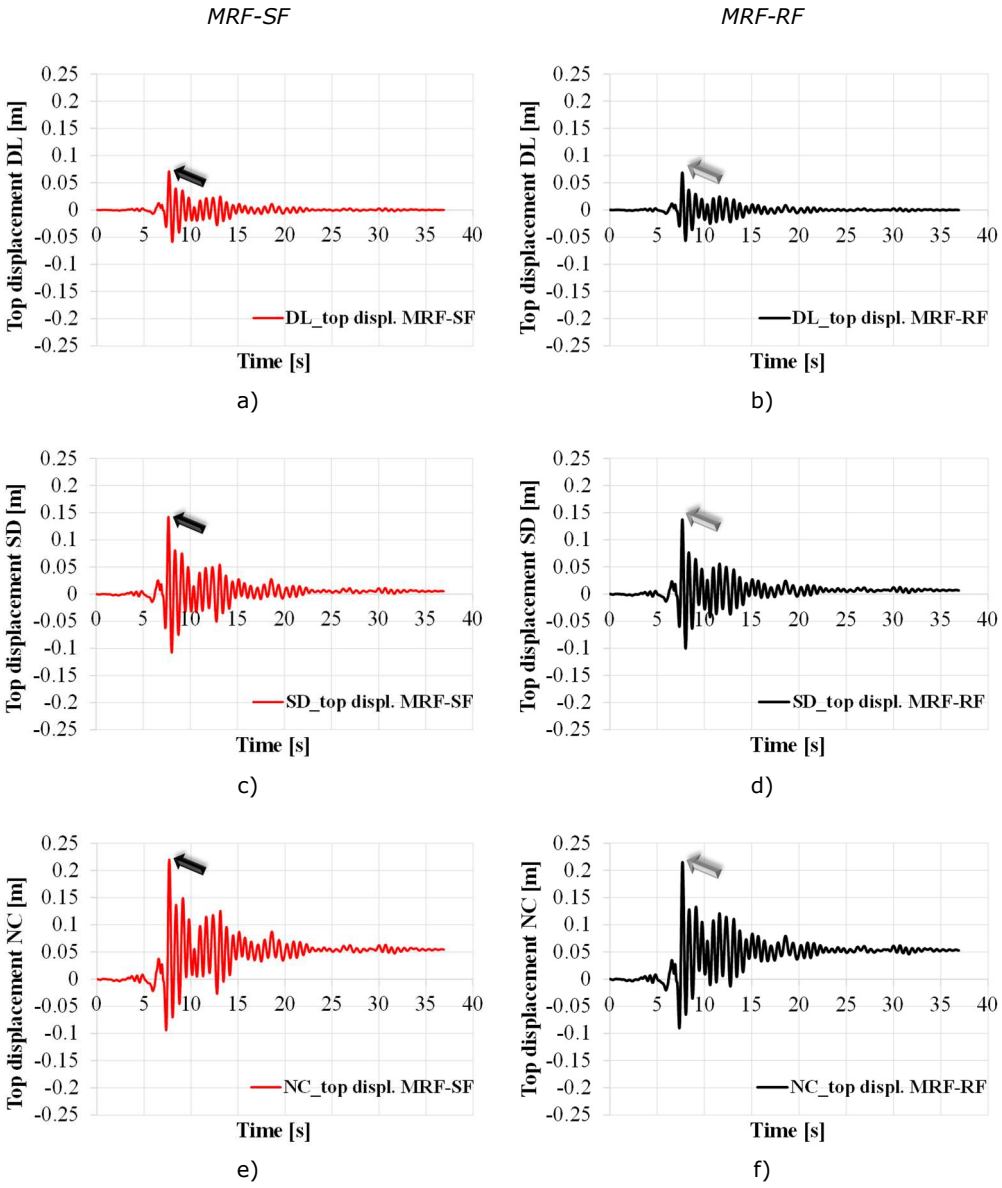

Fig. 6-99. Variation of top displacement from *RHA* with accelerogram *#A1*: a) c) e) top displacement of *MRF-SF* at DL, SD & NC; b) d) f) top displacement of *MRF-RF* at DL, SD & NC

Table 6-16 – Top displacements from *RHA* with accelerogram *#A1* of the *MRF-SF* and *MRF-RF* at DL, SD and NC

Limit States (LS)	*MRF-SF*	*MRF-RF*
Damage Limitation (DL)	0.071 m	0.068 m
Significant Damage (SD)	0.142 m	0.137 m
Near Collapse (NC)	0.220 m	0.215 m

Interstorey drifts were obtained in two scenarios: (i) average values taking into consideration all accelerograms and (ii) maximum values considering the most unfavourable accelerogram - *#A1*. Distributions of interstorey drifts on the height of the *MRF-SF* and *MRF-RF* at DL, SD and NC are shown in Fig. 6-100a,b, and Fig. 6-101a,b. According to prEN 1998-1-2 [51], the interstorey drift limits imposed on MRF systems at DL and SD are 7.5 mrad and 20 mrad, respectively. These are shown with vertical dashed lines together with interstorey drifts.

Regarding the average interstorey drift distributions and values, obtained from all accelerograms (see Fig. 6-100a,b, Table 6-17), the following were observed:

- at DL: the maximum of the average interstorey drifts was 6.5 mrad; this value was obtained at the 2nd storey of the *MRF-SF*; in case of the *MRF-RF*, the maximum of the average interstorey drifts was 6.4 mrad, and was also observed at the 2nd storey; both of the previously mentioned values are smaller than the interstorey drift limit of 7.5 mrad [51];
- at SD: the maximum of the average interstorey drifts was 13.1 mrad; this value was obtained at the 2nd storey of the *MRF-SF*; 13.0 mrad were obtained at the 2nd storey of the *MRF-RF*; both of the mentioned values are smaller than the interstorey drift limit of 20.0 mrad for MRFs [51].

MRF-SF

(average)

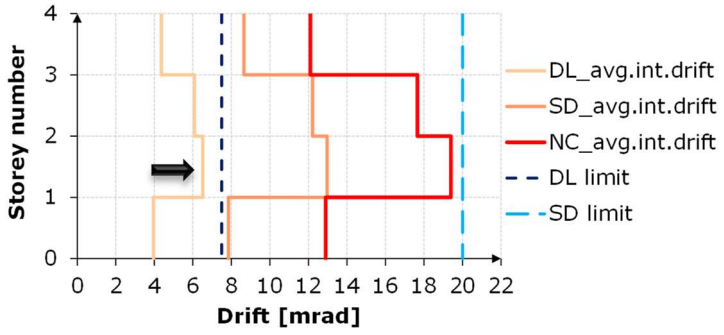

a)

MRF-RF

(average)

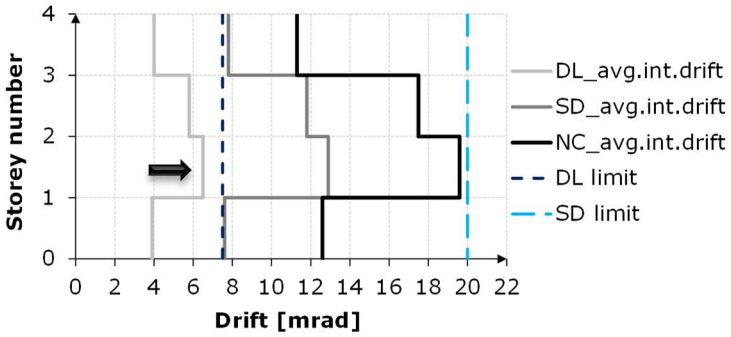

b)

Fig. 6-100. Average interstorey drifts from *RHA* (*#A1* ÷ *#A7*) of the: a) *MRF-SF*; b) *MRF-RF*

Distributions of maximum interstorey drifts obtained by applying the most unfavourable accelerogram, *#A1*, are shown in Fig. 6-101a,b. Maximum values of interstorey drifts at DL, SD and NC are centralised in Table 6-17. Taking into consideration the maximum values from Table 6-17 at DL and SD and the interstorey

drift limits of the code [51], the seismic response of the *MRF-SF* and *MRF-RF* was in accordance with the rules. Even in this case, the limits at DL and SD were not exceeded. Therefore, it could be concluded that an adequate seismic performance was evidenced in both the case of the *MRF-SF*, as well as of the *MRF-RF*.

MRF-SF (#A1)

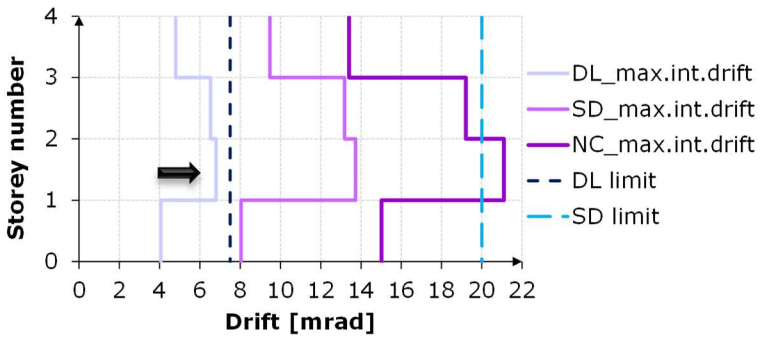

a)

MRF-RF (#A1)

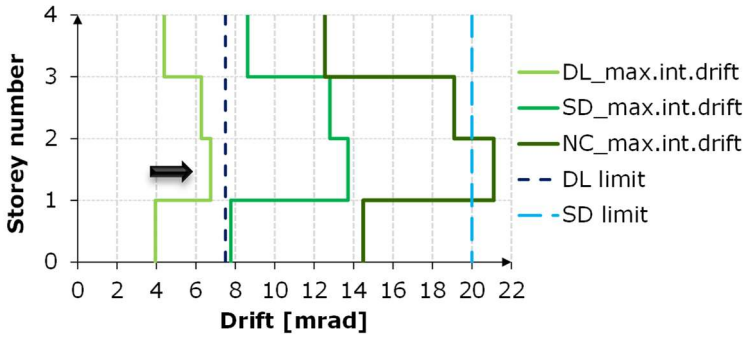

b)

Fig. 6-101. Maximum interstorey drifts from *RHA* with *#A1* of the: a) *MRF-SF*; b) *MRF-RF*

Table 6-17 – Interstorey drifts of *MRF-SF* and *MRF-RF* from *RHA*: maximum values (accelerogram *#A1*) and average values

Limit States (LS)	*MRF-SF*		*MRF-RF*	
	Max. drifts	Avg. drifts	Max. drifts	Avg. drifts
Damage Limitation (DL)	6.8 mrad	6.5 mrad	6.75 mrad	6.4 mrad
Significant Damage (SD)	**13.73 mrad**	**13.1 mrad**	13.72 mrad	13.0 mrad
Near Collapse (NC)	21.10 mrad	19.4 mrad	21.11 mrad	19.6 mrad

Plastic rotations sustained in the plastic hinges of the SF beams were calculated at the three Limit States. The values were obtained by applying the most unfavourable accelerogram, *#A1*, considering all the storeys of *MRF-SF*. The maximum values are the following ones:

- at DL: 0 mrad (elastic response);
- at SD: 4.53 mrad at the 2nd storey of *MRF-SF*;
- at NC: 12.9 mrad at the 2nd storey of *MRF-SF*.

More details and values regarding the rotations in the plastic hinges of the SF beams can be found in Annex D of the current document.

6.1.3 Concluding remarks

The evaluation of the seismic performance of a Moment-Resisting Frame with slim-floor beam-to-column joints, *MRF-SF*, with nonlinear static and dynamic analyses was presented. In parallel, a reference Moment-Resisting Frame with regular composite beams with partial shear interaction, i.e., *MRF-RF*, was developed.

The aim of the structural analyses was (i) to verify the rotation demand resulted from the seismic design situation on the SF beam-to-column joint, (ii) to compare it the experimental rotation capacity and (iii) to assess the seismic performance of the *MRF-SF* with SF beam-to-column joints. In accordance with the aims, the following objectives were established:

- development of a structural model for the tested SF beam-to-column joint;
- application of structural analyses in the nonlinear range, e.g., *Pushover* and *Response-History Analysis*;
- monitoring of the structural damage at the three Limit States, with particular interest at DL and SD, in terms of interstorey drifts and plastic rotation in the plastic hinges of the SF beams.

Structural model of SF beam-to-column joint. The modelling of the SF beam-to-column joint should be performed in detail in order to get the most realistic results. The conclusion was drawn from iterations on the modelling approach of the SF beam-to-column joint, which were validated against the experimental results. However, the results of other less demanding SF beam-to-column joints models were also explored and found to be adequate. In the case of the *MRF-SF*, should the modelling of the beam-to-column connection with link elements be replaced with a rigid connection, then the elastic stiffness of the frame would be slightly higher and the fundamental period would decrease with roughly 2 %. Nevertheless, this idealisation of the connection produced very similar results in the nonlinear range to the recommended herein, yet more demanding modelling procedure. Some results on this finding are available in Annex D of the current document.

The optimal modelling approach entailed the following steps:

- modelling of "full" section of the SF beam with:
  - tested geometry and material;
  - equivalent moment of inertia, $I_{eq,full\ section}$;
- modelling of dissipative zone with *RFS* of the SF beam:
  - tested geometry and material;
  - equivalent moment of inertia, $I_{eq,RFS}$;
  - plastic hinge model based on processed experimental data, which contained the plastic rotation of the dissipative zone of the SF beam;
- modelling of the beam-to-column connection:
  - linear elastic link;
  - contained the elastic stiffness of the connection;
- modelling of the panel zone:
  - rotational spring;
  - contained the stiffness of the web panel.

The contribution of the reinforced concrete slab to the resistance and stiffness of the SF beam-to-column joint was included in the structural model through the equivalent moment of inertia of the "full" section and of the dissipative zone with *RFS*. In addition, the plastic hinge model of the SF beams contained the plastic rotation of the dissipative zone, which included the reinforced concrete slab component.

The envelope curve of the dissipative zone of the SF beam was obtained from the cyclic curve by following the provisions of FEMA P-795 [47] and by considering the first cycle of each amplitude. The response parameters and the acceptance criteria

corresponding to the plastic hinge model of the dissipative zone were calculated based on Landolfo et al. [50].

Evaluation of seismic performance with nonlinear structural analyses. The seismic performance was evaluated with nonlinear static and dynamic analyses. The maximum interstorey drifts obtained from *Pushover* analyses on *MRF-SF* were: 7.8 mrad at DL, 16.8 mrad at SD and 24.3 mrad at NC. The average interstorey drifts obtained from *Response-History Analyses* on *MRF-SF* were: 6.5 mrad at DL, 13.1 mrad at SD and 19.4 mrad at NC. Finally, the maximum interstorey drifts obtained from *Response-History Analyses* with the most unfavourable accelerogram *#A1* on *MRF-SF* were: 6.8 mrad at DL, 13.7 mrad at SD and 21.1 mrad at NC. Although the application of *Pushover* analyses on the frames led to more conservative results than those obtained with *Response-History Analyses,* the outcomes of nonlinear analyses revealed an **overall acceptable seismic performance** of *MRF-SF*, as the frame evidenced desirable behaviour at each Limit State:

- at DL: elastic response; interstorey drifts within the imposed limit of 7.5 mrad on MRFs;
- at SD: development of plastic hinges at SF beam ends with deformations corresponding to pre-DL; interstorey drifts within the imposed limit of 20 mrad on MRFs;
- at NC: plastic hinges in the SF beams end reached deformations corresponding to DL; development of plastic hinges at the 1st storey column bases with deformations corresponding to DL.

The value of the target displacement at DL, SD and NC for the *MRF-SF*, which were calculated based on the outcomes of *Pushover* with *N2 method*, were similar to the top displacement values obtained from *Response-History Analyses* with the most unfavourable accelerogram *#A1:*

- target displacement at DL for *Pushover*: 80 mm;
- top displacement at DL from *RHA* with *#A1*: 71 mm;
- target displacement at SD for *Pushover*: 170 mm;
- top displacement at SD from *RHA* with *#A1*: 142 mm;
- target displacement at NC for *Pushover*: 250 mm;
- top displacement at NC from *RHA* with *#A1*: 220 mm.

Interstorey drift demand vs rotation capacity. The **average rotation demand at SD** from *Response-History Analyses* was **±13.1 mrad**. The maximum rotation demand at SD that resulted from applying *Response-History Analyses* with accelerogram *#A1* was ± 13.7 mrad. Considering that the SF beam-to-column joint specimens attained a rotation of **± 45.35 mrad at SD**, and that both the average and the maximum rotation demands were ±13.1 mrad, ± 13.7 mrad, respectively, an adequate seismic performance of the *MRF-SF* was proven. The **rotation demand is lower than the available rotation** of the SF beam-to-column joint.

Plastic rotation demand vs experimental plastic rotation capacity of the SF beams. Maximum plastic rotations within the plastic hinges of the SF beams at SD were obtained from *Pushover* and *Response-History Analyses*. Thus, a plastic rotation of 7.7 mrad was obtained from *Pushover*, and a value of 4.53 mrad from *RHA* with accelerogram *#A1*. Considering the joint rotations that were determined on the envelope curve (see Fig. 3-50a), the following rotations resulted: 16 mrad at DL, 45.35 mrad at SD and 60.5 mrad at NC. If the elastic joint rotation of 16 mrad was subtracted from the rotations at SD and NC, the plastic joint rotations would be 29.4 mrad at SD and 44.5 mrad at NC. As the maximum plastic rotation within the plastic hinges of the SF beam was 7.7 mrad, which is significantly smaller than the

plastic rotation capacity at SD of 29.4 mrad, it is concluded that the plastic rotation demand is smaller than the plastic rotation capacity.

Similarity between the analysed frames. Proof of the similarities between the *MRF-SF* and *MRF-RF* were the values of the top displacements and interstorey drifts. Important to note are also the elastic stiffnesses of the different sections the SF beam to those of the IPE-450 beam in the potential bare steel plastic zone:

- SF beam - "full" section: $I_{eq,SF,full}$ = 3.888×10^8 mm^4;
- SF beam - dissipative zone with *RFS*: $I_{eq,SF,RFS}$ = 2.800×10^8 mm^4;
- IPE-450 – potential plastic zone: I_1 = 3.374×10^8 mm^4.

Consequently, the bending stiffness of the experimentally tested SF beam could be regarded as being analogous to the bending stiffness of a bare steel IPE-450 beam. Concerning the space efficiency, while the total height of the slim-floor system is $h_{t,SFbeam}$ = 370 mm, that of the "classic" composite beam (i.e., concrete slab over the IPE-450 beam) is $h_{t,IPE450}$ = 570 mm. Therefore, despite the overall lower height of the slim-floor, its flexural stiffness is comparable to that of a bare steel IPE-450 profile.

Followingly, a simplified evaluation of the steel use per frame accounting for the beams, columns and secondary beams on the longitudinal direction (corresponding to one bay of 6 m) was performed. In the case of *MRF-SF*, the steel use is 22.3 tons or 51.5 kg/m^2. Oppositely, a steel use of 23.2 tons or 53.7 kg/m^2 is obtained in the case of the *MRF-RF*. Overall, the steel use is 3.9 % lower in the case of the *MRF-SF*. However, as this evaluation was performed on 2D frames, ignoring the rebars, the concrete and the steel decking, a more realistic approach would need to account for these aspects.

Ultimately, as the results of the nonlinear structural analyses evidenced, the integration of the SF beam into a lateral load-resisting system as the MRF was possible, and led to good results in the inelastic range. In order to develop an accurate model of the SF joint, the geometrical and mechanical characteristics need to be considered in the elastic domain. In the nonlinear range, the backbone curve should be constructed from the cyclic curve following the relevant provisions of the codes. Compared to the *MRF-RF*, a vertical space gain of 0.20 m per story was gained in the *MRF-SF* due to the reduced height of the flooring system. Thus, for relatively the same seismic performance, a total of 0.80 m in vertical space – corresponding to four storeys - were gained in the *MRF-SF*.

6.2 Concentrically-Braced Frame

6.2.1 Design considerations

The slim-floor system is best used for mid- and high-rise steel and composite structures, as it allows for enhanced architectural freedom due to the reduction of floor thickness or to the possibility of adding extra storeys [16]. However, judicious and economic seismic design of medium-tall structures is usually achieved by combining braced with unbraced structural systems, e.g., Dual Frames. As case studies on this subject are rather limited, the current study could be seen as an example of the application of slim-floors in the seismic design of tall structures. Consequently, the current case study is focused on achieving the following:

- adaptation of the developed SF beam-to-column joint model to the Concentrically-Braced Frame (CBF);
- evaluation of the: (i) plastic rotation demand in the plastic hinge of the SF beams, (ii) interstorey drift demand and (iii) overall seismic performance of the CBF with SF beam-to-column joints through nonlinear analyses.

An efficient design of seismic-resistant structures can be achieved by controlling the global mechanism through: ▪ the application of capacity design, ▪ the limitation of interstorey drifts and second order effects, ▪ ensuring seismic energy dissipation through plastic hinges. To this end, a balance between strength, stiffness and ductility should be achieved [110]. According to prEN 1998-1-2 [51], horizontal forces induced by seismic loads are resisted by the braces of CBFs, which are subjected to axial forces. Since the code [51] imposes the *tension-compression model* on braces of structures designed in DC3, the brace behaviour under both tension and compression should be considered in design. Thus, if one loading direction is taken into account, while some of the braces are under tension, the others are under compression, and vice versa. However, the failure under these internal forces differs. Whereas braces subjected to tension yield, those under compression buckle. Considering these phenomena, design rules are given in the code to ensure an adequate seismic behaviour of CBFs. In this context, the primary structural elements to dissipate seismic energy are the braces, while the SF beams are the second.

Analysed frame, initial data

A 2D CBF with the SF beam-to-column joints was designed for the current case study. A summary of the initial considerations is presented in Table 6-18.

Table 6-18 – Input data for the analysed *CBF-SF*

Characteristics:	
No. of spans & span length:	3 x 6.0 m
No. of storeys & storey height:	16 x 3.2 m
Flooring system:	Slim-floor system
Position of bracing system:	Central span of *CBF-SF*
Ductility Class:	DC3
Behaviour factor:	q = 4
Consequence Class:	CC2 (normal)
Ground conditions:	
Site category:	Type C
Peak Ground Acceleration:	$a_g = 0.30 \cdot g$

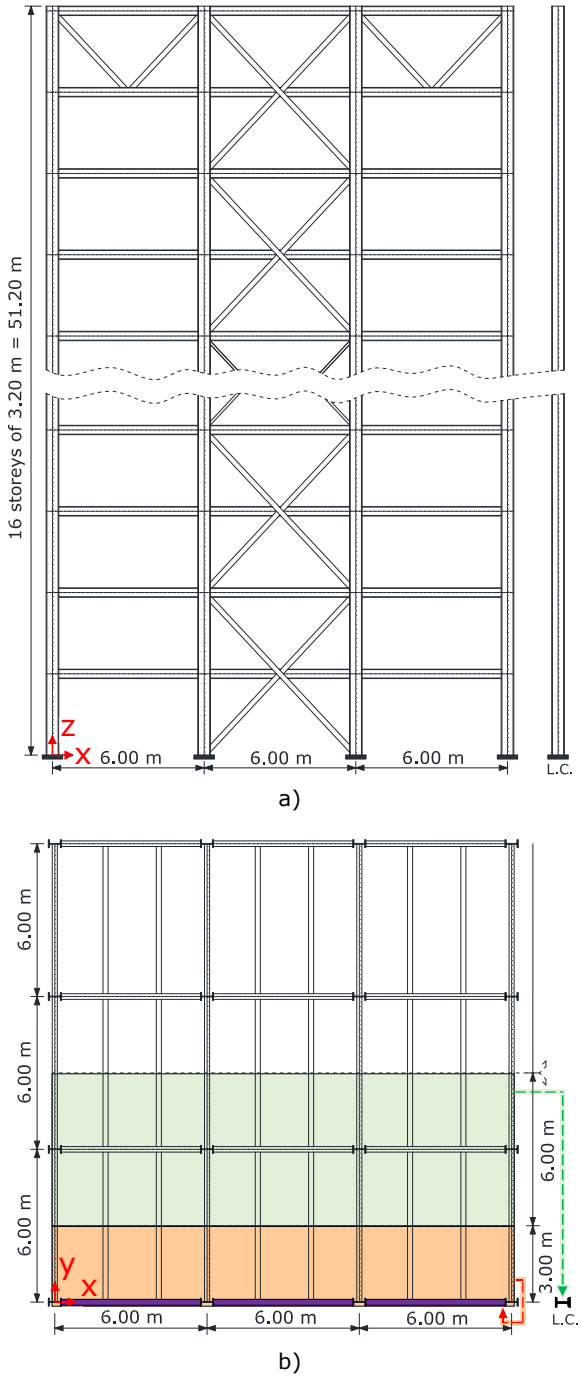

Fig. 6-102. Configuration of the *CBF*: a) elevation; b) floor layout

For simplicity, the analysed frame was labelled as ***CBF-SF***. The frame incorporated a central braced span and two unbraced outer spans (see Fig. 6-102a).

In direction X (transverse), each span of the *CBF-SF* had a length of 6.0 m. The total height of 51.2 m was divided into 16 storeys of 3.2 m. Considering the 3 span-by-3 bay floor plan (see in Fig. 6-102b), the *CBF-SF* was part of the lateral load-resisting system whose position was on the perimeter of the building. The rest of the structure was configured to withstand gravity loads. The Y direction (longitudinal) was considered only for the distribution of loads and seismic masses. The building category was office.

The *CBF-SF* consisted of SF beams, "X" braces and steel columns. The cross section of the SF beams was the same as the one used for the SF beams of the tested joint assemblies. Steel braces arranged in "X" spanning over two storeys were used throughout the whole height of the central span of the analysed frame. To optimise the steel use and to avoid a longer fundamental period of vibration, an outrigger belt truss was positioned at the top 16th storey. The columns were designed as steel structural elements.

Boundary conditions and loads

The SF beams in the braced span were incorporated into the lateral load-resisting system by using rigid connections. For this purpose, the stiffness of the joint was verified in accordance with prEN 1993-1-8 [79] and confirmed to be rigid. Consequently, the SF beams in the central braced span were considered to be rigidly connected to the columns. On the other hand, the SF beams in the unbraced spans were used for gravity loads and thereby had pinned end connections.

The bracing system consisted of "X" braces over the height of two storeys. Brace continuity was maintained over the height of two storeys, while the analogous brace was interrupted at the middle – the middle corresponding to one storey. Nominally pinned connections were assigned to brace ends. A rigid diaphragm constraint was assigned to each storey level, as one of the methods used to account for the concrete slab. Fixed supports were assigned to the column bases.

The same action values as those considered in the case study on MRFs were applied to the *CBF-SF*:

- permanent load uniformly distributed on floors of 5 kN/m^2;
- permanent load linearly distributed on marginal frames of 3.2 kN/m corresponding to 1 kN/m^2 of façade weight;
- live load uniformly distributed on floors of 3.8 kN/m^2;
- seismic load: response spectrum characterised by a_g = 0.3·g; soil type C, T_B = 0.1 s, T_C = 0.667 s, T_D = 3.94 s in accordance with prEN 1998-1-1 [45].

Gravity loads acting on the gravity load-resisting system were assigned to a leaning column. Loads corresponding to half of one bay (entire length of one bay was 6.0 m) were assigned to the analysed frame, as the load distribution in Fig. 6-102b shows. Following the allocation and assignment of loads, a mass of 117.4 tons resulted at each storey.

Modelling of CBF-SF

The upper value of the behaviour factor for CBF structural systems designed in DC3 is limited to 4 in the European seismic code [51]. This value of the behaviour factor was considered in the design of the *CBF-SF*.

According to prEN 1998-1-2 [51], lateral loads are resisted through tension and compression forces which develop in the braces of CBFs. This is valid for structures designed in DC3, on which the *tension-compression model* of braces is imposed by the code. In consequence, the dissipation of seismic energy takes place through the yielding of the braces under tension and their buckling under

compression. However, the development of plastic hinges in braces is required by the seismic code [51] to occur prior to the yielding or buckling of the beams or columns, and to the failure of the connections. To achieve this hierarchy of resistances in the *CBF-SF* in DC3, the following provisions of prEN 1998-1-2 [51] were applied:

- cross section of braces corresponded to class 1;
- local slenderness was verified according to the seismic code;
- non-dimensional slenderness was verified ($\lambda \leq 2$);
- the maximum buckling overstrength $\Omega_{b,i}$ did not differ with more than 25 % from the minimum value of Ω_b;
- non-buckling requirement of the braces at the top storey was fulfilled.

In addition, to ensure a similar behaviour at each storey, braces were placed over the entire height of the central span of the *CBF-SF*. Design of braces in the elastic range was performed considering the rules of prEN 1998-1-2 [51] and prEN 1993-1-1 [54]. In accordance with [54], the buckling resistance of braces under compression was verified. For this purpose, the buckling length was calculated based on the distance measured between connections, and on the type of the connections. The connections of the braces were considered nominally pinned in the current study.

The SF beams located in the central braced span of the *CBF-SF* were modelled using the same considerations as those in Section 6.1.1 and 6.1.2. Therefore, the geometry, material and stiffnesses of the tested SF beams were applied, e.g.:

- SF beams included the dissipative zone with *RFS* and the "full" section;
- equivalent moment of inertia I_{eq} calculated in the dissipative zone with *RFS* and in the "full" section under sagging and hogging bending (see Table 6-9) were introduced in the structural model; both were calculated accounting for the presence of the reinforced concrete slab (i.e., only parts of the concrete slab under compression were considered);
- nonlinear response of the SF beam was defined through the cyclic envelope curve, which contained the plastic rotation of the dissipative zone.

In the outer spans of the frame, the connections of the SF beams to the steel columns were nominally pinned, and modelled accordingly. Their cross section was designed to withstand the maximum bending moment that resulted from gravity load combinations at the Ultimate Limit State. Thus, their cross section was comprised of an IPE-300 steel profile with an additional steel plate (width: 280 mm; thickness: 12 mm) welded on the lower flange. The steel profile was encased in concrete.

Equivalent static design

The rules of prEN 1993-1-1 [54] and prEN 1998-1-2 [51] were considered for the verification of the structural elements of the analysed frame. The hierarchy of resistances was achieved by designing the beams and the columns of the *CBF-SF* with overstrength. To determine the value of the overstrength factor Ω for structures designed in DC3, Eq. (6.73) and Eq. (6.74) from the code [51] were used. According to [51], Ω_b is obtained from the minimum ratio of the buckling resistance to the design action effect from the braces. In this case, Ω_b was 1.06. The value of the overstrength factor Ω is calculated with Eq. (6.74), which accounts for the strain hardening factor γ_{sh} and the material overstrength factor γ_{rm}. The strain hardening factor for CBFs is 1.1 according to the seismic code [51]. The material overstrength factor was selected from the seismic code considering the steel grade S275 of the braces, e.g., γ_{rm} = 1.35. Therefore, the value of the overstrength factor Ω was 1.6. Considering the resistance and displacement checks performed during the equivalent elastic analysis, it was concluded that the **design was governed by resistance** and that the *CBF-SF* was not susceptible to second-order effects [50]. A summary of the design

outcomes obtained by applying equivalent elastic analyses with SAP2000 [105] is shown in Table 6-19.

$$\Omega_b = min\left(\frac{N_{b,Rd,i}}{N_{Ed,i}}\right) \tag{6.73}$$

$$\Omega = \Omega_b \cdot \gamma_{sh} \cdot \gamma_{rm} \tag{6.74}$$

Table 6-19 – Results of equivalent elastic analyses on the *CBF-SF*

	Structural elements:		
	▪ SF beams (central span), S355 ▪ SF beams (outer spans), S355		
Flr.	▪ Outer columns:	▪ Inner columns:	▪ Braces:
16	HE 800 A; S355	HE 800 A; S355	Outrigger belt truss: HE 300 B; S355
15	HE 800 A; S355	HE 800 A; S355	CHS-133.0 x 6.3 mm; S275
14	HE 800 A; S355	HE 800 A; S355	CHS-139.7 x 5.0 mm; S275
13	HE 800 A; S355	HE 800 A; S355	CHS-159.0 x 6.3 mm; S275
12	HE 800 B; S355	HE 800 B; S355	CHS-168.3 x 6.3 mm; S275
11	HE 800 B; S355	HE 800 B; S355	CHS-177.8 x 6.3 mm; S275
10	HE 800 B; S355	HE 800 B; S355	CHS-177.8 x 6.3 mm; S275
9	HE 800 B; S355	HE 800 B; S355	CHS-177.8 x 7.1 mm; S275
8	HE 800 B; S355	HE 800 B; S355	CHS-177.8 x 6.3 mm; S275
7	HE 800 B; S355	HE 800 B; S355	CHS-177.8 x 7.1 mm; S275
6	HE 800 B; S355	HE 800 M; S355	CHS-177.8 x 7.1 mm; S275
5	HE 800 B; S355	HE 800 M; S355	CHS-193.7 x 10.0 mm; S275
4	HE 800 B; S355	HE 800 M; S355	CHS-193.7 x 8.0 mm; S275
3	HE 800 B; S355	HE 900 M; S460	CHS-193.7 x 10.0 mm; S275
2	HE 800 B; S355	HE 900 M; S460	CHS-193.7 x 8.0 mm; S275
1	HE 800 B; S355	HE 900 M; S460	CHS-193.7 x 7.1 mm; S275
	Lateral displacement checks in the seismic design situation:		
	▪ Damage Limitation: $d_{r,max,DL}$ = 0.0072 < 0.0075 => OK	▪ Significant Damage: $d_{r,max,SD}$ = 0.0141 < 0.015 => OK	
	Fundamental period of vibration: $T_{1,CBF\text{-}SF}$ = 2.33 s		

6.2.2 Evaluation of seismic performance

Definition of nonlinear behaviour

According to the study of D'Aniello et al. [111], the nonlinear behaviour of *tension-compression* braces is characterised by yielding under tension and buckling under compression. In addition to these phenomena, moderate hardening and high pinching at load reversal were also evidenced. After iterations, it was concluded that the numerical model of the braces should be adapted to each type of nonlinear analysis, due to convergence difficulties that were encountered. Thus, in the *Pushover* analyses, an axial force-axial deformation phenomenological model (*P hinge*) was defined. The acceptance criteria from FEMA 356 [108] were adopted (see Table 6-20). In this table, Δ_C represented the axial deformation at the anticipated buckling load, while Δ_T was the axial deformation at the anticipated tensile yielding load. Following recommendations of the previously mentioned study, e.g., [111], the hysteretic response of the braces was defined by assigning two physical theory models

(*P-M2-M3 fibre plastic hinge*) to each brace and by adding an initial imperfection in the nonlinear dynamic analyses. The cross section contained a total of 100 fibres, with 2 fibres on the thickness. The same acceptance criteria of FEMA 356 [108] were applied to this model as to the phenomenological one (see Table 6-20).

According to [111] [112] [113], the modelling procedure and the initial camber value are important to obtain accurate results. These studies showed that the initial imperfection value affects the buckling strength of the braces, leading either to the underestimation (causing premature failure) or to the overestimation (causing delayed failure) of it. In the current study, the initial imperfection was calculated as recommended by Maquoi and Rondal [114], resulting in a value of Δ_o = 6.5 mm. The imperfection was modelled in-plane with the braces.

Table 6-20 –Modelling parameters & acceptance criteria of CHS braces from FEMA 356 [108]

CHS braces in tension:					
Modelling parameters:			Acceptance criteria:		
a	b	c	IO / DL	LS / SD	CP / NC
$11 \cdot \Delta_T$	$14 \cdot \Delta_T$	0.8	$0.25 \cdot \Delta_T$	$7 \cdot \Delta_T$	$9 \cdot \Delta_T$
CHS braces in compression:					
Modelling parameters:			Acceptance criteria:		
a	b	c	IO / DL	LS / SD	CP / NC
$0.5 \cdot \Delta_C$	$9 \cdot \Delta_C$	0.4	$0.25 \cdot \Delta_C$	$4 \cdot \Delta_C$	$6 \cdot \Delta_C$

Table 6-21 – Details of brace models used in nonlinear static and dynamic analyses

Parameters:		Static nonlinear analysis	Dynamic nonlinear analysis
Member subdivision:		No (one element)	Yes (two subdivisions)
Initial camber:		No	Yes
Plastic hinge	- model:	Phenomenological (*P hinge*)	Physical theory model (*P-M₂-M₃ fibre plastic hinge*)
	- location:	Middle	Middle
	- number:	One	Two
	- length:	2 x D; (D: outer brace diameter)	
Material curve:		Bilinear material curve	

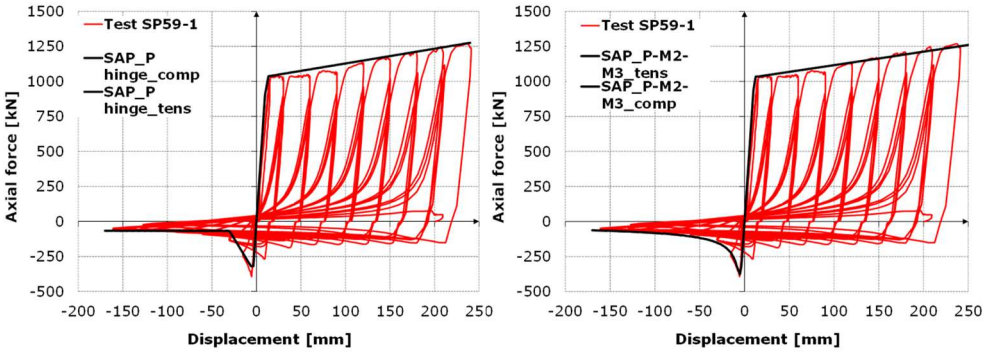

a) b)

Fig. 6-103. Comparison of *F-δ* curves of the tested brace *SP59-1* [115] to the numerical brace models: a) phenomenological (*P hinge*); b) physical theory (*P-M₂-M₃ fibre plastic hinge*)

The output data of all plastic hinges obtained after the *Pushover* (axial force vs. axial deformation curve) and the *Response History Analyses* (axial force vs. axial deformation curve and bending moment vs. rotation curve) were manually processed

to obtain the force-deformation curve corresponding to each brace. The maximum deformations were compared to the acceptance criteria corresponding to braces under compression or tension from FEMA 356 [108], rated and marked accordingly on the structural element. The nonlinear modelling and post-processing procedures of braces were verified in relation to the experimental data of a cyclic test performed on a double pinned CHS brace (*SP59-1* [115]). Comparisons of the force and deformation of the test brace specimen and the numerical models (phenomenological and physical theory) are shown in Fig. 6-103a,b, which evidence adequate results. A summary of the modelling information regarding the braces is presented in Table 6-21.

In general, the inelastic response of the SF beams from the central span was defined as in Section 6.1.2. However, the SF beam-to-column joint was considered to be rigid as the bracing system of the frame reduced the horizontal displacement by more than 80 %. In this case, based on the stiffness classification of the code [79], the SF beam-to-column joint is rigid. The plastic hinge type for the dissipative zone of the SF beam was suitable for members subjected to flexure and contained the plastic rotation of the dissipative zone (including the reinforced concrete slab) - obtained from processed experimental data. The response of the columns in the inelastic range was defined by plastic hinges for members subjected to combined axial force and flexure, and the acceptance criteria from EN 1998-3 [106] were imposed: $1 \cdot \theta_y$ at DL; $6 \cdot \theta_y$ at SD; $8 \cdot \theta_y$ at NC.

A "modal" pattern of lateral forces was applied prior to the *Pushover*. Definition of forces was performed by considering the modal shape of the fundamental mode (see Fig. 6-104a). The lateral distribution of forces is shown in Fig. 6-104b.

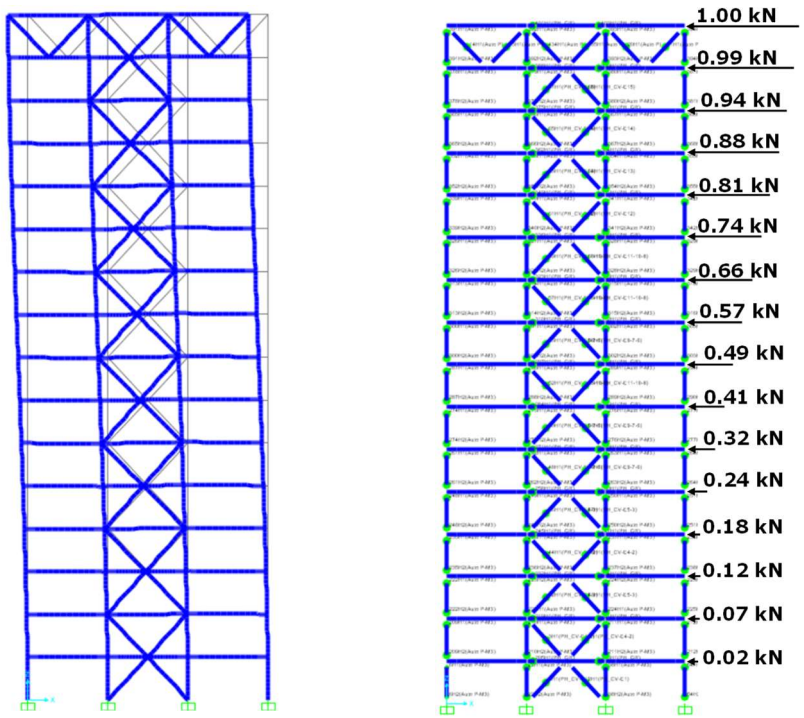

a) b)

Fig. 6-104. Lateral load distribution of forces for *Pushover* on the *CBF-SF*: a) modal shape of the fundamental mode; b) "modal" pattern of forces

Results of nonlinear static analyses (Pushover)

The performance factors corresponding to Consequence Class 2 (CC2) and the return periods that are presented in Table 6-22 were taken into account for the nonlinear *Pushover* analysis. The capacity curve corresponding to the *CBF-SF* is expressed in terms of base shear and top displacement, and is shown in Fig. 6-105. Followingly, the three target displacements calculated for the DL, SD and NC seismic intensity levels were obtained from the application of the *N2 method* [107]. The target displacement values were, as follows: 0.27 m at *DL*; 0.54 m at SD; 0.81 m at NC (see Table 6-22 and Fig. 6-105). Structural damage of the *CBF-SF* consistent with the previously mentioned target displacements at DL, SD and NC is shown in Fig. 6-106, and revealed the following:

- at DL: elastic response of the frame except for four compressed braces located at mid-height; these sustained deformations consistent with DL; four other braces attained deformations consistent with pre-DL;
- at SD: plastic hinges corresponding to DL were relatively uniform developed in braces over the height of the frame; two compressed braces attained deformations corresponding to SD, one attained NC deformations; between the 5th and 9th storeys, some plastic hinges corresponding to pre-DL were developed in five SF beams located in the central span of the *CBF-SF*;
- at NC: except for the 15th and 16th storeys, plastic hinges were developed in the rest of the braces; structural damage to the braces was extensive: three attained NC deformations, while 4 others sustained deformations beyond NC; between the 3rd and 10th storey, plastic hinges were developed in the SF beams; the deformations in the SF beams corresponded to pre-DL in some cases, and DL in others; plastic hinges were not developed in columns.

Table 6-22 – Seismic action parameters for CC2 and target displacements of *CBF-SF*

Limit States (LS)	Return period of action $T_{LS,CC2}$	Performance factors $\gamma_{LS,CC2}$	Target displacements $D_{t,\,DL}$, $D_{t,\,SD}$, $D_{t,\,NC}$
Damage Limitation (DL)	60 years	0.5	0.27 m
Significant Damage (SD)	475 years	1.0	0.54 m
Near Collapse (NC)	1600 years	1.5	0.81 m

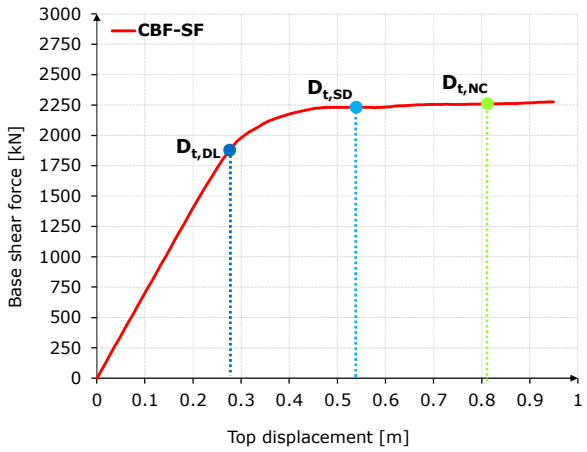

Fig. 6-105. *Pushover* analysis results: capacity curve corresponding to the *CBF-SF*

On the legend in figure Fig. 6-106, the structural damage is classified according to the acceptance criteria of FEMA 356 [108]. However, a correlation to the European standard prEN 1998-1-2 [51], could be considered as follows: Immediate Occupancy (IO) corresponds to DL; Life Safety (LS) corresponds to SD; Collapse Prevention (CP) corresponds to NC.

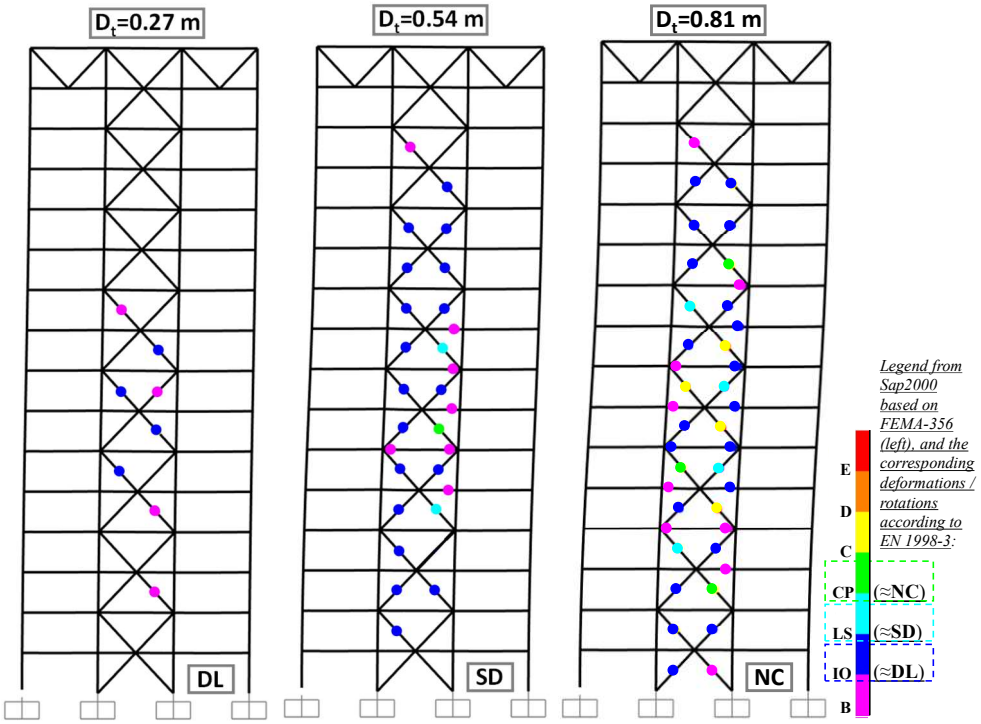

Fig. 6-106. *Pushover* results: structural damage of the *CBF-SF* at: a) DL; b) SD; c) NC

The maximum interstorey drifts obtained from *Pushover* on the *CBF-SF* are centralised in Table 6-23. According to the seismic code [51], the interstorey drift limit is 7.5 mrad at DL and 15 mrad at SD. As shown in Table 6-23, the 7.5 mrad interstorey drift limit at DL was only slightly exceeded. However, the maximum interstorey drift at SD was 18.5 mrad, which is 23.3 % larger than the limit imposed by the code for braced structural systems. Finally, the maximum interstorey drift at NC was 28.1 mrad. Based on the interstorey drifts resulted from the *Pushover* analysis, it is considered that the performance of the *CBF-SF* at SD could be improved.

Table 6-23 – Maximum interstorey drifts of the *CBF-SF* from *Pushover*

Limit states (LS)	Maximum interstorey drifts	prEN 1998-1-2 limits [51]
Damage Limitation (DL)	7.6 mrad	7.5 mrad
Significant Damage (SD)	**18.5 mrad**	15 mrad
Near Collapse (NC)	28.1 mrad	-

The plastic rotation within the plastic hinges of the SF beams located in the central span were verified at SD, the maximum value being 8.62 mrad. All rotation values that were obtained from the SF beams at SD are centralised in Table 6-24.

Table 6-24 – Plastic rotations in SF beams of the ***CBF-SF*** at **SD**, ***Pushover*** analysis

Storey	SF beams (central span)			
	PH-left		PH-right	
	θ_{pl} [mrad]	$M_{y,max}$ [kNm]	θ_{pl} [mrad]	$M_{y,max}$ [kNm]
16th	0.00	141	0.00	81
15th	0.00	56	0.00	41
14th	0.00	43	0.00	109
13th	0.00	121	0.00	169
12th	0.00	188	0.00	255
11th	0.00	253	0.00	402
10th	0.00	425	0.00	493
9th	0.00	407	3.90	623
8th	1.33	611	3.50	623
7th	0.00	571	**8.62**	638
6th	2.52	616	4.94	621
5th	0.00	411	7.80	635
4th	0.00	542	0.10	609
3rd	0.00	366	0.00	500
2nd	0.00	281	0.00	350
1st	0.00	219	0.00	173

Results of nonlinear dynamic analyses (Response-History Analyses)

The assessment of the seismic performance of the *CBF-SF* was completed with *Response History Analyses* (*RHA*), which according to Deierlein et al. [116], provide a more reliable seismic performance assessment and are more suitable for taller buildings. To this end, a set of seven semi-artificial accelerograms matching the target spectrum and meeting the criteria of the seismic code [45] was received as input and used in the current study. The set of accelerograms was selected from a database [109]. Details regarding these accelerograms are presented in Section 6.1.2, Table 6-15, and in Annex D of the current document. The results obtained from applying *RHA* on the *CBF-SF* are further discussed in terms of:

- average response values (obtained from the average of all accelerograms);
- maximum response values (obtained from the most unfavourable accelerogram). The most unfavourable accelerogram is considered to be the one that produces the greatest structural damage. In the current case study on the *CBF-SF*, the most unfavourable accelerogram is *#A4*.

The structural response of the *CBF-SF* under accelerogram *#A4* is shown in Fig. 6-107a,b,c at DL, SD and NC, and described in the following:

- at DL: elastic response of structural elements except for six braces located at mid-frame height; the deformations sustained by these braces were consistent with DL;
- at SD: plastic hinges were developed in most of the braces; the deformations sustained by the majority of these braces corresponded to DL; five braces located at mid-height of the frame ($7^{th} \div 11^{th}$ storeys) sustained deformations consistent with SD; from the 5^{th} to the 11^{th} storey, plastic hinges were also developed in the SF beams (roughly 34 % of the total number of potential plastic zones of the SF beams) with deformations corresponding to pre-DL;
- at NC: except for the 16^{th} and the 15^{th} storeys, plastic hinges were developed in all other braces; the damage to the braces was extensive – deformations corresponding to DL (eleven braces), SD (six braces), NC (six braces) and beyond NC (four braces); 75 % of all potential plastic zones in the SF beams

were activated at NC; the rotations within the plastic hinges of the SF beams were consistent with pre-DL and DL; at the base one central column from the 1st storey, a plastic hinge was developed; the deformation in this plastic hinge corresponded to DL (see Fig. 6-107c).

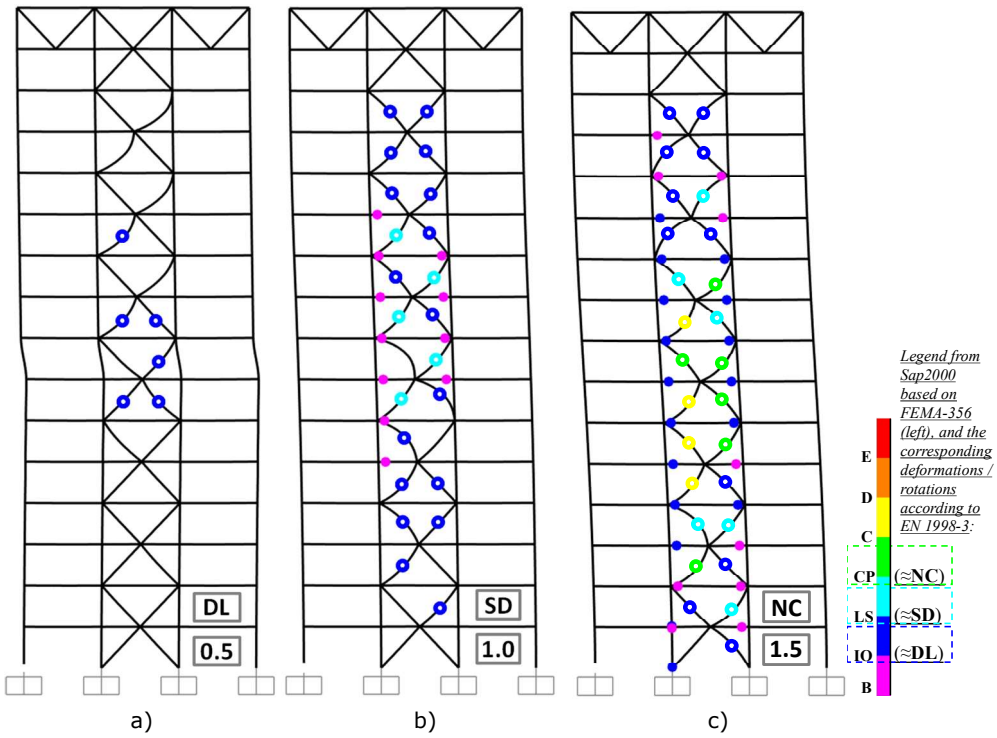

Fig. 6-107. Structural damage on the *CBF-SF* from *RHA* with accelerogram *#A4* at: a) DL; b) SD; c) NC

Average and maximum interstorey drifts of the *CBF-SF* were calculated and are presented in Table 6-25 together with the corresponding code limits. The average values, which were obtained as the mean of all seven accelerograms, are within the imposed limits of the code at both DL and SD. This is considered to be an indicator of adequate seismic performance. Maximum interstorey drifts in Table 6-25 were obtained by applying accelerogram *#A4*.

The distribution of average interstorey drifts over the height of the frame are shown in Fig. 6-108a. To be able to represent an average distribution of lateral deformation, values from all accelerograms at each individual storey were considered. In addition to the resulted distributions at DL, SD and NC, the interstorey drift limits imposed on braced structural systems by the seismic code [51] were represented in Fig. 6-108a with vertical dashed lines. As it can observed, neither of the interstorey drift limits at DL and SD was exceeded and the highest interstorey drift values were obtained at mid-height of the frame, e.g., $7^{th} \div 8^{th}$ storeys.

Accelerogram *#A4* was applied in order to obtain the maximum interstorey drifts, which are shown in Fig. 6-108b in the form of distributions over the height of the frame at each Limit State. The interstorey drift limits at DL and SD from the seismic code [51] are also depicted in this figure. As accelerogram *#A4* is the most unfavourable, the representation of the maximum interstorey drifts differs from the

one shown in Fig. 6-108a (obtained from average values). By applying accelerogram *#A4*, the highest interstorey drift values were obtained at the upper levels of the frame. For example, the maximum interstorey drift value at DL was 7.6 mrad, and occurred at the 11th storey. At SD, the values obtained between the 7th and the 11th storeys exceeded the limit of 15 mrad.

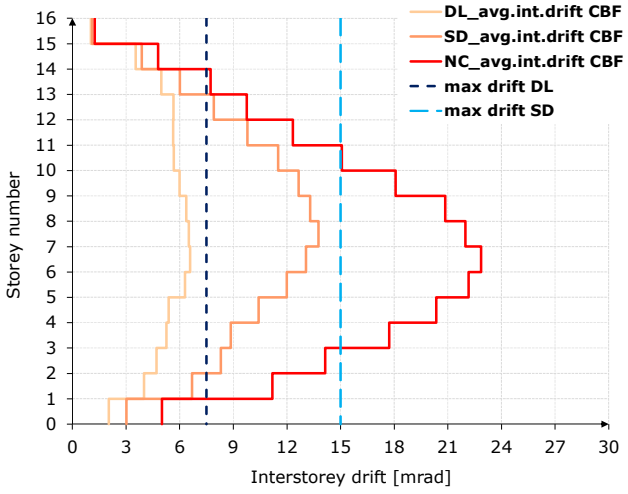

a)

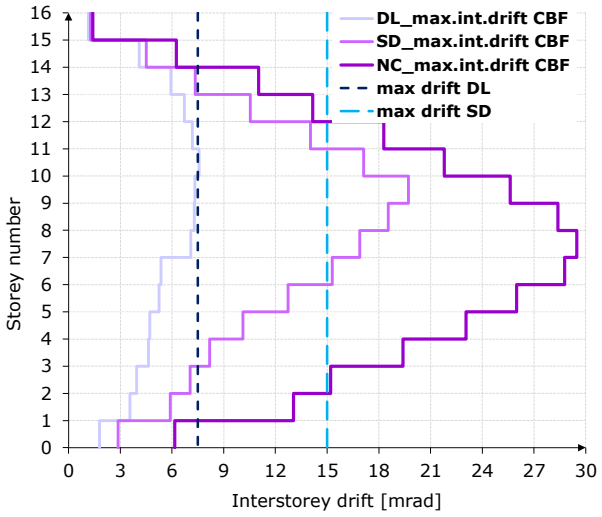

b)

Fig. 6-108. Distributions of interstorey drifts of the *CBF-SF* from *RHA* with: a) average values; b) maximum values (obtained from accelerogram *#A4*)

Table 6-25 – Average and maximum interstorey drifts of the *CBF-SF* from *RHA*

Limit states (LS)	Average drifts	Maximum drifts	prEN 1998-1-2 limits
Damage Limitation (DL)	6.6 mrad	7.6 mrad	7.5 mrad
Significant Damage (SD)	**13.8 mrad**	19.7 mrad	15.0 mrad
Near Collapse (NC)	22.9 mrad	29.5 mrad	-

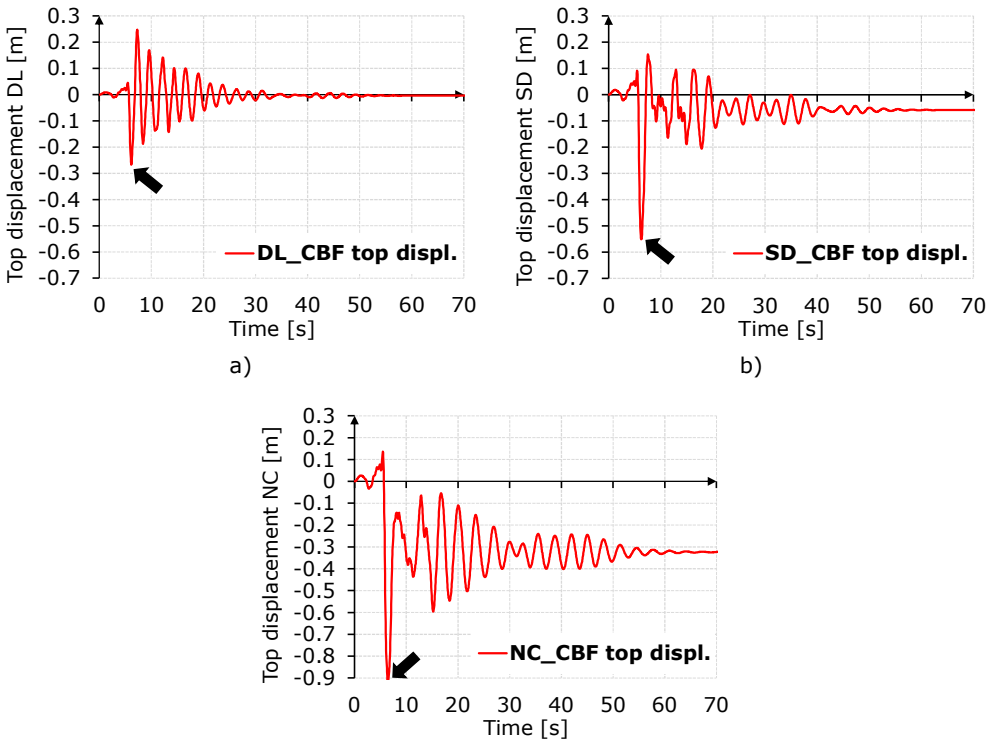

Fig. 6-109. Variation of top displacement in time of the *CBF-SF* from *RHA* with accelerogram *#A4* at: a) DL; b) SD; c) NC

Table 6-26 – Plastic rotations in SF beams of ***CBF-SF*** at **SD**, ***RHA*** with ***#A4***

Storey	SF beams (central span)			
	PH-left		PH-right	
	θ_{pl} [mrad]	$M_{y,max}$ [kNm]	θ_{pl} [mrad]	$M_{y,max}$ [kNm]
16th	0.00	93	0.00	145
15th	0.00	60	0.00	63
14th	0.00	50	0.00	48
13th	0.00	210	0.00	164
12th	0.00	516	0.00	448
11th	2.53	620	0.00	545
10th	4.97	627	2.68	620
9th	**8.82**	638	3.05	621
8th	7.24	634	4.95	627
7th	6.47	632	2.21	619
6th	1.88	621	0.00	600
5th	3.00	620	0.00	280
4th	0.00	428	0.00	360
3rd	0.00	572	0.00	160
2nd	0.00	344	0.00	275
1st	0.00	200	0.00	208

The variation of the top / roof displacement at DL, SD and NC, obtained by applying accelerogram *#A4*, is shown in Fig. 6-109a,b,c. As it can be observed in

these figures, a peak occurs at about 7 seconds, causing the following top displacements: 0.27 m at DL; 0.55 m at SD; 0.92 m at NC.

An evaluation of the plastic rotation from the plastic hinges of the SF beams was performed at SD by applying the most unfavourable accelerogram *#A4*. Values from all plastic hinges of SF beams are centralised Table 6-26. Considering the results in Table 6-26, the maximum is 8.82 mrad, which is similar to the value obtained at SD by performing *Pushover* (e.g., 8.62 mrad).

6.2.3 Concluding remarks

The current case study presented the evaluation of the seismic performance of a 16-storey Concentrically-Braced Frame with slim-floor beam-to-column joints (*CBF-SF*), which was assessed by nonlinear static and nonlinear dynamic analyses (e.g., *Pushover*, *RHA*) with SAP2000 [105].

The aim of the case study on the *CBF-SF* was (i) to verify the rotation demand resulted from the seismic load on the SF beam-to-column joint, (ii) to compare the joint demand to the experimental rotation capacity and (iii) to assess the seismic performance of the *CBF-SF* with SF beam-to-column joints. In accordance with the aims, the following objectives were established:

- adaptation of the developed numerical model for the SF beam-to-column joint to the braced structural system;
- application of structural analyses in the nonlinear range, e.g., *Pushover* and *Response-History Analysis* to the subject frame;
- monitoring of the structural damage at the three Limit States, with particular interest at DL and SD, in terms of interstorey drifts and plastic rotation within the plastic hinges of the SF beams.

Structural modelling. In general, the inelastic response of the SF beams from the central span was defined as in Section 6.1.2. In comparison to the joint model used for the case studies on MRFs, the joint model for the *CBF-SF* was considered to be rigid. The stiffness of the joint was verified in accordance with the code [79], this calculation allowing for the rigid classification. A rigorous approach was also taken to the modelling of braces. Based on information from the literature and on several iterations, two models of the "X" braces were developed, e.g., **phenomenological model** (*P hinge*) for *Pushover* analyses and **physical theory model** (*P-M2-M3 fibre plastic hinge*) for *RHA*. Comparisons to an experimental force-deformation curve of a brace with the same cross section (brace specimen *SP59-1* from [115]) provided information on the reliability of the developed models, which was proven to be adequate.

Evaluation of seismic performance with nonlinear structural analyses. The seismic performance of the *CBF-SF* was assessed based on the following criteria:

- development of global mechanism, which includes the history of plastic hinges, the location of plastic hinges and the value of the deformations sustained by plastic hinges in relation to the acceptance criteria of prEN 1998-1-2 [51];
- interstorey drifts values at DL and SD.

Depending on the type of nonlinear analysis, the seismic performance of the *CBF-SF* could be characterised differently. Based on the outcomes, the ***Pushover* analyses provided more conservative results**, which in terms of interstorey drifts, are similar to the ones obtained from applying *RHA* with accelerogram *#A4*, which was the most unfavourable. A good example of this is the interstorey drift at SD, which according to the results of the *Pushover* analyses, exceeded the limit of the

code [51] (e.g., 18.5 mrad interstorey drift > 15 mrad limit at SD) and was similar to the maximum value resulted from *RHA* with *#A4*, e g., 19.7 mrad. Judging solely by the *Pushover* results, the seismic performance of the *CBF-SF* could be improved at SD. However, the average results obtained by applying *RHA* with a set of seven accelerograms, proved the contrary. The **average interstorey drift values at DL and SD** (e.g., **6.6 mrad and 13.8 mrad,** respectively) obtained from *RHA*, which were within the imposed limits of the code, can be considered indicators of **adequate seismic performance**.

Another indicator of adequate seismic performance is the development of the global mechanism. In braced frames, **the development of plastic hinges needs to occur in braces prior to other structural elements**, as required by the seismic code. This condition is **principally satisfied** regardless of the nonlinear analysis applied to the frame. By the time plastic hinges within the dissipative zone of the SF beams attain pre-DL and DL deformations, extensive structural damage is already sustained by most of the braces.

The target displacements that were calculated at the three Limit States prior to performing *Pushover* analyses are similar to the maximum roof displacements obtained by applying *RHA* with accelerogram *#A4*:

- target displacement at DL, *Pushover*: 0.27 m;
- maximum roof displacement at DL, *RHA* with *#A4:* 0.27 m;
- target displacement at SD, *Pushover*: 0.54;
- maximum roof displacement at SD, *RHA* with *#A4:* 0.55 m;
- target displacement at NC, *Pushover*: 0.81;
- maximum roof displacement at NC, *RHA* with *#A4:* 0.92 m;

Interstorey drift demand vs rotation capacity. The **demands in terms of interstorey drifts** on SF beam-to-column joints, as resulted from nonlinear static and dynamic analyses applied to the *CBF-SF*, are as follows:

- **18.5 mrad** at SD from *Pushover*;
- **13.8 mrad** at SD from *RHA* (average of seven accelerograms).

In this context, the **available experimental rotation capacity** of the SF beam-to-column joint of **±45.35 mrad at SD** is **higher** than the **interstorey drift demand** that resulted from analyses on the *CBF-SF*.

Plastic rotation demand vs experimental plastic rotation capacity of the SF beams. Plastic rotations within the plastic hinges of the SF beams at SD were obtained from *Pushover* and *Response-History Analyses*, as follows: **8.62 mrad** from *Pushover* and **8.82 mrad** from *RHA* with accelerogram *#A4*. Considering the experimental plastic rotation capacity of the dissipative zone of the SF beam of 29.4 mrad at SD, the **demand is considerably lower than the available rotation**.

6.3 Dual Concentrically-Braced Frame

6.3.1 Design considerations

Dual Frames are stand-alone structural typologies in which different sub-systems are integrated. Consequently, some rules of the seismic code [51] refer to the integrated sub-systems, e.g., Moment-Resisting Frame, Concentrically-Braced Frame, while others to the entire structural system, e.g., Dual Frame. From the seismic design perspective, the main fuses to dissipate seismic energy in Dual Frames, consisting of CBF and MRFs, are the braces. This has implications for the beams of the MRF sub-systems, which play a secondary role in seismic energy dissipation. However, the beams of the MRF sub-systems could dissipate seismic energy in plastic hinges, thus participating in the global plastic mechanism; another possibility would be to help re-centre the structure after a seismic event, together with the columns and the moment-resisting connections, as shown in [117] [118] and [119].

The tested SF beam-to-column joint assemblies attained a rotation capacity of ± 45.35 mrad at SD by dissipating seismic energy through the development of a plastic hinge in the dissipative zone. While the stiffness classification of prEN 1993-1-8 [79] places the tested joint in a semi-rigid zone in the context of unbraced structural system such as the MRF, when the same joint is integrated into a braced system like a Dual Frame, it can be considered rigid in the analyses. By applying capacity design principles, the braces, followed by the SF beams, could dissipate seismic energy in plastic hinges, i.e., lead to a ductile global mechanism of the Dual Frame. Thus, the applicability of the SF beam-to-column joint to multi-storey structures subjected to seismic action is justified. The current case study on a Dual Frame consisting of CBF and MRFs is focused on achieving the following:

- adaptation of the SF beam-to-column joint model to the Dual Frame (*D-CBF*);
- evaluation of the: (i) plastic rotation demand in the plastic hinge of the SF beams, (ii) interstorey drift demand and (iii) overall seismic performance of the CBF with SF beam-to-column joints with nonlinear analyses;
- evaluation of the re-centring potential of the MRF sub-systems contained in the *D-CBF* following seismic events up to SD intensities.

Analysed frame, initial data

A 2D Dual Concentrically-Braced Frame *D-CBF* with SF beam-to-column joints was designed for the current case study. The initial data is presented in Table 6-27.

Table 6-27 – Input data for the analysed *D-CBF*

Characteristics:	
No. of spans & span length:	3 x 6.0 m
No. of storeys & storey height:	16 x 3.2 m
Flooring system:	Slim-floor system
Position of bracing system:	Central span of the *D-CBF*
Ductility class:	DC3
Behaviour factor:	q = 4.8
Consequence class:	CC2 (normal)
Ground conditions:	
Site category:	Type C
Peak Ground Acceleration:	a_g = 0.30·g

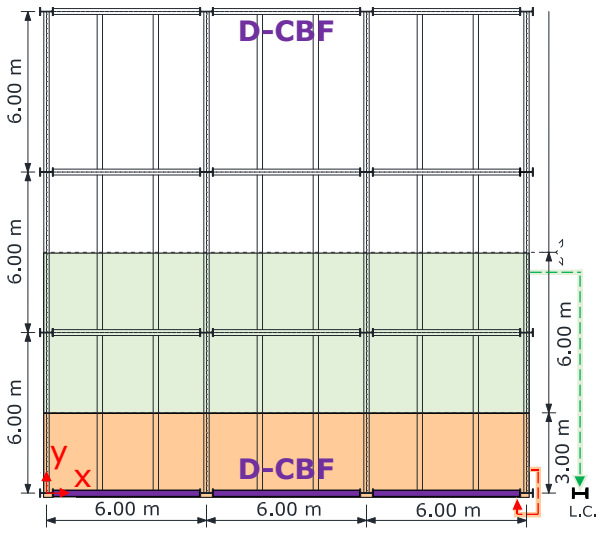

Fig. 6-110. Floor layout of the *D-CBF*

The configuration of the ***D-CBF*** on its height is the same as that of the *CBF-SF* (see Section 6.2.1, Fig. 6-102a). The floor layout is shown in Fig. 6-110. In the transverse X direction, the frame consisted of three spans of 6.0 m. The central span was braced over the entire height of the frame (CBF sub-system). Outer spans were unbraced (MRF sub-systems). The total height of the *D-CBF* was 51.2 m divided into 16 storeys of 3.2 m. Referring to Fig. 6-110, the lateral load-resisting system on the transverse X direction was comprised of two *D-CBFs*, whose position was on the perimeter of the floor layout. The rest of the structure in the transverse direction was considered to be part of the gravity load-resisting system. The longitudinal Y direction was considered only for the distribution of loads and seismic masses. The building category was office.

Boundary conditions and loads

The SF beams of the *D-CBF* were considered rigidly connected to the steel columns. For this purpose, the stiffness of the SF beam-to-column joints was verified as requested in prEN 1993-1-8 [79] and thereby classified as rigid. The bracing system was positioned in the central span of the *D-CBF* and consisted of "X" braces over the height of two storeys. Nominally pinned connections were assigned to brace ends. Fixed supports were defined at the bases of the columns.

The following load values were considered:

- permanent load uniformly distributed on floors of 5 kN/m^2;
- permanent load linearly distributed on marginal frames of 3.2 kN/m corresponding to 1 kN/m^2 of façade weight;
- live load uniformly distributed on floors of 3.8 kN/m^2;
- seismic load: response spectrum characterised by a_g = 0.3·g; soil type C, T_B = 0.1 s, T_C = 0.667 s, T_D = 3.94 s according to prEN 1998-1-1 [45].

Gravity loads acting on the gravity load-resisting system were assigned to a leaning column. Loads corresponding to half of one bay were assigned to the *D-CBF*, as shown in Fig. 6-110. A mass of 116.4 tons resulted at each storey.

Modelling of D-CBF

The structural elements of the *D-CBF* were: SF beams in the braced and unbraced sub-systems, "X" braces and steel columns. The cross section of the SF beams was the same as the one used for the SF beams of the tested joint assemblies. Steel braces arranged in "X" spanning over two storeys were used throughout the whole height of the central span. The modelling of the SF beams and braces was performed using the same considerations as those for the central span of the *CBF-SF* (see Section 6.2.1). The columns were made of H-steel profiles. A rigid diaphragm constraint was assigned to each storey level, as one of the methods used to account for the presence of the concrete slab. To optimise the steel use and avoid a longer fundamental period of vibration, an outrigger belt truss was positioned at the 16th storey. The columns were designed as steel structural elements.

The upper limit value of the behaviour factor for Dual Frames designed in DC3 was considered, q = 4.8.

Equivalent static design

Outcomes of the equivalent elastic design are presented in Table 6-28.

Table 6-28 – Results of equivalent elastic analyses on the *D-CBF*

	Structural elements:		
	▪ SF beams (CBF and MRF sub-systems included), S355		
Flr.	▪ Outer columns:	▪ Inner columns:	▪ Braces:
16	HE 360 B; S355	HE 360 B; S355	Outrigger belt truss: HE 200 B; S355
15	HE 360 B; S355	HE 360 B; S355	CHS-114.3 x 5.0 mm; S275
14	HE 360 B; S355	HE 360 B; S355	CHS-114.3 x 6.3 mm; S275
13	HE 360 B; S355	HE 360 B; S355	CHS-133.0 x 6.0 mm; S275
12	HE 360 B; S355	HE 360 B; S355	CHS-133.0 x 6.3 mm; S275
11	HE 360 B; S355	HE 360 B; S355	CHS-139.7 x 6.0 mm; S275
10	HE 450 B; S355	HE 450 B; S355	CHS-139.7 x 6.0 mm; S275
9	HE 450 B; S355	HE 450 B; S355	CHS-139.7 x 7.1 mm; S275
8	HE 500 B; S355	HE 500 B; S355	CHS-139.7 x 7.1 mm; S275
7	HE 500 B; S355	HE 500 B; S355	CHS-159.0 x 6.3 mm; S275
6	HE 600 B; S355	HE 600 B; S355	CHS-159.0 x 6.3 mm; S275
5	HE 600 B; S355	HE 600 B; S355	CHS-168.3 x 8.0 mm; S275
4	HE 600 B; S355	HE 600 M, S355	CHS-168.3 x 7.1 mm; S275
3	HE 600 B; S355	HE 600 M, S355	CHS-168.3 x 10.0 mm; S275
2	HE 600 B; S355	HE 700 M, S355	CHS-168.3 x 8.0 mm; S275
1	HE 700 M, S355	HE 700 M, S355	CHS-168.3 x 7.1 mm; S275
	Lateral displacement checks in the seismic design situation:		
	▪ Damage Limitation: $d_{r,max,DL}$ = 0.0062 < 0.0075 => OK		▪ Significant Damage: $d_{r,max,SD}$ = 0.0123 < 0.020 => OK
	Fundamental period of vibration: $T_{1,D\text{-}CBF}$ = 2.14 s		

The verification of structural elements was performed with the specific rules for steel members of prEN 1993-1-1 [54] and for seismic design in DC3 of prEN 1998-1-2 [51]. As the analysed frame was comprised of a central CBF sub-system and outer MRF sub-systems, verifications characteristic of each structural type from prEN 1998-1-2 [51] were followed. These rules are provided in the corresponding case studies on MRF and CBF in Section 6.1 and in Section 6.2. According to the seismic code, the

rule specific to Dual Frames imposes a contribution of the MRF sub-systems to the total resistance of the frame of at least 25 %. If the condition is fulfilled, the upper limit value of the behaviour factor q for a Dual Frame could be considered 4.8. The method to verify this requirement is presented in a separate section.

According to capacity design, structural elements are divided into dissipative (e.g., braces, dissipative zone of the SF beams) and non-dissipative (e.g., columns, connections) components. Non-dissipative components are designed by including the overstrength factor Ω. In Dual Frames, the value of the overstrength factor Ω should be taken as the maximum value between Ω_b, which comes from the braces, and Ω_d, which comes from the beams. In the current case, Ω_d was further considered in design, its value being 1.84. The value of Ω_b was smaller, e.g., 1.06. The overstrength value Ω results from assessments performed on the different sub-systems of the *D-CBF* multiplied by the strain hardening factor (γ_{sh} = 1.1) and by the material overstrength factor (γ_{rm} = 1.25 for steel S355), and was 2.53.

The results of the equivalent elastic design revealed that the design of the *D-CBF* was **governed by resistance**. The verification of the frame's sensitivity to second order effects was performed at each storey and, as the value of θ was under 0.10, the *D-CBF* was considered to be unaffected by second order effects.

6.3.2 Evaluation of seismic performance

Definition of nonlinear behaviour

A conceptual sketch of the nonlinear modelling of the D-CBF, with particular interest to the SF beam-to-column joints and braces is shown in Fig. 6-111.

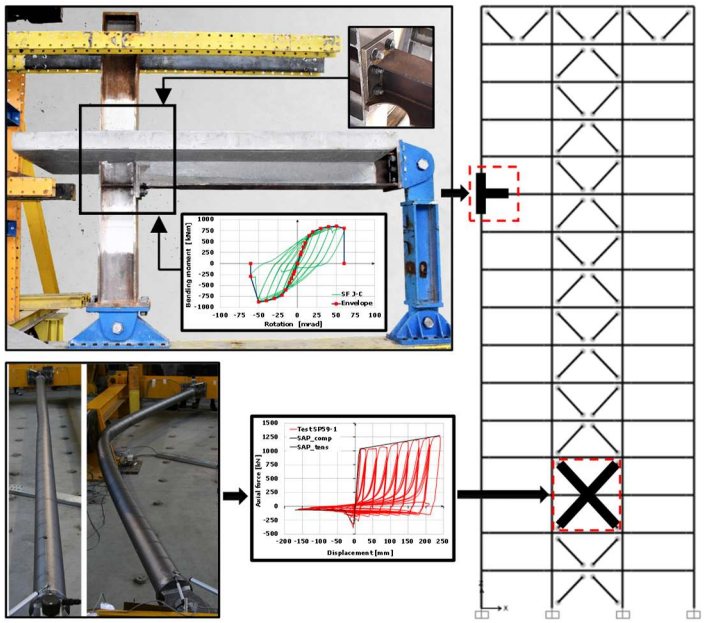

Fig. 6-111. Conceptual sketch of the nonlinear behaviour modelling of SF beams and braces

A full description of the nonlinear definition of the SF beams was presented in Section 6.1.2. Some of the main considerations are:

- plastic hinge type was suitable for members subjected to flexure;

- envelope curve was obtained from the cyclic experimental curve, from which the elastic part was removed; the envelope curve contained the plastic rotation of the dissipative zone of the SF beam, including the surrounding reinforced concrete slab.

The nonlinear response of the columns was defined through plastic hinges for members subjected to combined axial loading and flexure. The acceptance criteria for the columns were selected from EN 1998-3 [106].

Section 6.2.2 presents the modelling approach for the "X" braces in both the linear and nonlinear ranges. Two numerical models were developed for the braces: a phenomenological (*P hinge*) and a physical theory model (*P-M2-M3 fiber plastic hinge*). The solution was preferred due to some convergence issues that were encountered during several iterations. The acceptance criteria of FEMA 356 [108] for CHS braces (see Table 6-20) were applied. The accuracy of the models was confirmed by comparing the results (in terms of force and deformation) with experimental results of a brace with the same cross section as the numerically modeled ones. Given the similarity to the experimental results (see Fig. 6-103a,b), the phenomenological model was used for *Pushover* analyses, while the physical theory model - for *RHA*.

Contribution of MRF sub-systems to total resistance

According to prEN 1998-1-2 [51], MRFs sub-systems of Dual Frames are required to provide a contribution of at least 25 % to the global resistance of the frame. This verification is specific to Dual Frames and it conditions the use of the upper limit value of the behaviour factor *q* for this structural type. The upper limit value of *q* for Dual Frames with CBF is 4.8. As the seismic code does not provide a particular method for this check, a few existing analytical approaches were implemented. For instance, Eq.(6.75), Eq. (6.76) and Eq. (6.77) were used by Vulcu et al. [120]. Eq. (6.78) is proposed in [121].

Method 1. Assuming a contribution of at least 25 % of the MRF sub-systems to the total resistance of the frame, individual assessments of the resistance of sub-systems included in the *D-CBF* were performed at each storey. According to Eq. (6.77), the resistance of the CBF sub-system is provided by the horizontal projection of the axial plastic resistance under tension N_{pl}^{+} and by 30 % of the buckling resistance of the braces N_{pl}^{-}. The resistance of the MRF sub-systems corresponding to a Dual Frame with 2 MRF bays results from the plastic moment resistance of the dissipative zone $M_{pl,b}$ multiplied by four (two beams with four dissipative zones per storey) and divided by the storey height *H* (see Eq. (6.78)). By using this set of formulae, a contribution of **43 % of two MRF sub-systems** resulted. This value corresponded to both the MRF sub-systems, i.e., **21.5 % per one MRF sub-system**.

$$V_{Rd,i}^{MRFs} \geq 0.25 \cdot V_{Rd,i}^{DUAL} \tag{6.75}$$

$$V_{Rd,i}^{DUAL} = \frac{1}{0.75} \cdot V_{Rd,i}^{CBF} \tag{6.76}$$

$$V_{Rd,i}^{CBF} = \left(N_{pl}^{+} + 0.3 \cdot N_{pl}^{-}\right) \cdot cos\,\alpha_i \tag{6.77}$$

$$V_{Rd,i}^{MRF} = \frac{4 \cdot M_{pl,b}}{H} \tag{6.78}$$

Method 2. The resistance of the CBF, as described by formula Eq. (6.77), is calculated by taking into consideration only the resistance of braces. Since the *D-CBF* consists of a CBF sub-system with rigidly connected SF beams, the present study proposes that their resistance is calculated using Eq. (6.79). Results of this calculation at each storey are shown in Table 6-29, where the minimum contribution of two MRF sub-systems can be observed at the 3rd storey. By taking into account the braces and SF beams to calculate the resistance of the CBF sub-system with Eq. (6.79), the contribution of the CBF sub-system is higher than if calculated with Eq. (6.77). In this case, the contribution of the **two MRF sub-systems** decreases to **31 %**, nevertheless this value fulfils the criterion of the seismic code.

$$V_{Rd,i}^{CBF} = V_{Rd,i}^{CBF,braces} + V_{Rd,i}^{CBF,beams} = \left[\left(N_{pl}^{+} + 0.3 \times N_{pl}^{-}\right) \times cos\,\alpha_i\right] + \left(\frac{2 \times M_{pl,b}}{H}\right) \quad (6.79)$$

Table 6-29 – Contribution of MRF sub-systems to total resistance of the *D-CBF*

Flr.	Brace	$CBF_{subsys.}$		$MRF_{subsys.}$	D-CBF		Contribution
		V_{Rd}^{CBF}	V_{Rd}^{MRF}	V_{Rd}^{MRFs}	$V_{Rd}^{D\text{-}CBF}$	$0.25 \cdot V_{Rd}^{D\text{-}CBF}$	MRF_{subsys} %
16	-	-	-	-	-	-	-
15	-	-	-	-	-	-	-
14	CHS 114.3*6.3	536.7	382.6	765.3	1684.6	421.2	45
13	CHS 133*6	620.3	382.6	765.3	1768.2	442.0	43
12	CHS 133*6.3	649.5	382.6	765.3	1797.4	449.3	43
11	CHS 139.7*6	659.4	382.6	765.3	1807.3	541.8	42
10	CHS 139.7*6	659.4	382.6	765.3	1807.3	451.8	42
9	CHS 139.7*7.1	772.8	382.6	765.3	1920.6	480.2	40
8	CHS 139.7*7.1	772.8	382.6	765.3	1920.6	480.2	40
7	CHS 159*6.3	809	382.6	765.3	1956.8	489.2	39
6	CHS 159*6.3	809	382.6	765.3	1956.8	489.2	39
5	CHS 168.3*8	1086	382.6	765.3	2234.0	558.5	34
4	CHS 168.3*7.1	970.1	382.6	765.3	2117.9	529.5	36
3	CHS 168.3*10	1338	382.6	765.3	2486.4	621.6	**31**
2	CHS 168.3*8	1086	382.6	765.3	2234.0	558.5	34
1	CHS 168.3*7.1	970	382.6	765.3	2117.9	529.5	36

Method 3. To confirm the 31 % that was analytically obtained, another approach to assess the contribution of MRF sub-systems is used. This method implies the use of a structural analysis software, e.g., SAP2000 [105]. The objective is to obtain the base shear force - top displacement curves (i.e., the capacity curves) of the following structures:

- the whole frame – the *D-CBF*;
- the MRF sub-systems of the *D-CBF*;
- the CBF sub-system of the *D-CBF.*

For this purpose, a "modal" pattern of lateral forces is applied to: (i) the *D- CBF*, (ii) to the MRF sub-systems of the *D-CBF* and (iii) to the CBF sub-system of the *D-CBF* (see Fig. 6-112a-c). Description of the approach, as follows:

- approach for the *D-CBF*: the capacity curve corresponding to the *D-CBF* was obtained following nonlinear definitions (see Fig. 6-112a);
- approach for the MRF sub-systems of the *D-CBF*: on the following frame model, the influence of the CBF sub-system was disregarded in order to obtain the contribution of the MRF sub-systems of the *D-CBF*. For this, the braces were removed from the frame model and the rigid beam-to-column

connections from the CBF sub-system were changed to nominally pinned (see Fig. 6-112b). Followingly, a *Pushover* analysis was performed on this frame (containing only the contribution of the MRF sub-systems) and the corresponding capacity curve was obtained;

- approach for the CBF sub-system of the *D-CBF*: on the third frame model, the contribution of the MRF sub-systems was disregarded by changing the beam-to-column connections from these spans from rigid to nominally pinned (see Fig. 6-112c). The *Pushover* analysis provided the corresponding capacity curve.

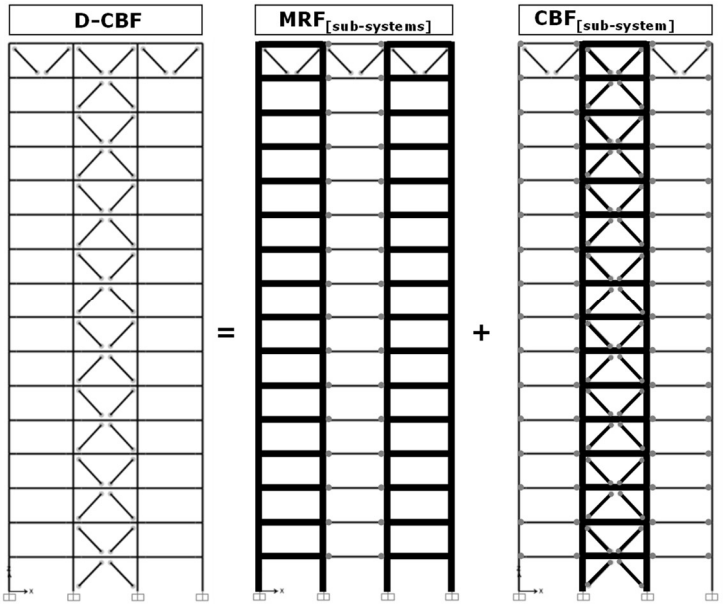

Fig. 6-112. Frame models developed to assess the contribution of the MRF sub-systems to the total resistance of the D-CBF: a) *D-CBF*; b) MRF sub-systems; c) CBF sub-system

The resulted capacity curves corresponding to the three different frame models, e.g., *D-CBF*, MRF sub-systems of *D-CBF* and CBF sub-system of *D-CBF*, are shown in Fig. 6-113 in parallel. These were evaluated at DL, SD and NC. For this purpose, the capacity curves of the frames were compared at displacement values equal to the target displacements of the *D-CBF*: 0.25 m at DL; 0.50 m at SD; 0.75 m at NC. The target displacements, as well as the resulted base shear forces at DL, SD and NC of the three frame models are centralised in Table 6-30. Based on the value of the base shear forces at the target displacements, the following contribution of the **two MRF sub-systems** to the total resistance of the D-CBF was obtained:

- at DL: approximately **25 %**;
- at SD: approximately **35 %**;
- at NC: approximately **36 %**.

Considering these results, it is concluded that the rule of the seismic code prEN 1998-1-2 [51], which requires a minimum contribution of 25 % of the MRF sub-systems to the total resistance of the *D-CBF*, was **fulfilled**.

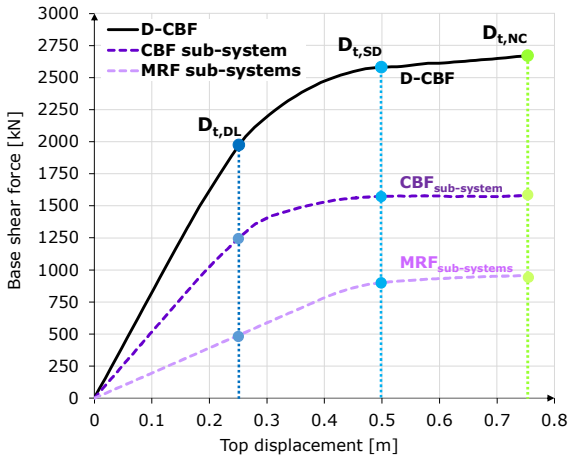

Fig. 6-113. Comparison of capacity curves: the *D-CBF*, MRF sub-systems and CBF sub-system

Table 6-30 – Target displacements (D-CBF) & base shear forces of *D-CBF* & MRF sub-systems

Limit States (LS)	Target displacements $D_{t,DL}$, $D_{t,SD}$, $D_{t,NC}$	Base shear force	
		D-CBF	MRF sub-systems
Damage Limitation (DL)	0.25 m	1974.2 kN	484.8 kN
Significant Damage (SD)	0.50 m	2580.3 kN	900.0 kN
Near Collapse (NC)	0.75 m	2671 kN	955.8 kN

Results of nonlinear static analyses (Pushover)

The "modal" distribution of lateral forces in Fig. 6-114a,b was applied to the *D-CBF* prior to performing the *Pushover* analysis considering the modal shape of the fundamental mode of vibration (see Fig. 6-114a). The performance factors corresponding to CC2 were applied, as follows: a_g / a_{gr} = 0.5 at DL; a_g / a_{gr} = 1.0 at SD and a_g / a_{gr} = 1.5 at NC. The target displacements presented in Table 6-30 were calculated using the *N2 method* [107] and are marked on the capacity curve in Fig. 6-115. The structural damage that was sustained at the three target displacements, is shown in Fig. 6-116a-c, and revealed the following:

- at DL: elastic response of the frame except for seven compressed braces located at mid-height (5^{th}÷11^{th} storeys); plastic hinges were developed in these braces with deformations corresponding to DL; in three other braces from the first storeys plastic hinges were developed, however the attained deformations were consistent with pre-DL;
- at SD: plastic hinges were developed in the braces of the CBF sub-system at most storeys (1^{st}÷14^{th} storeys); in most of these, the deformations corresponded to DL; plastic hinges in three braces attained SD deformations; deformations sustained in one brace exceeded NC; in the SF beams of the MRF sub-systems plastic hinges with deformations corresponding to pre-DL were developed (3^{rd}÷10^{th} storeys); in four SF beams from the CBF sub-system plastic hinges with deformations corresponding to pre-DL were developed (5^{th}÷8^{th} storeys); the columns remained in the elastic range;
- at NC: the deformations in approximately half of the braces corresponded to DL; in the other half of the braces, deformations corresponding to either SD

or post-NC were evidenced; plastic hinges were developed in the SF beams from the MRF sub-systems (2nd ÷ 10th storeys) with deformations attaining pre-DL and DL; plastic hinges were also developed in the SF beams from the CBF sub-system (deformations corresponding to pre-DL and DL); plastic hinges were not developed in the columns.

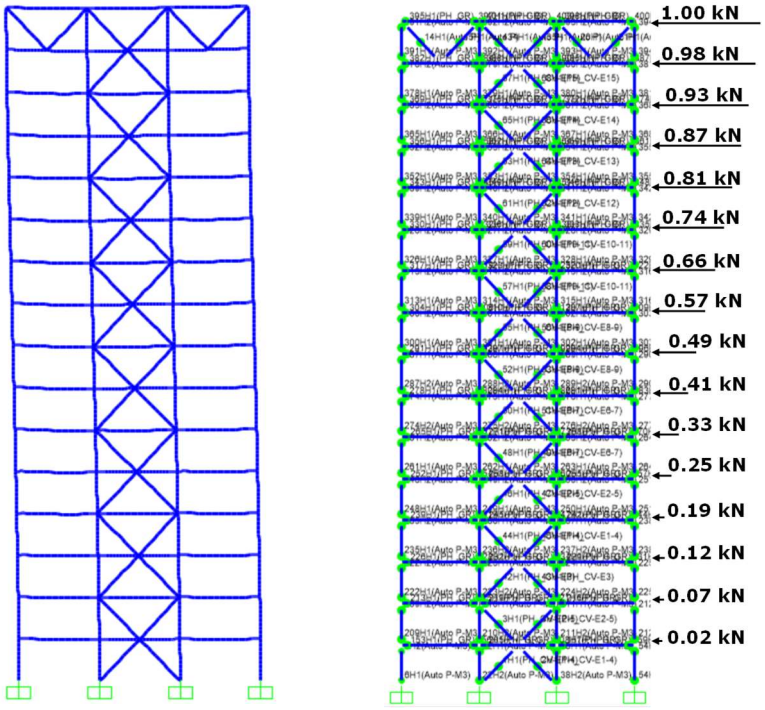

a) b)

Fig. 6-114. Lateral load distribution of forces for *Pushover* on the *D-CBF*: a) modal shape of the fundamental mode of vibration; b) "modal" pattern of forces

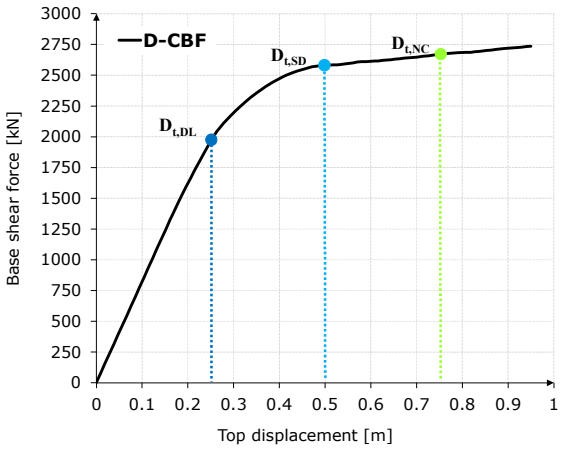

Fig. 6-115. *Pushover* analysis results: capacity curve corresponding to the *D-CBF*

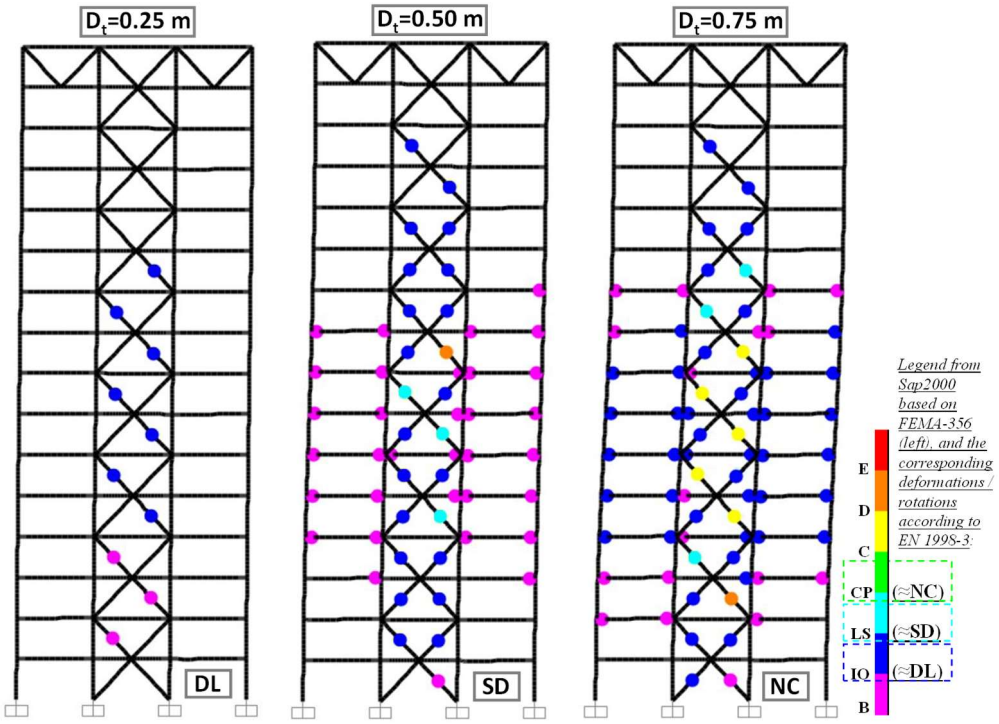

a) b) c)

Fig. 6-116. *Pushover* results: structural damage of the *D-CBF* at: a) DL; b) SD; c) NC

A correlation between the acceptance criteria of FEMA 356 [108] and the European standard prEN 1998-1-2 [51] was made in terms of structural damage on the legend in figure Fig. 6-116c. The correlation could be considered as follows: Immediate Occupancy (IO) corresponds to DL; Life Safety (LS) corresponds to SD; Collapse Prevention (CP) corresponds to NC.

The maximum interstorey drifts that were obtained from the *Pushover* analysis on the *D-CBF* are centralised in Table 6-31 together with the interstorey drift limits for Dual Frames of prEN 1998-1-2 [51]. The highest interstorey drift value at DL occurred at the 9th storey. At SD, the maximum value was evidenced at the 7th storey. In comparison to the code limits at DL and SD (i.e., 7.5 mrad, 20 mrad, respectively), the interstorey drifts corresponding to the *D-CBF* at the same Limit States were smaller, e.g., 6.7 mrad at DL and 17 mrad at SD. This is considered to be an indicator of adequate seismic performance.

Table 6-31 – Maximum interstorey drifts of the *D-CBF* from *Pushover*

Limit states (LS)	Maximum interstorey drifts	prEN 1998-1-2 limits [51]
Damage Limitation (DL)	6.7 mrad	7.5 mrad
Significant Damage (SD)	**17.0 mrad**	20 mrad
Near Collapse (NC)	28.2 mrad	-

The plastic rotations in the SF beams, that resulted from the *Pushover* analysis, were assessed at SD. These are centralised in Table 6-32 and Table 6-33,

sorted by sub-systems. The **highest plastic rotation demand** for the SF beams belonging to the MRF sub-systems was **8.60 mrad**. A smaller demand resulted for the SF beams from the CBF sub-system, e.g., 4.22 mrad.

Table 6-32 – Plastic rotations in SF beams: MRF sub-systems of the *D-CBF* at SD, *Pushover*

Storey	MRF sub-system left, SF beams				MRF sub-system right, SF beams			
	PH-left		PH-right		PH-left		PH-right	
	θ_{pl} [mrad]	$M_{y,max}$ [kNm]	θ_{pl} [mrad]	$M_{y,max}$ [kNm]	θ_{pl} [mrad]	$M_{y,max}$ [kNm]	θ_{pl} [mrad]	$M_{y,max}$ [kNm]
16th	0.00	25	0.00	64	0.00	7.9	0.00	63
15th	0.00	61	0.00	114	0.00	133	0.00	158
14th	0.00	157	0.00	237	0.00	200	0.00	288
13th	0.00	207	0.00	284	0.00	257	0.00	346
12th	0.00	278	0.00	353	0.00	324	0.00	415
11th	0.00	390	0.00	463	0.00	408	0.00	518
10th	0.00	528	0.00	582	0.00	551	1.52	615
9th	4.89	610	2.95	617	0.12	608	4.49	621
8th	3.29	621	4.84	626	3.26	617	7.18	629
7th	4.88	624	6.48	632	4.59	625	**8.60**	634
6th	5.00	621	6.57	627	4.86	621	8.20	635
5th	3.44	618	5.60	625	3.21	617	6.47	631
4th	0.87	615	3.02	617	0.79	610	3.84	624
3rd	0.00	540	0.34	609	0.00	538	0.50	610
2nd	0.00	413	0.00	474	0.00	412	0.00	480
1st	0.00	234	0.00	311	0.00	254	0.00	317

Table 6-33 – Plastic rotations in SF beams: CBF sub-system of the *D-CBF* at SD, *Pushover*

Storey	CBF sub-system, SF beams			
	PH-left		PH-right	
	θ_{pl} [mrad]	$M_{y,max}$ [kNm]	θ_{pl} [mrad]	$M_{y,max}$ [kNm]
16th	0.00	107	0.00	27
15th	0.00	42	0.00	21
14th	0.00	10	0.00	75
13th	0.00	26	0.00	87
12th	0.00	43	0.00	40
11th	0.00	92	0.00	252
10th	0.00	249	0.00	340
9th	0.00	275	0.00	584
8th	0.00	531	0.00	613
7th	0.00	593	2.81	617
6th	0.00	612	2.81	621
5th	0.00	457	**4.22**	623
4th	0.00	501	0.00	580
3rd	0.00	310	0.00	581
2nd	0.00	300	0.00	375
1st	0.00	260	0.00	207

Based on the results obtained from *Pushover* analyses, the D-CBF evidenced an **adequate seismic performance**.

Results of nonlinear dynamic analyses (Response-History Analyses)

The seismic performance assessment of the *D-CBF* with *Response-History Analysis* is presented in the current section. *RHA* was performed by using a set of

seven accelerograms [109] (see Section 6.1.2, Table 6-15 and in Annex D). The seismic performance of the *D-CBF* was assessed considering two different situations:

- average response values (obtained as the average from all accelerograms);
- maximum response values (obtained by applying the most unfavourable accelerogram from the set of seven). In this case, the accelerogram that causes the greatest structural damage is accelerogram *#A3*.

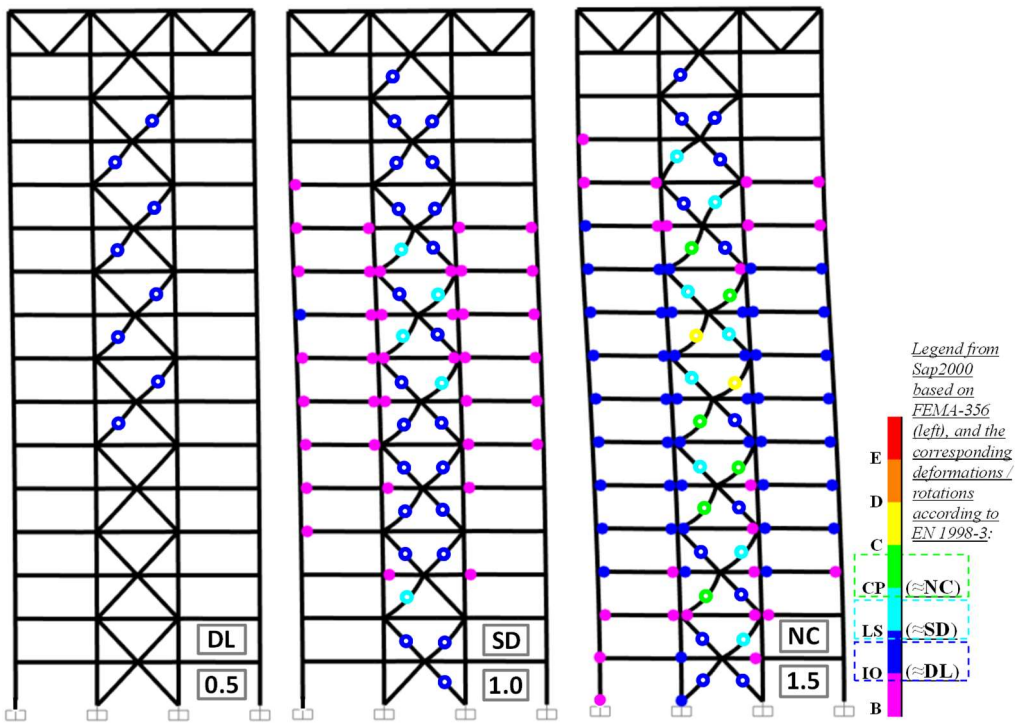

Fig. 6-117. Structural damage on the *D-CBF* from *RHA* with accelerogram *#A3* at: a) DL; b) SD; c) NC

The structural state at DL, SD and NC, that was caused by the most unfavourable accelerogram *#A3*, is shown in Fig. 6-117a-c. Damage to the *D-CBF* can be described as follows:

- at DL: elastic response of the frame except for eight compressed braces (7^{th} ÷14^{th} storeys); deformations sustained by these braces corresponded to DL; plastic hinges were not developed in the SF beams or columns;
- at SD: plastic hinges were developed in most of the braces (1^{st}÷15^{th} storey); except for the plastic hinges of five braces, which attained deformations consistent with SD (3^{rd}, 8^{th}÷11^{th} storeys), plastic hinges in other diagonal members sustained deformations corresponding to DL; plastic hinges were also developed in the SF beams of the MRF and CBF sub-systems; in the MRF sub-systems, the rotations reached in the plastic hinges of the SF beams corresponded to pre-DL (3^{rd}÷12^{th} storeys); at the 3^{rd}, 5^{th}, 7^{th}÷10^{th} storeys, some plastic hinges were developed in the SF beams from the CBF sub-

systems; the rotations corresponded to pre-DL; the columns remained in the elastic range;

- at NC: plastic hinges were developed in all braces (exception: 15th storey); in half of the braces, DL deformations were attained; in the remaining half, the deformations corresponded to either SD, NC or post-NC; the plastic hinges with the highest deformations were developed in the braces located at the 8th and 9th storeys; compared to SD, a higher number of plastic hinges were developed in the SF beams from all sub-systems; most of the plastic hinges in the SF beams from the MRF and CBF sub-systems attained DL rotations; plastic hinges were developed at the base of two columns (1st storey); the deformations in these plastic hinges corresponded to pre-DL in the outer column and to DL in the inner column.

The variation of the roof or top displacement of the *D-CBF*, that was caused by the most unfavourable accelerogram, i.e., *#A3*, at DL, SD and NC is presented in Fig. 6-118a,b,c. As it can be observed in Fig. 6-118a,b,c, the peak values in roof displacement occurred at approximately 6 seconds. These peak values were as follows: 0.25 m at DL; 0.53 m at SD and 0.85 m at NC. Residual roof displacements were evidenced at SD and NC.

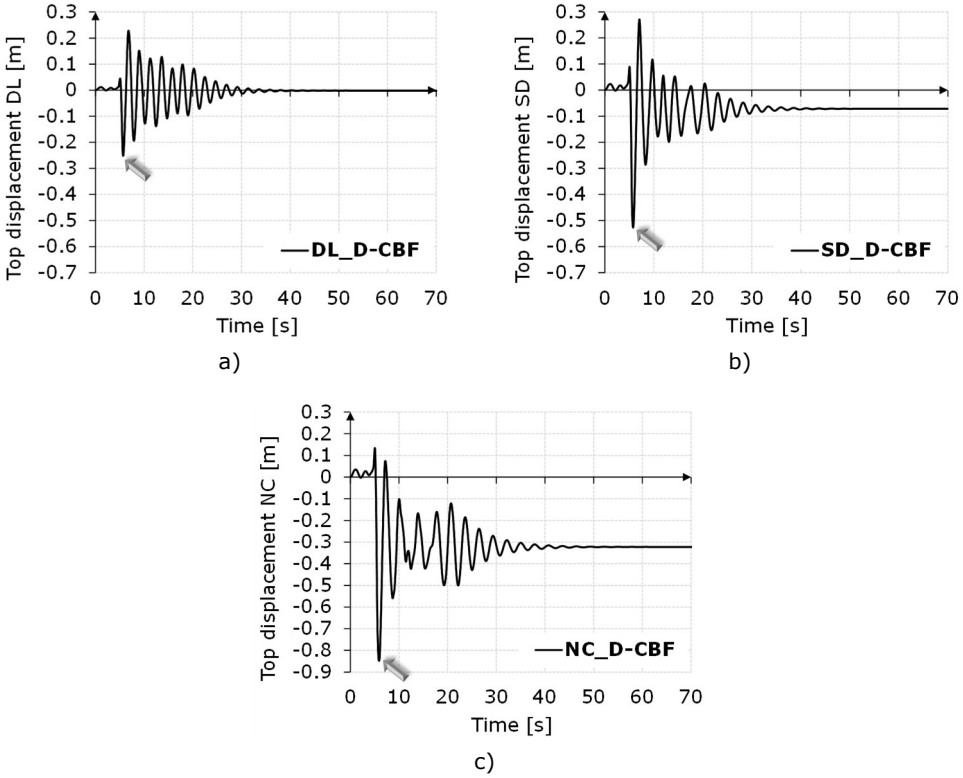

Fig. 6-118. Variation of top displacement in time of the *D-CBF* from *RHA* with accelerogram *#A3* at: a) DL; b) SD; c) NC

Average and maximum interstorey drifts of the *D-CBF* are centralised in Table 6-34 together with the limits of the prEN 1998-1-2 [51]. Whereas the average values

were obtained as the mean of the seven accelerograms, the maximum ones - by applying accelerogram *#A3*. As it can be observed in Table 6-34, the interstorey drifts at DL and SD (7.1 mrad at DL; **11.7 mrad at SD**) were within the imposed limits. Distributions of the average and maximum interstorey drifts are shown in Fig. 6-119a,b in parallel to the acceptance criteria of [51]. The average interstorey drift distributions at DL and SD evidenced **values within acceptable limits**.

Table 6-34 – Average and maximum interstorey drifts of the *D-CBF* from *RHA*

Limit states (LS)	Average drifts	Maximum drifts	prEN 1998-1-2 limits
Damage Limitation (DL)	7.1 mrad	8.9 mrad	7.5 mrad
Significant Damage (SD)	**11.7 mrad**	19.4 mrad	20.0 mrad
Near Collapse (NC)	20.6 mrad	27.3 mrad	-

Average transitory interstorey drifts vs. prEN 1998-1-2 criteria

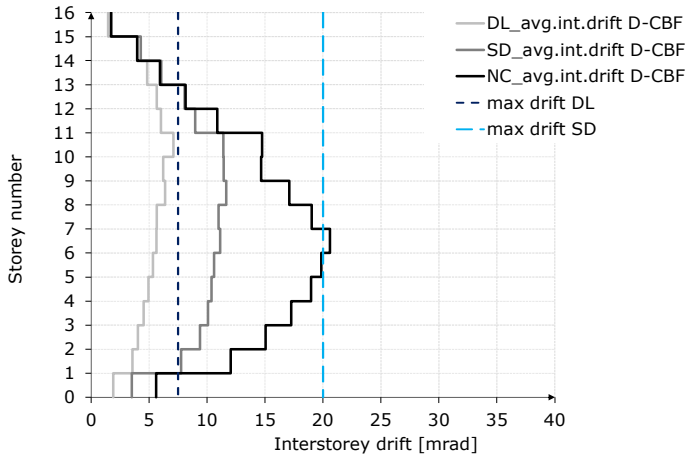

a)

Maximum transitory interstorey drifts vs. prEN 1998-1-2 criteria

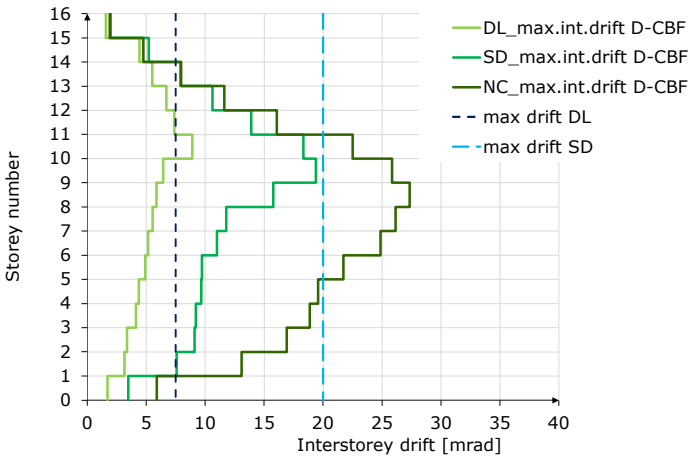

b)

Fig. 6-119. Distributions of interstorey drift of the *D-CBF* from *RHA* with: a) average values; b) maximum values (obtained from accelerogram *#A3*)

Permanent interstorey drifts vs. FEMA 356 criteria

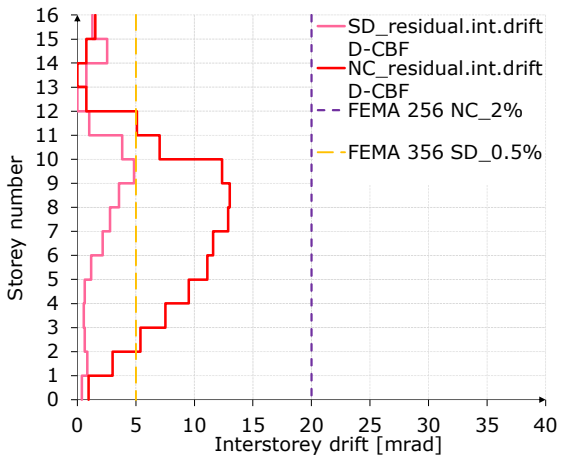

Fig. 6-120. Distributions of permanent interstorey drifts of the *D-CBF* from *RHA* with *#A3*

The permanent interstorey drifts corresponding to the *D-CBF* were assessed at SD and NC, and represented in Fig. 6-120. According to the acceptance criteria of FEMA 356 [108], permanent drifts of braced structural systems should be:

- negligible at DL;
- limited to 0.5 % at SD;
- limited to 2 % at NC.

The limits of FEMA 356 [108] at SD and NC are also shown in Fig. 6-120 in order to facilitate the comparison to the permanent drifts of the *D-CBF*. As it can be observed in this figure, the **permanent interstorey drifts were smaller** than the **limits of FEMA 356** at both the SD and the NC Limit States.

Table 6-35 – Plastic rotations in SF beams: MRF sub-systems of the *D-CBF* at SD, *RHA* with accelerogram *#A3*

Storey	MRF sub-system left, SF beams				MRF sub-system right, SF beams			
	PH-left		PH-right		PH-left		PH-right	
	θ_{pl}	$M_{y,max}$	θ_{pl}	$M_{y,max}$	θ_{pl}	$M_{y,max}$	θ_{pl}	$M_{y,max}$
	[mrad]	[kNm]	[mrad]	[kNm]	[mrad]	[kNm]	[mrad]	[kNm]
16th	0.00	60	0.00	53	0.00	68	0.00	56
15th	0.00	214	0.00	175	0.00	170	0.00	145
14th	0.00	430	0.00	349	0.00	390	0.00	325
13th	0.00	566	0.00	448	0.00	496	0.00	431
12th	2.22	619	0.00	556	0.00	603	0.00	555
11th	5.70	629	0.65	614	2.86	621	1.58	617
10th	**9.54**	642	5.18	628	6.64	632	5.71	629
9th	8.31	645	6.33	631	7.56	637	4.56	632
8th	7.06	639	4.79	626	6.44	632	3.44	627
7th	6.36	632	2.56	620	4.41	626	2.75	621
6th	3.91	624	0.69	614	2.46	620	0.70	613
5th	1.76	618	0.00	570	1.29	616	0.00	582
4th	0.68	614	0.00	550	0.00	610	0.00	548
3rd	0.00	607	0.00	517	0.00	612	0.00	530
2nd	0.00	566	0.00	479	0.00	539	0.00	466
1st	0.00	383	0.00	324	0.00	370	0.00	296

Table 6-36 – Plastic rotations in SF beams: CBF sub-system of the *D-CBF* at SD, *RHA* with accelerogram *#A3*

Storey	CBF sub-system, SF beams			
	PH-left		PH-right	
	θ_{pl} [mrad]	$M_{y,max}$ [kNm]	θ_{pl} [mrad]	$M_{y,max}$ [kNm]
16th	0.00	99	0.00	108
15th	0.00	46	0.00	37
14th	0.00	209	0.00	113
13th	0.00	344	0.00	164
12th	0.00	402	0.00	280
11th	0.00	567	0.00	423
10th	3.60	623	0.76	614
9th	**6.39**	631	0.95	615
8th	3.33	622	0.69	614
7th	0.22	613	0.00	604
6th	0.00	556	0.00	460
5th	1.05	615	0.00	248
4th	0.00	438	0.00	352
3rd	2.90	621	0.00	125
2nd	0.00	447	0.00	363
1st	0.00	210	0.00	415

The plastic rotations within the plastic hinges of the SF beam from all sub-systems of the D-CBF were assessed at SD. For this purpose, accelerogram *#A3*, which is the most unfavourable, was applied on the frame. The results in terms of plastic rotation and maximum bending moment in each plastic hinge are centralised in Table 6-35 and Table 6-36. Judging by the results from these tables, the **maximum demand in plastic rotation is 9.54 mrad**. This value was evidenced in the SF beams from the MRF sub-systems at the 10th storey.

Considering the results of the *D-CBF* obtained from *RHA*, **an adequate seismic performance** was evidenced.

Comparison of D-CBF results: Pushover vs Response-History Analysis

Comparisons in terms of interstorey drifts obtained from applying *Pushover* and *RHA* are presented in the current section. Firstly, in the case of *RHA*, the results used in these comparisons represent the average values of the seven accelerograms. Distributions of interstorey drifts from the two analyses are shown at SD in Fig. 6-121a and at NC in Fig. 6-121b. As it can be observed in both of these figures, the *Pushover* analysis provided higher interstorey drift values at SD and NC than the results obtained from *RHA* (average values):

- *Pushover*, at SD: 17 mrad; at NC: 28.2 mrad;
- *RHA* (average), at SD: 11.7 mrad; at NC: 20.6 mrad.

Followingly, by comparing the interstorey drifts obtained from *Pushover* to those obtained from *RHA* with the most unfavourable accelerogram *#A3*, the difference between the results is significantly reduced at SD and NC (see Fig. 6-121c,d). Considering the maximum results obtained from *RHA* with *#A3*, the following interstorey drifts were evidenced: 19.4 mrad at SD and 27.3 mrad at NC.

These comparisons between the *Pushover* and the *RHA* results evidence a **more conservative character of the nonlinear static analysis results**. This conclusion is supported by the similarity of the *Pushover* results to those obtained from the most unfavourable accelerogram.

Pushover vs. *RHA* (**average**) transitory interstorey drifts at **SD**

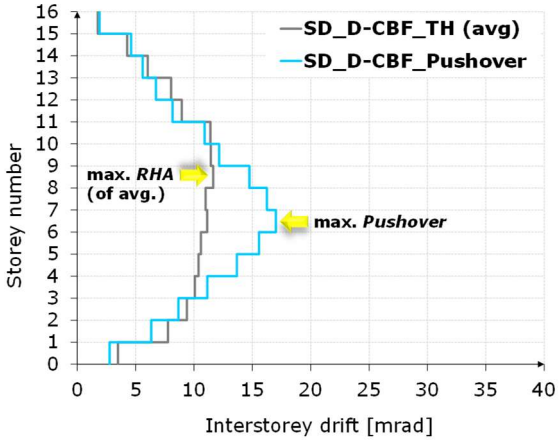

a)

Pushover vs. *RHA* (**average**) transitory interstorey drifts at **NC**

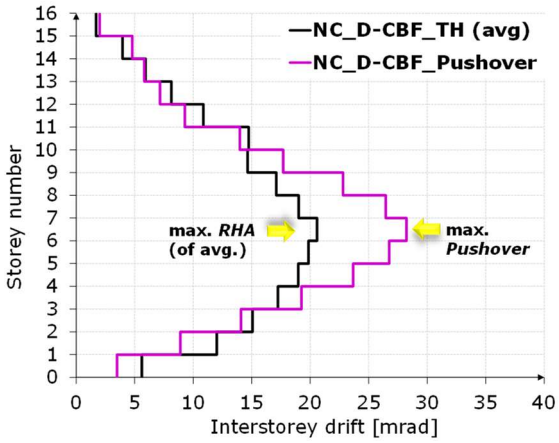

b)

Pushover vs. *RHA* (**maximum**) transitory interstorey drifts at **SD**

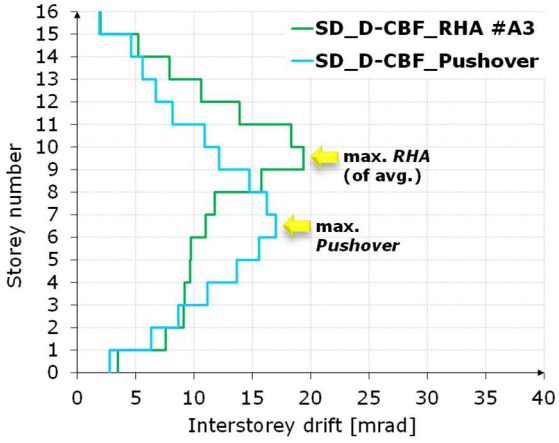

c)

Pushover vs. *RHA* (**maximum**) transitory interstorey drifts at **NC**

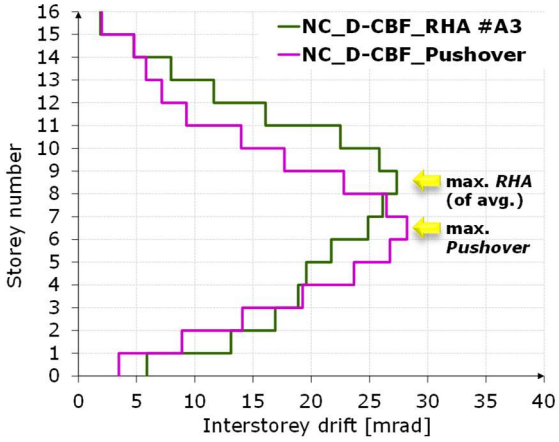

d)

Fig. 6-121. Comparison of *Pushover* to *RHA* interstorey drifts (average) of the *D-CBF* at: a) SD; b) NC

Comparisons between the plastic rotation demands on the SF beams of the *D-CBF* are also discussed in this section. *Pushover* results at SD (see Table 6-32, Table 6-33) are compared to the plastic rotations obtained from *RHA* with the most unfavourable accelerogram *#A3* (see Table 6-35, Table 6-36). As expected, the highest plastic rotation demand on the SF beams resulted from the MRF sub-systems of the *D-CBF*. The results of the *Pushover* and *RHA* have been shown to be the same from this point of view. Although the **demands** obtained from these analyses at SD **were similar** (*Pushover*: 8.60 mrad; *RHA* with *#A3*: **9.54 mrad**), the maximum value was provided by the *RHA*.

6.3.3 Re-centring verification

According to prEN 1998-1-8 [51], Dual Frames designed in Ductility Class 3 could provide re-centring if the yield deformation of the MRF sub-systems, $\Delta_{y,MRF}$, is higher than the ultimate storey deformation of the CBF sub-system, $\Delta_{u,CBF}$ (see Eq. (6.80) [51]). If fulfilled, dissipative components could be designed to be replaceable, which would prolong the design service life of the structure and reduce the overall impact of the construction sector on the environment by avoiding demolition. As no method of verification was provided in the code, a few approaches were explored.

$$\Delta_y^{MRF} > \Delta_u^{CBF} \tag{6.80}$$

Verification of re-centring capacity based on Pushover results

The approach was based on the individual assessment of the sub-systems of the *D-CBF*, i.e., CBF and MRF sub-systems, in the nonlinear range with *Pushover* analyses. For this purpose, the *D-CBF* was "divided" into its sub-systems by using the method described in Section 6.3.2, *"Verification of MRF sub-systems contribution to total resistance"*. The resulted frames, which contained the individual sub-systems of the *D-CBF* (see Fig. 6-122) were labelled as follows:

- $MRF_{sub\text{-}systems}$ - contained the two MRF spans of the *D-CBF*, which were linked by pinned SF beams, as replacement for the CBF span;

- $CBF_{sub\text{-}system}$ - contained the CBF span of the *D-CBF*, which was adjoined by another two spans consisting of pinned SF beams, as replacement for the MRF spans.

Followingly, *Pushover* analyses were performed on the frames consisting of the individual sub-systems, i.e., $MRF_{sub\text{-}systems}$ and $CBF_{sub\text{-}system}$.

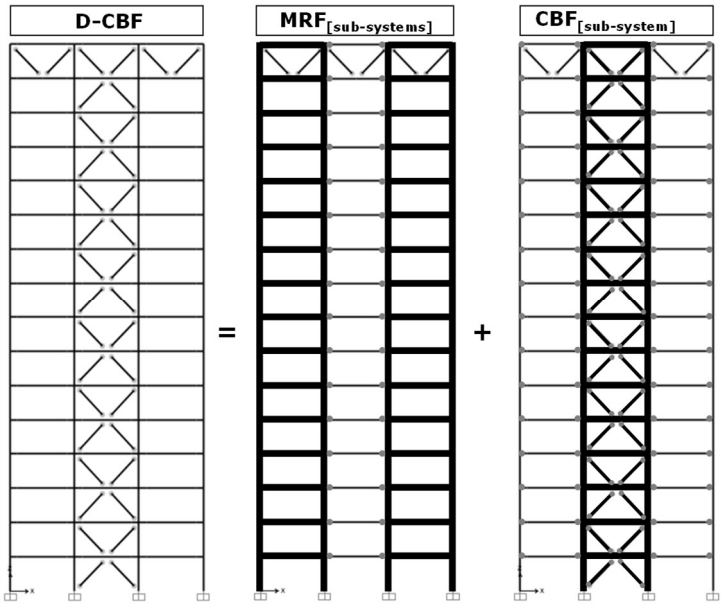

Fig. 6-122. The *D-CBF* and its corresponding sub-systems

In the frame $\boldsymbol{MRF_{sub\text{-}systems}}$, which contained the two MRF spans, the initiation of yielding corresponding to the SF beams was monitored. Yielding was considered to occur once the plastic hinges in the SF beams attained deformations corresponding to pre-DL. In this case, the yielding of the SF beams was initiated in the *Pushover* analysis at a top displacement value of 0.44 m. The damage state of the $MRF_{sub\text{-}systems}$ at this step of the analysis is shown in Fig. 6-123a.

In the frame $\boldsymbol{CBF_{sub\text{-}system}}$, which contained the middle CBF span, the same procedure was applied. However, in this case, the ultimate deformation of the braces was monitored. Ultimate deformations of the braces were considered to be achieved once the plastic hinges attained deformations corresponding to NC or beyond NC. Following the *Pushover* analysis, ultimate brace deformations were recorded at a top displacement of 0.30 m. The damage state of the $CBF_{sub\text{-}system}$ in this step of the analysis is shown in Fig. 6-123b.

The interstorey drifts corresponding to the frames $MRF_{sub\text{-}systems}$ and $CBF_{sub\text{-}system}$ were calculated at the above mentioned top displacements. In the case of the $MRF_{sub\text{-}systems}$, the interstorey drifts corresponded to the yielding initiation of the SF beams. In the case of the $CBF_{sub\text{-}system}$, the resulted interstorey drifts corresponded to the attaining of the ultimate deformation of braces. Considering these conditions, the following **maximum interstorey drifts** were obtained:

- $MRF_{sub\text{-}systems}$: interstorey drift of **12.3 mrad**;
- $CBF_{sub\text{-}system}$: interstorey drift of **8.9 mrad**.

Therefore, at an interstorey drift of 12.3 mrad, the yield deformation of SF beams was attained, while the ultimate brace deformation was reached at 8.9 mrad.

A summary of the results is shown in Table 6-37. A comparison of the base shear force-top displacement curves, which was obtained by performing *Pushover* on the *D-CBF* and on the frames containing sub-systems of the *D-CBF* is shown in Fig. 6-124.

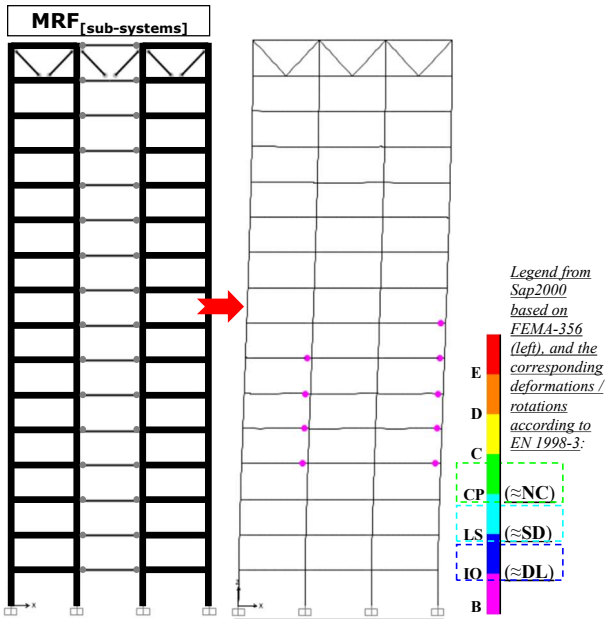

a)

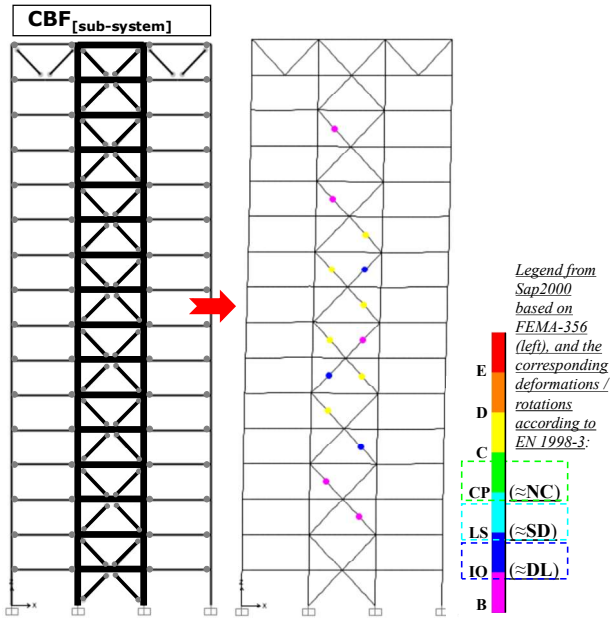

b)

Fig. 6-123. Structural state following *Pushover* analyses on the: a) $MRF_{sub\text{-}systems}$ at yielding of SF beams; b) $CBF_{sub\text{-}system}$ at ultimate brace deformation

Table 6-37 – Summary of *Pushover* results on the $MRF_{sub\text{-}systems}$ and $CBF_{sub\text{-}system}$

Deformation	Top displacement	Maximum interstorey drift
Ultimate deformation of braces $\Delta_{u,CBF[sub\text{-}system]}$	0.30 m	8.90 mrad
Yield deformation of SF beams $\Delta_{y,MRF[sub\text{-}systems]}$	0.44 m	12.3 mrad

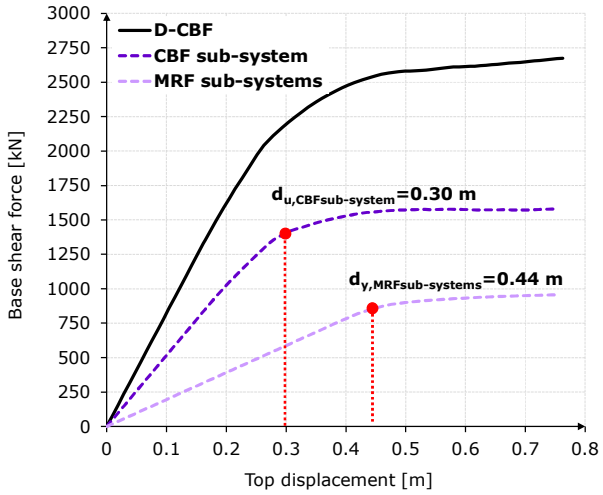

Fig. 6-124. Comparison of capacity curves of the *D-CBF*, $MRF_{sub\text{-}systems}$ and $CBF_{sub\text{-}system}$

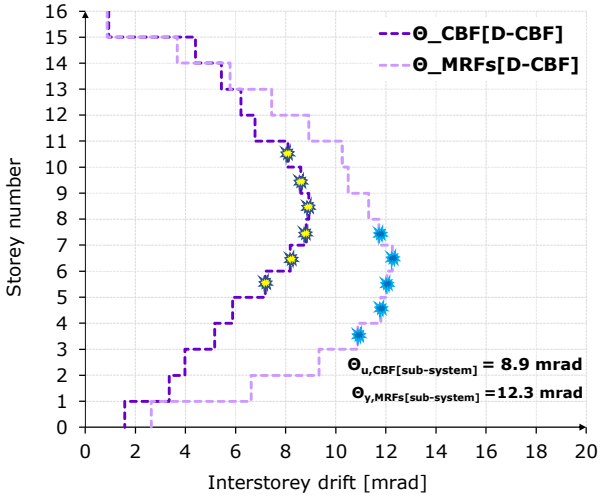

Fig. 6-125. Comparison of the interstorey drift distributions of $MRF_{sub\text{-}systems}$ and $CBF_{sub\text{-}system}$

Distributions of interstorey drifts corresponding to the $MRF_{sub\text{-}systems}$ to $CBF_{sub\text{-}system}$ were calculated and are shown side by side in Fig. 6-125. In the case of the $MRF_{sub\text{-}systems}$, these values were obtained at the top displacement of the frame

corresponding to the initiation of the yielding in the SF beams, i.e., 0.44 m. As for the $CBF_{sub\text{-}system}$, the interstorey drifts were calculated at a roof displacement of 0.3 m, which corresponded to the ultimate brace deformation. Interstorey drifts with similar values to that matching the yield deformation of the SF beams (12.3 mrad) and the ultimate brace deformation (8.9 mrad) were marked in Fig. 6-125. This shows that, in the $CBF_{sub\text{-}system}$, similar interstorey drifts to 8.9 mrad were obtained at six storeys. In the case of the $MRF_{sub\text{-}systems}$, similar interstorey drifts to 12.3 mrad resulted at five storeys. Considering these results, the following can be concluded:

- the **yield deformations in SF beams** of the $MRF_{sub\text{-}systems}$ are **higher** than ultimate brace deformations of the $CBF_{sub\text{-}system}$;
- the **yielding of the SF beams occurs after the braces attain their corresponding ultimate deformation**.

To verify these results, *Pushover* analyses were also carried out on the Dual Frame, *D-CBF*. In this case, the following maximum interstorey drifts were obtained:

- yielding of the SF beams: at an interstorey drift of 12.4 mrad;
- ultimate brace deformation: at an interstorey drift of 9.0 mrad.

Results obtained by performing *Pushover* on the *D-CBF* are centralised in Table 6-38. The similitude of the outcomes of the *D-CBF* (see Table 6-38) to those of the sub-systems of the *D-CBF* (see Table 6-37) are obvious. Consequently, based on the results of the *Pushover* analyses on the sub-systems of the *D-CBF* and on the results of the *D-CBF*, the **re-centring capacity was demonstrated**.

Table 6-38 – Summary of *Pushover* analyses results on the *D-CBF*

Deformation	Top displacement	Maximum interstorey drift
Ultimate deformation of braces $\Delta_{u,CBF[sub\text{-}system]}$	0.315 m	9.0 mrad
Yield deformation of SF beams $\Delta_{y,MRF[sub\text{-}systems]}$	0.404 m	12.4 mrad

Verification of re-centring capacity based on RHA results

The second approach that was employed to verify the re-centring capacity of the MRF sub-systems of the *D-CBF* entailed the combination of the *RHA* and *Pushover* results. The aim was to compare the average interstorey drifts of the entire *D-CBF* resulted from *RHA* to the interstorey drift matching the yield deformation of the SF beams, i.e., 12.3 mrad. The value of 12.3 mrad was obtained following *Pushover* analysis on the MRF sub-systems of the *D-CBF*.

Distributions of interstorey drifts over the height of the *D-CBF* are shown in Fig. 6-126 and Fig. 6-127. The values were obtained from *RHA* and represent the average results of seven accelerograms at DL and SD. Also shown in both of the figures is the drift corresponding to the yield deformation of the SF beams from the MRF sub-systems. As shown in these figures, the interstorey drifts of the Dual Frame *D-CBF* are smaller than 12.3 mrad. Based on these results, it is concluded that the MRF sub-systems with SF beams could help re-centre the structure affected by seismic events up to SD intensity. This conclusion is based on the fact that the yield deformation of the SF beams (from the MRF sub-systems) is not only higher than the ultimate deformation of the braces, but also higher than the average interstorey drifts of the Dual Frame (e.g., 7.1 mrad at DL, 11.7 mrad at SD).

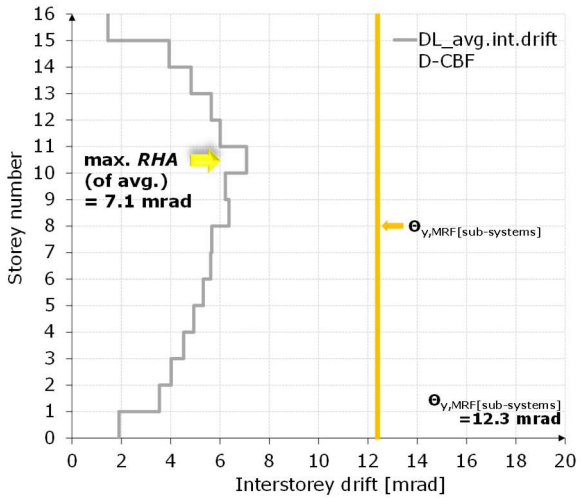

Fig. 6-126. Comparison of average interstorey drifts of the *D-CBF* at DL to interstorey drift corresponding to the yield deformation of the SF beams

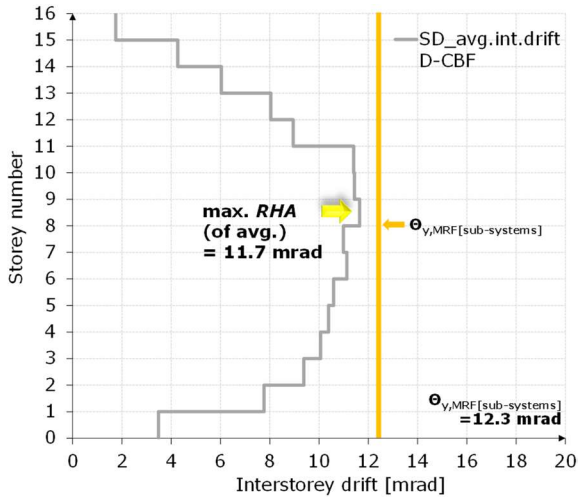

Fig. 6-127. Comparison of average interstorey drifts of the *D-CBF* at SD to the interstorey drifts corresponding to the yield deformations of the SF beams

6.3.4 Concluding remarks

In the current case study, the evaluation of the seismic performance of a 16-storey Dual Concentrically-Braced Frame with slim-floor beam-to-column joints (*D-CBF*) was presented. The seismic performance evaluation was performed with nonlinear static and dynamic analyses, i.e., *Pushover* with *N2 method* and *Response-History Analysis*. The aim of the case study on the *D-CBF* was (i) to verify the rotation demand resulted from the seismic situation on the SF beam-to-column joint, (ii) to compare the joint demand to the experimental rotation capacity, (iii) to assess the seismic performance of the Dual Frame with SF beam-to-column joints and (iv) to

verify whether the *D-CBF* can be re-centred. In accordance with the aims, the following objectives were established:

- implementation of the developed numerical model for the SF beam-to-column joint to the structural system;
- application of structural analyses in the nonlinear range, e.g., *Pushover* and *Response-History Analysis* to the subject frame;
- ensuring an adequate contribution of the MRF sub-systems to the total resistance of the Dual Frame;
- monitoring of the structural damage at the three Limit States, with particular interest to DL and SD, in terms of interstorey drifts and plastic rotation within the plastic hinges of the SF beams;
- assessment of the re-centring potential of the MRF sub-systems from the *D- CBF* following seismic events up to SD intensities.

Evaluation of seismic performance with nonlinear structural analyses.
The seismic performance of the *D-CBF* was assessed based on the following criteria:

- contribution of the MRF sub-systems to the total resistance of the D-CBF;
- development of global mechanism, which includes the history of plastic hinges, the location of plastic hinges and the value of the deformations sustained by plastic hinges;
- interstorey drifts at DL and SD.

The 25 % contribution of the MRF sub-systems to the total resistance of the Dual Frame was verified using three methods, all of which having evidenced a **sufficient strength / capacity of the unbraced spans**. This allowed for the use of the upper limit value of the behaviour factor for Dual Frames with a CBF sub-system, i.e., 4.8. The first method was based on existing formulae from different studies. As part of the second used method, a different approach to the evaluation of a CBF sub-system with rigidly-connected beams was proposed. In the proposed analytic approach, apart from the resistance of the braces, the resistance of the beams from the CBF sub-system can also be taken into consideration. The third method consisted of an individual resistance assessment of the sub-systems of the Dual Frame by means of nonlinear analyses. The obtained results are as follows:

- using method 1 (analytical): 43 % contribution of two MRF sub-systems;
- using method 2 (analytical) : **31 %** contribution of two MRF sub-systems;
- using method 3 (nonlinear static analyses): 25 % at DL, 35 % at SD and 36 % at NC contribution of two MRF sub-systems.

Although generally the ***Pushover* results** were more **conservative** than the **average *RHA*** results, both the results of nonlinear static and dynamic analyses evidenced an **adequate seismic performance** of the Dual Frame *D-CBF*. Similar to the case study on the *CBF-SF* (see Section 6.2), the *Pushover* analysis provided results that were comparable to those obtained by applying the most unfavourable accelerogram for *RHA*, which in this case was accelerogram was *#A3*.

Indicators of adequate seismic performance are the transitory interstorey drifts at DL and SD. As the obtained values were smaller than the seismic code limits [51], e.g., 7.5 mrad at DL and 20.0 mrad at SD, both the **interstorey drift criteria were satisfied**.

The development of the global mechanism of the Dual Frame could be broadly characterised as follows:

- at DL: elastic except for some braces;
- at SD: DL and SD plastic hinges were developed in almost all braces, thereby satisfying the hierarchy of resistances required by the seismic code [51];

plastic hinges with deformations corresponding to pre-DL were developed in the SF beams of the MRF sub-systems and in a few SF beams of the CBF sub-system;

- at NC: half of the plastic hinges in the braces attained deformations corresponding to SD, NC or post-NC; plastic hinges were developed in most of the SF beams of the MRF sub-systems, with deformations matching pre-DL and DL; plastic hinges were developed in some of the SF beams of the CBF sub-system; pre-DL and DL plastic hinges were evidenced in two column bases, but only by applying the most unfavourable accelerogram, *#A3*.

As the development of plastic hinges occurs in braces prior to other structural elements, the condition of the seismic code can be considered satisfied.

Interstorey drift demand vs rotation capacity. The demands in interstorey drifts on the SF beam-to-column joints, as resulted from nonlinear static and dynamic analyses applied to the *D-CBF*, were as follows:

- **17.0 mrad** at SD from *Pushover*;
- **11.7 mrad** at SD from *RHA* (average of seven accelerograms).

Considering these results and the experimental rotation capacity of the SF beam-to-column joint of **± 45.35 mrad at SD**, it is evident that the **demand is lower than the available rotation capacity**.

Plastic rotation demand vs experimental plastic rotation capacity of the SF beams. According to the results of both the nonlinear static and dynamic analyses, the highest plastic rotation demand on the SF beams resulted from the MRF sub-systems of the *D-CBF*. As the experimental plastic rotation capacity of the dissipative zone of the SF beam was 29.4 mrad at SD, the **maximum demand** at SD was **9.54 mrad** (obtained from *RHA* with accelerogram *#A3*) – a value **considerably lower than the available rotation capacity**.

Re-centring of the Dual Frame. A method to verify whether the Dual Frame *D-CBF* can be re-centred by means of nonlinear structural analyses was adopted. This method allowed for the determination of the interstorey drifts at which: (i) the yielding of the SF beams from the MRF sub-systems is initiated and (ii) the ultimate deformation of the braces from the CBF sub-system is attained. As the **yielding of the SF beams occurs after the braces attain their corresponding ultimate deformation**, this was considered to satisfy the requirement of prEN 1998-1-2 [51]. In addition, residual interstorey drifts were calculated and compared to the acceptance criteria of FEMA 356 [108] for permanent drifts of braced structural systems. According to the obtained results, the permanent interstorey drifts corresponding to the *D-CBF* were within the limits of FEMA 356 [108].

6.4 Comparison between the D-CBF and the CBF-SF

In the current section, the Dual Concentrically-Braced Frame *D-CBF* and the Concentrically-Braced Frame with slim-floor beam-to-column joints *CBF-SF* are compared in terms of seismic performance and structural steel use. The comparison is justified by the analysed frames, e.g., same span length, storey height and number of spans, loads, distribution of seismic masses, use of SF beam-to-column joints.

6.4.1 Comparison in terms of seismic performance

The seismic performance comparison is based on the results obtained from nonlinear static and nonlinear dynamic analyses. The fundamental period of vibration of the *D-CBF* was $T_{1,D\text{-}CBF}$ =2.14 s. In the case of the *CBF-SF*, this was $T_{1,CBF}$ = 2.33 s. This similarity in stiffness is reflected in the values of the target displacements, which are centralised in Table 6-39 for both the *D-CBF* and *CBF-SF*.

A comparison in terms of base shear resistance is shown in Fig. 6-128. As it can be observed in the figure, the base shear force corresponding to the *D-CBF* at a top displacement of 0.95 m is higher than that of the *CBF-SF*. To quantify the difference in base shear strength between the two curves, the curve segments following the target displacements at DL were considered, as illustrated in Fig. 6-128. On the curve segments from the emphasized area, the base shear resistance corresponding to the *D-CBF* is 13 to 21 % higher than that of the *CBF-SF*.

Table 6-39 – Target displacements & interstorey drifts (from *Pushover*): *D-CBF* vs. *CBF-SF*

Limit States (LS)	Target displacements		Maximum interstorey drifts	
	D-CBF	*CBF-SF*	*D-CBF*	*CBF-SF*
Damage Limitation (DL)	0.25 m	0.27 m	6.7 mrad	7.6 mrad
Significant Damage (SD)	0.50 m	0.54 m	**17.0 mrad**	**18.5 mrad**
Near Collapse (NC)	0.75 m	0.81 m	28.2 mrad	28.1 mrad

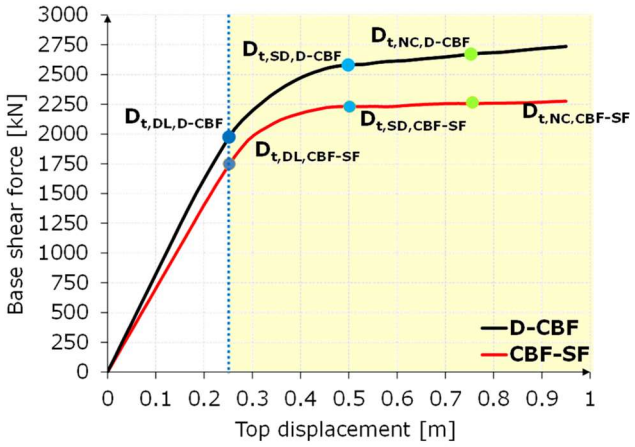

Fig. 6-128. Comparison of base shear resistance: the *D-CBF* vs. the *CBF-SF*

Maximum interstorey drifts that were obtained by applying *Pushover* with *N2* [107] are also centralised in Table 6-39. Since the elastic stiffness of the two frames is similar, the interstorey drifts are expected to be comparable, which is in fact the

case. Comparing the seismic code interstorey drift limits to the results from *Pushover* analyses, the following can be highlighted:

- the drift limit of 7.5 mrad at DL was not exceeded in the *D-CBF*;
- the drift limit of 7.5 mrad at DL was exceeded in the *CBF-SF*;
- the drift limit of 20 mrad at SD was not exceeded in the *D-CBF*;
- the drift limit of 15 mrad at SD was exceeded by the *CBF-SF*.

In the comparison between the results of the frames from *RHA*, only the average values are considered (see Table 6-40). As it can be observed, the values obtained at DL, SD and even NC are similar. Except for the interstorey drift at DL, the values corresponding to the *D-CBF* are smaller than those of the *CBF-SF*. This is also easily observable on the distributions of average interstorey drifts of the two frames, shown in Fig. 6-129. In comparison to the drift limits of prEN 1998-1-2 [51], neither the *D-CBF*, nor the *CBF-SF* evidenced values exceeding the acceptance criteria.

Table 6-40 – Average interstorey drift resulted from *RHA on the D-CBF* and *CBF-SF*

Limit State	Avg. int. drifts. *D-CBF*	Code limits [51] Dual Frames	Avg. int. drifts. *CBF-SF*	Code limits [51] CBF
DL	7.10 mrad	7.5 mrad	6.60 mrad	7.5 mrad
SD	**11.7 mrad**	20.0 mrad	**13.8 mrad**	15.0 mrad
NC	20.6 mrad	-	22.9 mrad	-

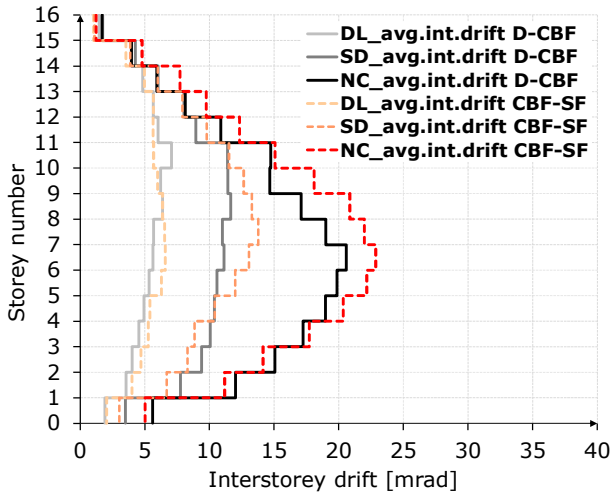

Fig. 6-129. Distributions of average interstorey drifts obtained from *RHA* on the *D-CBF* and the *CBF-SF* at DL, SD, NC

In terms of plastic rotation demand on the SF beams, values were obtained from *Pushover* and *RHA* performed on the *CBF-SF* and *D-CBF*. In both case studies, the maximum demand at SD resulted from *RHA*. Accelerogram *#A4* was the most unfavourable for the *CBF-SF*, while *#A3* - for the *D-CBF*. Maximum plastic rotation demands on the SF beams at SD are as follows:

- 8.82 mrad resulted from the *CBF-SF*;
- **9.54 mrad** resulted from the *D-CBF*.

As the experimental plastic rotation capacity of the dissipative zone of the SF beam is 29.4 mrad at SD, the maximum demands at SD, which resulted from *RHA* on the *CBF-SF* and *D-CBF*, are considerably lower than the available rotation capacity.

In order to compare the roof displacement of the frames, results were obtained from same accelerogram, which in this case was *#A4*. This accelerogram caused roughly the maximum roof displacement. Comparisons between roof displacements at DL, SD and NC are presented in Fig. 6-130a-c, which revealed comparable results. At SD and NC, the variation of the roof displacement of the *D-CBF* is attenuated faster than those of the *CBF-SF* towards the end of the accelerogram, which is partly due to the higher elastic stiffness of the Dual Frame (and implicitly, lower period of vibration).

The average results of the *RHA* revealed an adequate seismic performance in both the case of the *D-CBF*, as well as of the *CBF-SF*.

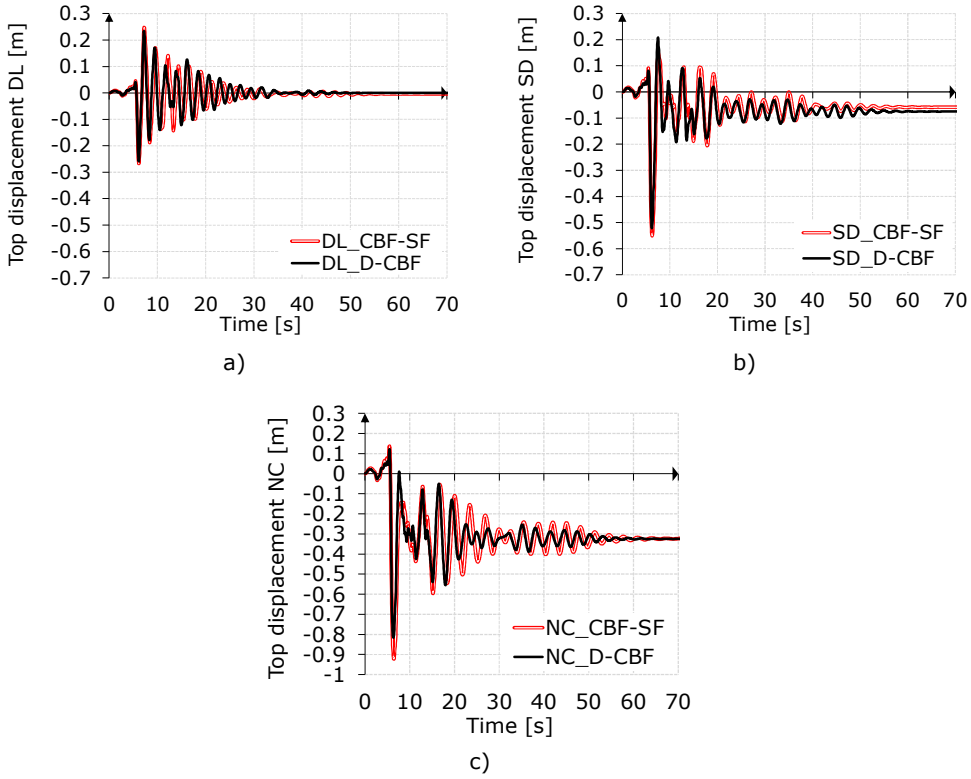

Fig. 6-130. Top displacements obtained from *RHA* with accelerogram *#A4* on the *D-CBF* and the *CBF-SF* at: a) DL; b) SD; c) NC

6.4.2 Comparison in terms of steel use

As previously mentioned, the *CBF-SF* and *D-CBF* case studies focus mainly on the use of SF beams. In the *CBF-SF*, two different SF beams cross sections were used: (i) central span: ½ IPE-600 with a welded steel plate as the lower flange (width x thickness: 380 x 20 mm) and (ii) outer spans: IPE-300 with an additional welded lower steel plate (width x thickness: 280 x 12 mm). Throughout the *D-CBF* one SF beam cross section was used: ½ IPE-600 with a welded steel plate as the lower flange (width x thickness: 380 x 20 mm). The main reasons for this were, on the one hand to ensure an adequate contribution of 25 % of the MRF sub-systems to the total resistance of the *D-CBF*, and on the other to be able to achieve re-centring capability

up to SD seismic intensity. Depending on the Limit State, it was proven that for the current case study, the MRF sub-systems contributed to the total resistance with 25 % at DL, 35 % at SD and 36 % at NC. As a result, SF beam cross sections could be optimized to reduce the contribution of both MRF sub-systems to 25 %. However, this would decrease the capability of the *D-CBF* to be re-centred.

The steel use was assessed on both the *D-CBF* and *CBF-SF* by taking into consideration their position in the selected floor plan. The tonnage included the following structural elements: columns, braces and SF beams (rigidly-connected in the *D-CBF* and in the central span of the *CBF-SF*; nominally pinned in the outer spans of the *CBF-SF*). However, the total tonnage did not include the weight of the connections, of the concrete and of the reinforcement. The results of the assessment are presented in the form of histograms in Fig. 6-131. As it can be seen in this figure, apart from a lower steel use in terms of columns and braces, the overall steel use corresponding to the *D-CBF* is lower than that of the *CBF-SF*.

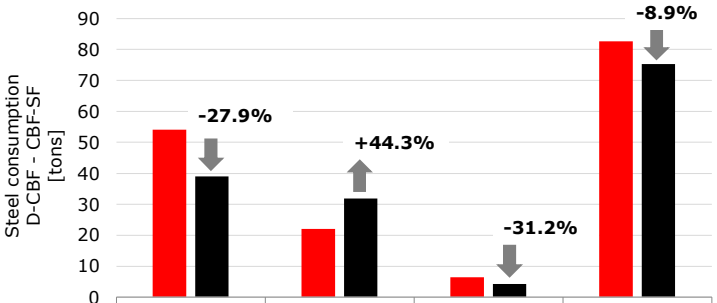

	Columns	Beams	Braces	Total
CBF-SF	54.1	22.1	6.4	82.7
D-CBF	39.0	31.9	4.4	75.3

Fig. 6-131. Comparison of steel use: the *D-CBF* vs. *CBF-SF*

6.4.3 Concluding remarks

In terms of seismic performance, the *Pushover* results revealed 13 ÷ 21 % higher resistance of the *D-CBF*, which is expected considering that the Dual Frame consisted of 2 MRF sub-systems in addition to a CBF sub-system. The contribution of the MRF sub-systems to the total resistance of the *D-CBF* ranged between 25 ÷ 36 %, depending on the Limit State, which could explain the higher resistance of the *D-CBF*.

The maximum plastic rotation demand on the SF beams resulted from *RHA* on the Dual Frame *D-CBF*, 9.54 mrad. Considering that the experimental plastic rotation capacity of the SF beam's dissipative zone is 29.4 mrad at SD, the demand is considerably lower than the available rotation.

The interstorey drifts corresponding to the *D-CBF* were generally lower than those of the *CBF-SF*. In comparison to the drift criteria of the seismic code, the interstorey drifts obtained from *Pushover* and corresponding to the *D-CBF* were within the allowable limits at DL and SD. In the case of the *CBF-SF*, these exceeded both the DL and the SD limits. However, the comparison of the average interstorey drifts obtained from *RHA* proved an adequate seismic performance of both frames.

Except for the capability of the Dual Frame *D-CBF* to provide re-centring after seismic events up to SD intensity, thereby prolonging the design service life, the seismic performance of the two analysed frames was comparable. If the steel use is considered, then the *D-CBF* would provide more cost-effective results.

7. FINAL CONCLUSIONS

The slim-floor is an alternative flooring system characterized by the integration of members into one structural element. This means that the main structural member, the asymmetric steel beam, and other components are incorporated into the concrete slab. Due to the current typology of the slim-floor beam-to-column connections, e.g., pinned end connections, and to the fact that the slim-floor beams are designed exclusively for gravity loads in the elastic range, the flooring system is incompatible with the seismic design of frame systems. A further issue resides in the actual design of the slim-floor system, which is predominantly regulated by technical approvals. Until the release of the new version of the composite European code, prEN 1994-1-1 [55], in which some rules are included, and a range of application for slim-floors is defined, the design is not easily approachable, and applications are rather limited.

The current study is developed with the aim to provide a **technical solution for slim-floor beam-to-column joints**, which would make the shallow flooring system applicable to structures designed not only for medium, but also for high seismicity. In order to apply the capacity design principles to the slim-floor beam-to-column joints, thus to meet Ductility Class 3 resistance, stiffness and rotation capacity criteria according to prEN 1998-1-2 [51] and to AISC 341-16 [30], a structured procedure entailing the following main steps is presented in the current study:

- **Design of joint assemblies**
  - estimation of demand on seismic-resistant structures with SF beam-to-column joints;
  - design based on FEM of the SF beam-to-column joints;
- **Experimental investigations**
  - experimental campaign with monotonic and cyclic tests on joints;
  - interpretation and evaluation of experimental results;
- **Numerical investigations**
  - calibration of numerical model and development of parametric study with FEM;
  - interpretation and evaluation of numerical results;
- **Development of design procedure and detailing**
  - evaluation of mechanical characteristics of the SF beam;
  - capacity design of the SF beam-to-column joint;
  - classification of stiffness and resistance of the SF beam-to-column joint according to the code;
  - detailing rules for SF beam-to-column joints;
- **Structural analyses and seismic performance evaluations**
  - development of a simplified numerical SF beam-to-column joint model for integration into MRF, CBF and D-CBF structures;
  - validation of SF beam-to-column joint model against experimental data;
  - calculation of plastic rotation demand on SF beams, interstorey drift demand on SF beam-to-column joints and generally, seismic performance evaluation of Moment-Resisting Frames, Concentrically-

Braced Frames and Dual Concentrically-Braced Frames with slim-floor beam-to-column joints with nonlinear static and dynamic analyses.

Main conclusions on the experimental program. The SF beam-to-column joint specimens *SF J-M* and *SF J-C* developed considerable and relatively symmetric bending moment resistance and rotation capacity regardless of the applied loads and loading direction, (i.e., monotonic / cyclic; hogging / sagging bending), as follows:

- monotonic experimental test, values at column centreline:
  - maximum hogging bending and joint rotation: 907 kNm, 93 mrad;
  - maximum sagging bending and joint rotation: 787.2 kNm, 52.9 mrad;
- cyclic experimental test, values at column centreline:
  - maximum hogging bending and joint rotation: 795.4 kNm, 53.3 mrad;
  - maximum sagging bending and joint rotation: 816.1 kNm, 50.1 mrad.

As the resistance of the bolted connection was higher than that of the SF beam in its "reduced" section under hogging and sagging bending moments, the SF beam-to-column joint is considered full-strength according to resistance criterion of the European seismic code prEN 1998-1-2 [51]. Considering the stiffness criterion of EN 1993-1-8 [62] and guidelines from state-of-the-art research on Moment-Resisting Frame joints for Ductility Class 3, the beam-to-column connection of the tested SF joints was semi-rigid for unbraced frames and rigid for braced structural systems.

The joint rotations at the three Limit States, DL, SD, NC, were calculated using the procedure, described in Vulcu et al. [48], and the following values were obtained: ± 16 mrad at Damage Limitation, ± 45.4 mrad at Significant Damage and ± 60.5 mrad at Near Collapse. Considering the obtained value at SD of ± 45.4 mrad and the ± 40 mrad criterion of AISC 341-16 [30], the SF beam-to-column joint fulfils the required joint rotation.

Taking into consideration the full-strength and semi-rigid classifications of the joint, the joint rotation capacity of ± 45.4 mrad at SD, the dissipative zone of the SF beam as the main source of energy dissipation, the stable and symmetric hysteretic response with low degradation of stiffness and capacity under cyclic loads, and the ductile failure mechanism, an adequate seismic performance was provided by the SF beam-to-column joint.

Main conclusions on the numerical program. The calibrated reference FE model of the SF beam-to-column joint, referred to as the *RM*, proved good compatibility with the monotonic curve (e.g., differences in the range of 0.1 ÷ 3.2 %), supported the experimental findings in terms of the failure mechanism and main source of energy dissipation, and allowed for the development of a parametric study.

Based on the results of the calibrated model, the *RM*, the ductile failure mechanism consisted of the development of a plastic hinge in the dissipative zone of the SF beam regardless of the bending direction. Although other joint components, such as the continuity plates and some of the bolts, had sustained localised plastic deformations, most of the phenomenon occurred in the dissipative zone of the SF beam. Thus, considering that the plastic deformation in the bolted connection was significantly lower and limited to a few finite elements, the response of the component was characterised as mainly elastic.

Considering the results of the numerical investigations, which were performed in the framework of the study, it was concluded that the ductile response of the SF beam-to-column joint is attributed to the *RFS* and to the reinforced concrete slab. On the one hand, the *RFS* was proven to provide adequate ductility under flexure and to balance the hogging and sagging responses, which are generally asymmetric in composite beams. On the other hand, the presence of the reinforced concrete slab increases the bending resistance, stiffness and rotation capacity, to those provided

by a bare steel joint. Separately, the influence of the analysed parameters could be characterised as follows:

- the *Reduced Flange Section RFS*: the *RFS* provides ductility, balances the hogging and sagging bending response and ensures even distributions of stresses and plastic strains; if the *RFS* is not applied, a different failure mechanism occurs (i.e., bolts fail in sagging bending);
- the reinforced concrete slab: increases the bending resistance, elastic stiffness and rotation capacity;
- the concrete dowels: as a stand-alone parameter, its removal was marginally influential; if combined with "*frictionless*" contact between components, the relative slip increases substantially, e.g., 17.6 mm from 0.83 mm in the *RM*;
- increased reinforcement ratio: leads to a different failure (crushing of the concrete slab in the portion located behind the column);
- the backing plates / rib stiffener / decoupled dissipative zone: all parameters led to a similar result – decrease in plastic strain within the bolts; highest reduction was obtained by adding a rib stiffener on the top flange of the SF beam;
- increased concrete class: leads to higher elastic stiffness; not influential on the initiation and propagation of cracks in the slab;
- reinforced concrete ribs and / or trapezoidal steel sheets: the plastic hinge development in the dissipative zone of the SF beam was not hindered by these parameters.

Main conclusions on the design and detailing procedure. The basis of the proposed design procedure is represented by the following: (i) some design rules from the pre-normative version of prEN 1994-1-1 [55] for slim-floors and by (ii) the main principles of capacity design for steel and composite joints of MRF (DC3). In addition to these, a method for ensuring ductility of the SF beam through the implementation of a *Reduced Flange Section* was proposed herein.

An adequate seismic performance of SF beam-to-column joints with similar cross section to the one tested in the current study, can be achieved by full-strength and rigid or semi-rigid joints, that can develop a joint rotation capacity of ± 40 mrad at SD (according to AISC 341-16 [30]) or a joint plastic rotation of ± 30 mrad (according to prEN 1998-1-2 [51]). Although the web panel is considered in the literature to be a source of plastic deformation, recommendations, as those in [50], advice against allowing for the phenomenon to occur.

The proposed design and detailing procedure follow the main principles of capacity design, which are applied to ensure the necessary hierarchy of resistances (see [46]) in order to create a clear distinction between dissipative and non-dissipative components. However, for the principles of capacity design for DC3 joints of MRFs to be applicable to the SF beam-to-column joints, the beam should be the primary source of plastic deformation (i.e., dissipative component), while the rest of the components, e.g., bolted connection, welds, web panel, continuity plates, should remain elastic (non-dissipative). Consequently, the following main rules are proposed to be followed:

- ensuring the ductility of the SF beam
  - material selection (S355÷S420 [19]; $f_u / f_y \geq 1.10$, elongation higher than 15 %)
  - section class 1 (see [55]);
  - application of *RFS*, as follows:
    - trimming applied only to the lower flange of the SF beam;

        - type of the cut: radius cut;
        - dimensions of the *RFS*: (i) centre of *RFS* ($l_{RFS,cf}$); (ii) length of *RFS* (l_{RFS}); (iii) width of *RFS* (b_{RFS});
- designing by overstrength of the bolted connection
    - considering effects of the material overstrength γ_{rm} and of the strain hardening factor γ_{sh};
    - two-way extended end-plates;
    - high strength bolts (grade 10.9);
    - use of a rib stiffener on the top flange of the SF beam;
- designing by overstrength of the welds
    - critical welds are between the flanges of the SF beam and the end plate and between the continuity plates and the column flanges;
    - should be realised as full penetration groove welds and the roots should be rewelded;
- designing by overstrength of the web panel;
    - supplementary plates such as continuity and doubler plates could be added if deemed as necessary;
    - shear resistance $V_{wp,Rd}$ of the web panel should be taken as the elastic shear resistance of the web panel without a surplus of resistance provided by continuity plates [46] [50];
- design of joints as full-strength and rigid or semi-rigid (see [50]);
- ensuring full composite action (see *Z-26.4-59* [19]), which is necessary in order to activate the longitudinal rebars close to the connection zone; otherwise, the resistance of the connection should be calculated by taking into consideration only the contribution of the bolts.

The proposed dimensions of the *RFS* were based on AISC 358-16 [102] for *Reduced Beam Section* (*RBS*) connections. However, due to the larger width of the lower beam flange and to the partial concrete encasement of the steel SF beam– both of which set apart the slim-floor systems from downstand composite configurations – the dimensions of the *RFS* were adapted to particularities of shallow flooring systems.

Adequate seismic performance is achievable if the plastic hinge development is directed to the ends of the SF beam, while the bolted connection, the adjoining welds and the column are designed as non-dissipative.

Main conclusions on the structural modelling. The section dedicated to structural modelling and analysis is comprehensive, consisting of individual case studies on multistorey braced and unbraced frames with slim-floor beam-to-column joints. Considering the intended application of SF beam-to-column joints to the seismic design of DC3 frame systems, nonlinear static and dynamic analyses, e.g., *Pushover* with *N2*, *Response-History Analysis* with a set of seven accelerograms, were applied to four storeys unbraced and sixteen mid-rise braced frames using a software for structural analysis. The aim was to assess the seismic performance based on criteria such as: the plastic rotation demand on SF beams, the interstorey drift demand, an adequate contribution of the MRF sub-systems to the total resistance of the Dual Frame, the development of global ductile plastic mechanism, the re-centring potential of the Dual Frame after seismic events corresponding to SD intensity.

For reasons of reliability of the developed SF beam-to-column joint model, the modelling procedure was validated against the experimental data. Iterations on the modelling approach of the SF beam-to-column joint have shown that a rigorous approach, involving an accurate geometrical ("full" section, dissipative zone with *RFS*), material (tested materials) and mechanical ($I_{eq,full\ section}$, $I_{eq,RFS}$) modelling leads to the most realistic results.

The optimal modelling procedure of the SF beam-to-column joint consisted in the definition of: (i) the inelastic response of the SF beam through a plastic hinge, (ii) of the bolted connection through a link element containing the stiffness of the tested bolted connection and (iii) of the web panel through a spring (containing the stiffness of the web panel) combined with end-length properties. To capture the rotation capacity of the composite SF beam, a plastic hinge model was defined based on the experimental plastic rotation of the SF beam and the surrounding concrete.

Due to the presence of the concrete in the SF joint solution, the influence of this component was included in the rotation capacity of the joint, in the bending resistance of the SF beam and in the equivalent moment of inertia of the "full" section and of the dissipative zone with *RFS*.

As the bolted beam-to-column connection was semi-rigid in the case study on the *MRF-SF* (Moment-Resisting Frame with SF beam-to-column joints), the component was explicitly modelled by a link element containing its stiffness. Considering the stiffness classification for joints of braced frames, a recalculation was made in the study cases on braced frames, the result allowing for the modelling of the connection as rigid. In the elastic range, the explicit modelling of the bolted connection and of the web panel influences the elastic stiffness of the SF beam-to-column joint, though to a limited extent. By comparison to a *MRF* of four storeys, in which the definitions of the connection and web panel were disregarded, only a decrease of approximately 2 % in elastic stiffness could be determined.

Experimental data was used to check the reliability of the brace model, which was used in the case studies on braced frames, e.g., Concentrically-Braced Frame *CBF-SF* and Dual Concentrically-Braced Frame *D-CBF*. Iterations have shown that the brace model had to be adapted to the type of the nonlinear analysis. In consequence, a phenomenological model was used for the *Pushover* analysis and a physical theory model for the *Response-History Analysis* – both of which were previously validated against the experimental data corresponding to a brace with the same cross section.

Main conclusions on the seismic performance of the *MRF-SF*. Nonlinear structural analyses, e.g., *Pushover* with *N2* (*PO*) and Response-History Analysis (*RHA*), were performed to assess the seismic performance of frames. The seismic performance of the *MRF-SF* was characterised based on criteria of the latest version of the European seismic code, prEN 1998-1-2 [51], and on AISC 341-16 [30].

The seismic performance of the *MRF-SF* was confirmed by the results of the nonlinear static and nonlinear dynamic analyses. On a macro or structural level, acceptable demands in terms of interstorey drifts (*PO*: 7.8 mrad / average *RHA*: 6.5 mrad < 7.5 mrad code limit) were obtained at DL. Doubled by satisfactory interstorey drifts at SD from *Pushover* and *RHA* (*PO*: 16.8 mrad / average *RHA*: 13.1 mrad < 20 mrad code limit), the criteria of the European seismic code for MRFs was fulfilled. In comparison to the experimental joint rotation capacity of ± 45.4 mrad at SD, the average demand from *RHA*, e.g., 13.1 mrad, is smaller. In conclusion, the demand was lower than the available rotation capacity.

On the micro or component level, the plastic rotation demand on the SF beams was obtained from *PO* and *RHA* results and compared to the experimental rotation capacity of the dissipative zone of the SF beam. Comparisons have shown that, the demand in plastic rotation (*PO*: 7.7 mrad; average *RHA*: 4.53 mrad) is lower than the available capacity of the SF beams (29.4 mrad at SD).

Considering the damage state of the *MRF-SF* at the SD Limit State, the global mechanism was developed according to Performance-Based Design principles for basic facilities affected by rare earthquakes. This means that the structural response under *PO* and *RHA* could be characterised as elastic at DL, slightly in the plastic range due to the development of plastic hinges in the SF beams at SD, and plastic at NC,

though collapse or severe generalised damage was not evidenced. Considering Performance-Based Design principles for basic facilities, the *MRF-SF* proved adequate seismic behaviour.

The *Pushover* with *N2* results in terms of interstorey drifts, plastic rotations of the SF beams and top displacements were generally higher than those obtained by applying *RHA*. This result proves a more conservative character of the *Pushover* analysis.

Generally, the results of the two analysed MRFs, e.g., *MRF-SF* and *MRF-RF*, were similar, which could be attributed to a comparable flexural stiffness of the SF beam to that of a bare steel IPE-450 profile, despite the overall lower height of the first. Thus, the two frames had the same column cross sections, similar fundamental periods, top displacements and interstorey drifts. However, in terms of space efficiency, the height of the slim-floor beam was 0.2 m lower that of the floor consisting of a composite IPE-450 beam with partial shear interaction. Considering the 0.2 m gain per storey, a total of 0.8 m of vertical space could be saved on a 4-storey frame if the slim-floor beam-to-column joints would be used.

Main conclusions on the seismic performance of the *CBF-SF*. An adequate seismic performance of the *CBF-SF* was demonstrated. In terms of interstorey drifts at DL and SD, both the limits of prEN 1998-1-2 [51] were exceeded (*PO* at DL: 7.6 mrad > 7.5 mrad code limit; *PO* at SD: 18.5 mrad > 15.0 mrad code limit), thus accentuating the need for improvement in seismic performance. However, taking into consideration the average *RHA* results in terms of interstorey drifts, the need for improvement was contradicted, as neither of the code limits was exceeded (*RHA* at DL: 6.6 mrad < 7.5 mrad code limit; *RHA* at SD: 13.8 mrad < 15.0 mrad code limit). Based on the *RHA*'s enhanced ability to assess the seismic performance of relatively high structures, the criteria of the European seismic code [51] can be considered as fulfilled by the *CBF-SF*.

By comparing the average *RHA* interstorey drift of ± 13.8 mrad at SD to the experimental joint rotation capacity of ± 45.4 mrad at SD, it can be concluded that the demand is lower than the available rotation capacity.

In terms of plastic rotation demand on the SF beams, similar values were obtained at SD from both the *Pushover* and the *RHA* analyses, e.g., *PO*: 8.62 mrad, maximum *RHA*: 8.82 mrad. Considering the experimental plastic rotation of 29.4 mrad at SD of the SF beam, the demand is considerably lower than the available rotation capacity.

The global mechanism of the *CBF-SF* was developed in accordance with the European seismic code [51], with plastic mechanisms in braces occurring prior to those in the SF beams and the columns. Judging by the damage state of the *CBF-SF* at the three DL and SD Limit States, the frame responded mainly in the elastic range at DL (except for a few braces) and evidenced the development of plastic hinges with deformations corresponding to DL in the braces at SD.

Based on the outcomes, the *Pushover* analysis provided more conservative results, which in terms of interstorey drifts, top displacements and development of global mechanism, are similar to the ones obtained from applying *RHA* with accelerogram *#A4*, which was the most unfavourable.

Main conclusions on the seismic performance of the *D-CBF*. The seismic performance evaluation of the Dual Frame, consisting of a central CBF sub-system adjoined by two outer MRF sub-systems, provided results which revealed an adequate response of the *D-CBF*. Consistent with observations on the *MRF-SF* and *CBF-SF*, the *Pushover* analysis led to more conservative results on the *D-CBF* than the average ones from *RHA*.

The contribution of the MRF sub-systems to the overall resistance of the Dual Frame was verified and found to fulfil the 25 % requirement of the European seismic code, prEN 1998-1-2 [51]. Depending on the used method, the contribution of the two MRF sub-systems of the *D-CBF*, ranged from 31 % to 43 %, which corresponds to 15.5 % to 21.5 % for one sub-system. Although the results fulfil the previously mentioned rule of the code, the contribution of the MRF sub-systems could be reduced for a better steel use. However, a reduction in steel use might would lead to a lower contribution of the MRF sub-systems to the recentring of the *D-CBF* after seismic events up to SD intensity, which was one of the goals of the current case study.

As the existing formula used to evaluate the resistance of the CBF sub-system is based exclusively on the resistance (tensile and compressive) of the braces, it is suggested in the current study also to take into account the beams. The proposal is motivated by the fact that the beams (here, SF beams) in the CBF span are rigidly-connected to the columns and should, therefore, be included in the assessment of the resistance of the CBF sub-system. The second proposed method is based on the individual assessment of the sub-systems of the Dual Frame, and of the D-CBF itself, by performing *Pushover* and comparing the base shear resistance at the three Limit States. Provided that a structural analysis software is available and nonlinear modelling familiarity exists, the second method could offer a way to assess the contribution of a Dual Frame's sub-systems in a relatively short period of time.

In terms of interstorey drifts, both the *Pushover* and the average *RHA* results at DL and SD were within the acceptable limits (i.e., 7.5 mrad at DL and 20.0 mrad at SD) of the European seismic code, prEN 1998-1-2 [51]. The average interstorey drift demands at DL and SD were 7.1 mrad and 11.7 mrad, respectively. Considering the available rotation capacity of the SF beam-to-column joint of ±45.4 mrad at SD, the resulted demand of 11.7 mrad was considerably lower.

Assuming the plastic rotation capacity of 29.4 mrad of the SF beams, the resulted the plastic rotation demand of 9.54 mrad at SD (obtained as maximum from *RHA*) is lower than the available capacity.

The global mechanism of the Dual Frame was developed progressively following the requirement of the European seismic code, prEN 1998-1-2 [51], in terms of the braces being the main structural elements to dissipative seismic energy. Whereas the *D-CBF* responded mainly elastic at DL, most of the braces at SD attained deformations corresponding to DL. Simultaneously, the initiation of plastic mechanisms in the SF beams of the MRF sub-systems was evidenced. At NC, while some braces attained SD and NC deformations, rotations corresponding to DL were reached in the SF beams.

In order to verify whether the potential of the MRF sub-systems to contribute to the recentring of the *D-CBF*, a simplified method was adopted, which was based on structural nonlinear analyses. It should be underlined that, while the recentring potential was verified, the subject did not represent the main focus of the current study. The recentring was investigated due to the potential of MRF sub-systems to help recentre the *D-CBF* following seismic events up to SD intensities. The adopted method allowed for the calculation of the interstorey drifts at which: (i) the yielding of the SF beams from the MRF sub-systems was initiated and (ii) the ultimate deformation of the braces from the CBF sub-system was attained. Considering that the yielding of the SF beams occurred after the braces attained their corresponding ultimate deformation, the requirement of prEN 1998-1-2 [51] was considered satisfied. Additionally, residual interstorey drifts were calculated and compared to the acceptance criteria of FEMA 356 [108] for permanent drifts of braced structural systems. As the permanent interstorey drifts corresponding to the *D-CBF* were within the limits of FEMA 356 [108], this could be regarded as an indicator of the frame's re-

centring ability. In comparison to the *CBF-SF*, the *D-CBF* with MRF sub-systems containing slim-floor beam-to-column joints, evidenced an improved performance and a slightly lower steel consumption – the latter being based on a simplified evaluation.

Taking into consideration the experimental results, the FEA results of the reference model and of the parametric study, the outcomes of the structural nonlinear static and nonlinear dynamic analyses on the *MRF-SF*, *CBF-SF* and *D-CBF*, the possibility to adapt the slim-floor beam-to-column joints to the requirements of the European seismic code [51] for Ductility Class 3 frame systems is confirmed. Capacity design principles are applicable to the slim-floor beam-to-column joints and adequate seismic performance is achievable if the seismic energy dissipation is directed to the ends of the beams, while the bolted connection, the adjoining welds and the web panel provide overstrength. For this purpose, full-strength and rigid / semi-rigid joint classifications should be met together with an adequate joint rotation capacity of ± 40 mrad at Significant Damage.

7.1 Contributions of the author

The main contributions of the author to the current study are summarized, as follows:

- study and review of the state-of-the-art on slim-floor systems and beam-to-column joints for framed steel and steel-concrete composite structures;
- initiation of pre-test numerical investigations with advanced Finite Element Analyses on different slim-floor beam-to-column joint configurations and contribution to the development of the technical solution which allows for the formation of a plastic hinge in the dissipative zone of a slim-floor beam;
- design of test specimens consisting of two single-sided slim-floor beam-to-column joint assemblies;
- interpretation and evaluation of monotonic and cyclic experimental results of the joint specimens;
- development of a numerical program with Finite Element Analyses, interpretation of FEA results and optimisation of the slim-floor beam-to-column joint solution;
- development of a design and detailing procedure for moment-resisting slim-floor beam-to-column joints;
- development of a slim-floor beam-to-column joint numerical model based on experimental data; integration of joint model into mid-rise Moment-Resisting Frames, high-rise Concentrically-Braced Frames and Dual Concentrically-Braced Frames subjected to nonlinear static and dynamic analyses (i.e., *Pushover* with *N2 method*, *Response History Analysis*); interpretation and evaluation of nonlinear structural analyses results;
- elaboration of scientific papers for publication in conference proceedings or journals containing results obtained in the framework of the current study;
- elaboration of the Doctoral Dissertation.

7.2 Dissemination of results

The results and the main conclusions of the current study were published in scientific journals and international conference proceedings, as follows:

- **Don**, R., Vulcu, C., Ciutina, A., Stratan, A. (2022): Seismic performance of dual-concentrically braced frames with slim-floor beam-to-column joints. In:

Mazzolani, F.M., Dubina, D., Stratan, A. (eds) Proceedings of the 10th International Conference on Behaviour of Steel Structures in Seismic Areas. STESSA 2022. Lecture Notes in Civil Engineering, vol 262. Springer, Cham. https://doi.org/10.1007/978-3-031-03811-2_58.

- **Don**, R., Vulcu, C., Ciutina, A., Stratan, A. (2022): Slim-floor beam-to-column joints for seismic-resistant structures: design approach and detailing. In: Mazzolani, F.M., Dubina, D., Stratan, A. (eds) Proceedings of the 10th International Conference on Behaviour of Steel Structures in Seismic Areas. STESSA 2022. Lecture Notes in Civil Engineering, vol 262. Springer, Cham. https://doi.org/10.1007/978-3-031-03811-2_65.
- Ciutina, A., **Don**, R., Vulcu, C., Stratan, A. (2022): Experimental evaluation of a continuous slim-floor beam-to-column joint. In: Santiago, A., da Silva, L.S., Wald, F. (eds) Connections IX, 9th Int. Workshop on Connections in Steel Structures, 1st Edition 2022. ISBN: 978-92-9147-195-9.
- **Don**, R., Ciutina, A., Stratan, A., Vulcu, C. (2021): Slim-floor beam-to-column-joints for seismic-resistant structures: joint performance and case study on MRFs. 9th International Conference on Composite Construction in Steel and Concrete, Stromberg, Germany (in press).
- **Don**, R., Ciutina, A., Vulcu, C., Stratan, A. (2020): Seismic-resistant slim-floor beam-to-column joints: experimental and numerical investigations. Journal of Steel and Composite Structures, 37(3), pp. 307-321. DOI: https://doi.org/10.12989/scs.2020.37.3.307.
- Vulcu, C., **Don**, R., Ciutina, A., Stratan, A. (2020): Experimental and numerical investigation of beam-to-column joints for slim-floor systems in seismic zones. 2nd International Conference on Seismic Design of Industrial Facilities (*SeDIF*), 4th – 5th March 2020, Aachen, Germany.
- Vulcu, C., **Don**, R., Ciutina, A. (2019): Beam-to-column joints for slim-floor systems in seismic zones: numerical investigations and experimental program. In: Wald and Jandera (eds.) Stability and Ductility of Steel Structures 2019, Czech Technical University in Prague, Czech Republic. ISBN: 978-0-367-33503-8.
- Vulcu, C., **Don**, R., Ciutina, A. (2019): Beam-to-column joints for slim-floor systems in seismic zones. International Conference on Steel and Aluminium Structures, 3rd – 5th July 2019, Bradford, UK.
- Vulcu, C., **Don**, R., Ciutina, A. (2018): Semi-continuous beam-to-column joints for slim-floor systems in seismic zones. 12th International Conference on Advances in Steel-Concrete Composite Structures (ASCCS), 27th – 29th June 2018, Valencia, Spain.
- Vulcu, C., **Don**, R., Ciutina, A., Dubina, D. (2017): Numerical investigation of moment-resisting slim-floor beam-to-column connections. 8th International Conference on Composite Construction in Steel and Concrete (CCVIII), 30th July – 2nd August 2017, Spring Creek Ranch in Jackson, Wyoming, USA.

In addition, the author was involved in further research activities, from which the following publications resulted:

- **Don**, R., Balaskas, G., Vulcu, C., Hoffmeister, B. (2023): Steel and composite joints with dissipative connections for MRFs in moderate seismicity. Steel Construction 16, No. 1, pp. 31-43. https://doi.org/10.1002/stco.202200044
- **Don**, R., Balaskas, G., Vulcu, C., Hoffmeister, B. (2023): Composite moment-resisting frame with dissipative connections: monotonic versus numerical results. 10th Eurosteel Conference, 12th – 14th September, Amsterdam, The Netherlands (in press).
- Balaskas, G., **Don**, R., Vulcu, C., Hoffmeister, B. (2023): Steel joints for moment-resisting frames in moderate seismicity: experimental and numerical investigations. 10th Eurosteel Conference, 12th – 14th September, Amsterdam, The Netherlands (in press).
- Händeler, D., **Don**, R., Vulcu, C, Hoffmeister, B. (2023): Experimental and numerical programs on laser-cut I-beam-to-CHS/SHS column joint components. 10th Eurosteel Conference, 12th – 14th September, Amsterdam, The Netherlands (in press).
- Balaskas, G., **Don**, R., Vulcu, C., Hoffmeister, B. (2023): Experimental system identification and damage detection in steel-concrete composite frames subjected to monotonic and cyclic lateral loads. 10th International Conference on Experimental Vibration Analysis for Civil Engineering Structures. 30th August – 1st September, Milano, Italy (in press).
- **Don**, R., Balaskas, G., Vulcu, C., Hoffmeister, B. (2022): Steel and Composite joints for MRFs in moderate seismicity: experimental and numerical program. ce/papers 5, No. 4, pp. 857–866. Special issue: SDSS 2022. https://doi. org/10.1002/cepa.1828

References

[1] Ahmed, I.M., Tsavdaridis, K.D.: The evolution of composite flooring systems: applications, testing, modelling and Eurocode design approaches. Journal of Constructional Steel Research, 155, pp. 286-300 (2019).

[2] Mullet, D.L., Lawson, R.M.: Slim Floor construction using deep decking. The Steel Construction Institute, SCI Publication P127 (9781870004893) (1993).

[3] Braun, M., Hechler, O., Obiala, R.: Untersuchungen zur Verbundwirkung von Betondübeln. Anwendung von tiefliegenden Betondübeln bei Slim-Floor-Konstruktionen (CoSFB). Stahlbau, 83(5), pp. 302-308 (2014).

[4] Hauke, B., Kuhnhenne, M., Lawson, M., Veljkovic, M., in collab. with Siebers, R. (editors): Sustainable Steel Buildings: A practical guide for structures and envelopes. Wiley Blackwell (2016). ISBN 9781118740798 (PDF).

[5] Lam, D., Dai, X., Kuhlmann, U., Raichle, J., Braun, M.: Slim-floor construction – design for ultimate limit state. Journal of Steel Construction, 8(2), pp. 79-84 (2015).

[6] Lawson, R.M., Bode, H., Brekelmans, J.W.P.M., Wright, P.J., Mullet, D.L.: Slimflor and slimdeck construction: European developments. The Structural Engineer, 77(8), pp. 28-32 (1999).

[7] ArcelorMittal: Slim-floor – an innovative concept for floors (brochure). ArcelorMittal Europe – Long Products Sections and Merchant Bars (2021).

[8] Tata Steel. www.tatasteeleurope.com

[9] Ju, Y.K., Chun, S-C., Kim, S-D.: Flexural test of a composite beam using asymmetric steel section with web openings. Journal of Structural Engineering, 135(4), pp. 448-458 (2009).

[10] Peikko Group Corporation: Deltabeam 2021. Composite beams – Slim floor structure with integrated fireproofing – technical manual. Lahti, Finland. www.peikko.com/products/deltabeam-slim-floor-structures/overview

[11] Kloeckner Metals UK. www.kloecknermetalsuk.com/westock/products/ultra-shallow-floor-beam.

[12] Lawson, R.M., Mullett, D.L., Rackham, J.W.: Design of asymmetric slimflor beams using deep composite decking. The Steel Construction Institute, SCI Publication P175 (1997).

[13] Beckmann, O., Cyllok, M.: Deltabeam composite slim-floor beams supporting prestressed hollowcore slabs in fire case – fire tests for assessment of indirect and flexible support. Peikko Group Corp. 9th Int. Conference on Composite Construction in Steel and Concrete, Stromberg, Germany, July 26-30 (2021).

[14] Tsavdaridis, K-D.: Structural performance of perforated steel beams with novel web openings and with partial concrete encasement (PhD Dissertation,

in English). City University London, School of Engineering and Mathematical Sciences (2010).

[15] Schäfer, M., Braun, M.: Entwicklung der Slim-Floor-Bauweise in Europa. Stahlbau, 88(7), pp. 618-624 (2019).

[16] ArcelorMittal: High-rise buildings. ArcelorMittal Europe (brochure) – Long Products Sections and Merchant Bars (2017).

[17] CEN European Committee for Standardization: Eurocode 4: Design of composite steel and concrete structures - Part 1-1: General rules and rules for buildings (EN 1994-1-1:2004), Brussels, Belgium.

[18] British Standards Institution (BSI): British Standard: Structural use of steelwork in building. Part 1: Code of practice for design in simple and continuous construction: hot rolled sections. London, The United Kingdom (1992).

[19] DIBt (Deutsches Institut für Bautechnik): National Technical Approval, No. Z-26.4-59, CoSFB-Betondübel, Applicant: ArcelorMittal Belval & Differdange S.A., Berlin (2014).

[20] DIBt (Deutsches Institut für Bautechnik): National Technical Approval, No. Z-26.2-49, Delta Verbundträger, Berlin (2020).

[21] Chen, Q., Shi, Y.J., Wang, Y.Q., Chen, H., Zhang, Y.: Structural analysis on light steel frame with steel-concrete composite slim beam. Building Structures, 32(2), pp. 17-20 (2002).

[22] Constructalia, ArcelorMittal. Montevideo Rotterdam, The Netherlands: https://constructalia.arcelormittal.com/en/case_study_gallery/netherlands/montevideo_rotterdam_a_residential_high_rise_with_hybrid_structure.

[23] Montevideo Rotterdam, The Netherlands. Source of the photographs: https://en.wikipedia.org/wiki/File:Montevideo(Rotterdam).jpg.

[24] Montevideo Rotterdam, The Netherlands. Source of the photographs: https://en.wikipedia.org/wiki/File:Montevideo_tower.jpg.

[25] Constructalia, ArcelorMittal. Area 22 Building, Trento, Italy: https://constructalia.arcelormittal.com/en/case_study_gallery/italy/innovative_steel_structure_for_the_mixed_use_building_area_22.

[26] Constructalia, ArcelorMittal. Brussels Environment, Brussels, Belgium. https://constructalia.arcelormittal.com/en/case_study_gallery/belgium/bruxelles_environnement_building_sustainable_transparent_and_flexible_with_slimfloor_beams.

[27] Brussels Environment in Brussels, Belgium. Source of the photographs: https://upload.wikimedia.org/wikipedia/commons/6/68/Brussels_Environnement_building_%281%29.jpg.

[28] Constructalia, ArcelorMittal. Delft city hall & train station, The Netherlands: https://constructalia.arcelormittal.com/en/case_study_gallery/netherlands/delft-city-hall-and-train-station-an-unforgettable-arrival-with-histar-and-ifb.

[29] Delft city hall and train station, The Netherlands. Source of the photographs: https://en.wikipedia.org/wiki/File:Municipal_Offices_and_Train_Station,_Delft_01.jpg.

[30] ANSI/AISC 341-16: Seismic provisions for structural steel buildings. American Institute for Steel Construction, Chicago, USA (2016a).

[31] Malaska, M.: Behaviour of a semi-continuous beam-column connection for composite slim-floors (PhD Dissertation, in English). Helsinki University of Technology, Laboratory of Steel Structures (2000).

[32] Lu, X., Mäkeläinen, P.: Strength and stiffness of composite slim floor beams. Proceedings of the 4th Pacific Structural Steel Conference, pp. 93-100, Singapore (1995).

[33] Ma, Z., Mäkeläinen, P.: Behaviour of composite slim floor structures in fire. Journal of Structural engineering, 126(7), pp. 830-837 (2000).

[34] Mäkeläinen, P., Ma, Z.: Fire resistance of composite slim floor beams. Journal of Constructional Steel Research, 54(3), pp. 345-363 (2000).

[35] Wang, Y., Yang, L., Shi, Y., Zhang, R.: Loading capacity of composite slim frame beams. Journal of Constructional Steel Research, 65(3), pp. 650-661 (2009).

[36] Zhang, R.H.: Flexural stiffness and bending capacity of frame composite slim beam with deep deck (Master Thesis). Tsinghua University, Beijing, China (2006).

[37] De Nardin, S., El Debs, Ana L.H.C.: Composite connections in slim-floor system: An experimental study. Journal of Constructional Steel Research, 68(1), pp. 78-88 (2012).

[38] Braun, M., Hechler, O., Obiala, R., Kuhlmann, U., Eggert, F., Hauf, G., Konrad, M.: Experimentelle Untersuchungen von Slim-Floor-Trägern in Verbundbauweise. Anwendung von tiefliegenden Betondübeln bei Slim-floor-Konstruktionen – CoSFB. Stahlbau, 83(10), pp. 741-749 (2014).

[39] Kuhlmann, U., Hauf, G., Konrad, M.: Push-out and girder tests for the determination of the bending capacity and longitudinal shear capacity of Composite Slim-Floor girder with Cofradal 200 deck elements. Versuchsbericht (unpublished). Institut für Konstruktion und Entwurf, Universität Stuttgart (2010).

[40] Kuhlmann, U., Hauf, G., Eggert, F.: Push-out-Versuche zur Bestimmung der Längsschubtragfähigkeit von Verbund "Slim-Floor"-Trägern. Versuchsbericht (unveröffentlicht / unpublished). Institut für Konstruktion und Entwurf, Universität Stuttgart (2013).

[41] Yang, L., Wang, Y., Shi, Y.: Full-scale test of two-storey composite slim floor under pseudo-dynamic and pseudo-static loadings. Advances in Structural Engineering, 18(2), pp. 173-188 (2015).

[42] Duarte da Costa, J.: Structural properties of steel-concrete composite joints (PhD Dissertation, in English). University of Luxembourg, The Faculty of Sciences, Technology and Communication (2018).

[43] Duarte da Costa, J., Obiala, R., Odebreit, C.: Rotation capacity of composite joints for slim-floor beams. Stahlbau, 88(7), pp. 675-684 (2019).

[44] Kyriakopoulos, P., Peltonen, S., Spyrakos, C., Vayas, I., Leskela, M.V.: Experimental and analytical investigation of shallow floor composite beams under extreme deformation. Journal of Structural Engineering, 148(2), (2022).

[45] CEN European Committee for Standardization: Eurocode 8: Design of structures for earthquake resistance - Part 1-1: General rules and seismic action (EN 1998-1-1:2020, pre-normative), Brussels, Belgium.

[46] CEN European Committee for Standardization: Eurocode 8: Design of structures for earthquake resistance - Part 1: General rules, seismic actions and rules for buildings (EN 1998-1:2004), Brussels, Belgium.

[47] FEMA P-795: Quantification of building seismic performance factors: Component equivalency methodology. Federal Emergency Management Agency, Washington, D.C, USA (2011).

[48] Vulcu, C., Stratan, A., Ciutina, A., Dubina, D.: Beam-to-CTF High-Strength Joints with External Diaphragm. I: Design and Experimental Validation. Journal of Structural Engineering, 143(5) (2017).

[49] ECCS (European Convention for Constructional Steelwork): Recommended testing procedures for assessing the behaviour of structural elements under cyclic loads. Brussels, Belgium (1986).

[50] Landolfo, R., Mazzolani, F., Dubina, D., da Silva, L.S., D'Aniello, M.: Design of Steel Structures for Buildings in Seismic Areas. 1st Edition. ECCS – European Convention for Constructional Steelwork (2017), ISBN (ECCS): 978-92-9147-138-6, ISBN (Ernst & Sohn): 978-3-433-03010-3.

[51] CEN European Committee for Standardization: Eurocode 8: Design of structures for earthquake resistance - Part 1-2: Earthquake resistance design of structures (EN 1998-1-2:2021, pre-normative), Brussels, Belgium.

[52] CEN European Committee for Standardization: Eurocode 0: Basis of structural and geotechnical design (EN 1990:2019, pre-normative), Brussels, Belgium.

[53] Bertero, V.V.: Earthquake engineering (Lecture notes). University of California, Berkeley (1997).

[54] CEN European Committee for Standardization: Eurocode 3: Design of steel structures - Part 1-1: General rules and rules for buildings (EN 1993-1-1:2020, pre-normative), Brussels, Belgium.

[55] CEN European Committee for Standardization: Eurocode 4: Design of composite steel and concrete structures - Part 1-1: General rules and rules for buildings (EN 1994-1-1:2021, pre-normative), Brussels, Belgium.

[56] CEN European Committee for Standardization: Eurocode 2: Design of concrete structures - Part 1-1: General rules and rules for buildings (EN 1992-1-1:2004), Brussels, Belgium.

[57] Fujitani, H., Teshigawara, M., Gojo, W., Hirano, Y., Saito, T., Fukuyama, H.: Framework for Performance-based design of building structures. Computer-aided civil and infrastructure engineering, 20(1), pp. 62-77 (2005).

[58] Structural Engineers Association of California: Vision 2000 – a framework for performance-based design. Sacramento, California (1995).

[59] Itoi, T., Iita, Y., Sekimura, N.: A framework for seismic design of items in safety-critical facilities for implementing a risk-informed defence-in-depth-based design. Frontiers in Built Environment, 3(27) (2017).

[60] Stratan, A.: Studiul comportării clădirilor multietajate cu cadre metalice duale amplasate în zone seismice (PhD Thesis, in Romanian). Politehnica University Timișoara, Civil Engineering and Architecture Faculty, Department of Steel Construction and Structural Mechanics (2003).

[61] CEN European Committee for Standardization: Eurocode 8: Design of structures for earthquake resistance – Part 3: Assessment and retrofitting of buildings and bridges (EN 1998-3:2021, pre-normative), Brussels, Belgium.

[62] CEN European Committee for Standardization: Eurocode 3: Design of steel structures – Part 1-8: Design of connections (EN 1993-1-8:2005), Brussels, Belgium.

[63] El Jisr, H., Elkady, A., Lignos, D.G.: Composite steel beam database for seismic design and performance assessment of composite-steel moment-resisting frame systems. Bulletin of Earthquake Engineering, 17(6), pp. 3015-3039 (2019).

[64] Elkady, A., Lignos, D.: Modeling of the composite action in fully restrained beam-to-column connections: implications in the seismic design and collapse capacity of steel special moment frames. Earthquake Engineering and Structural dynamics, 43(13), pp. 1935-1954 (2014).

[65] Hajjar, J.F., Leon, R.T., Gustafson, A., Shield, C.K.: Seismic response of composite moment-resisting connections. II: Behavior. Journal of Structural Engineering, 124(8), pp. 877-885 (1998).

[66] Plumier, A.: The dogbone: back to the future. Engineering Journal (New York), 34(2nd quarter), pp. 61-67 (1997).

[67] Jones, S.L., Fry, G.T., Engelhardt, M.D.: Experimental evaluation of cyclically loaded reduced beam section moment connections. Journal of Structural Engineering, 128(4), pp. 441-451 (2002).

[68] Engelhardt, M.D., Fry, G.T., Jones, S.L., Venti, M., Holliday, S.: Behaviour and design of radius cut, reduced beam section connections. SAC/BD-00/17, SAC Joint Venture, Sacramento, California (2000).

[69] Gilton, C.S., Uang, C-M.: Cyclic response and design recommendations of weak-axis reduced beam section moment connection. Journal of Structural Engineering, 128(4), pp. 452-463 (2002).

[70] Uang, C-M., Fan, C-C.: Cyclic stability criteria for steel moment connections with reduced beam section. Journal of Structural Engineering, 127(9), pp. 1021-1027 (2001).

[71] Zhang, X., Ricles, J.M.: Experimental evaluation of reduced beam section connections to deep columns. Journal of Structural Engineering, 132(3), pp. 346-357 (2006).

[72] Hauf, G.: Trag- und Verformungsverhalten von Slim-Floor Trägern under Biegebeanspruchung (PhD Dissertation, in German). Institut für Konstruktion und Entwurf Stahl- Holz- und Verbundbau, Universität Stuttgart (2010).

[73] Romero, M.L., Cajot, L-G., Conan, Y., Braun, M.: Fire design methods for slim-floor structures. Steel Construction, 8(2), pp. 102-109 (2015).

[74] Hauf, G., Kuhlmann, U.: Deformation calculation methods for slim floors. Steel Construction, 8(2), pp. 96-101 (2015).

[75] Hicks, S., Peltonen, S.: Design of slim-floor construction for human-induced vibrations. Steel Construction, 8(2), pp. 110-117 (2015).

[76] Demonceau, J-F.: Steel and composite building frames: sway response under conventional loading and development of membrane effects in beams further to an exceptional action (PhD Dissertation, in English). Université de Liège, Faculté de Sciences Appliquées (2008).

[77] Don, R.: The numerical investigation of beam-to-column connections for slim-floor systems, (Master Thesis, in English), Politehnica University Timisoara, Department of Steel Structures and Structural Mechanics, Romania (2016).

[78] FEMA 547: Techniques for the seismic rehabilitation of existing buildings. Federal Emergency Management Agency, Washington, D.C, USA (2006).

[79] CEN European Committee for Standardization: Eurocode 3: Design of steel structures – Part 1-8: Design of connections (EN 1993-1-8:2020, pre-normative), Brussels, Belgium.

[80] Vulcu, C.M.: Seismic performance of dual frames of CFRHS and welded beam-to-column joints (PhD Dissertation, in English). Politehnica University Timisoara, Faculty of Civil Engineering (2013).

[81] Abaqus v2019. Dassault Systèmes, Waltham, USA (2019).

[82] Ahmed, B., Nethercot, D.A.: Effect of column axial load on composite connection behaviour. Engineering Structures, 20(1-2), 113-128 (1998).

[83] Calado, L., Castiglioni, C.A., Bernuzzi, C.: Seismic behaviour of welded beam-to-column joints: experimental and numerical analysis. Proceedings. of the 4th Workshop on Connections in Steel Structures, American Institute of Steel Connection, Roanoke, October (2000).

[84] Chou, C.C., Wu, C.C., Jao, C.K., Wang, Y.Y.: Weakened and strengthened steel moment connections. Proceedings of the 4th International Conference on Earthquake Engineering, National Center for Research on Earthquake Engineering, Chinese Taiwan Society for Earthquake Engineering, Taipei, October (2006).

[85] Shin, K.J., Kim, Y.J., Oh, Y.S., Moon, T.S.: Behaviour of welded CFT column to h-beam connections with external stiffeners. Engineering Structures, 26(13), 1877-1887 (2004).

[86] Kim, Y.J., Shin, K.J., Kim, W.J.: Effect of stiffener details on behaviour of CFT column-to-beam connections. International Journal of Steel Structures, 8(2), 119-133 (2008).

[87] Kiamanesh, R., Abolmaali, A., Ghassemieh, M.: The effect of stiffeners on the strain patterns of welded connection zone. Journal of Constructional Steel Research, 66(1), 19-27 (2010).

[88] Schäfer, D., Eichler, B., Amlung, L.: Modern Plastic Design for Steel Structures. Directorate-General for Research and Innovation, Brussels, Belgium, ISSN 1018-5593 (2010).

[89] Vegte, G.J., Makino, Y.: Numerical simulations of bolted connections – Implicit versus explicit approach. Proceedings of the 5th International Workshop on Connections in Steel Structures, Delft, June (2004).

[90] Li, Y., Cao, S., Jing, D.: Analytical compressive stress–strain model for concrete confined with high-strength multiple-tied-spiral transverse reinforcement. Structural Design of Tall and Special Buildings, 27:e1416 (2017).

[91] Grassl, P., Xenos, D., Nyström, U., Rempling, R., Gylltoft, K.: CDPM2: A damage-plasticity approach to modelling the failure of concrete. International Journal of Solids and Structures, 50(24), pp. 3805-3816 (2013).

[92] European Commission, Directorate-General for Research and Innovation, Kesti, J., Rebelo, C., Portioli, F. et al: High strength steel in seismic resistant building frames (HSS-SERF): final report, Publications Office, Brussels, Belgium (2015). https://data.europa.eu/doi/10.2777/725123

[93] CEN European Committee for Standardization: Eurocode 3: Design of steel structures - Part 1-5: Plated structural elements (EN 1993-1-5:2006), Brussels, Belgium.

[94] ArcelorMittal Construction: Cofraplus 220. The optimised solution for long span composite floors. ArcelorMittal Construction (brochure) (2016).

[95] Dinu, F., Dubina, D., Neagu, C., Vulcu, C., Both, I., Herban, S.: Experimental and numerical evaluation of an RBS coupling beam for moment-resisting steel frames in seismic areas. Journal of Steel Construction, 6(1), pp. 27-33 (2013).

[96] Takeuchi, T., Hajjar, J.F., Matsui, R., Nishimoto, K., Aiken, I.D.: Local buckling resistant condition for core plates in buckling restrained braces. Journal of Constructional Steel Research, 66(2), pp. 139-149 (2010).

[97] Takeuchi, T.:Buckling-restrained brace: history, design and applications. 9th International Conference on Behaviour of Steel Structures in Seismic Areas, Christchurch, New Zealand, February 14-16 (2018).

[98] Inamasu, H., de Castro e Sousa, A., Lignos, D.G.: Development and experimental validation of dissipative embedded column base connections for enhanced seismic performance of steel moment-resisting frames. Journal of Structural Engineering, 148(3): 04021280 (2022).

[99] Watanabe, A., Hitomi, Y., Saeki, E., Wada, A., Fujimoto, M.: Properties of brace encased in buckling-restraining concrete and steel tube. Proceedings of

9th World Conference on Earthquake Engineering, Tokyo-Kyoto, Japan, August 2-9 (1988).

[100] Landolfo, R., D'Aniello, M., Tartaglia, R., Costanzo, S., Demonceau, J-F., Jaspart, J-P., Stratan, A., Jakab, D., Dubina, D., Elghazouli, A., Bompa, D.: Equaljoints PLUS Volume with pre-normative design recommendations for seismically qualified steel joints. ECCS – European Convention for Constructional Steelwork, 1st Edition, ISBN: 978-92-9147-144-7 (2018).

[101] Landolfo, R., D'Aniello, M., Costanzo, S., Demonceau, J-F., Jaspart, J-P., Stratan, A., Jakab, D., Dubina, D., Elghazouli, A., Bompa, D.: Equaljoints PLUS Volume with information brochures for 4 seismically qualified joints. ECCS – European Convention for Constructional Steelwork, 1st Edition, ISBN: 978-92-9147-143-0 (2018).

[102] ANSI/AISC 358-16: Prequalified connections for special and intermediate steel moment frames for seismic applications. American Institute for Steel Construction, Chicago, USA (2016c).

[103] Vayas, I.: Verbundkonstruktionen auf der Grundlage des Eurocode 4. Ernst & Sohn, Bauingenieur-Praxis, ISBN 3-433-01757-3, Berlin (1999).

[104] CEN European Committee for Standardization: Eurocode 3: Design of steel structures – Part 1-1: General rules and rules for buildings (EN 1993-1-1:2005), Brussels, Belgium.

[105] CSI Berkley: SAP2000 v21. Copyright Computers and Structures (2019).

[106] CEN European Committee for Standardization: Eurocode 8: Design of structures for earthquake resistance - Part 3: Assessment and retrofitting of buildings (EN 1998-3:2005), Brussels, Belgium.

[107] Fajfar, P.: A nonlinear analysis method for performance-based seismic design. Earthquake Spectra, 16(3), pp. 573-92 (2000).

[108] FEMA 356: Prestandard and commentary for the seismic rehabilitation of buildings. Federal Emergency Management Agency, Washington, D.C. (2000).

[109] Akkar, S., Sandikkaya, M.A., Senyurt, M., Azari Sisi, A., Ay, B., Traversa, P., Douglas, J., Cotton, F., Luzi, L., Hernandez, B., Godey, S.: Ref. database for seismic ground-motion in Europe (RESORCE). Bulletin of Earthquake Engineering, 12(1), pp. 311-339 (2014).

[110] Dubina, D., Dinu, F., Stratan, A.: Tower Centre International building in Bucharest - Part II: Performance-based seismic evaluation and robustness. Steel Construction - Design and Research, Ernst & Sohn, 3(1), pp. 14-18 (2010).

[111] D'Aniello, M., L.M. Ambrosino, G., Portioli, F., Landolfo, R.: Modelling aspects of the seismic response of steel concentric braced frames. Journal of Steel and Composite Structures, 15(5), pp. 539-566 (2013).

[112] Dicleli, M., Calik, E.: Physical theory hysteretic model for steel braces. Journal of Structural Engineering, ASCE, 134(7), pp. 1215-1228 (2008).

[113] D'Aniello, M., L.M. Ambrosino, G., Portioli, F., Landolfo, R.: The influence of out-of-straightness imperfection in physical theory models of bracing

members on seismic performance assessment of concentric braced frames. The Structural Design of Tall and Special Buildings, Wiley, 24(3), pp. 176-197 (2015).

[114] Maquoi, R., Rondal, J.: Mise en équation des nouvelles courbes européennes de flambement. Construction Métallique 1, pp. 17-30 (1978).

[115] Gabor, G., Vulcu, C., Stratan, A., Dubina, D., Voica, F., Marcu, D., Alexandrescu, D.: Experimental and numerical validation of the technical solution of a brace with pinned connections for seismic-resistant multi-story structures. 15th World Conf. on Earthquake Eng., Lisbon, Portugal, paper 4431 (24-28.09.2012).

[116] Deierlein, G.G, Reinhorn, A., Willford, M.R.: Nonlinear structural analysis for seismic design. NEHRP Seismic design technical brief no 4 produced by the NEHRP Consultants Joint Venture, a partnership of the Applied Technology Council and the Consortium of Universities for Research in Earthquake Engineering, for the National Institute of Standards and Technology, Gaithersburg, MD, NIST GCR 10-917-5 (2010).

[117] European Commission, Joint Research Centre, Institute for the Protection and Security of the Citizen, Sabau, G-A., Poljansek, M., Taucer, F., Pegon, P., Molina, F.J., Tirelli, D., Viaccoz, B., Stratan, A., Ioan-Chesoan, A., Dubina, D. et al: Full-scale experimental validation of dual eccentrically braced frame with removable links. Luxembourgh Publications Office of the European Union (2014). ISBN 978-92-79-44717-4 (PDF).

[118] Ioan, M. A.: Seismic performance of re-centring dual eccentrically braced frames with removable links (PhD Dissertation, in English). Politehnica University Timisoara, Faculty of Civil Engineering (2015).

[119] Ioan, A., Stratan, A., Dubina, D., Poljansek, M., Molina, F., Taucer, F., Pegon, P., Sabau, G.: Experimental validation of re-centring capability of eccentrically braced frames with removable links. Engineering Structures, 113(2016), pp. 335-346. http://dx.doi.org/10.1016/j.engstruct.2016.01.038.

[120] Vulcu, C., Stratan, A., Dubina, D., D'Aniello, M., Landolfo, R., Cermelj, B., Beg, D., Comeliau, L., Demonceau, J.F., Long, H.V., Kleiner, A., Kuhlmann, U., Fülöp, L.A.: WP6: Guidelines for seismic design and performance based evaluation of Dual Steel Building Frames. WP 6 from High Strength Steel in Seismic Resistant Building Frames (HSS-SERF) (2013).

[121] Ioannis Vayas (Ed.): Innovative anti-seismic devices and systems. Chapter 7: Replaceable bolted link. Authors: Chesoan, A., Stratan, A., Dubina, D. (2017). ISBN: 978-92-9147-136-2

Annex A

On-site observations taken during the monotonic experimental test:

Specimen: ***SF J-M*** (**s**lim-**f**loor **j**oint, **m**onotonic);

Loading: monotonic;

Date: 10.07.2019;

- load applied in displacement control in the "pull" direction; the SF beam-to-column joint is subjected to hogging bending;
- deformation of the *RFS* is observed;
- development of transverse cracks in the concrete slab (between 100 kN and 200 kN actuator force);
- cracks in the concrete slab are developed in the proximity of the dissipative zone of the SF beam-to-column joint;
- small detachment of concrete from the *RFS* after applied displacement of 200 mm;
- maximum displacement in actuator: 288 mm; maximum top displacement recorded by LVDT: 278 mm;
- load applied in displacement control in the "push" direction; the SF beam-to-column joint is subjected to sagging bending;
- gap of approximately 2 cm between the concrete slab and the column flange is observed at load reversal; the gap is located behind the column;
- stiffener-to-column flange weld fractures at 263 kN actuator force;
- lower flange of SF beam-to-end plate fractures at 286 kN actuator force;
- monotonic test is stopped.

On-site observations taken during the cyclic experimental test:

Specimen: ***SF J-C*** (**s**lim-**f**loor **j**oint, **c**yclic);

Loading: cyclic (AISC 341-16 protocol [30]);

Date: 30.08.2019;

- 6 cycles of ± 3.75 mrad, of ± 5.0 mrad and of ± 7.5 mrad:
  - elastic response, similar stiffness under hogging and sagging bending;
- 4 cycles of ± 10.0 mrad:
  - initiation of transverse cracks in the reinforced concrete slab;
  - fine cracks in the concrete slab diagonal to the edges of the column flanges are observed;
- 2 cycles of ± 15.0 mrad:
  - transverse cracks in the concrete slab begin to open;
  - visible deformation of the *RFS* under sagging bending;
  - minor deformation of the end plate under sagging bending;
- 2 cycles of ± 20.0 mrad:
  - elongation and opening of cracks in the reinforced concrete slab; deformation increases in the *RFS*;
  - pinching is observed;
- 2 cycles of ± 30.0 mrad:
  - diagonal cracks in the concrete slab widen; the length of the diagonal cracks starts from the edges of the column flange and elongate towards the margins of the concrete slab;

- large deformations are developed in the *RFS*;
- detachment of column flange from the concrete slab (portion located behind the column);

- 2 cycles of ± 40.0 mrad:
  - severe cracking of the concrete slab accompanied by loud noises;
  - cracks in the concrete slab behind the column and diagonal to the column flanges are open and significant in width;
- 2 cycles of ± 50.0 mrad:
  - hogging and sagging bending resistances slowly decrease;
  - lower stiffener-to-column flange weld fractures;
  - initiation of fine crack in the SF beam lower flange-to-end plate weld;
- 2 cycles of ± 60.0 mrad:
  - bending resistance drops from 878 kNm to 300 kNm;
  - however, under sagging bending, the specimen attains 45 mrad;
  - strengthening of lower stiffeners fractures;
  - lower SF beam flange-to-end plate weld fractures;
  - cyclic test is stopped.

Sketches of material coupons from the IPE-600 profile and from the welded beam flange are shown in Fig. A-132:

IPE 600 steel profile

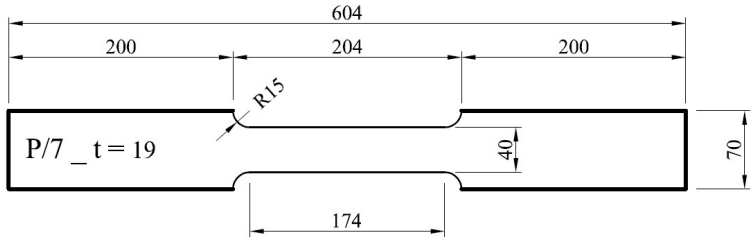

Welded steel beam flange

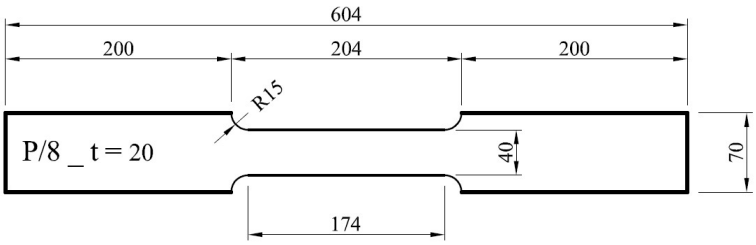

Fig. A-132. Material coupons from the IPE 600 and from the welded SF beam flange

Annex B

Results of the ***RM*** are shown in Fig. A-133:

Hogging bending

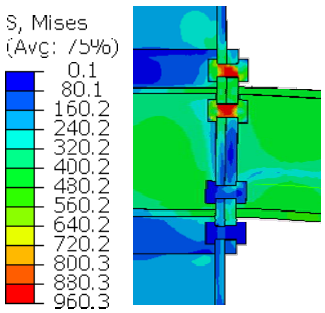

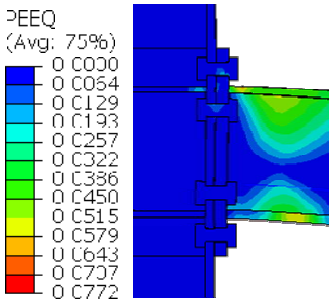

Sagging bending

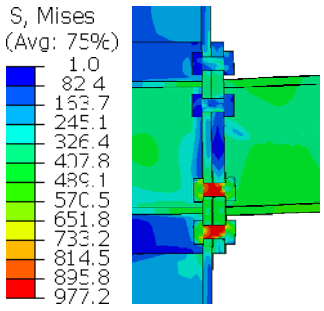

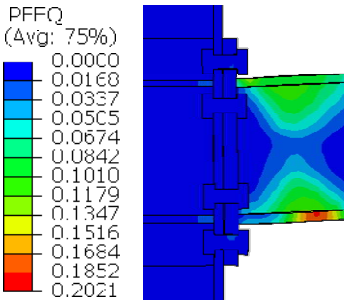

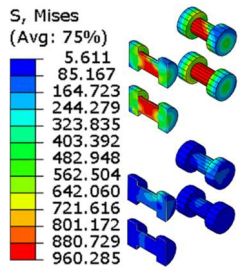

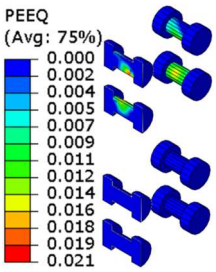

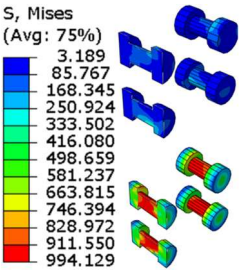

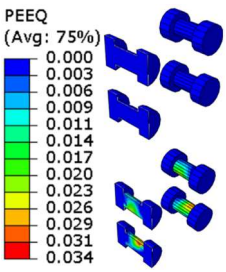

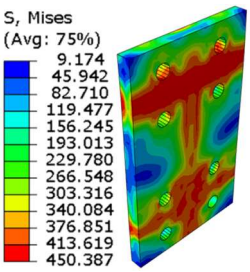

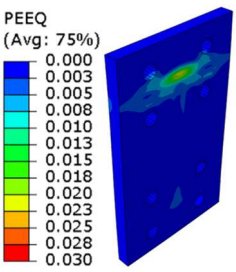

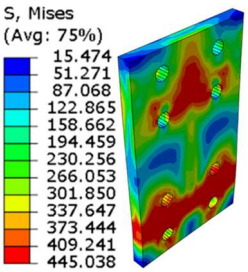

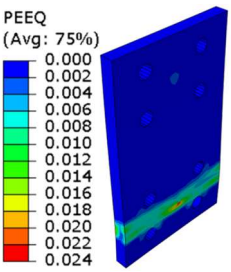

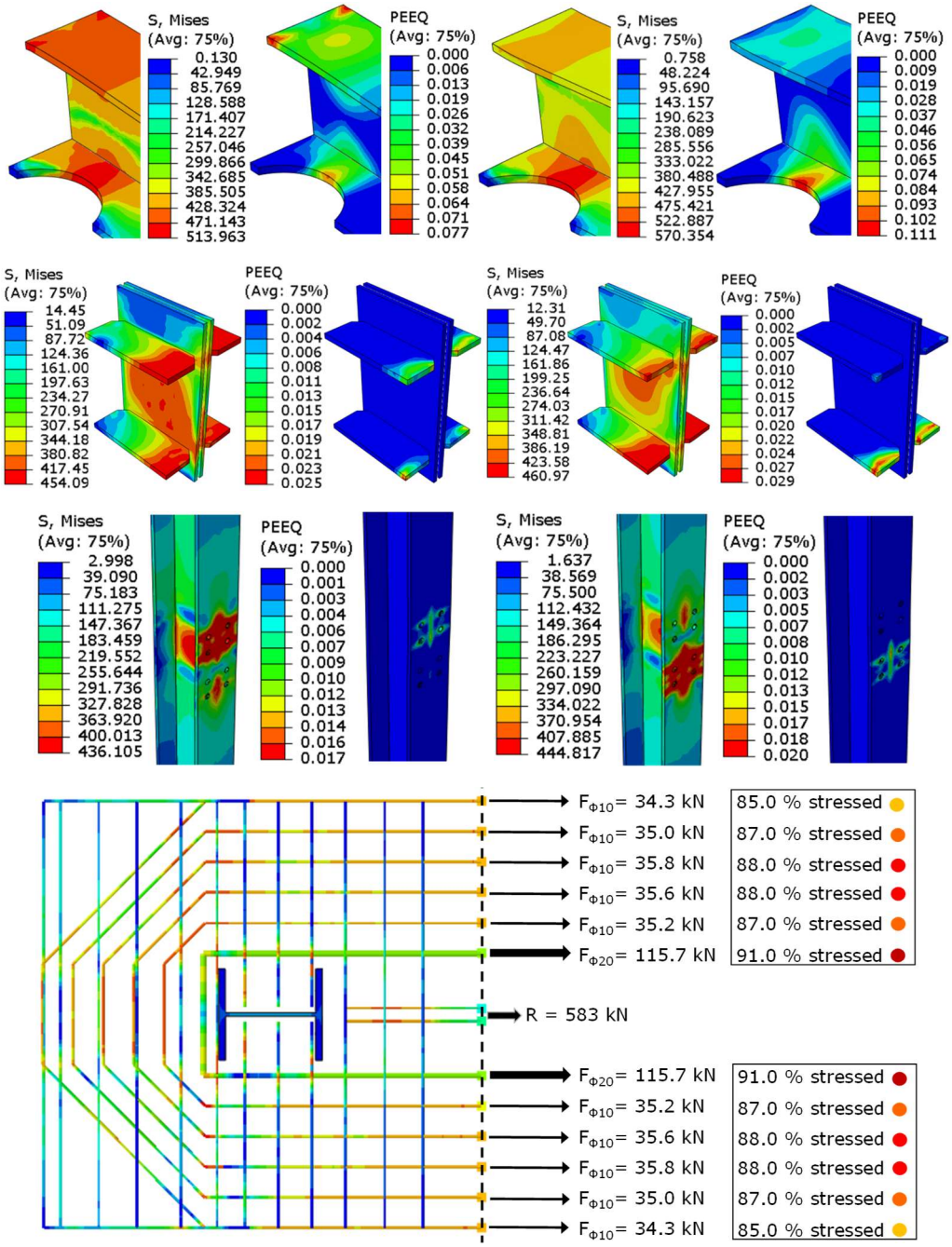

Fig. A-133. FEA on the *RM* under hogging and sagging bending moment

Results corresponding to the reinforced concrete of the ***RM*** under sagging and hogging bending are further shown in Fig. A-134 and Fig. A-135:

Sagging bending moment: ≈ **45 mrad**
PEEQ: Top view

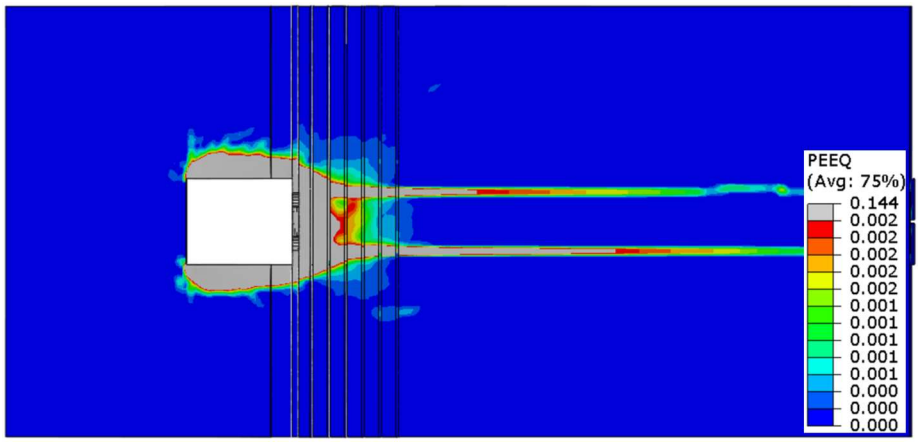

Sagging bending moment: ≈ **45 mrad**
PEEQ: Bottom view

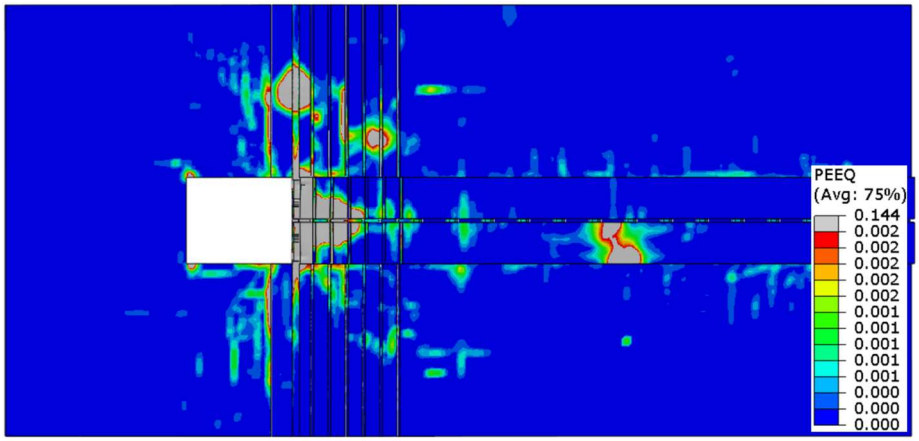

Sagging bending moment: ≈ **93 mrad**
PEEQ: Top view

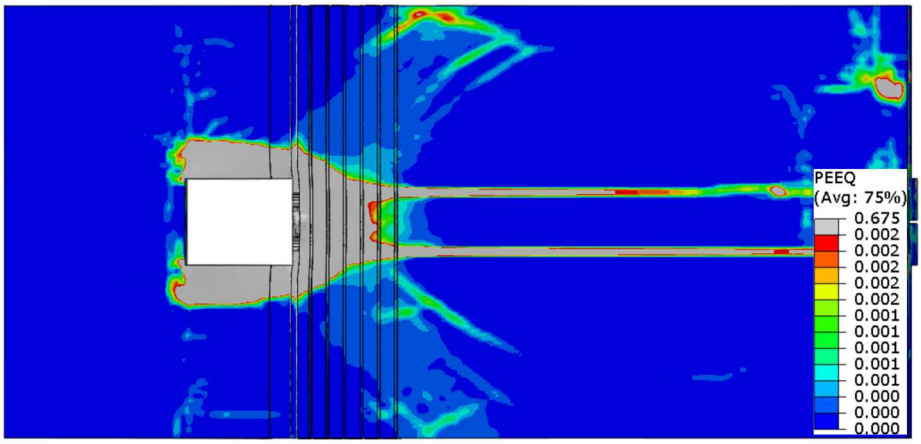

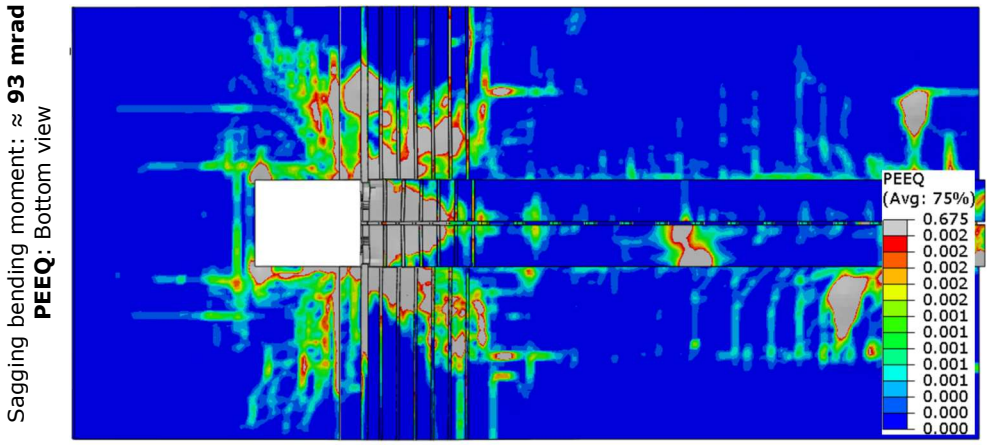

Fig. A-134. Results corresponding to the reinforced concrete slab of the *RM* under sagging bending at interstorey drifts equal to 45 and 93 mrad (end of FEA)

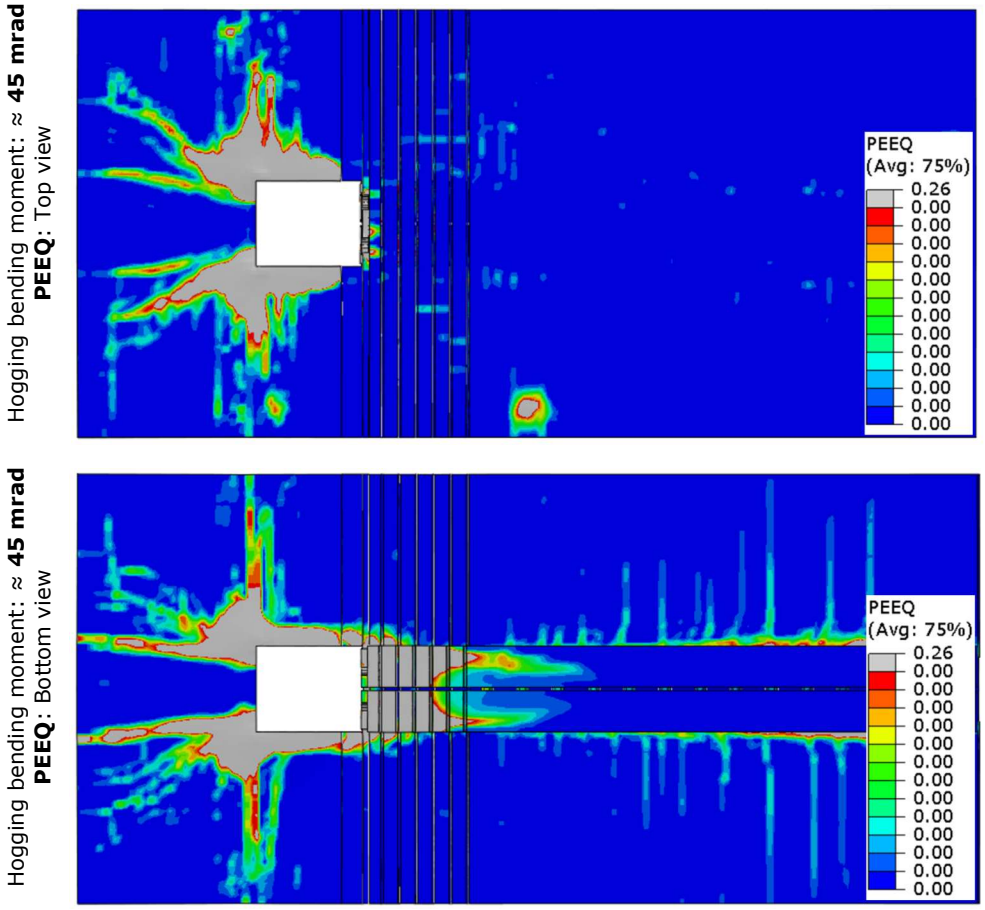

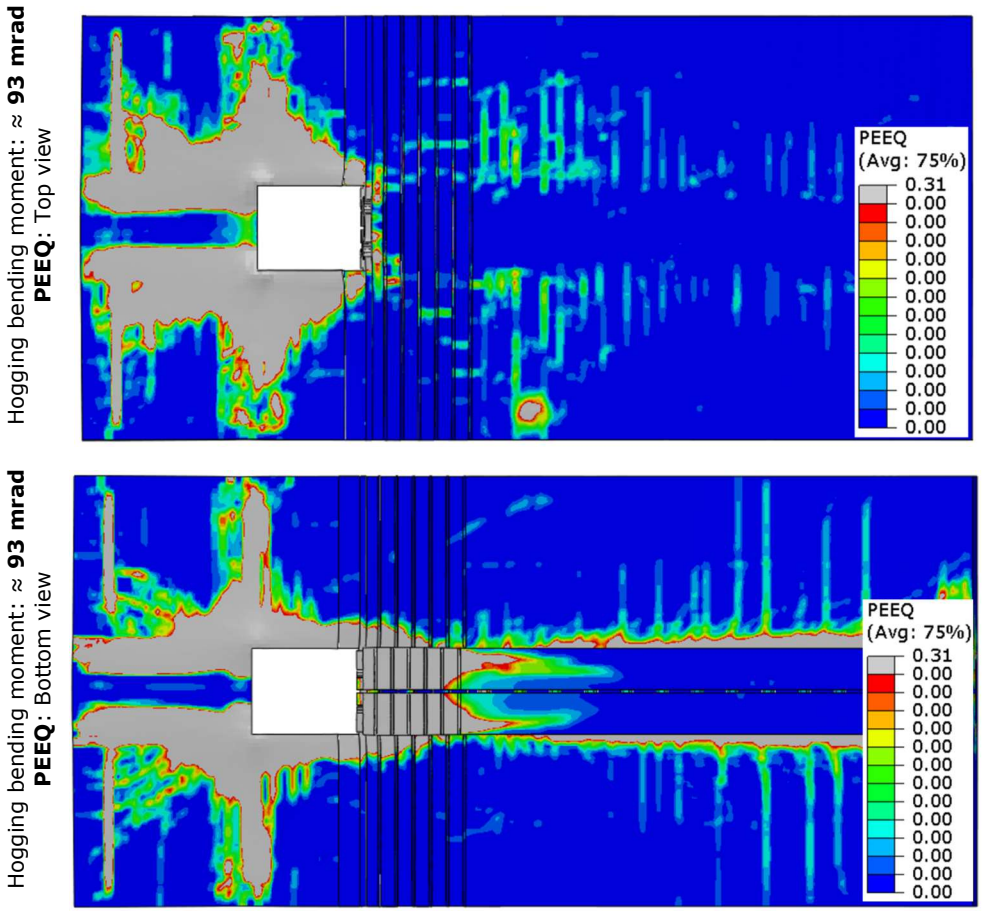

Fig. A-135. Results corresponding to the reinforced concrete slab of the *RM* under hogging bending at interstorey drifts equal to 45 and 93 mrad (end of FEA)

Results of the model ***M5*** are shown in Fig. A-136:

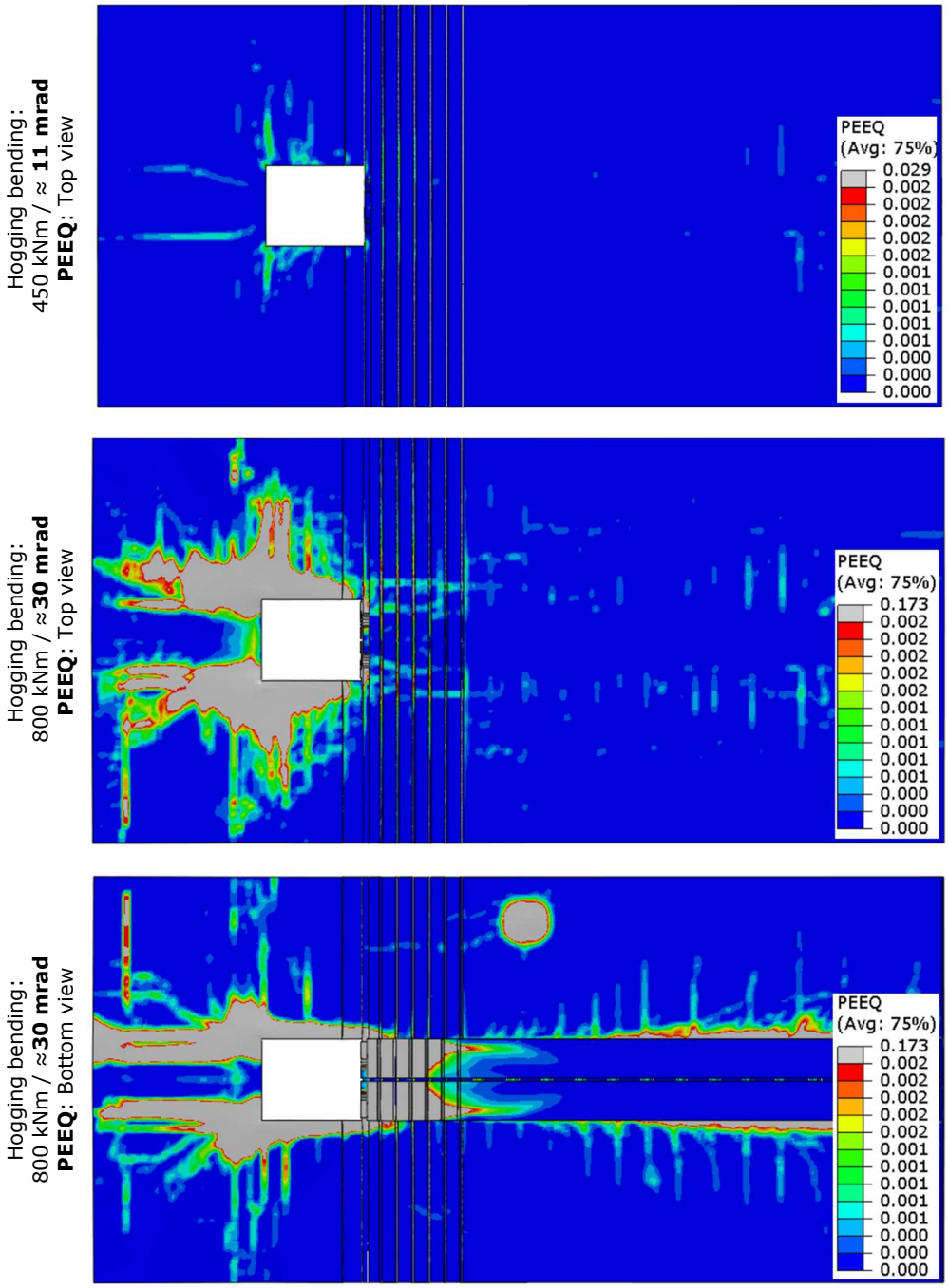

Fig. A-136. Results corresponding to the reinforced concrete slab of model M_5 under hogging bending at joint rotations equal to 11 mrad (initiation of concrete cracking) and 30 mrad (severe cracking of concrete)

Results of the model ***M₇*** are shown in Fig. A-137:

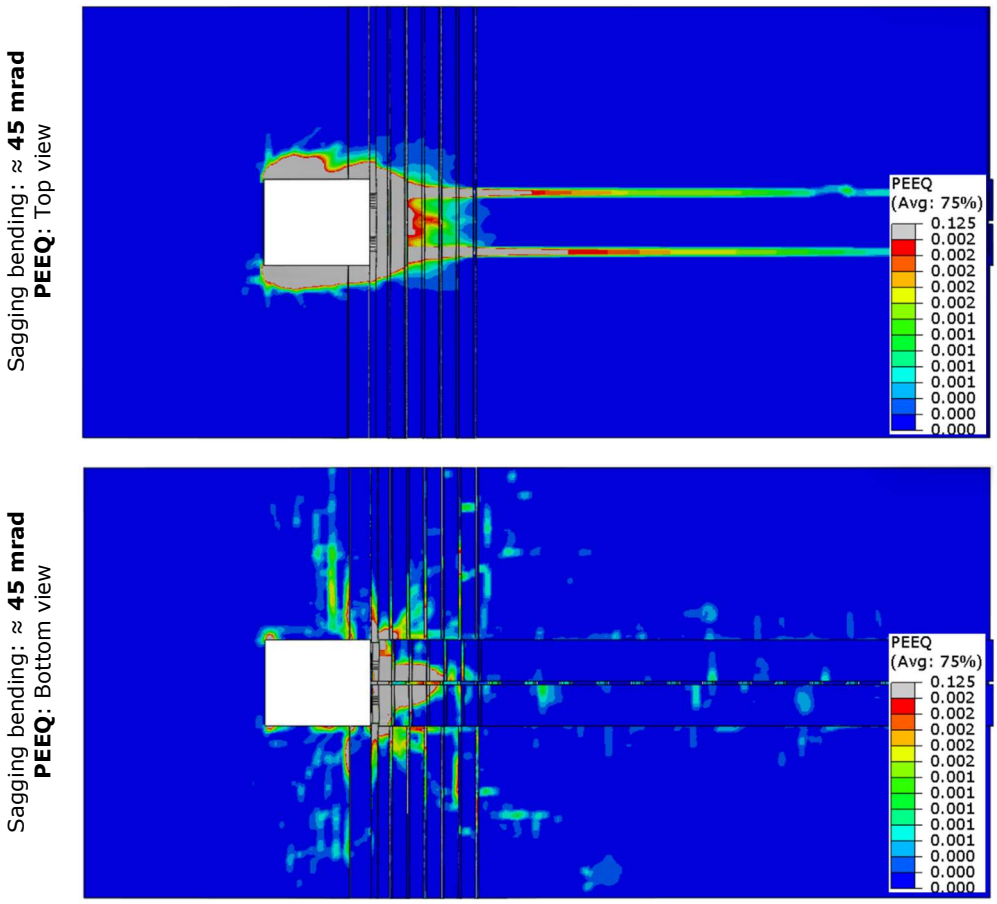

Fig. A-137. FEA on the M_7 under sagging bending moment at interstorey drifts equal to 45 mrad and 93 mrad (end of FEA)

Results of the model ***M8*** are shown in Fig. A-138:

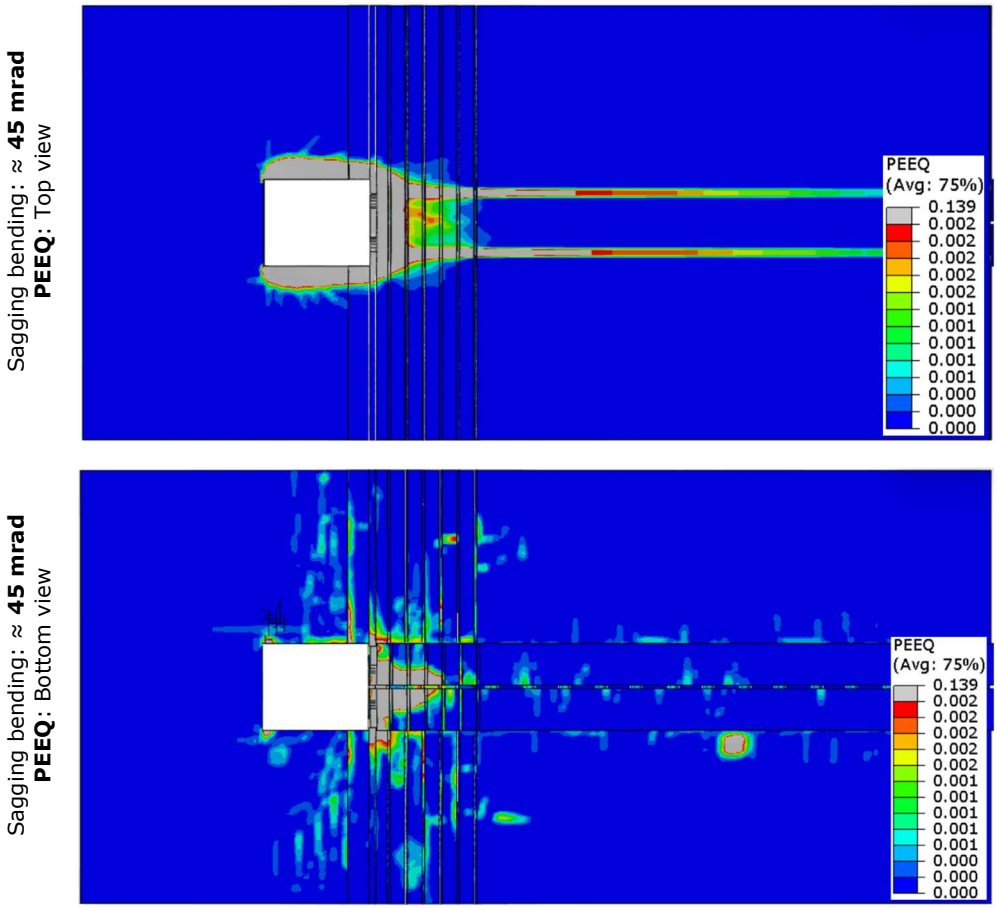

Fig. A-138. FEA on the M_8 under sagging bending moment at interstorey drifts equal to 45 mrad and 93 mrad (end of FEA)

Results corresponding to all analysed FE models from the current study are centralised in Table A-41.

Table A-41 – Results from the numerical program (at interstorey drift of ± 93 mrad; exception: models M_3, M_4, M_9 and M_{10})

	Results - hogging bending				Results - sagging bending			
	M_y	M_{max}	Φ_{Mmax}	$S_{j,ini}$	M_y	M_{max}	Φ_{Mmax}	$S_{j,ini}$
FE model	[kNm]	[kNm]	[mrad]	[kNm/rad]	[kNm]	[kNm]	[mrad]	[kNm/rad]
RM	714.0	903.9	98.2	37951	678.0	839.3	98.8	37351
M_1	758.0	944.5	89.5	37951	800.0	979.9	81.3	38728
M_2	605.0	726.1	92.9	32622	615.0	738.2	93.2	32991
M_3*	733.0	917.0	84.8	33939	677.0	850.8	90.4	36236
M_4*	675.0	850.7	87.4	36488	623.0	751.0	90.0	32699
M_5	745.0	940.1	88.3	40275	-	-	-	-
M_6	-	-	-	-	685.0	820.9	89.7	36718
M_7	-	-	-	-	684.0	836.4	93.6	37540
M_8	-	-	-	-	695.0	850.7	92.6	37378
M_9*	722.0	879.0	88.3	37550	677.0	838.8	89.6	36753
M_{10}*	748.0	910.9	91.8	38272	688.0	840.6	88.3	36929
M_{11}	725.0	922.6	98.0	38379	682.0	826.0	98.6	36672
M_{12}	685.0	864.9	89.5	37762	672.0	814.2	92.4	37345

***** symbol used to mark FE models that were stopped before attaining the end of the analyses.

The results that are presented in this table were obtained by applying a monotonic load in displacement control. The load under both hogging and sagging bending was 265 mm, which corresponded to a drift of approximately 93 mrad (being the maximum rotation obtained during the experimental monotonic test).

Observations:

- FEA on models M_3, M_4, M_9 and M_{10} were stopped before reaching the imposed displacement (corresponding to an interstorey drift of ± 93 mrad); this has particular importance on the value of the rotations at the maximum bending moment;
- M_y (yield bending moment) was obtained using the ECCS procedure;
- S_{jini} (elastic stiffness) was calculated at a value of the bending moment of approximately 400 kNm, and corresponds to the SF beam-to-column joint assembly, not to the bolted connection;
- All values from Table A-41 were calculated at the column centreline;
- Conclusions on the numerical program should be based on both the results in Table A-41 and on the observations related to the local behaviour of the SF beam-to-column components (e.g., distribution of von Mises stresses and equivalent plastic strains in individual components).

Annex C

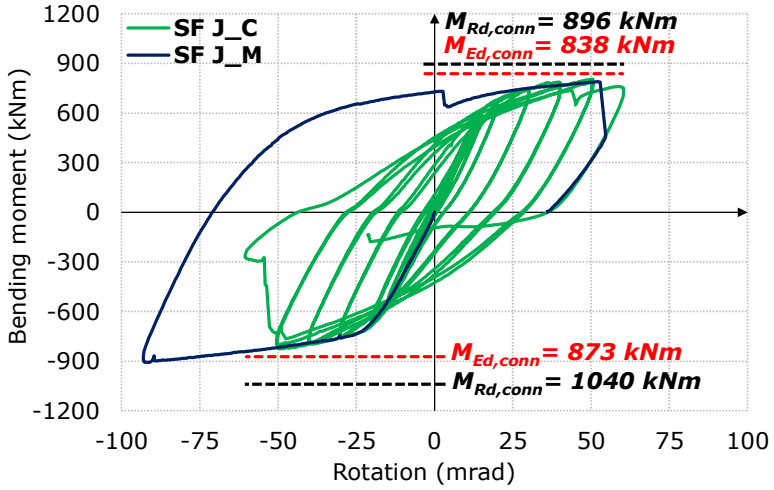

Fig. A-139. Maximum bending moments of joints from the experimental monotonic & cyclic curves vs. maximum bending moment resistances of the bolted connection

under development

Annex D

Plastic rotations that were developed in the **plastic hinges of the SF beams** (***MRF-SF***) at **SD** due to ***Pushover*** with *N2 method* are shown in Fig. A-140.

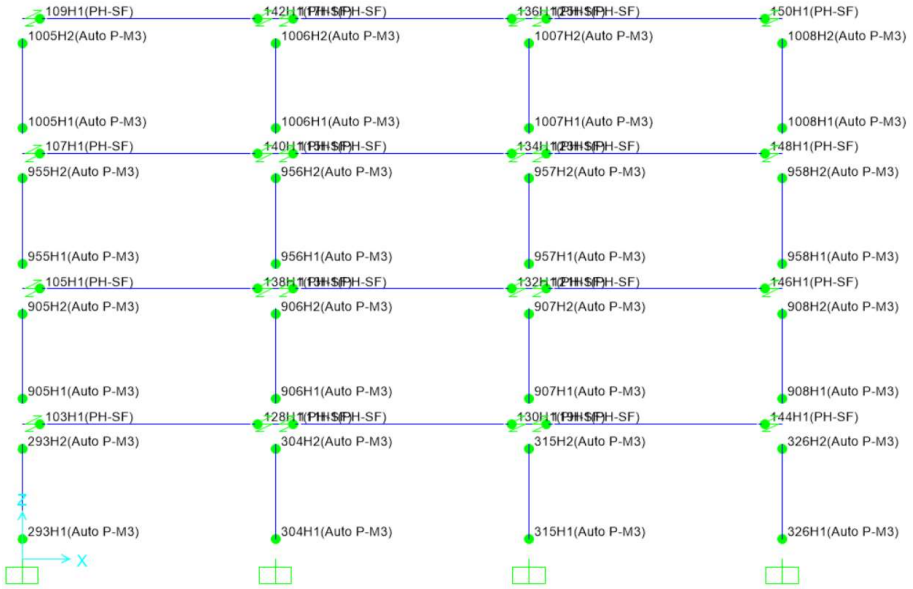

PH rotation of SF beams at SD (N2 method) - 4th storey

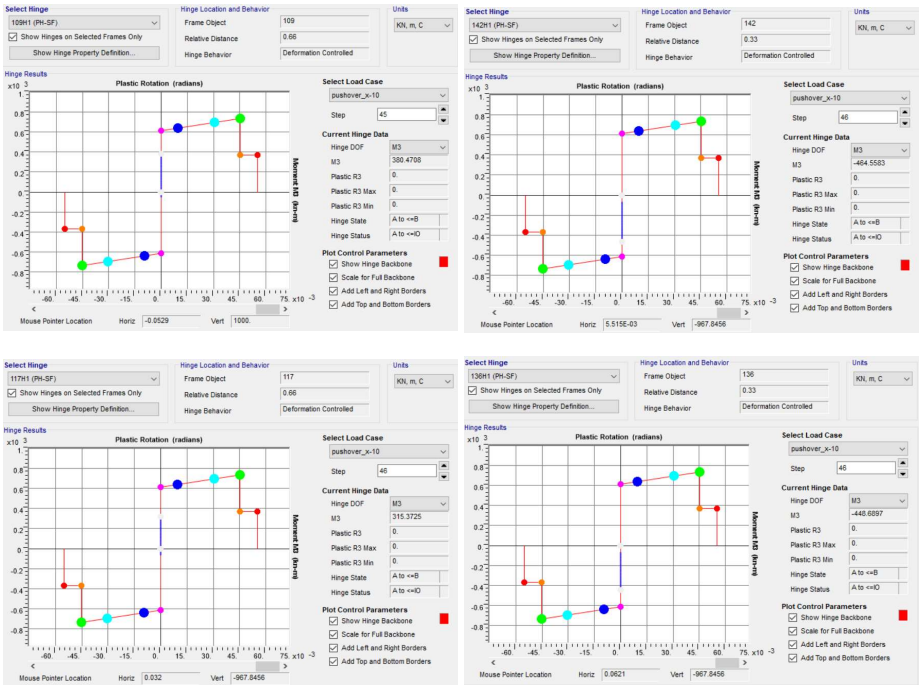

PH rotation of SF beams at SD (N2 method) - 3rd storey

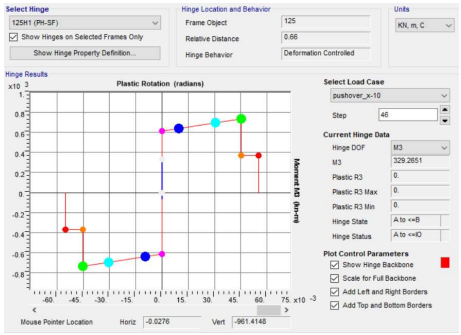

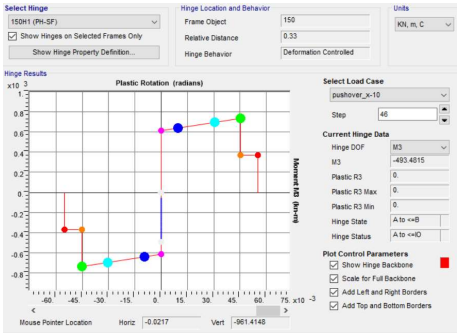

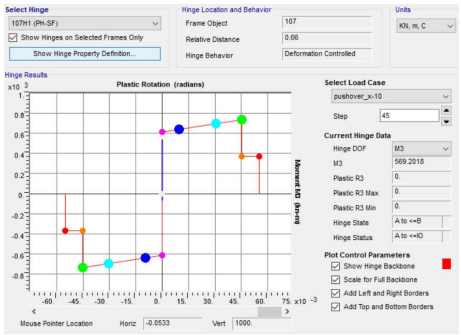

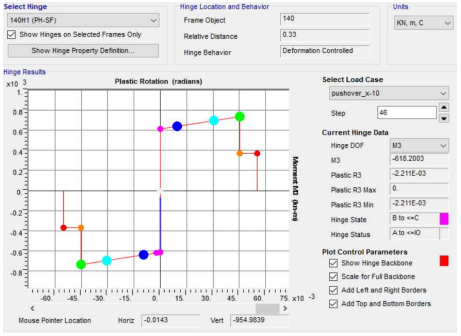

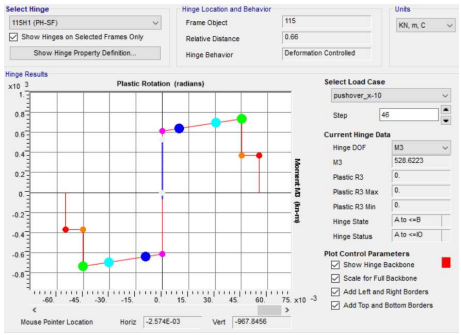

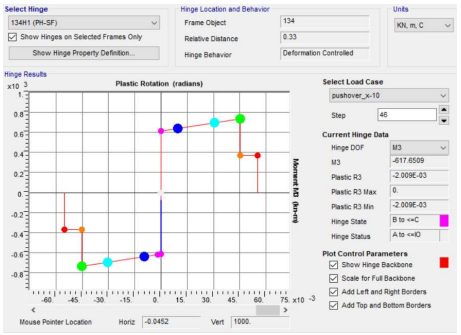

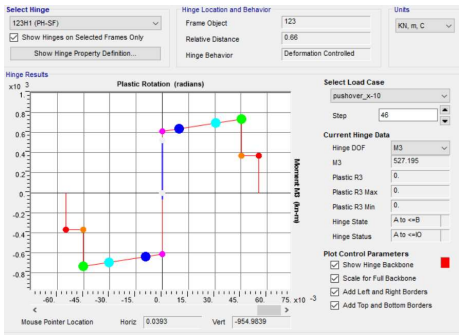

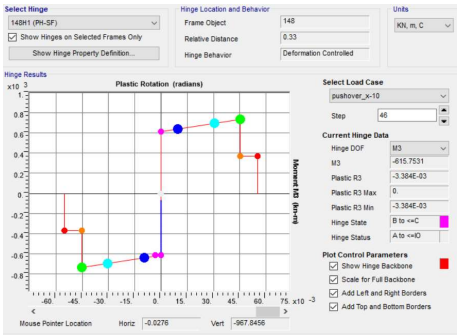

PH rotation of SF beams at SD (N2 method) – 2nd storey

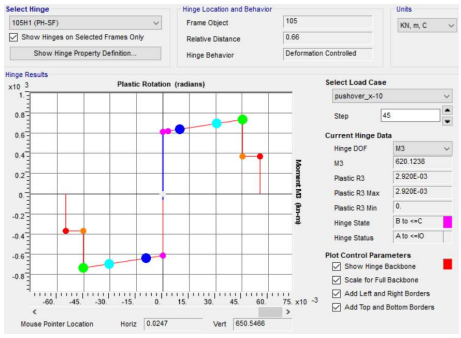

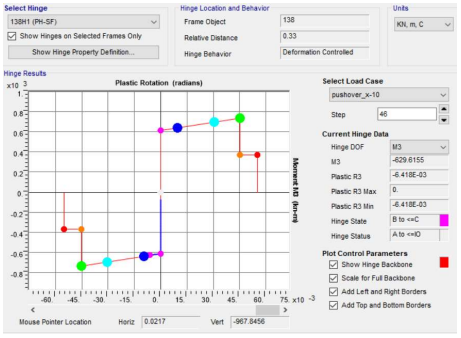

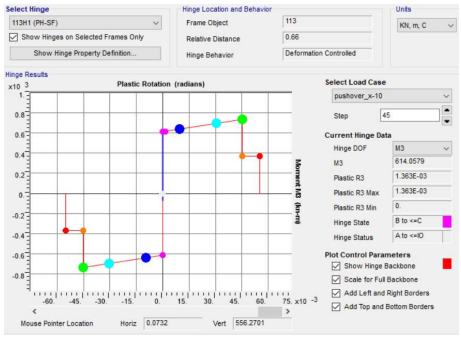

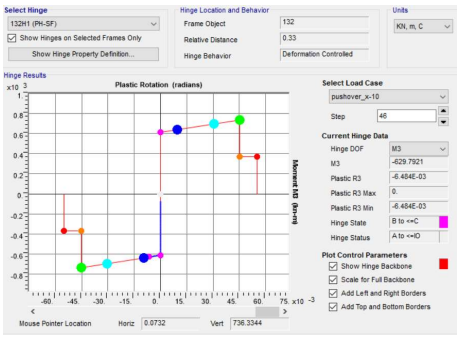

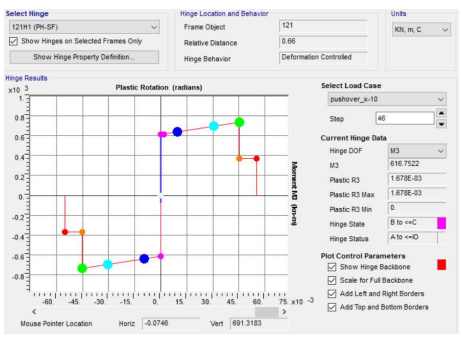

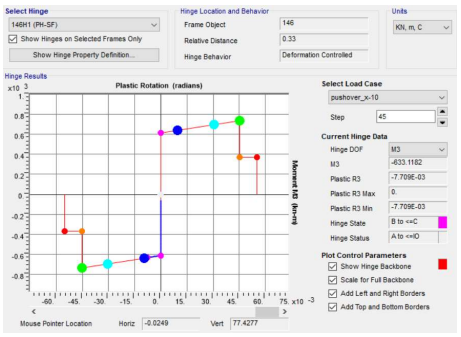

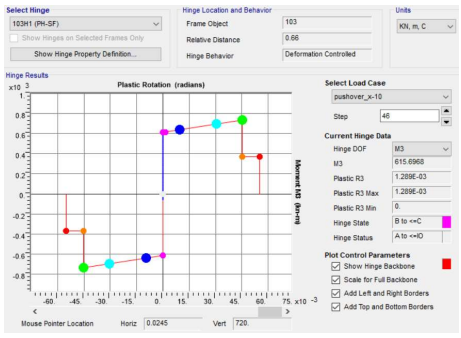

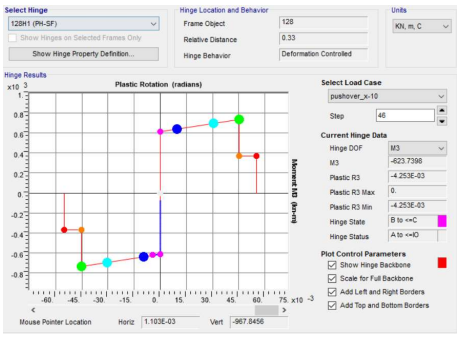

PH rotation of SF beams at SD (N2 method) – 1st storey

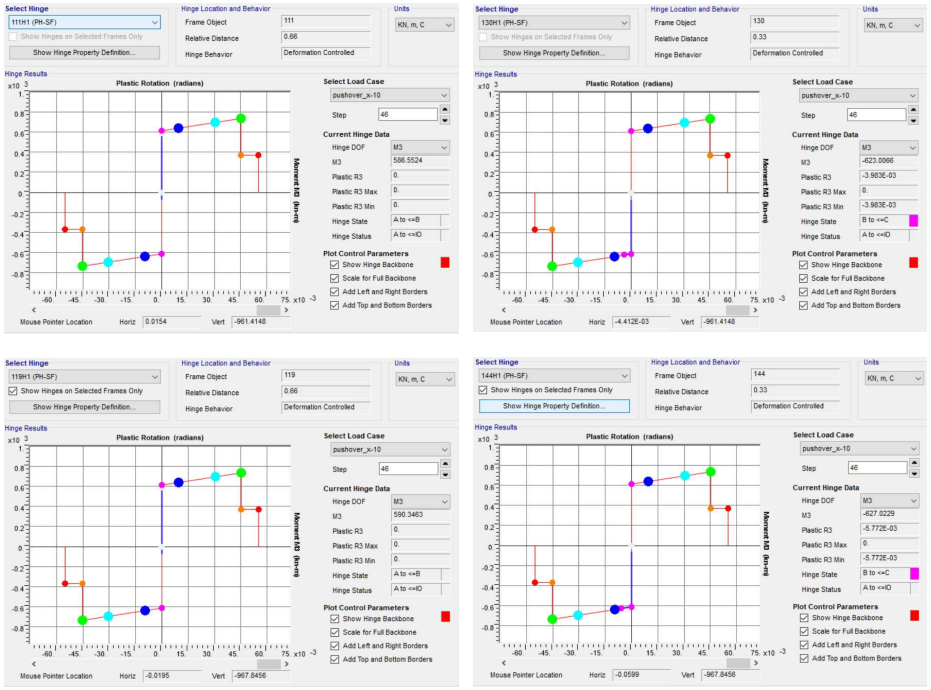

Fig. A-140. Plastic rotations in plastic hinges of SF beams (**MRF-SF**) at **SD**, *Pushover* analysis

Plastic rotations that were developed in the **plastic hinges of the SF beams** (***MRF-SF***) at **SD** due to ***RHA*** with ***#A1*** are shown in Fig. A-141.

PH rotation of SF beams at SD (*RHA*) - 4th storey

PH rotation of SF beams at SD (*RHA*) - 3rd storey

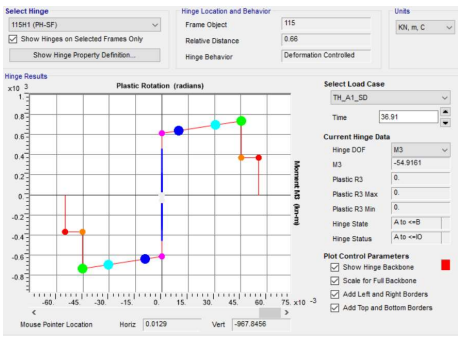

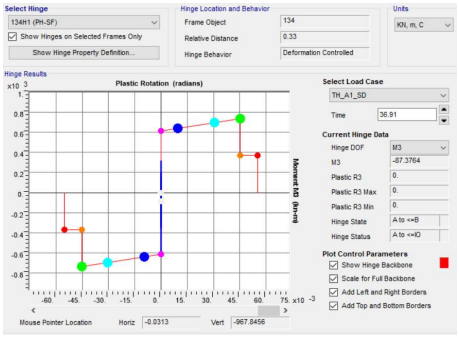

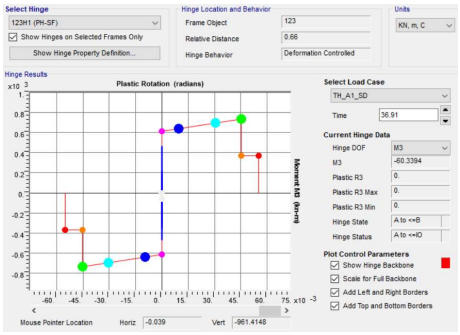

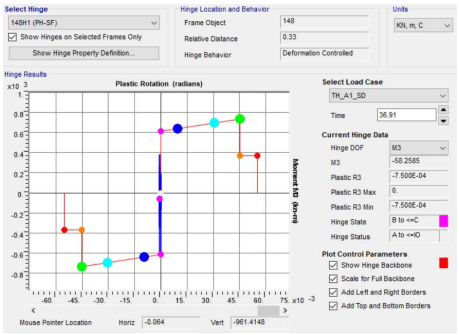

PH rotation of SF beams at SD (*RHA*) – 2nd storey

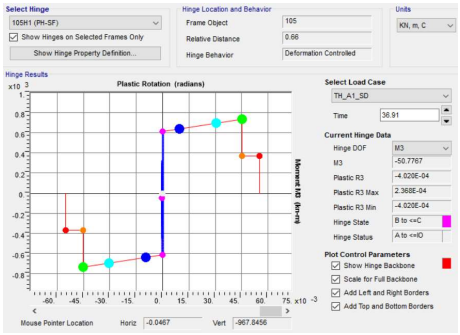

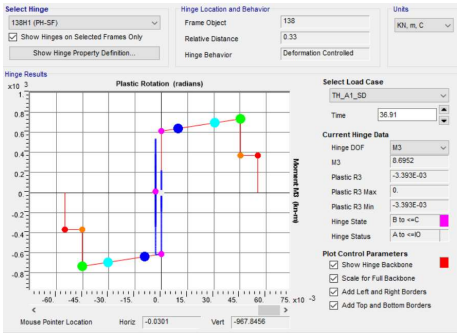

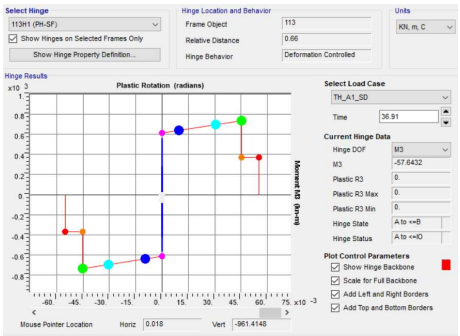

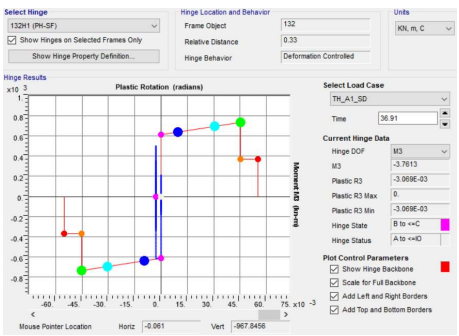

PH rotation of SF beams at SD (*RHA*) – 1st storey

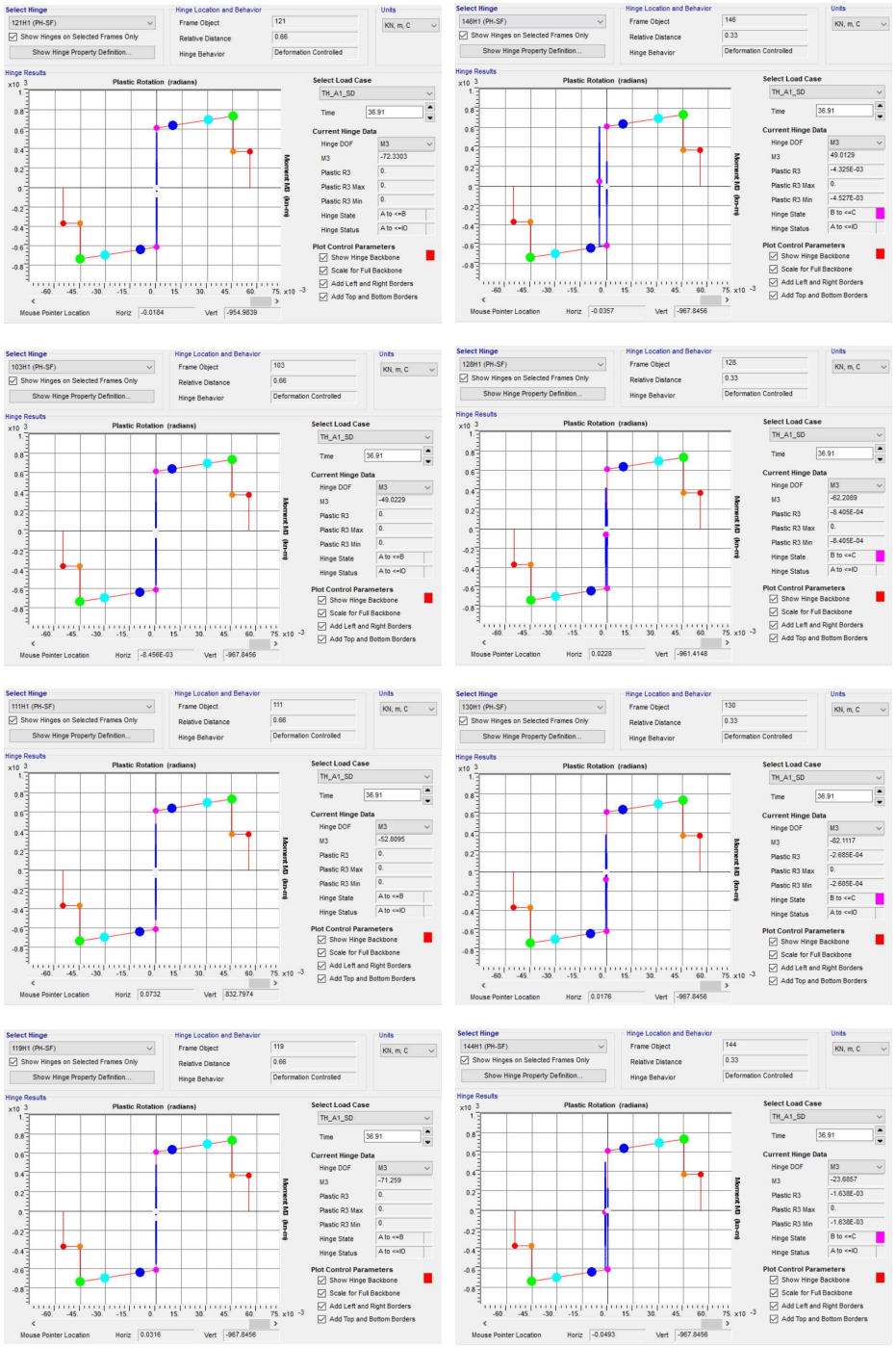

Fig. A-141. Plastic rotations in plastic hinges of SF beams (**MRF-SF**) at **SD, *RHA*** with ***#A1***

A comparison between the seismic performance of MRFs with SF beam-to-column joints containing different considerations regarding the modelling of the beam-to-column connection is shown in the following (see Fig. A-142a-d):

- beam-to-column connection modelled with a linear elastic link, which accounts for the elastic stiffness of the connection (see Fig. A-142a);
- beam-to-column connection is modelled as rigid (see Fig. A-142b).

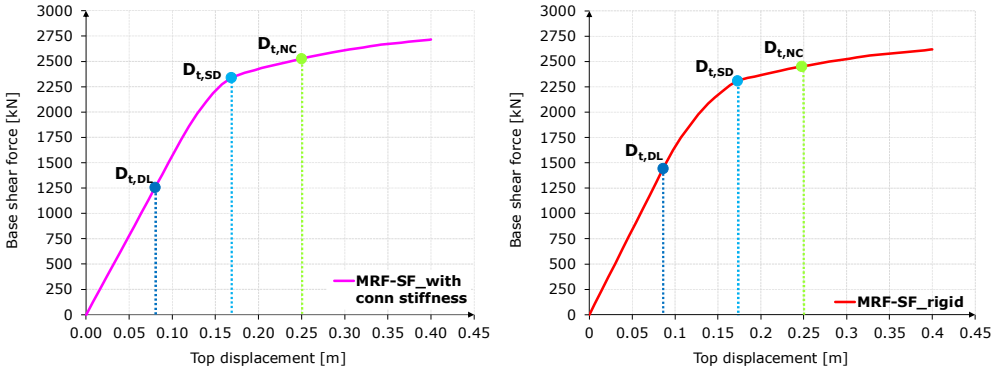

a) *MRF-SF* (considering **connection stiffness**)

b) *MRF-SF* with **rigid connection**

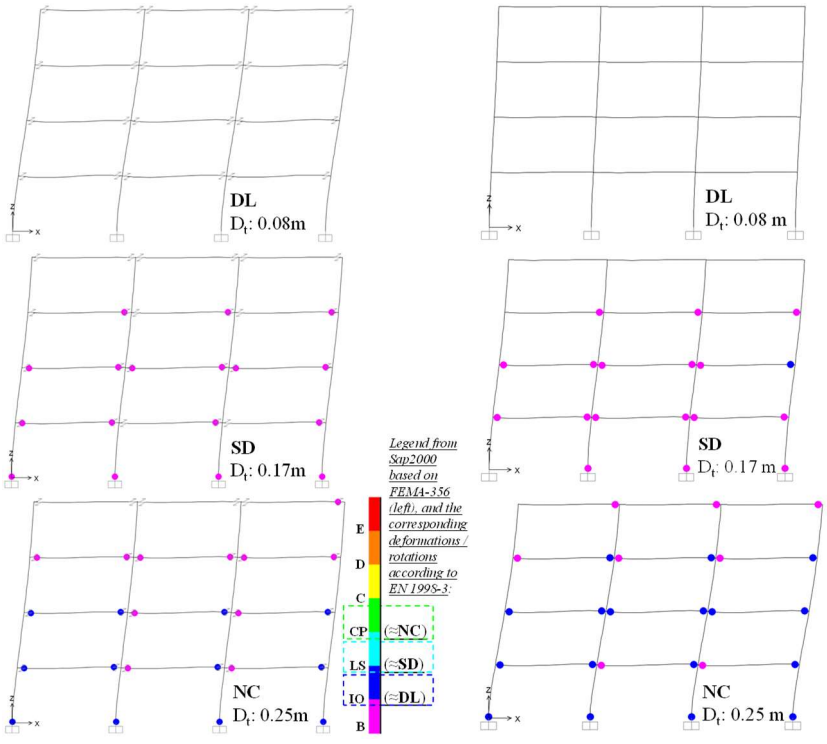

c) d)

Fig. A-142. *Pushover* results: a) b) capacity curves; c) d) damage state of *MRF-SF* with connections which included their stiffness (left) & *MRF-SF* with rigid connections (right)

Comparison between structural damage of MRFs with SF beam-to-column joints considering two different modelling methods of connections (see Fig. A-143):

MRF-SF (considering **connection stiffness**) *MRF-SF* with **rigid connection**

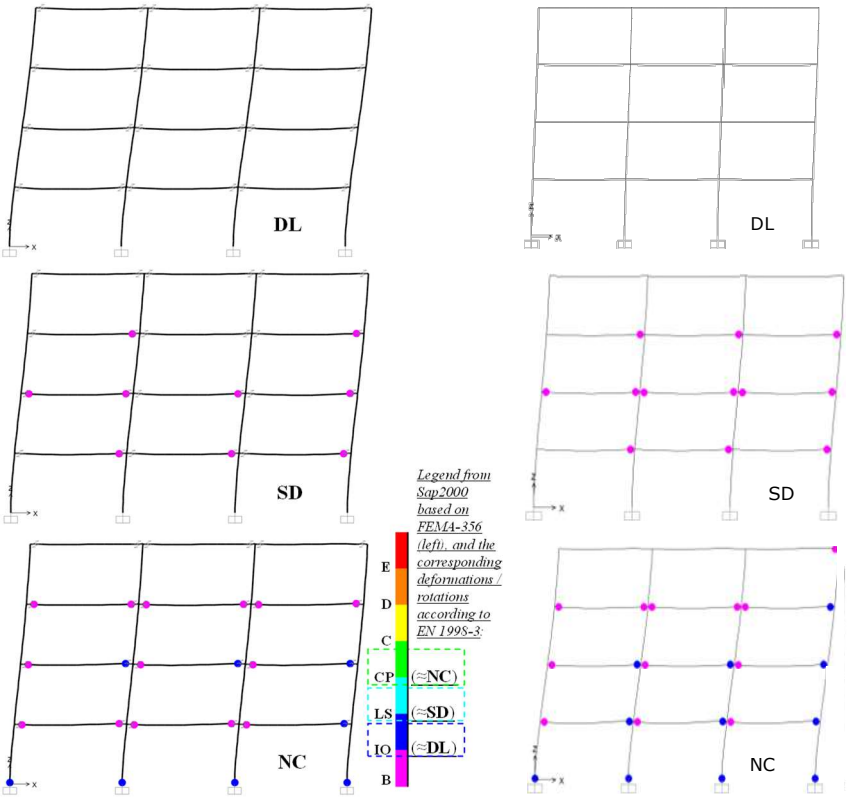

a) b)

Fig. A-143. *RHA with #A1* (the most unfavourable) results: a) damage state of *MRF-SF* with connections which included their stiffness; b) damage state of *MRF-SF* with rigid connections

The set of seven **accelerograms** which were used to perform ***Response-History Analysis*** in the current study are shown in Fig. A-144.

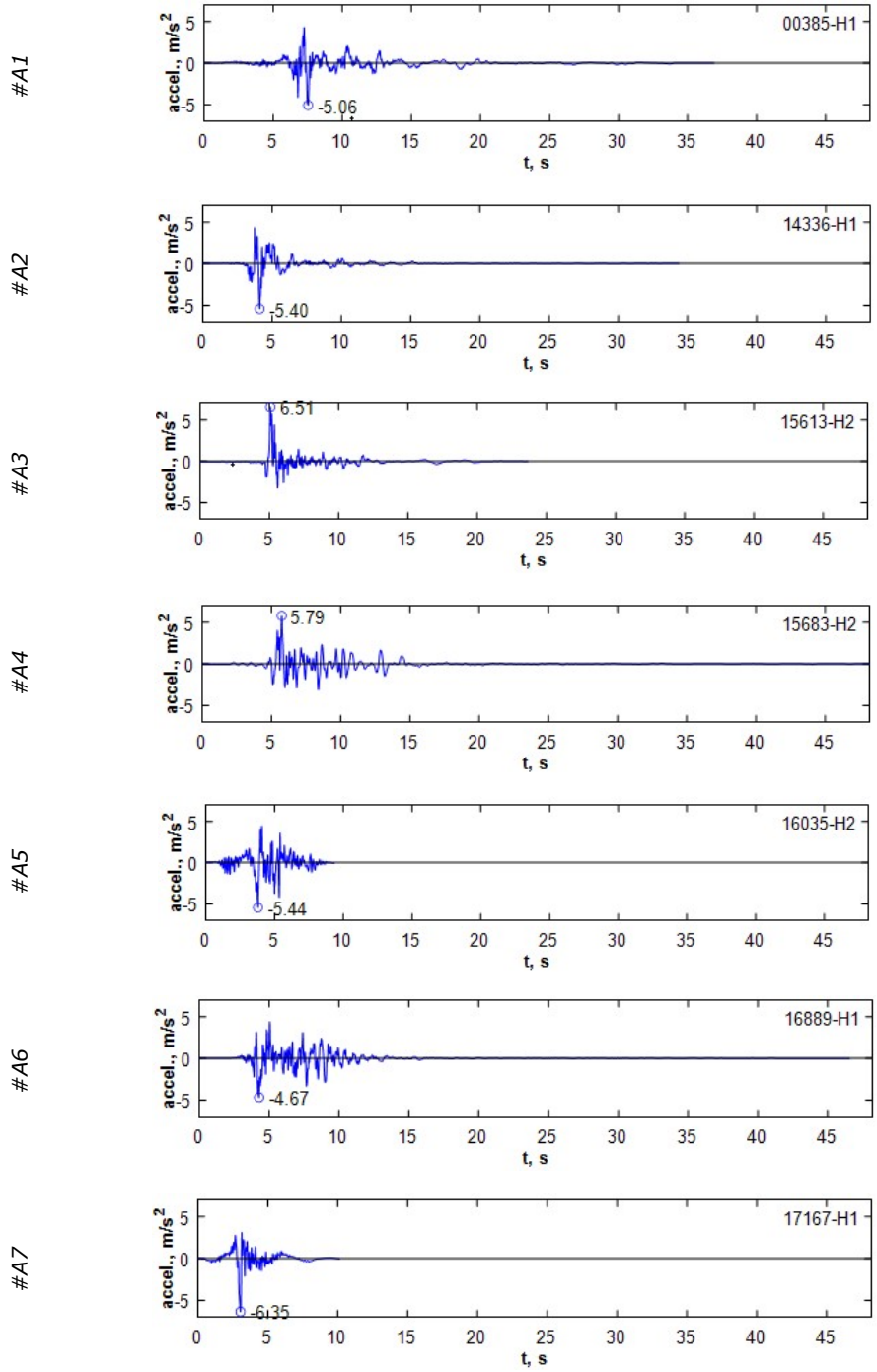

Fig. A-144. Accelerograms for Response History Analysis: acceleration vs. time